UNIVERSITY COLLEGE LONDON

Faculty of Mathematics and Physical Sciences

Department of Physics & Astronomy

PROBING GALAXY EVOLUTION THROUGH INTERSTELLAR DUST AND GAS PROPERTIES

Thesis submitted for the Degree of Doctor of Philosophy of the University of London

by

Isabella Lamperti

Supervisors:

Prof. Amélie Saintonge

Dr. Ilse De Looze

Examiners:

Prof. Richard Ellis

Dr. Caroline Bot

February 5, 2021

I, Isabella Lamperti, confirm that the work presented in this thesis is my own. Where information has been derived from other sources, I confirm that this has been indicated in the Thesis. In particular, I note these contributions:

- The work presented in Chapter 2 (and Appendix A) has been published in Lamperti et al. (2020). The reduction of the CO(3-2) data was conducted by Hao He for the xCOLD GASS sample and by Dr. Michael J. Koss for the BASS sample. The simulations of the galaxy gas profiles were performed by Prof. Amélie Saintonge.

- The work presented in Chapter 3 (and Appendix B) has been published in Lamperti et al. (2019). The observations with the JCMT telescope were conducted by several members of the JINGLE collaboration, including myself. The reduction of the SCUBA-2 data was conducted by Dr. Matthew W. L. Smith and is described in Smith et al. (2019).

- The work presented in Chapter 5 (and Appendix D) will shortly be submitted for publication in Lamperti, I., Harrison, C. M., Mainieri, V., et al. (in prep.). The reduction of the SINFONI data was conducted by Dr. Darshan Kakkad and Dr. Michele Perna and is described in Kakkad et al. (2020) and in M. Perna et al. (in prep.), respectively.

- I also acknowledge and thank (in order of Thesis Chapters) the following people, who have contributed to aspects of the research in this Thesis either via useful discussions with myself, or via the private communication of data or codes: Felix Priestly, Boris Leistedt, Frédéric Galliano, Luca Cortese, Lorne Whiteway, Taro Shimizu, Daizhong Liu, Gabriela Calistro-Rivera, Chiara Circosta, Ian Smail, Bitten Gullberg, Chian-Chou Chen, and the anonymous referees of the resulting publications.

Abstract

Molecular gas is an important ingredient in galaxy evolution, since it is the fuel of star formation. This Thesis explores different methods of measuring molecular gas masses in galaxies, and their applicability as a function of global galaxy properties, redshift, and presence of an active galactic nucleus (AGN). While CO(1-0) is the most commonly used emission line tracer of molecular gas for nearby galaxies, higher transitions such as CO(3-2) are more readily accessible for high-redshift galaxies. In order to connect studies at low and high redshift, we investigate which parameters are responsible for variations of the r_{31} = CO(3-2)/CO(1-0) luminosity line ratio in the local Universe and if the presence of an AGN influences the observed line ratio. Dust emission is often used as a molecular gas tracer in the literature, but to improve its accuracy, we need to know how dust properties change within the galaxy population and to quantify the uncertainties in measuring the dust masses. We study how the dust properties (in particular dust temperature and emissivity index) vary in a sample of ~ 500 nearby ($z < 0.05$) galaxies from the JINGLE and HRS surveys and derived scaling relations between the dust properties and other general galaxy properties. Moreover, we explore how the dust properties and scaling relations evolve with redshift using data from the A^{3}COSMOS catalogue. Dust emission in the far-infrared (FIR) is also used to trace star-formation, in particular in the case of AGN, where other star-formation tracers may be more heavily contaminated by the AGN emission. We combine FIR continuum observations with spatially resolved observations of the ionized gas in $z \sim 2$ AGN and we find no evidence of star-formation suppression due to AGN outflows.

Impact Statement

An important ingredient to understand the evolution of galaxies is the interstellar medium (ISM), which consists mainly of dust and gas. With the advent of the ALMA telescope, it is now possible to detect molecular lines and dust emission up to very high redshifts. In order to interpret these observations, it is necessary to develop the tools to measure the gas and dust content of galaxies from these observations and to characterize the variations of the ISM properties as a function of redshift and galaxy properties.

In this thesis, we perform an analysis of the dust properties of a statistical sample of about (~ 500) galaxies in the local Universe. Additionally, we expand the analysis up to redshift $z = 3.5$ and investigate how the dust properties evolve with cosmic time. This work will be used as a reference for the studies of dust in galaxies at low and high redshift.

We employ Bayesian statistics to extract as much information as possible from our data and exploit the potential of having a large sample of galaxies. We developed a code to model the far-infrared SED of galaxy samples within a hierarchical Bayesian framework. The power of the hierarchical method is that it uses the information from the distribution of properties of the galaxy population to place better constraints on the properties of the individual galaxies. This code allows us to break the degeneracy between dust parameters and for the first time to study their independent relations with galaxy properties, like for example the star-formation rate and stellar mass. This hierarchical SED fitting code can be applied to other samples of galaxies: for example, it is currently being used to study the submm excess in dwarf galaxies and the dust properties in a sample of early-type galaxies. Additionally, the hierarchical Bayesian framework can be applied to numerous problems within and outside Astrophysics.

Moreover, we investigate the impact of active galactic nuclei (AGN) on the interstellar

medium (ISM) properties of the host galaxies. The role of AGN in galaxy evolution and the relation between AGN and star-formation activity is an active field of research. This thesis contributes to advance our knowledge of the effect of AGN on the excitation of the CO molecules (a tracer of molecular gas), on the size of the dust traced by FIR emission in AGN host galaxies, and on the effect of ionized outflows from AGN on star-formation.

Two chapters of this thesis have been published in the Monthly Notices of the Royal Astronomical Society and The Astrophysical Journal, respectively, while the remaining two will be submitted for publication. This work was part of several large scientific collaborations (JINGLE, BASS, and SUPER surveys) and has contributed to reaching the scientific goals of these surveys. While the work presented in this thesis does not give a complete picture of the dust and gas properties of galaxies, it gives important constraints on the ISM properties to the scientific community and helps to advance our understanding of galaxy evolution.

Acknowledgements

There are many people that have supported me during this journey and without them this thesis would not have been possible.

First, I would like to thank my supervisor, Prof. Amélie Saintonge, for giving me the possibility to pursue a Ph.D., for supporting me during each step, both in the difficult and in more rewarding moments. Thank you especially for trusting me and my work, even more than I do. Thank you for the freedom you gave me in my research and for always being available. You have been a wonderful supervisor and I could not have wished any better.

I would like to thank my second supervisor, Dr. Ilse De Looze, for the support and encouragement during my Ph.D. Thank you for your positivity and enthusiasm about the projects. It has been a pleasure working with you.

I would like to thank my supervisors at ESO, Dr. Vicenzo Mainieri and Dr. Chris Harrison. Thank you for the opportunity to spend part of my Ph.D. at ESO, for the stimulating discussions and for allowing me to work on a 'SUPER' project.

I would also like to thank Prof. Serena Viti for the help in understanding and using `UCL-PDR`. Thank you to Dr. Mike Koss for the collaboration on the CO project, it is always fun working with you. Thank you to Dr. Michele Perna and Dr. Darshan Kakkad for providing me the reduced SINFONI maps and for bearing with all my emails and countless requests. Thank you to Dr. Matthew Smith for sharing with me my first observing run at JCMT: not a very successful run, but certainly the most adventurous!

I would also like to thank all my collaborators and co-authors of the papers which are part of this thesis for the useful comments and feedback, in particular the members of the JINGLE, BASS and SUPER collaborations.

I would like to thank Dr. Edd Edmonson and Dr. John Deacon for the help and support in the dealing with computers, in particular for solving all the issues that have arisen while using the super-computer Henrietta. I would like to thank Dr. Miguel Pereira-Santaella and the INTA institute for lending me a computer to be able to finish to write my thesis. I would like to thank Kay Nakum, Nelma Silva and Stella-Maria Chasiotis-Klingner for the help with the administrative part of the Ph.D.

I would also like to thank the current and past members of the UCL galaxies research group (Guido, Tom, Matt, Lucy, Maria, Chiara, Dirk, Tania, Paula, Seung Jae, Kanishk, and Iga) for the nice atmosphere and collaborative environment. Special thanks to Matt for the bit of humour you brought to each group meeting.

Thank you to the members of the Breakfast Club (Guido, Romain, Franzi, Maria, Andrew, Chiara, and Aayush), for the countless coffee breaks in the office which were the best way to start my day. Thank you also for the virtual coffee breaks during lock-down, they really helped me through those hard times.

A special thank you go to my 'Ph.D. brother' Guido for all the chats over coffee, the scientific discussions on the whiteboard and all the support along this journey, to Franzi for all the laughs and for being such a good friend and office mate, to Chiara for being a wonderful collaborator and for the support during the application for the ESO studentship, to Romain for bringing some 'Swissness' to the Astro group (I haven't forgotten about the plan of a post-viva fondue), to Aishwarya for the support during the last months of thesis writing, and to the 'ESO amigos' for the nice time in Munich. Thank you to my group of friends from the J-floor (Linda, Arianna, Caroline, Lorenza) for the nice weekends spent together visiting each others around Europe. A special thank you to Linda and Vlas for the warm welcome in Munich, and to Arianna for carefully proof-reading the introduction of this thesis. Thank you to Lei for your friendship and for helping me to appreciate the best side of living in London. Thank you to Pedro for always being there to listen to me. Thank you to my friends back home for the warm welcome every time I came back to Switzerland.

Finally, thank you to my family for the support and the love along this journey: it would not have been possible without you.

Contents

List of Figures

List of Tables

This page was intentionally left blank

Chapter 1

Introduction

1.1 Galaxy evolution along the star-formation main-sequence

Galaxies grow their stellar mass by turning gas into stars, a process known as star-formation. The level of star-formation varies between galaxies, within galaxies, and also as a function of cosmic time.

The evolution of the star-formation rate density (SFRD), defined as the star-formation rate (SFR, i.e. the amount of stellar mass formed per unit time) per unit volume (in units of [$M_\odot$ yr^{-1} Mpc^{-3}]) across cosmic history has been described by Madau & Shull (1996), Madau et al. (1998) and Lilly et al. (1996). They found that the SFRD reached a peak at redshift $z \sim 2$ and then declined exponentially until the present time. Figure 1.1, taken from Madau & Dickinson (2014), shows the SFRD as a function of redshift, where the SFRD is computed from far-ultraviolet (FUV) and infrared (IR) measurements. This figure is also known as the 'Lilly-Madau' plot.

At any given redshift up to at least $z \sim 3$, the majority of star-forming galaxies lie on a tight (about ± 0.3 dex scatter), nearly linear relation between SFR and stellar mass, which is called 'star-formation main-sequence' (MS, Noeske et al. 2007). About 90% of the cosmic star-formation between $z = 0 - 2.5$ occurs in galaxies on the MS (Rodighiero et al. 2011; Sargent et al. 2012; Rodighiero et al. 2015). This relation has been observed to hold at various redshifts: $z \sim 0$ (Brinchmann et al. 2004), $z \sim 1$ (Noeske et al. 2007; Elbaz et al. 2007), $z \sim 2$ (Daddi et al. 2007; Pannella et al. 2009; Rodighiero et al. 2011;

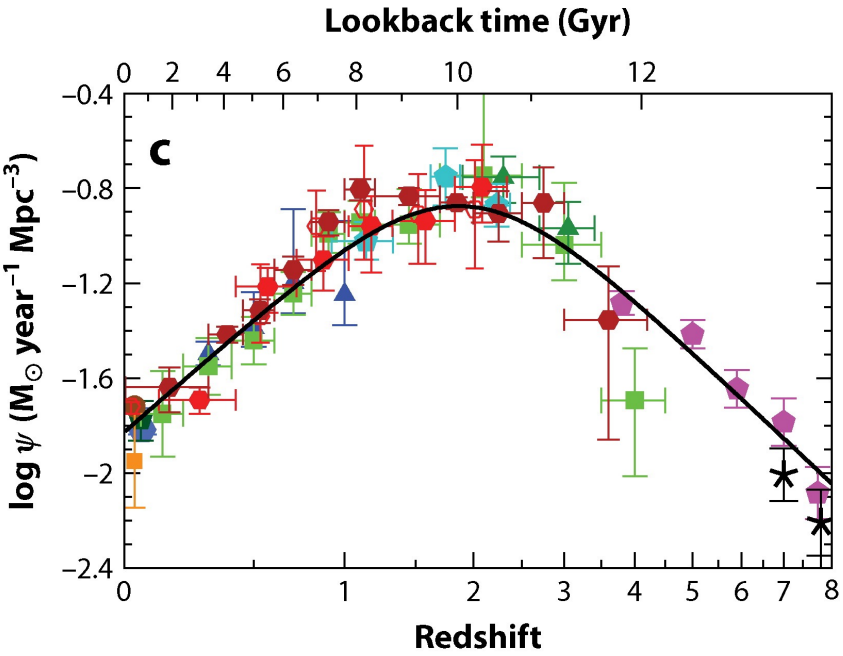

Figure 1.1. Figure from Madau & Dickinson (2014). Evolution of the cosmic SFR density as a function of time. The SFRD measurements come from rest-frame FUV and infrared observations. The solid line shows the best-fit SFR density. The SFR density peaks at $z \sim 1.9$, corresponding to ~ 3.5 Gyr after the Big Bang.

Whitaker et al. 2012), $z = 3 - 4$ (Daddi et al. 2009; Magdis et al. 2010; Heinis et al. 2013; Pannella et al. 2015). Figure 1.2 illustrates the star-formation main-sequence in the local Universe ($0.01 < z < 0.05$) using galaxies from the Sloan Digital Sky Survey (SDSS) DR7 (Abazajian et al. 2009).

The normalization of the main-sequence increases with redshift, i.e. the typical specific SFR (SSFR = SFR/M_*) for a galaxy on the MS was higher in the past. The SSFR on the MS varies as SSFR $\propto (1+z)^3$ up to $z \sim 2$, and as SSFR $\propto (1+z)^{1.5}$ at $z > 2$ (e.g. Lilly et al. 2013). This shift in the normalization has been observed between redshift $z = 0 - 4$ (Schreiber et al. 2015 , see Figure 1.3). Additionally, there is evidence for a flattening of the MS relation at high stellar masses ($\log M_*/M_\odot > 10.5$), that is more prominent at low redshift ($z < 2$) (Schreiber et al. 2015). The redshift evolution of the MS normalization can be explained either by an increase at high redshift of the gas fraction, i.e. of the fuel available for star-formation, or of the star-formation efficiency (SFE=SFR/M_{H_2}), i.e. the efficiency in forming stars from a given amount of molecular gas.

While most of the star-forming galaxies lie on the MS, some galaxies deviate from

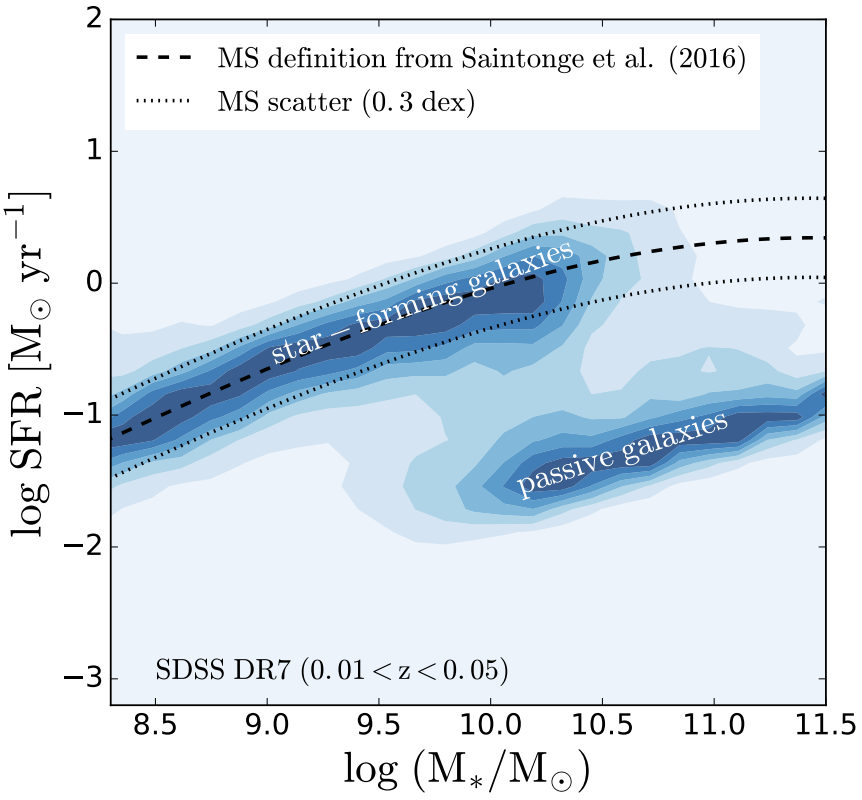

Figure 1.2. Illustration of the star-formation main-sequence (MS) in the nearby Universe. The contours show the distribution of galaxies from SDSS DR7 (Abazajian et al. 2009) in the redshift range $0.01 < z < 0.05$. The dashed curve shows the MS definition from Saintonge et al. (2016) and the 0.3 dex scatter around it (dotted curves). Passive galaxies have lower SSFR and lie below the MS.

this relation. Galaxies above the MS have higher SSFR and are called 'starburst' galaxies (Elbaz et al. 2011). There are also galaxies that lie below the MS, called 'passive galaxies'. In Figure 1.2, passive galaxies lie on a specific region (cloud) with log SFR$\sim$ [-1, -2]. This is mainly due to the difficulty in precisely measuring low SFR values. In reality, the range of SFRs of passive galaxies extends as a smooth sequence below the MS (Eales et al. 2017; Corcho-Caballero et al. 2020). The mechanism that causes the decline or the stopping of star-formation in galaxies is called 'quenching' and it is currently the object of many studies.

There are many mechanisms that can prevent a galaxy from forming stars. One possibility is that the galaxy runs out of fuel (i.e. gas) to form stars and the inflow of gas is not sufficient to maintain the current star-formation activity. Another possibility is that the gas is prevented from cooling, fragmenting and forming stars. The quenching mechanisms

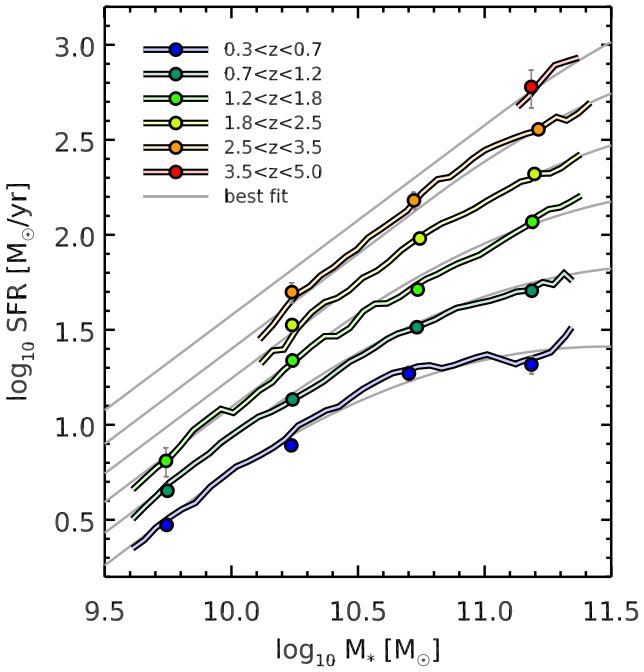

Figure 1.3. Figure from Schreiber et al. (2015). Evolution of the average SFR of star-forming galaxies with mass and redshift. The circles show their results from stacking. The light gray curves show the best-fit relation for the main-sequence.

are usually divided into internal and external (Smethurst et al. 2017). Examples of internal mechanisms are mass quenching (Peng et al. 2010, 2012), morphological quenching (Bluck et al. 2014; Fang et al. 2013), and feedback from Active Galactic Nuclei (AGN; e.g., review by Fabian 2012). Proposed external quenching mechanisms are mergers and environmental quenching (e.g., review by Boselli & Gavazzi 2006), which includes processes as starvation (Larson et al. 1980), ram pressure stripping (Gunn & Gott 1972), viscous stripping (Nulsen 1982) and thermal evaporation (Cowie & Songaila 1977).

In the next section, we explore in more detail the role that AGN feedback plays in galaxy evolution.

1.2 Role of AGN feedback in galaxy evolution

Most massive galaxies in the present day Universe host at their center a super-massive black hole (SMBH) with mass in the range $\sim 10^6 - 10^{10}$ $M_\odot$ (Kormendy & Richstone 1995; Schödel et al. 2003; Kormendy & Ho 2013). These black holes (BHs) grow mainly through episodes of radiatively-efficient accretion of gas, when they become extremely luminous and visible as AGN. AGN can release $\sim 10\%$ of the rest-mass energy of accreted material

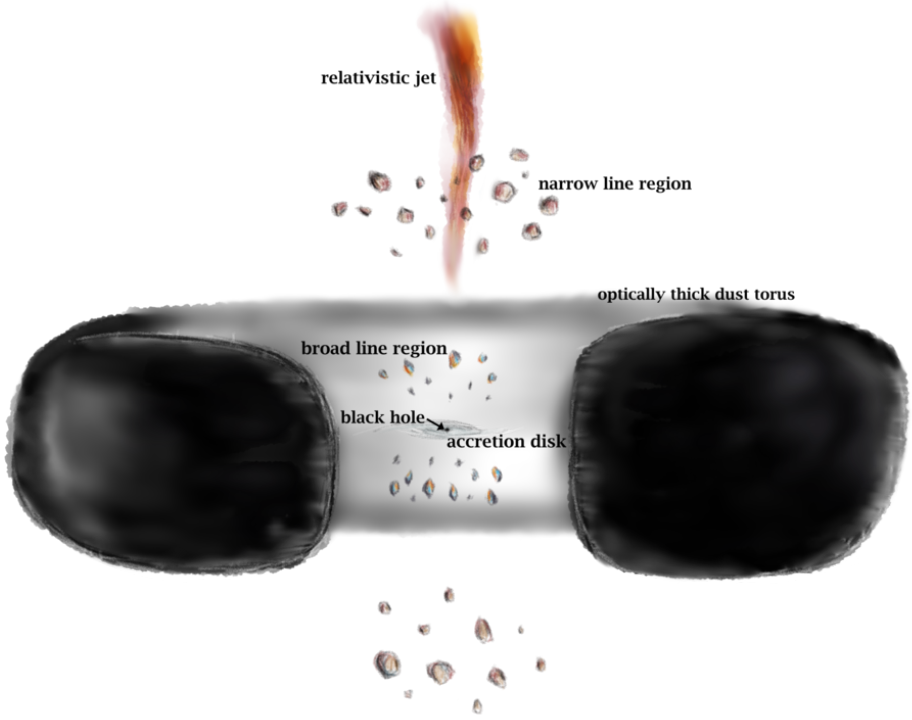

Figure 1.4. Figure from Oh (2014). Schematic illustration of the typical AGN structure, not to scale.

into their surroundings (Marconi et al. 2004; Shapiro et al. 1983). This energy can have an impact on the host galaxy: it has the potential to modify the condition of the gas and influence the star-formation in the host, an effect which is called 'AGN feedback'.

Before discussing the different forms of AGN feedback, we briefly describe the structure of the AGN and the characteristics of the AGN emission across wavelengths.

1.2.1 AGN structure and emission across the electromagnetic spectrum

AGN structure

In this section we describe the structure and the main components of an AGN. For more details, see for example Osterbrock & Ferland (2006), Fabian (2012), Netzer (2013), Yuan & Narayan (2014), Heckman & Best (2014), Ramos Almeida & Ricci (2017), Padovani (2017). A schematic illustration of the structure of a typical AGN is shown in Figure 1.4.

The central super-massive black hole is surrounded by an **accretion disk** (with a typical size $\sim 5 \times 10^{-4}$ pc for a black hole with mass $M_{BH} = 10^8$ $M_\odot$). In moderately to highly accreting black holes, the accretion disk is assumed to be optically thick and

geometrically thin (Shakura & Sunyaev 1973).

Around the accretion disk there is a hot ($\sim 10^9$ K) **corona** of hot and relativistic electrons. In the corona, the UV emission from the accretion disk is expected to Compton up-scatter to the X-ray part of the spectrum (Haardt & Maraschi 1991). The exact location, geometry and properties of the corona are currently an active field of research.

The **broad line region (BLR)** consists of gas clouds with high column density ($\sim 10^{23}$ cm^{-2}) and high velocity (~ 3000 km s^{-1}) (Netzer 2013). The BLR is located at a distance of $\sim 0.05 - 0.5$ pc for a black hole with mass $M_{BH} = 10^8$ M$_\odot$. The radiation from the accretion disk ionizes the clouds leading to the emission of permitted (e.g. Hα, Lyα) and semi-forbidden (e.g. C III]λ1909, O III]λ1663) emission lines. Some of the large-column-density clouds are partly neutral and produce strong lines of H I, Mg II, and Fe II (Netzer 2013). The name of this region originated from the Doppler broadening of the emission lines due to the high velocity of the gas clouds. AGN showing broad lines in their optical spectra are classified as Type 1.

A second region of gas clouds with smaller column densities ($\sim 10^{20-21}$ cm^{-2}) and velocities (< 1000 km s^{-1}) forms the **narrow line region (NLR)**, which extends from ~ 10 pc to ~ 1 kpc (Capetti et al. 1996). Due to the lower density ($\sim 10^4$ cm^{-3}), emission from the NLR includes permitted (e.g. Lyα) and forbidden (e.g. [N II]λ6584, [O III]λ5007) emission lines.

A dusty obscuring structure surrounding the central region of the AGN is commonly referred to as the '**torus**'. The size of the torus is $\sim 0.1 - 10$ pc (e.g., Packham et al. 2005; Radomski et al. 2008; Burtscher et al. 2013; Imanishi et al. 2016; García-Burillo et al. 2016; Gallimore et al. 2016). Depending on the viewing angle, the direct emission from the BLR may be obscured by the torus. AGN in which the BLR is obscured are classified as Type 2. The exact geometry of the torus is currently debated. Different models considering smooth, clumpy and cloud-like distributions of material have been proposed (e.g., Pier & Krolik 1992; Nenkova et al. 2002; Dullemond & van Bemmel 2005; Elitzur & Shlosman 2006; Hönig & Kishimoto 2010; Assef et al. 2013). Recently, the parsec-scale environment of the AGN has been spatially-resolved thanks to high-angular-resolution IR and submillimeter interferometric observations. Emission from molecular lines showed the presence of a large, massive disk (e.g., Gallimore et al. 2016; García-Burillo et al. 2016; Imanishi et al. 2016; Alonso-Herrero et al. 2018, 2019; Combes et al. 2019), while the IR observations revealed a strong polar component (e.g., Hönig et al. 2012, 2013; López-

Gonzaga et al. 2014; Tristram et al. 2014; López-Gonzaga et al. 2016; Leftley et al. 2018), which can be interpreted as a dusty wind (Hönig & Kishimoto 2017; Stalevski et al. 2017). Hönig (2019) presented a model which unifies these two observations and consists of a geometrically-thin disk in the equatorial plane and a hollow dusty cone toward the polar region.

Some AGN show **radio jets** that can reach up to a few Mpc in size (e.g., Hada et al. 2013; Solovyov & Verkhodanov 2011; Clarke et al. 2017). Currently, about $10-30\%$ of AGN are classified as 'radio loud' (e.g., White et al. 2000; Mushotzky 2004), although different definitions of radio-loudness are used in the literature (for example a high level of radio emission, a high ratio of radio-to-optical luminosity or the presence of powerful radio jets).

AGN emission

AGN emit energy across the whole electromagnetic spectrum and they can be identified through specific features in their spectral energy distribution (SED). An illustration of an AGN SED from the radio to the X-ray is shown in Figure 1.5. The main characteristics of the AGN continuum SED are (see, e.g., Elvis et al. 1994; Risaliti & Elvis 2004; Padovani 2017):

- **Optical/ultra-violet (UV)**: Thermal emission from the accretion disk of the AGN is responsible for producing the primary emission in the optical/UV, dominating the continuum emission in the range $\sim 300-3000$ Å. For an optically thick accretion disk (e.g., Shakura & Sunyaev 1973), the resulting continuum emission would be thermal with a black-body temperature of $\sim 2\times10^5$ K, peaking in the UV at $\sim 10-400$ nm for a typical AGN with black hole mass 10^8 $M_\odot$ and accretion rate $L_{bol}/L_{Edd}\sim 0.1$. The majority of the AGN bolometric luminosity is emitted in the UV.

- **X-ray**: X-ray emission of AGN (in the energy range $\sim 0.1-300$ keV) can be divided in different components: a primary power law, a soft excess at energies < 1 keV, and a reflection component (Boissay et al. 2016). The primary X-ray emission is produced in the corona region by inverse Compton scattering of UV photons produced by the accretion disk. This emission is approximated by a power law with photon index $\Gamma \sim 1.8-2$ (e.g., Nandra & Pounds 1994; Mainieri et al. 2002; Piconcelli et al. 2005; Ricci et al. 2011), with an high energy cut-off at a few hundreds keV (e.g.,

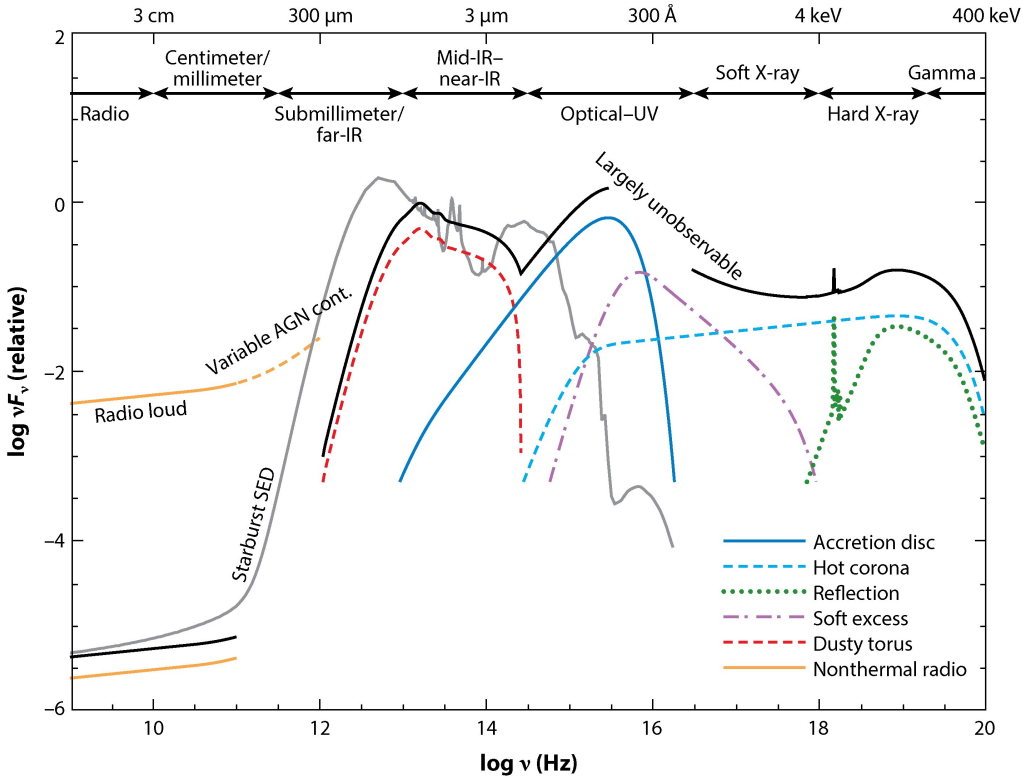

Figure 1.5. Figure from Hickox & Alexander (2018), adapted from Harrison (2014). Schematic representation of the SED of an unobscured AGN (black curve), separated into the main components (coloured curves). The illustration of an SED of a star-forming galaxy is shown for comparison (grey curve).

Ricci et al. 2017). The soft-excess is usually observed below 2 keV and it originates from various processes including blurred relativistic reflection and comptonisation of accretion disk photons in colder plasma (Ricci et al. 2017 and references therein). The reflection component is produced when the primary emission is reprocessed by the torus and/or the accretion disk (e.g., George & Fabian 1991). The two main features of the reflection spectrum are the iron Kα line at 6.4 keV and the Compton 'hump' peaking at $\sim$ 30 keV (e.g., Matt et al. 1991; Nandra & Pounds 1994; Murphy & Yaqoob 2009).

A large fraction (from 5% to 40%) of the AGN bolometric luminosity is emitted in the X-rays (Ward et al. 1987). Since AGN are the only sources capable of producing X-ray luminosity above a given threshold, X-ray selection is one of the most reliable tool to separate AGN from inactive galaxies. However, X-rays are absorbed by obscuring material around the AGN, especially in the low energy band (soft X-ray

< 10 keV). The most obscured AGN, so called Compton-thick AGN (with column densities $> 10^{24}$ cm^{-2}), are hard to identify with X-ray imaging below 10 keV, which is the accessible range to most of the more sensitive X-ray satellites at the moment, like *Chandra* (Weisskopf et al. 2000) and *XMM/Newton* (Jansen et al. 2001).

- **Mid-infrared (MIR)**: The emission between a few μm to $\sim$70 μm is mainly due to thermal emission by hot dust heated by the AGN, with temperatures in the range $50 - 1000$ K. This emission is characterized by a bump at about $10 - 30$ μm and a steep decrease at longer wavelengths due to the decreasing emitting efficiency of dust grains (e.g., Pier & Krolik 1992; Polletta et al. 2000).

- **Sub-millimeter/far-infrared (FIR)**: In the majority of AGN, this wavelength regime is dominated by thermal emission from cool dust heated by the star-formation of the host galaxy. The contribution from dust heated by the AGN is usually considered to be minimal, even though some works show that AGN light reprocessed by diffuse dust may contribute non-negligibly to the FIR emission, at least in the central region of the galaxy (e.g., Schneider et al. 2015; Symeonidis et al. 2016; Symeonidis 2017; Viaene et al. 2020). For radio-loud AGN, the non-thermal emission, which peaks in the radio, can contribute substantially also to the emission in the submm/FIR regime.

- **Radio**: In the radio regime, the AGN emission is mainly due to non-thermal synchrotron radiation which originates from the acceleration of charged particles due to their movements through magnetic fields. The synchrotron emission can be approximated by a power law, with a typical median spectral index of -0.7 (Smolčić et al. 2017).

1.2.2 AGN feedback

Models of galaxy formation require energy or momentum injection by AGN into the surrounding gas in the most massive galaxies to match the observations. For example, AGN feedback is required to explain the low efficiency in forming stars in the most massive halos (Somerville et al. 2008; Behroozi et al. 2013 , see Figure 1.6). AGN feedback is also necessary to explain the low rate of gas cooling in galaxy clusters (Fabian 1994). Moreover, AGN feedback is one possible mechanism that can explain the quenching of massive galaxies and the population of 'red' passive massive galaxies (Strateva et al. 2001). The scaling

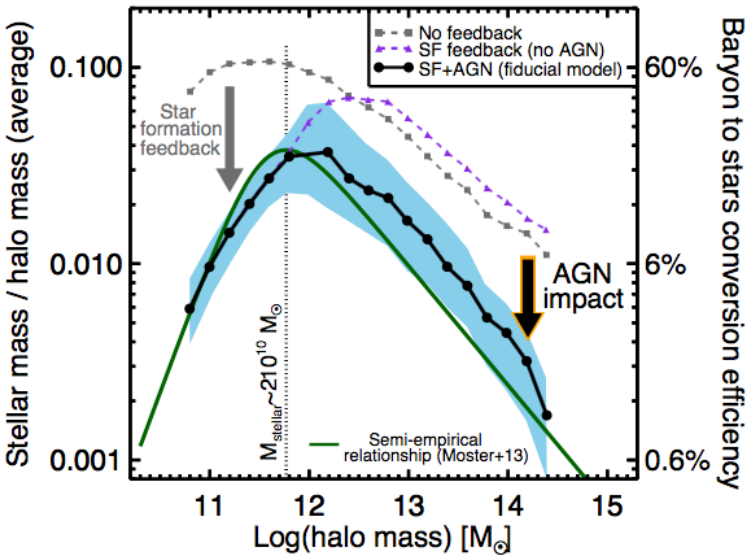

Figure 1.6. Figure from Harrison (2017). Stellar mass to halo mass ratio as a function of halo mass for three different runs of simulations by Somerville et al. (2008) and the semi-empirical relationship by Moster et al. (2013). The right y-axis shows the efficiency for turning baryons into stars. Including star-formation feedback in the model reduces the efficiency of converting baryons into stars in low mass halos, while AGN feedback reduces the efficiency in massive halos.

relations between BH mass and host galaxy properties (as for example the stellar mass and velocity dispersion of the bulge) have been seen as evidence of co-evolution between the black hole and the host (Magorrian et al. 1998; Kormendy & Ho 2013). However, it has been argued that the BH-galaxy bulge mass relation could arise also from repeated mergers, with no need of AGN feedback (e.g. Peng 2007; Jahnke & Macciò 2011).

There are two main feedback modes:

- **Radiative (or quasar/wind) mode**: In this feedback mode, radiation pressure and winds from the AGN accretion disk couple with the ISM gas generating shocks and propagating in the form of high velocity outflows through the galaxy (e.g., King & Pounds 2015; Costa et al. 2018). These outflows could ultimately be responsible for the removal or destruction of cold molecular gas from the galaxy, reducing the fuel available for star-formation (e.g., Hambrick et al. 2011; Fabian 2012; Vogelsberger et al. 2013; Roos et al. 2015; Hopkins et al. 2016; Bieri et al. 2017). This mode is found in high-luminosity, high accretion rate AGN, and is most effective at $z \sim 2-3$, when AGN were more active and galaxies were more gas-rich. AGN outflows have indeed been observed in high-luminosity objects (AGN bolometric luminosity

$> 10^{46}$ erg s^{-1}) at redshifts $z \sim 2-3$ (e.g. Cano-Díaz et al. 2012; Harrison et al. 2012; Carniani et al. 2015). This feedback mode is more common in galaxies with on-going star-formation and young stellar populations (Hickox et al. 2009; Heckman & Best 2014).

- **Kinetic (or mechanical/jet/radio/maintenance) mode**: This feedback mode keeps the gas hot, preventing the gas from cooling and fragmenting to form stars (e.g. Peterson & Fabian 2006; McNamara & Nulsen 2007; Somerville et al. 2008; Fabian 2012; Davé et al. 2019). The kinetic mode is found in radiatively inefficient AGN with low accretion rate and it is associated with powerful radio jets (e.g. Fabian 2012; Harrison 2017). The mechanical energy of jets can for example create bubbles in the hot gas, that are observed in X-ray images of galaxy clusters with a central AGN (e.g. Bîrzan et al. 2004; Rafferty et al. 2006; McNamara & Nulsen 2012; Vantyghem et al. 2014). Rather than removing gas, this mode of AGN feedback acts by heating the gas, preventing star-formation. In numerical simulations and semi-analytic models, the kinetic mode is often used as a way to keep passive galaxies quiescent by preventing them from re-starting star-formation (e.g., Matthews et al. 1964; Best et al. 2005; Hickox et al. 2009; Smolčić et al. 2009). This feedback mode is predominantly found in massive galaxies ($M_*> 10^{11}$ M$_\odot$) with old stellar populations (Hickox et al. 2009; Heckman & Best 2014).

AGN feedback is usually invoked to explain the suppression of star-formation and the quenching of galaxies, but AGN feedback can also enhance star-formation ('positive' feedback). For example, the observation of star-formation near the edge of an outflow has been interpreted as evidence that the outflow can shock the gas and trigger star-formation (Cresci et al. 2015b). Recently, some studies have also claimed to detect star-formation within ionized outflows (Maiolino et al. 2017; Gallagher et al. 2019; Perna et al. 2020). However, the amount of star-formation detected in the outflow is only a small fraction (∼2%) of the galaxy's total star-formation.

1.2.3 Observations of AGN outflows

AGN outflows have been observed in different gas phases: ionized, neutral atomic and molecular. Since outflows have a multi-phase nature, it is important to trace all phases to measure the overall mass of the outflowing gas and the kinetic energies carried by it

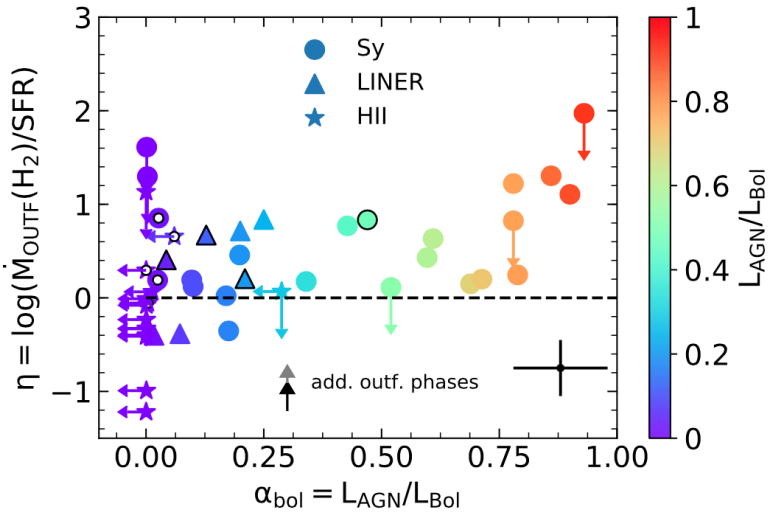

Figure 1.7. Figure from Fluetsch et al. (2019). Molecular gas mass loading factor (defined as molecular outflow rate divided by SFR, $\eta = \dot{M}_{OUTF}(H_2)/\mathrm{SFR}$) as a function of AGN fractional contribution to the bolometric luminosity (L_{AGN}/L_{bol}). Circles indicate Seyfert host-galaxies, triangles indicate LINERs and stars are purely star-forming galaxies. The data points with black edges are molecular outflows inferred from OH measurements by González-Alfonso et al. (2017). The black dashed line shows the relation for $\dot{M}_{OUTF}(H_2)$ =SFR. For objects that lie above this line, the molecular gas is being removed by outflows faster than it can be formed into stars.

(Cicone et al. 2018). The 'mass outflow rate' quantifies how much gas is carried away by the outflow per unit time. This quantity is usually compared to the SFR to assess whether the amount of gas impacted by the outflow is large enough to significantly affect the SFR of the host galaxy. For example, Fluetsch et al. (2019) compared the molecular mass-outflow rates to the SFRs in a sample of nearby AGN, LINERs and star-forming galaxies (see Figure 1.7). They show that the mass-outflow rate can be several times higher than the SFR in the objects with the highest AGN contribution to the total luminosity of the galaxy.

The characteristics of the main outflow phases are summarized below:

- **Highly ionized**: This phase is traced principally by X-ray absorption lines. It has an average gas temperature $T_{gas} = 10^6 - 10^7$ K and an average gas density $n_{gas} = 10^6 - 10^8$ cm^{-3} (Cicone et al. 2018). Absorptions lines from highly ionized iron (Fe XXV and Fe XXVI) in the hard X-ray ($E > 6$ keV) can trace the innermost gas close to the accretion disk (< 1 pc; Tombesi et al. 2010, 2013; Nardini et al.

2015). By comparing the energetics of these nuclear outflows with that of outflows observed at larger scales it is possible to constrain how much energy is transferred from the nucleus to kpc scales (Feruglio et al. 2017; Marasco et al. 2020). However, this comparison is complicated by AGN variability which may introduce a time-scale difference between the outflows at small and large spatial-scales.

- **Ionized**: The primary tracers are broad components of the optical [O III] and Hα emission lines. The average gas temperature of this phase is $10^3 - 10^4$ K and $n_{gas} = 10^2 - 10^4$ cm^{-3} (Cicone et al. 2018). Ionized outflows have been studied in thousands of low-redshift AGN, mostly from the Sloan Digital Sky Survey (e.g., Woo et al. 2016), and in a few hundreds of AGN up to redshift $z \sim 3$ (e.g., Harrison et al. 2012; Förster Schreiber et al. 2014; Brusa et al. 2015; Carniani et al. 2016; Kakkad et al. 2020). There is evidence that ionized outflows are present in all of the AGN above a certain bolometric luminosity (Woo et al. 2016). The mass-loss rates of the ionized phase can be ≥ 100 M$_\odot$ yr^{-1} in luminous AGN, similar to those of the molecular phase (e.g., Fiore et al. 2017). However, there are large uncertainties on these quantities due to the difficulty in quantifying the effect of metallicity, extinction and excitation. Additional uncertainties are due to the difficulty in measuring the electron density and determining the size and geometry of the outflows (see discussion in Harrison et al. 2018).

- **Neutral atomic**: The typical tracers are the NaD absorption doublet (Cazzoli et al. 2016; Perna et al. 2017; Concas et al. 2019; Roberts-Borsani & Saintonge 2019), the HI 21cm line in absorption (Morganti et al. 2016), and the [C II] emission line (Maiolino et al. 2012; Cicone et al. 2015; Janssen et al. 2016; Bischetti et al. 2019b). The neutral atomic phase has average $T_{gas} = 10^2 - 10^3$ K and $n_{gas} = 1 - 10^2$ cm^{-3} (Cicone et al. 2018). Concas et al. (2019) examined a sample of 600,000 nearby galaxies from SDSS and reported that neutral atomic outflows are found both in AGN and non-AGN star-forming galaxies, while ionized outflows traced by [O III] are detected only in AGN or composite AGN/star-forming systems. Roberts-Borsani & Saintonge (2019) also reported that neutral outflows are not enhanced in nearby galaxies hosting an AGN with respect to galaxies with no AGN.

- **Molecular**: The molecular phase is usually observed using CO, OH, or H_2 infrared lines. The gas in molecular outflows has average $T_{gas} = 10 - 100$ K and densities

$n_{gas} \geq 10^3$ cm^{-3} (Cicone et al. 2018). Molecular outflows have been observed in several nearby AGN host galaxies (e.g., Feruglio et al. 2010; Cicone et al. 2012, 2014; Fluetsch et al. 2019). The molecular mass-outflow rates can be up to several 100 $M_\odot$ yr^{-1} (Sturm et al. 2011; Cicone et al. 2014). These high outflow rates show that the AGN have the potential to directly impact the cold molecular gas reservoir, which is linked to star-formation.

It is important to measure the mass outflow rates in the different gas phases to understand which gas phase is more affected by AGN feedback (e.g., Fiore et al. 2017; Bischetti et al. 2019a; Fluetsch et al. 2020). Only a small number of studies have characterized multiple outflow phases in the same galaxy. For example, studies of the AGN IC 5063 found that the kinematics of the ionized, neutral atomic and molecular outflow phases are very similar (Morganti et al. 2015; Oosterloo et al. 2017). Multi-phase observations of two other targets (HE 1353-1917 and IRAS F08572+3915) revealed that the molecular and ionized outflows have a similar spatial distributions (Husemann et al. 2019; Herrera-Camus et al. 2020). Recently, Fluetsch et al. (2020) collected information about the ionized, neutral atomic and molecular gas phase for a sample of 26 local luminous and ultra-luminous infrared galaxies ((U)LIRGs), including AGN and non-AGN. They found that the molecular phase accounts for more than 60% of the mass-outflow rate in most objects, while the neutral atomic phase contributes $\sim$ 10% and the ionized phase has a negligible contribution.

1.2.4 AGN and star-formation

The impact of AGN feedback on star-formation has been investigated using different methods. One possibility is to use spatially resolved observations to look for evidence of star-formation suppression at the location of the outflow. Another approach is to compare the star-formation properties of statistical samples of galaxies with and without an AGN.

Spatially resolved observations of a few AGN at $z \sim 1-3$ found evidence that the Hα emission, a tracer of star-formation, is suppressed at the location of the ionized outflow (Cano-Díaz et al. 2012; Cresci et al. 2015b; Carniani et al. 2016). These observations may indicate that the outflow is reducing star-formation, but an alternative explanation is that the outflow propagates preferentially in the path of least resistance, avoiding the dense star-forming regions (Gabor & Bournaud 2014). On the other hand, AGN-driven outflows

have also been observed to be coincident with high levels of star-formation (Cicone et al. 2014; Wylezalek et al. 2016). Even though negative AGN feedback on star-formation has been observed inside galaxies, it is important to determine whether AGN can suppress star-formation in the entire host galaxy or only locally, and whether AGN feedback can keep the galaxy 'quenched' for a long period.

Several studies have investigated the star-formation rates in large samples of AGN host galaxies, comparing them with matched samples of non-AGN galaxies. Studies of mechanical dominated (radio) AGN find that they are predominantly located in low-SFR host galaxies (Hardcastle et al. 2013; Ellison et al. 2016; Leslie et al. 2016). For radiative-dominated AGN, the results are less clear. Different studies have reported star-formation enhanced in the most luminous AGN (Lutz et al. 2010; Bonfield et al. 2011), suppressed in the most luminous AGN (Page et al. 2012), unrelated to AGN luminosity (Mainieri et al. 2011), or both reduced and enhanced depending on the wavelength used to measure the AGN luminosity (Zinn et al. 2013; Karouzos et al. 2014) or depending on the position with respect to the main-sequence (Masoura et al. 2018). The difference in these results may be explained by the different samples and approaches used (Harrison 2017). For example, it is challenging to convert photometric data into SFR because of dust attenuation in the optical and UV and because the AGN contribution needs to be accurately removed from all wavelengths. Additionally, sample selection can affect the results. For instance, surveys that consider only AGN with FIR detections are biased toward higher SFRs. Moreover, it is important to take into account the correlation between SFR and both stellar mass and redshift. A relation between SFR and AGN luminosity could be partly due to the fact that the most luminous AGN are found in high stellar-mass galaxies (see discussion in Harrison 2017). Studies that have carefully controlled for stellar mass and redshift and that have used uniform techniques across their sample find that the average SFR is not related to the AGN luminosity (Rosario et al. 2013; Azadi et al. 2015; Stanley et al. 2015; Shimizu et al. 2017).

Difficulties in assessing the impact of AGN on star-formation are related also to the different time-scales of AGN episodes and star-formation variation. The AGN luminosity can vary on time-scales of < 1 Myr, significantly shorter than the time-scales of star-formation episodes (e.g., Hickox et al. 2014; King & Nixon 2015; Schawinski et al. 2015). Consequently, the instantaneous AGN luminosity is not a good estimate of the average AGN activity over a long time-scale (see Figure 1.8). Thus, it is not surprising that it is

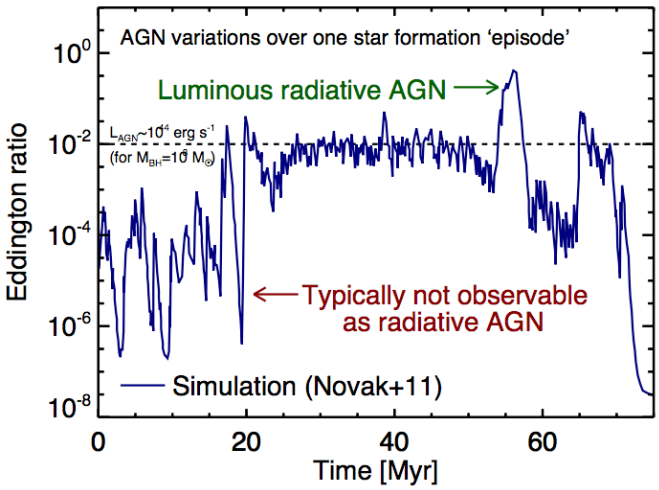

Figure 1.8. Illustration of AGN variability from Harrison (2017). Eddington ratio (defines as AGN bolometric luminosity divided by the Eddington luminosity) as a function of time from an example hydrodynamical simulation (Novak et al. 2011). AGN luminosities can vary on time scales $\lesssim$ 1 Myr, which are much shorter than the typical timescale of star-formation episodes ($\gtrsim$ 100 Myrs).

difficult to find a link between the AGN luminosity and the average SFR. Multiple AGN episodes may be required to significantly suppress the star-formation in the host galaxy over a time-scale of hundreds of Myrs (Gabor & Bournaud 2014).

In this context, combining observations with simulations can be useful to investigate the role of AGN in galaxy evolution. Scholtz et al. (2018) compared observations with model predictions from the EAGLE hydrodynamical simulation (Evolution and Assembly of GaLaxies and their Environments, Schaye et al. 2015). They found that the simulation does not predict a strong relationship between the SSFR distribution and the instantaneous AGN luminosity. They also found that a signature of AGN feedback is a broader distribution of SSFR for all galaxies with stellar masses $\geq 10^{10}$ M_*, not only for galaxies hosting an AGN. Simulations with and without AGN feedback have also shown that AGN are responsible for the bending of the main-sequence of star-formation at high stellar masses and for reducing the total number of massive galaxies (Schaye et al. 2015; Crain et al. 2015; Beckmann et al. 2017).

A key ingredient for understanding galaxy evolution is the relation between the fuel of star-formation, i.e. molecular gas, and the star-formation activity of galaxies. Many studies investigate the molecular gas content of galaxies with and without AGN, in order to understand whether the presence of an AGN is related to the molecular gas, finding

contradicting results. At low redshift ($z < 1$), most studies found no difference between AGN and non-AGN (e.g. Saintonge et al. 2012; Husemann et al. 2017; Saintonge et al. 2017; Rosario et al. 2018; Jarvis et al. 2020; Shangguan et al. 2020). At high redshift, the picture is more complicated, with some studies reporting lower molecular gas fractions in AGN (Carilli & Walter 2013; Brusa et al. 2015; Carniani et al. 2017; Kakkad et al. 2017; Fiore et al. 2017; Perna et al. 2018; Talia et al. 2018; Loiacono et al. 2019), and some works finding no difference between AGN and non-AGN (Kirkpatrick et al. 2019; Herrera-Camus et al. 2019; Spingola et al. 2020). It is possible that these different results at different redshifts are related to the change of ISM conditions with cosmic time, since the impact of AGN outflows depends on the properties of the medium through which AGN winds expand.

In the next section, we discuss the role of molecular gas in the context of galaxy evolution and the different methods used to measure the molecular gas content.

1.3 Molecular gas

Molecular gas plays an important role in the formation of stars and consequently in the evolution of galaxies. Stars are formed from the collapse of dusty molecular gas (McKee & Ostriker 2007; Kennicutt & Evans 2012). In the nearby Universe, stars form in dense ($n(H_2) \sim 10^2 - 10^5$ cm^{-3}), and cold ($T \sim 10 - 40$ K) molecular clouds, with masses of $10^4 - 10^{6.5}$ M$_\odot$ and radii of $\sim 25 - 50$ pc (Solomon et al. 1987; McKee & Ostriker 2007; Bolatto et al. 2008). The relation between star-formation and gas extends also to galaxy scales. The global star-formation of galaxies is related to their gas content, as it is shown by the Kennicutt-Schmidt law (Schmidt 1959; Kennicutt 1998), a relation between the star-formation rate surface density and the cold gas surface density.

An important quantity connecting star-formation and molecular gas is the molecular gas depletion time (defined as $t_{dep} = M(H_2)/SFR$), which represents the time in which the molecular gas would be depleted given the current SFR of the galaxy, assuming no exchange of gas with the intergalactic medium (IGM). The inverse of t_{dep} is called 'star-formation efficiency' ($SFE = SFR/M(H_2)$). It has been shown that t_{dep} depends mainly on the distance from the MS, with galaxies above the MS having shorter t_{dep}, both in the nearby Universe (Saintonge et al. 2013; Popesso et al. 2020) and at high redshift (Tacconi et al. 2013; Genzel et al. 2015; Scoville et al. 2017; Liu et al. 2019b).

We know that the star-formation activity peaked at $z \sim 2$ and then decreased (Madau & Dickinson 2014 , see Figure 1.1). The higher star-formation in the past could be explained by an higher gas mass fraction in galaxies at high-z, or by a higher efficiency in forming stars. Studies of the molecular gas at high redshift suggest that the former process, rather than the latter, is the main explanation for the higher SFR at $z \sim 2$ (e.g., Daddi et al. 2010; Riechers et al. 2011; Ivison et al. 2011; Tacconi et al. 2013, 2018; Bothwell et al. 2013; Genzel et al. 2015; Scoville et al. 2017; Kaasinen et al. 2019).

Several studies measured the cosmic molecular-gas mass density ($\rho(H2)$) as a function of cosmic time (Decarli et al. 2014, 2016; Walter et al. 2016; Aravena et al. 2016; Riechers et al. 2019; Lenkić et al. 2020). They find that $\rho(H2)$ increases between $z = 5$ and $z = 1$, and then decreases steeply from $z = 1$ to $z = 0$ (see Figure 1.9). This behaviour follows closely the evolution of the cosmic SFR density in this redshift range. However, due to the difficulty in measuring molecular gas masses for large samples of galaxies at high redshift, the uncertainties on these measurements remain large (see Figure 1.9). In the next section, we will give an overview of the main methods used to measure the molecular gas content of galaxies.

1.3.1 Methods to measure molecular gas masses

In order to study the link between the molecular gas content of galaxies and the process of star-formation on galaxy scales, it is necessary to have a reliable method to measure the molecular gas mass. The majority of the molecular gas mass in galaxies consists of molecular hydrogen (H_2). Unfortunately, the H_2 molecule can not be observed directly, because it lacks a permanent dipole moment and its quadrupole transitions require high excitation temperatures (e.g. Omont 2007). Additionally, due to its low mass, the rotational transitions of the H_2 molecule require high temperatures to excite, making most of H_2 in typical clouds invisible (Kennicutt & Evans 2012). Therefore we need to rely on indirect methods to measure the cold molecular gas masses in galaxies.

In the following we describe the most commonly used methods (see Hodge & da Cunha 2020):

- **CO lines observations:** Carbon monoxide (^{12}CO) is the second most abundant molecule in the interstellar medium after H_2. The low level rotational transition from the first excited state $J = 1$ to $J = 0$, CO(1-0), is the most common tracer

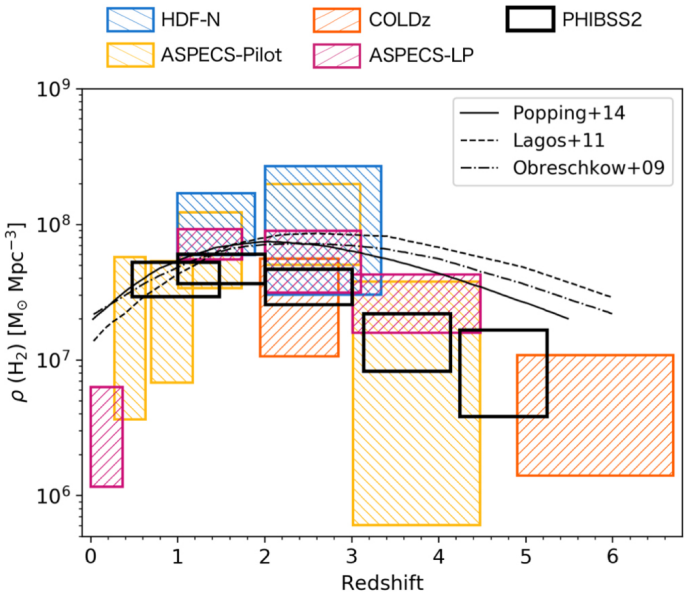

Figure 1.9. Figure from Lenkić et al. (2020). Evolution of the molecular gas mass density with redshift. The black boxes represent the constraints from the PHIBSS2 data (Lenkić et al. 2020). The orange right-hatched boxes show the constraints from the VLA COLDz measurements (Riechers et al. 2019), the purple right-hatched boxes the constraints from the ASPECS LP measurements (Decarli et al. 2019), the yellow left-hatched boxes the constraints from Decarli et al. (2016), and the blue left-hatched boxes the constraints from Walter et al. (2014). The black curves show the predictions from models derived by Obreschkow et al. (2009), Lagos et al. (2011), and Popping et al. (2014a,b).

used in the nearby Universe (e.g., Saintonge et al. 2011a; Kennicutt & Evans 2012; Saintonge et al. 2017), since its frequency (115.27 GHz) is accessible using submm and radio telescopes. CO(1-0) has a low critical density (2×10^3 cm^{-3}) and low excitation temperature (5.5 K) (Carilli & Walter 2013), therefore it is well suited to trace also the more diffuse gas (Dickman et al. 1986).

The CO(1-0) luminosity can be converted to molecular gas mass by applying a 'CO conversion factor' $\alpha_{CO} = M_{mol}/L'_{CO}$. It has been shown that α_{CO} varies with galaxy properties, and is thus a source of uncertainties (Bolatto et al. 2013). For example, several studies suggest that the CO conversion factor decreases with increasing metallicity (e.g., Leroy et al. 2011; Bolatto et al. 2013). Additionally, CO suffers from photo-dissociation effects. CO is more easily dissociated by the radiation field than H_2, and this effect may lead to underestimate the amount of molecular hydrogen. Figure 1.10 shows a schematic of a photo-dissociation region (PDR), i.e. a region of the ISM dominated by far-ultraviolet (FUV) photons (Hollenbach &

Tielens 1999). The diagram illustrates the different regions where H_2 is traced by CO and where CO instead is photo-dissociated. The CO conversion factor has also a second order dependence on the distance from the main-sequence (Accurso et al. 2017b). The typical α_{CO} adopted for main-sequence galaxies is $\alpha_{CO} = 4.3$ $M_\odot/(K$ km $s^{-1}pc^2)$ (Strong & Mattox 1996; Abdo et al. 2010; Bolatto et al. 2013). For galaxies above the main-sequence or star-bursts, an $\alpha_{CO} = 1$ $M_\odot/(K$ km $s^{-1}pc^2)$ is considered more appropriate (Bolatto et al. 2013).

When moving to higher redshift ($z = 1 - 2$), the CO(1-0) line frequency is shifted to higher values and it is not easily observable from the ground. In this redshift range, the commonly used transition is the CO(3-2) line (Tacconi et al. 2018). To convert the luminosity of higher CO transitions to the CO(1-0) luminosity, it is necessary to have a good knowledge of the CO Spectral Line Energy Distribution (SLED). Many factors can influence the shape of the CO SLED: gas density, cosmic ray ionization rate, strength of the far-ultraviolet (FUV) field, X-ray radiation (Meijerink et al. 2006; Banerji et al. 2009). This introduces additional uncertainties in the conversion from CO(3-2) line luminosity to molecular gas mass.

- **[CI]:** Papadopoulos & Greve (2004) suggested that the fine structure line of atomic carbon [C I] at 491 and 809 GHz can be used as an alternative molecular gas tracers (see Figure 1.10). An advantage of this method is the fact that for high-redshift ($z > 1$) galaxies, the observed frequencies of the [C I] line fall in the atmospheric windows and thus, it is more easily observable than low-J CO transitions. One main limitation of this method is the uncertainty on the [C I]-to-H_2 conversion factor. From a theoretical perspective, this factor depends for example on the cosmic ray physics and on the cloud evolutionary states (e.g., Glover & Clark 2016; Gaches et al. 2019). Some efforts have been done to calibrate this conversion factor from observations (e.g., Jiao et al. 2017; Valentino et al. 2018; Jiao et al. 2019; Bourne et al. 2019), but a calibration that can be applied to all types of galaxies at different redshift is still missing.

- **[CII]**: The [C II] $^2P_{3/2} - ^2P_{1/2}$ transition at 158 μm has been suggested as a tracer of molecular gas, especially for low metallicity galaxies (e.g. Madden et al. 1997; Carilli & Walter 2013). [C II] is one of the brightest fine structure lines emitted in star-forming galaxies (Carilli & Walter 2013), and therefore it is a promising way to

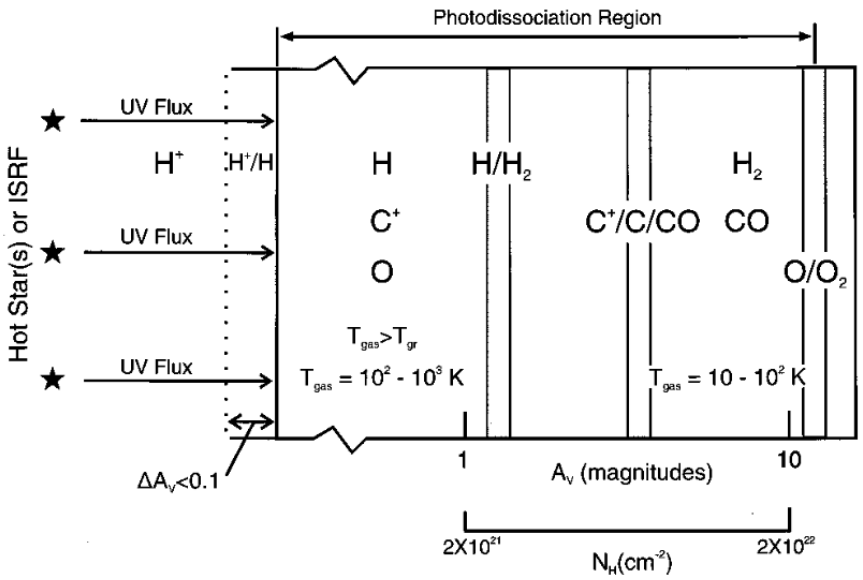

Figure 1.10. Schematic diagram of a photo-dissociation (or photon-dominated) region (PDR) from Hollenbach & Tielens (1999). The PDR is illuminated from the left and extends from the predominantly atomic surface region to the point where O_2 is not appreciably photodissociated ($A_V \simeq 10$). Hence, the PDR includes gas whose hydrogen is mainly H_2 and whose carbon is mostly CO. Large columns of warm O, C, C^+ (i.e. [C II]), and CO, and vibrationally excited H_2 are produced in the PDR. T_{gas} indicates gas temperature and T_{gr} represents the temperature of dust grains.

measure molecular gas at high redshift. Hughes et al. (2017) find a good correlation between [C II] luminosity and molecular gas mass at $0.03 < z < 0.2$. Recently, Zanella et al. (2018) expanded this analysis considering galaxies at higher redshift ($0 < z < 6$), reporting a mean absolute deviation of 0.2 dex in the correlation between [C II] luminosity and molecular gas mass. In the Milky Way, Pineda et al. (2013) and Velusamy & Langer (2014) find that ∼75% of the [C II] luminosity is related to molecular gas. Additionally, theoretical studies predict that $60 - 85\%$ of the [C II] emission is tracing molecular gas and importantly this percentage depends on the properties of the galaxies (Vallini et al. 2015; Olsen et al. 2017; Accurso et al. 2017a). However, this method is still controversial because [C II] has been used also as a tracer of star-formation rate in galaxies (e.g., Stacey et al. 2010; De Looze et al. 2014a; Herrera-Camus et al. 2015; Schaerer et al. 2020). It is not clear whether the correlation between [C II] and CO luminosity is a result of a uniform star-formation efficiency in the studied samples (Hodge & da Cunha 2020).

- **Other molecular lines**: Several molecular emission lines have been used to trace dense cold molecular gas in galaxies. For example, HCN, HCO^+, SiO and CS are used as tracers of molecular gas with critical densities $> 10^4$ cm^{-3} (e.g., Tan et al. 2018; Gao & Solomon 2004a,b; Wu et al. 2010; Zhang et al. 2014; Jiang et al. 2020; Scourfield et al. 2020). Thanks to their high critical densities, these molecular lines can be used to identify dense regions in the ISM where star-formation is taking place. However, these lines trace only the very dense gas and therefore can not be used to measure the 'total' cold molecular gas reservoir of galaxies. Additionally, these lines are several times fainter than CO, thus, they are more difficult to observe and require longer integration times.

  The hydrogen deuteride (HD) emission lines at 56 and 112 μm have also been used to trace cool molecular gas ($T \sim 30 - 50$ K) in the Milky Way (Wright et al. 1999; Bergin et al. 2013; McClure et al. 2016). Recently, Jones et al. (2020) attempted to observe the HD emission line in a strongly lensed galaxy at $z = 5.6$ using ALMA, but they could derive only an upper limit. With the advent of more sensitive telescopes, HD could be detectable in nearby galaxies, at least up to about 10 Mpc (van der Tak et al. 2018).

- **Dust masses:** Molecular emission lines are a fairly direct tracer of the molecular gas, but they require long integration times. Therefore, it is not feasible to observe molecular lines for large galaxy samples (> 100) beyond the local Universe. Another possibility is to use the dust mass to trace the molecular gas (e.g. Thronson 1988; Devereux & Young 1990; Israel 1997; Leroy et al. 2011). Dust and gas (both atomic and molecular) are well mixed in the ISM (e.g., Bohlin et al. 1978; Boulanger et al. 1996), therefore dust masses can be used to infer gas masses, provided that the gas-to-dust mass ratio is known.

  Dust masses are measured by fitting the far-infrared (FIR) spectral energy distribution (SED), that is considerably brighter and quicker to observe than molecular emission lines. This method has two main sources of uncertainties: the errors on the derived dust masses and the adopted gas-to-dust mass ratio.

  The uncertainties on the dust masses depend on the model used for the fitting and on the other dust parameters (temperature, emissivity index,..). In particular, knowing the dust temperature is critical to accurately determining the dust mass,

as it is shown by Casey (2012) (see left panel in Figure 1.11). This can lead to large uncertainties, especially when there is only a sparse coverage of the FIR SED. Additionally, to convert the observed FIR SED to a dust mass we need to assume a dust mass absorption coefficient (κ_λ). This parameter is model dependent and very uncertain (e.g., Draine 2003; Gall et al. 2011; Galliano 2018). Recently, Clark et al. (2019) compile a list of ~ 70 κ_λ values from the literature and find that they span 3.6 orders of magnitude with a standard deviation of 0.8. Additionally, laboratory measurements of dust analogues find higher κ_λ values than the ones typically used in dust models, which suggest that current dust mass measurements are over-estimated by a factor of $2 - 20$ (Fanciullo et al. 2020).

The second source of uncertainty is the gas-to-dust ratio (δ_{GDR}), which is defined as the ratio between the (molecular) gas mass and the dust mass. It is has been observed that the gas-to-dust ratio decreases with metallicity (see Figure 1.11), as predicted by dust formation models (e.g., Edmunds 2001), but the exact form of the dependency is not well known (e.g., Rémy-Ruyer et al. 2014; Leroy et al. 2011; Magdis et al. 2011, 2012; Santini et al. 2014). Rémy-Ruyer et al. (2014) suggested that a broken-power law is a better fit to relation between δ_{GDR} and metallicity, with a steeper slope at low metallicities (12+log(O/H) < 8).

The gas-to-dust ratio may also vary with redshift, with galaxies at redshift $z > 2$ having larger δ_{GDR} than galaxies at $z = 0$, at fixed metallicity (Saintonge et al. 2013). This evolution with redshift can have different explanations. One possibility is that there is a difference in dust properties at high redshift ($z > 2$), which can affect the models used to calculate the dust masses. A second possibility is that differences in the α_{CO} conversion factor at high-z can bias the molecular gas mass measurements. Additionally, it has been observed in high-redshift galaxies that the continuum and CO emission may have a different spatial extent, therefore, the dust emission may not trace the molecular gas accurately (e.g. Hodge et al. 2015; Chen et al. 2017; Calistro Rivera et al. 2018; Kaasinen et al. 2020).

It is still debated whether dust traces better the molecular, atomic or total gas mass. Recently, Casasola et al. (2020) studied scaling relations between dust, atomic and molecular gas in late-type galaxies in the Local Universe from the DustPedia project (Davies et al. 2017). They reported that the dust mass correlates better with atomic

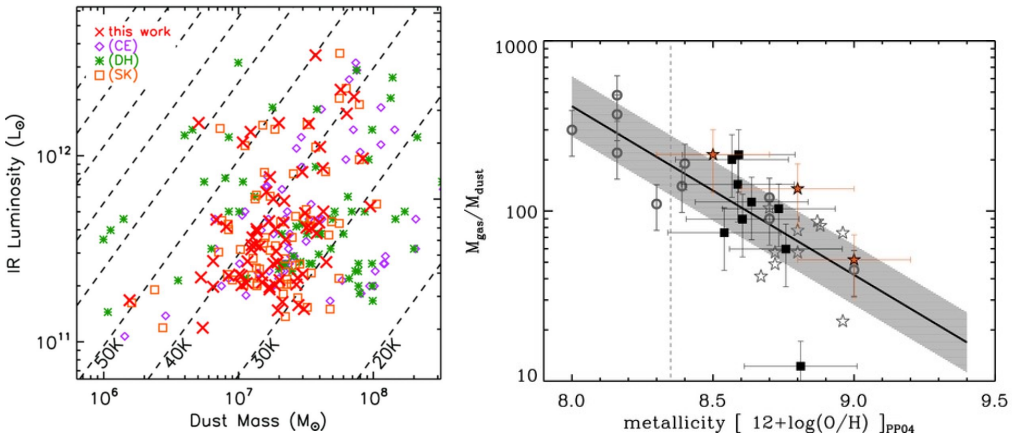

Figure 1.11. *Left:* Figure from Casey (2012). Dust mass versus the 8-1000 μm IR luminosity for galaxies from the GOALS sample using the SED fitting method from Casey (2012) and template SED libraries from Chary & Elbaz (2001) (CE), Dale & Helou (2002) (DH), and Siebenmorgen & Krügel (2007)(SK). Dashed lines show isotherms increasing by 10 K. This plot shows that dust mass is very sensitive to dust temperature. *Right:* Figure from Magdis et al. (2012). M_{gas}/M_{dust} versus metallicity for a sample of galaxies in the Local Group by Leroy et al. (2011) (grey circles) and local ultra-luminous infrared galaxies (ULIRGs) by Downes & Solomon (1998) (grey stars). The solid black line is the best linear regression fit to the sample from Leroy et al. (2011), and the gray shadowed area shows the dispersion of the correlation. Filled black squares and orange stars indicate the position of $z \sim 0.5 - 1.5$ main-sequence galaxies and high-z submm galaxies (SMGs), respectively.

gas mass or total gas mass than with molecular gas mass. Moreover, Bertemes et al. (2018) studied the cross-calibration between CO-based and dust-based molecular masses in a sample of nearby ($z < 0.2$) massive ($M_* > 10^{10}$) galaxies and found that dust traces not only the molecular gas, but also part of the HI reservoir. This suggests that variations in the atomic-to-molecular gas ratio should be taken into account when using the dust masses to infer $M(H_2)$.

- **Single band FIR continuum observations:** This approach was proposed by Scoville et al. (2014a) and Groves et al. (2015) and it is based on an empirical relation between the submm flux of galaxies, which measures the Rayleigh-Jeans part of the dust emission, and the gas masses measured through CO or CO and HI emission. Figure 1.12 shows the empirical relation between $L_{850\mu m}$ and L_{CO}, derived by Scoville et al. (2016) for low-z star-forming galaxies, ULIRGs (Ultra Luminous IfraRed Galaxies), and $z \sim 2$ submm galaxies (SMGs).

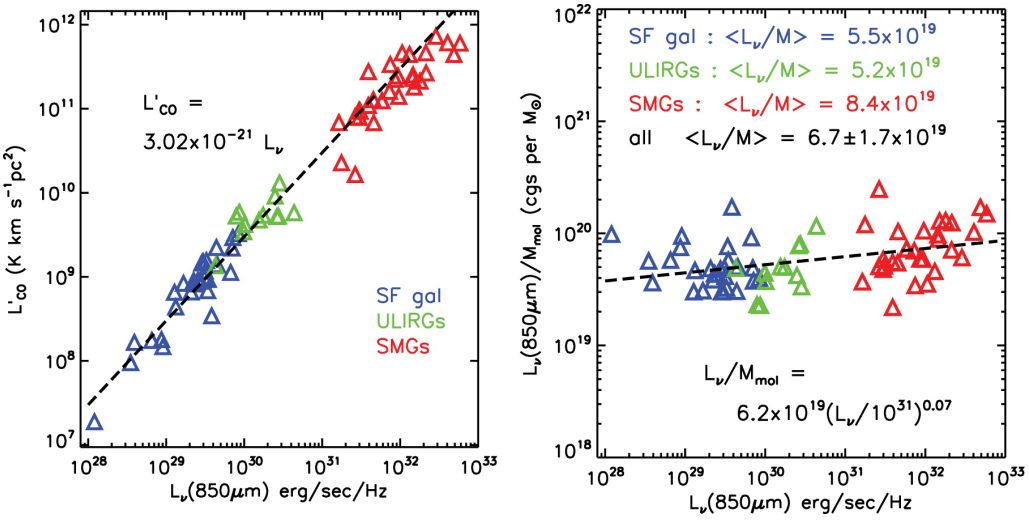

Figure 1.12. Figure from Scoville et al. (2014b). *Left:* the CO(1-0) luminosity and 850μm luminosity for three samples of galaxies: normal low-z star-forming galaxies, low-z ULIRGs, and $z \sim 2$ SMGs. All of the galaxies were selected to have global measurements of CO (1-0) and Rayleigh-Jeans dust continuum fluxes. The large range in apparent luminosities is enhanced by including high-z SMGs, many of which are strongly lensed in this sample. *Right:* the ratio of $L_{850\mu m}$ to the molecular gas mass M_{mol} is shown for the three samples of galaxies, indicating a very similar proportionality constant between the dust continuum flux and M_{mol} derived from CO(1-0) emission. The molecular masses were estimated from the CO (1-0) luminosities using a single standard Galactic $X_{CO} = 3 \cdot 10^{20}$ N(H_2) [cm^{-2} (K km s^{-1})$^{-1}$].

This method is very efficient as it requires only a single continuum observation, instead of observations in multiple continuum bands (for SED fitting) or line observations, that need longer integration time. Therefore, it can potentially be used for large samples of galaxies. Moreover, it does not require a priori knowledge of the precise redshift of the sources, which is instead required to observe the molecular lines and for the FIR SED fitting method.

This approach has also some disadvantages. Since it is calibrated using CO observations, it is susceptible to the same uncertainties of the CO method. Additionally, it assumes a single gas-to-dust ratio, but it is known that this empirical relation is not valid at low metallicities (e.g., Groves et al. 2015; Privon et al. 2018). Moreover, this method assumes a single temperature model for the cold dust, without taking into account the evolution with redshift (e.g. Magnelli et al. 2014; Schreiber et al. 2018). Privon et al. (2018) use cosmological zoom-in simulations of galaxy formation and dust radiative transfer calculations to investigate the use of the 850μm luminosity

($L_{850\mu m}$) as a molecular gas mass tracer. They find that the main driver of the scatter in the relation between $L_{850\mu m}$ and the molecular gas mass are variations in the molecular-gas-to-dust mass ratio, rather than differences in the dust temperature.

- **Dust extinction:** This method is based on the idea that the dust extinction can trace the dust mass and consequently also the molecular gas mass. Concas & Popesso (2019) presented an empirical method to estimate $M(H_2)$ using the Balmer Decrement (i.e. the ratio of the observed Hα and Hβ fluxes, BD = F(Hα)/F(Hβ)), which is a tracer of the dust extinction. They use data from local star-forming galaxies from the xCOLD GASS survey (Saintonge et al. 2011a, 2017) and find that the CO(1-0) luminosity and $M(H_2)$ can be approximated by a combination of BD and galaxy inclination, with a scatter of ∼0.3 dex. An independent study by Yesuf & Ho (2019) also investigates possible correlations between $M(H_2)$ and other galaxy parameters (such as dust extinction, galaxy radius, or galaxy morphology) using data from xCOLD GASS. They report that the dust attenuation A_V of both the continuum and nebular emission shows a good correlation with $M(H_2)$, even after removing the effect of the correlation with SFR. They find that a combination of A_V and metallicity can predict $M(H_2)$ within a factor of $2.5 - 3$ (~ 0.4 dex), and within a factor of 2 (~ 0.3 dex) if also the SFR is taken into account.

  This method has the advantage that the information about the dust extinction can be derived from the optical spectra and thus can be applied to large spectroscopic surveys. These relations are calibrated on local ($z < 0.05$) galaxies with high stellar masses ($M_* > 10^9 M_\odot$) and high metallicities (12+log (O/H)$>$ 8.45). Therefore, the applicability of this method to galaxies with lower M_*, lower metallicity or at higher redshift still needs to be verified and calibrated. On resolved scales, it has been shown that the dust attenuation inferred from the stellar continuum does not scale well with the dust mass (Kreckel et al. 2013). The Balmer decrement may be a better tracer, since it traces mostly the dust in star-forming region while the dust attenuation of the stellar continuum is mostly driven by the dust in the diffuse ISM, which is not directly linked to the cold molecular gas.

1.4 Dust in the interstellar medium

1.4.1 Origin and composition of interstellar dust

Interstellar dust consists of solid particles with sizes ranging from ∼0.3 nm to ∼0.3 μm (Galliano 2018). The exact composition of interstellar dust is not known, but information about the composition of interstellar dust can be extracted from spectral features (Draine 2003). The candidate materials to form the bulk of the interstellar dust are: silicates, carbonaceous materials (including graphite, diamond, amorphous carbon, hydrogenated amorphous carbon, policyclic aromatic hydrocarbon (PAH), and aliphatic hydrocarbons), and SiC (silicon carbide) grains (Draine 2003).

The two main places where dust is formed are in the ejecta of core-collapse supernovae and in the envelopes of asymptotic giant branch (AGB) stars (see review by Galliano et al. 2018). AGB stars are evolved stars with initial masses of $0.8 - 8$ $M_{\odot}$. They produce dust through the condensation of metals in their cooling dense ejecta (e.g. Michałowski 2015; Dell'Agli et al. 2015). An AGB star can produce $10^{-5} - 10^{-2}$ $M_{\odot}$ of dust (Morgan & Edmunds 2003; Ferrarotti & Gail 2006; Ventura et al. 2012; Nanni et al. 2013, 2014; Schneider et al. 2014). Expanding ejecta of supernovae are the second main place where dust is produced. Studies of several supernovae found a large amount of dust produced (e.g., Gall et al. 2014; Bevan et al. 2017; De Looze et al. 2017; Temim et al. 2017; Rho et al. 2018; Chawner et al. 2019). However, supernovae reverse shocks can also destroy part of the created and pre-existing dust (e.g., Bianchi & Schneider 2007; Cherchneff & Dwek 2010; Temim et al. 2015), and it is still not clear how much dust can survive on a long time-scale (e.g., Gall et al. 2014; Lau et al. 2015; Wesson et al. 2015; Bevan & Barlow 2016; Micelotta et al. 2016; Gall & Hjorth 2018; Matsuura et al. 2019; Kirchschlager et al. 2020).

These two production mechanisms alone however can not account for the amount of dust observed in high-redshift galaxies (Bertoldi et al. 2003; Priddey et al. 2003; Rowlands et al. 2014; Watson et al. 2015; Michałowski 2015). Grain growth in the ISM, which refers to the mechanism of adding gas atoms onto pre-existing dust seeds (e.g., Hirashita 2012), is another mechanism that can increase the dust content of a galaxy. Currently, it is not well understood how much this process can contribute to the total dust production (Barlow 1978; Ferrara et al. 2016; Ceccarelli et al. 2018). In order to resolve this discrepancy, we need first to improve our understanding of all the mechanisms of dust

production and growth. Second, it is necessary to have tools to accurately measure the dust content of distant galaxies and have a good understanding of the uncertainties on these measurements.

1.4.2 Role of dust in galaxy evolution

Interstellar dust plays an important role in the evolution of galaxies: it helps to balance gas heating and cooling and the surface of dust grains provides a favourable place for chemical reactions to occur (Gould & Salpeter 1963). Dust contributes only a small fraction of the mass of the interstellar medium (ISM), but in normal star-forming galaxies it can re-radiate up to $\sim 30\%$ of the stellar light in the infrared (e.g. Clements et al. 1996; Skibba et al. 2011; Bianchi et al. 2018).

Dust absorbs the light emitted at ultraviolet (UV) and optical wavelengths. Therefore, to recover the intrinsic UV-to-optical SED of galaxies, it is necessary to take dust attenuation into account. For this purpose, it is crucial to know the dust attenuation properties at different wavelengths. For example, the UV and Hα luminosity are often used as SFR estimators, but they can be affected by dust obscuration. Therefore, one needs to apply a correction in order to recover the total SFR of galaxies.

1.4.3 How to measure dust properties

The properties of the cold interstellar dust can be estimated from modelling of the FIR part of the spectral energy distribution. There are many different approaches used to model the FIR SED. In the following, we describe the main approaches and the respective advantages and disadvantages.

- **Physically motivated dust models:** These models consider the emission from different types of dust grains, which have different optical properties. Several grain populations have been considered by different authors, for example: graphite and olivine (Mathis et al. 1977); 'astronomical' (i.e. with empirically tuned optical properties) graphite and silicate (Draine & Lee 1984); 'astronomical' graphite, silicate and PAH (Siebenmorgen & Kruegel 1992; Dwek et al. 1997; Draine & Li 2001, 2007; Li & Draine 2001, 2002; Siebenmorgen et al. 2014), amorphous carbon, silicate, and PAH (e.g. Zubko et al. 2004; Compiègne et al. 2011; Galliano et al. 2011). One disadvantage of these models is that the different grain types are considered as sep-

arate populations, but in reality they are more likely to be mixed in the ISM (Jones et al. 2017). Some models indeed consider grains formed by different materials, like for example silicate grains with organic or hydrogenated amorphous carbon mantles (e.g., Greenberg 1986; Duley 1987; Jones et al. 1987)

These models are used to determine dust masses and dust properties by fitting the infrared SED, assuming a certain interstellar radiation field (ISRF). Using these models, it is possible to obtain not only estimates of the dust masses but also information about the properties of dust grains, like for example the relative abundance of different types of grains and the grain sizes. However, one limitation is that they depend on the assumption made on the different type of grains considered and on their optical properties.

- **Radiative Transfer models:** Radiative Transfer (RT) models study the effect of dust absorption and emission on the SED of galaxies, by modelling the star-light through the galaxies ISM (e.g., Baes et al. 2003; Bianchi 2008; Popescu et al. 2011). These models require to know the 3D geometry of the galaxy, which often is not well known. Radiative transfer models in 3D have been developed and applied only to a few nearby galaxies (e.g., De Looze et al. 2014b; Viaene et al. 2017; Williams et al. 2019; Verstocken et al. 2020; Nersesian et al. 2020; Thirlwall et al. 2020).

- **Empirical calibrated spectral libraries**: Another approach is to use IR observations to produce empirical spectral libraries. For example Chary & Elbaz (2001) and Dale & Helou (2002) present libraries of infrared spectra, that can be scaled to match the observed SED by using only one parameter: either the total IR luminosity or the intensity of the interstellar radiation field heating the dust. One limitation of this approach is that most existing libraries have been calibrated using samples of nearby galaxies, and may not represent well the infrared emission of high-redshift galaxies (e.g., Pope et al. 2006; Zheng et al. 2007).

- **Panchromatic empirical models**: Another possibility is to consider the full SED, from the UV to the FIR. An example of multi-component empirical model is the Multi-wavelength Analysis of Galaxy Physical Properties (`MAGPHYS`) code presented by da Cunha et al. (2008, 2015). This panchromatic model interprets the MIR and FIR SED consistently with the emission at UV, optical and NIR. The emission from dust in stellar birth clouds is modelled with three components: polycyclic aromatic

hydrocarbons (PAHs), emission from hot grains ($T \sim 130 - 250$ K) in the MIR, and grains in thermal equilibrium with temperature $T = 30 - 60$ K. An additional component of cold dust grains with temperature in the range $15 - 25$ K is included to account for the ambient ISM. Using this model it is possible to derive information about the dust properties, as well as other physical parameters like, for example, the star-formation rate and stellar masses. One disadvantage of this type of models is that it requires to have a good coverage of the SED of the galaxies, from the UV to the FIR.

- **Modified black-body models**: To first order, the FIR SED of galaxies can be modelled with a modified black-body (also known as grey-body). Using this model, the dust emission at wavelength λ (F_λ) can be expressed as (Hildebrand 1983):

$$F_\lambda(M_{dust}, T_{dust}, \beta) = \frac{M_{dust}}{D^2}\kappa_0 \left(\frac{\lambda_0}{\lambda}\right)^\beta B_\lambda(T_{dust}), \tag{1.1}$$

where D is the distance to the galaxy, B_λ is the Planck function, and κ_0 is the dust mass absorption coefficient at the reference wavelength λ_0. The three main parameters of this model are the dust mass M_{dust}, the dust temperature T_{dust}, which determines the wavelength position of the peak of the emission, and the dust emissivity index β, which regulates the slope of the SED at long wavelengths. Figure 1.13 shows an example of the single modified black-body (SMBB) model, illustrating the effect of changing T or β on the shape of the SED. This is one of the most widely used model thanks to its simplicity and the small number of free parameters. For these reasons, it can also be applied when only a few photometric data are available.

The SMBB model treats the dust as a single component, with a single temperature and emissivity index. We know that this is a simplification as interstellar dust is made of different types of dust grains and can have a range of temperatures. With this model, one can not derive information about the composition of the dust, but it is possible to have a first order estimate of the amount of dust present in a galaxy as well as its average temperature.

Another problem with this model is the intrinsic degeneracy between the T_{dust} and β. It has been shown that noise in the photometric data can introduce an artificial anti-correlation between T_{dust} and β (e.g., Shetty et al. 2009a,b). Hierarchical Bayesian

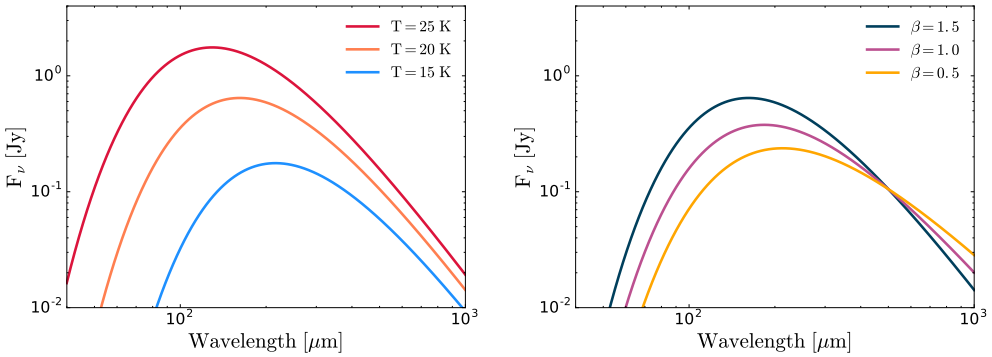

Figure 1.13. Examples of SMBB model showing the effect of changing dust temperature (T) or emissivity index (β). *Left:* The three models have the same dust mass ($\log M_{dust} = 8$) and $\beta = 1.5$, but three different temperatures (15, 20, 25 K). The model with higher T_{dust} peaks at shorter wavelength and has an higher peak flux density. *Right:* The three models have the same dust mass ($\log M_{dust} = 8$) and $T_{dust} = 20$ K, but three different emissivity indices *beta* (0.5, 1.0, 2.5). The model with higher β has a steeper slope and peaks at a short wavelength with a slightly higher peak flux density.

models can help to break this degeneracy (Kelly et al. 2012; Juvela et al. 2013; Veneziani et al. 2013; Galliano 2018), but they require a sample of galaxies in order to be effective, so they can not be applied to fit the SED of a single galaxy.

Different variations of the modified black-body (MBB) model have been used in the literature to model SEDs that are not well approximated by a single MBB. These variations can fit SEDs that deviate from a SMBB model by introducing additional free parameters. For example, Gordon et al. (2014) present two variations of the SMBB model and use them to fit the SED of the Large and Small Magellanic clouds. The first model consists of two modified black-bodies with different temperatures. The addition of a second component can account for emission from warmer dust that peaks at shorter wavelengths. The second model is a MBB model with a broken emissivity power law. This model can accommodate a change in the slope of the FIR SED, which is particularly useful to model an excess emission that has been observed at wavelengths > 500 μm (the so called 'submm excess'). Another example is the combination of MBB and power law model proposed by Casey (2012). This model adds to the MBB model a mid-infrared power law, which approximates the emission of hot dust, coming from AGN heating or from clumpy starbursting regions (see Figure 1.14).

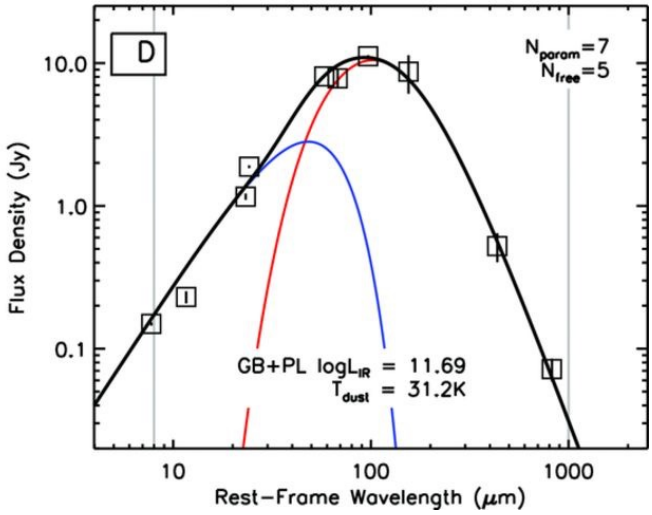

Figure 1.14. Example of FIR SED fit for the galaxy UGC02369 from Casey (2012). The fitting model consists of a modified black-body, which represents the reprocessed starburst emission in the entire galaxy, and a MIR power law, which represents the emission from hot dust heated by AGN or by clumpy starbursting regions.

1.4.4 Dust properties and scaling relations in the local Universe

The dust properties of galaxies in the nearby Universe have been the subject of many studies. In particular, thanks to the *Herschel Space Observatory* (Pilbratt et al. 2010), operating between 2009 and 2013, it has been possible to sample the FIR SEDs of a large number of nearby galaxies in the wavelength range $70 - 500$ μm. These observations have been used to study scaling relations between dust properties and other galaxy properties (as the stellar mass, SFR and gas content), which help to understand the role of dust in the context of galaxy evolution.

Cortese et al. (2012) explored the dust scaling relations using data from the *Herschel* Reference Survey, a magnitude- and volume-limited (i.e. $15 < z < 25$ Mpc) survey of ~ 300 nearby galaxies. They found that the dust fraction (i.e. the dust mass divided by stellar mass) decreases with stellar mass, stellar mass surface density and when moving from late to early-type galaxies. The similarity of these relations to the ones observed with the HI gas fraction supports the idea that dust is tightly coupled to the cold atomic gas component of the ISM. Rémy-Ruyer et al. (2015) studied the dust fraction of a sample of galaxies from the Dwarf Galaxy Survey (DGS, Madden et al. 2013) and from the Key Insights on Nearby Galaxies: a Far- Infrared Survey with *Herschel* survey (KINGFISH, Kennicutt et al. 2011). They argued that the relation between dust fraction and SSFR

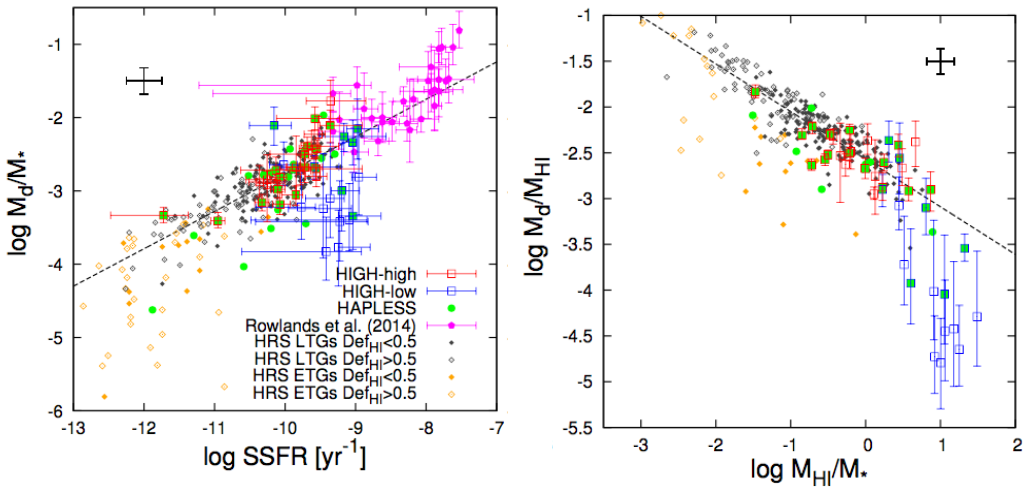

Figure 1.15. Figure from De Vis et al. (2017). Dust fraction (M_d/M_*) as a function of SSFR (left) and dust-to-atomic gas ratio as a function of gas fraction M_{HI}/M_* (right). The dashed line shows the 'best fit' to the high stellar mass HI-selected sample (HIGH-high), HAPLESS and HRS. The Early Type Galaxies (ETGs) are not included in the fit.

is more complex for low-metallicity galaxies with high SSFR, and depends also on the gas-to-dust ratio, which represents the chemical evolution stage of the source.

A subsequent study by De Vis et al. (2017) investigates the dust scaling relations using a collection of nearby ($z < 0.035$) galaxies selected by different methods: the HI-selected H-ATLAS sample (Eales et al. 2010), the dust-selected HAPLESS sample (Clark et al. 2015) and the stellar mass-selected HRS sample (Boselli et al. 2010b). They studied the dust-to-stellar mass ratio as a function of stellar mass, SSFR and HI-gas fraction and found that the most robust scaling relations for dust-to-stellar mass fraction are those related to SSFR and gas-fraction (see Figure 1.15). The right panel of Figure 1.15 shows the evolution of the dust-to-atomic gas ratio as a function of gas fraction. This relation can be interpreted as an evolutionary sequence. As a galaxy evolves, it converts gas into stars, therefore its gas-to-stellar mass ratio decreases, provided that the inflow of new gas is negligible. At the same time, dust is produced and the dust-to-gas mass ratio increases.

Cortese et al. (2014) focused on the scaling relation between galaxy properties and both the dust temperature and emissivity index β of the galaxies in the HRS sample, derived by fitting a single modified black-body (SMBB) model to the *Herschel* photometry. They found that the dust temperature correlates with SSFR and HI gas fraction (M_{HI}/M_*) and anti-correlates with gas-phase metallicity (12+log(O/H)). As shown in Figure 1.16,

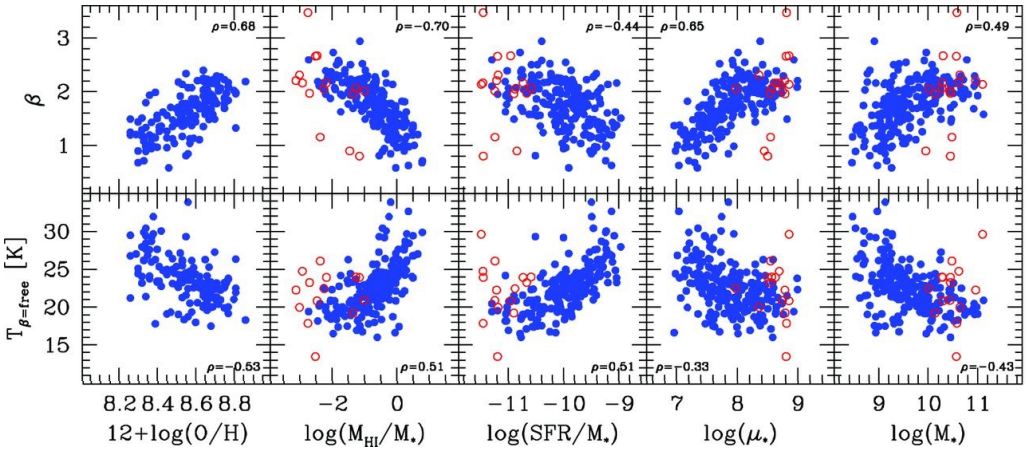

Figure 1.16. Figure adapted from Cortese et al. (2014). Dust scaling relations for the *Herschel* Reference Survey sample. The emissivity index β and the dust temperature are shown as a function of gas-phase metallicity (12+log(O/H)), HI gas fraction (M_{HI}/M_*), specific star-formation rate (SFR/M_*), stellar mass surface density (μ_*), and stellar mass. The filled and open circles show late- and early-type galaxies, respectively. The Pearson correlation coefficients for the whole sample are shown in each panel.

due to the $T-\beta$ degeneracy, they reported opposite correlations of the galaxy properties with β. Thus, they were unable to identify whether the main driver of the correlations is the dust temperature or β.

1.4.5 Evolution of dust properties with cosmic time

The properties of dust in galaxies vary also with cosmic time. Dust properties are related to global galaxy properties, like for example the SFR or the radiation field, which evolve with redshift. Of particular interest is the evolution with redshift of the dust temperature, since it is a crucial quantity necessary to measure reliable dust masses (e.g., Casey 2012).

Several studies have investigated the variation of the dust temperature (T_{dust}) with redshift and the relation between T_{dust} and the position of galaxies with respect to the main-sequence. Accurately measuring dust properties at high redshifts is challenging due to the lack of photometric coverage, low signal-to-noise in the data, and the difficulty in sampling the long-wavelength part of the FIR SED. Therefore, many studies of the dust in high-z galaxies relied on stacking or had to make assumptions about some dust quantities (T_{dust}, emissivity index, or the shape of the SED).

For example, Magdis et al. (2012) explored the FIR properties of main-sequence galax-

ies at $z = 0.5-2$, for individual galaxies and stacked ensembles. They found that the hardness of the radiation field, which is proportional to the dust temperature, increases with redshift. Later, Symeonidis et al. (2013) studied a sample of IR luminous ($L_{IR} > 10^{10} L_{\odot}$) galaxies in the range $0.1 < z < 2$ and reported a relation between T_{dust} and the IR luminosity (L_{IR}). Since L_{IR} can be used to estimate the SFR, this relation can be interpreted as a connection between the T_{dust} and SFR.

Magnelli et al. (2014) studied the evolution of T_{dust} for galaxies up to redshift $z \sim 2$, in relation to their location in the SFR-M_* plane. They used data from two *Herschel* survey: the PACS Evolutionary Probe (PEP, Lutz et al. 2011) and the *Herschel* Multi-tiered Extragalactic Survey (HerMES, Oliver et al. 2012). To measure T_{dust}, they stacked the FIR flux densities in bins of SFR-M_*-z and fit the stacked SEDs using templates from Dale & Helou (2002). They found that in each redshift bin, T_{dust} increases with IR luminosity (L_{IR}), SSFR, and distance with respect to the main-sequence ($\Delta log(SSFR)_{MS}$). Additionally, T_{dust} increases with redshift at fixed $\Delta log(SSFR)_{MS}$. They suggest that this trend can be explained by the global decrease with redshift of the galaxy metallicities (Tremonti et al. 2004; Erb et al. 2006) or by the increase with redshift of the SFE of main-sequence galaxies (Tacconi et al. 2013).

The increase of T_{dust} with redshift and with distance from the main-sequence was confirmed by subsequent studies using stacking techniques (Béthermin et al. 2015; Schreiber et al. 2018). Recently, Faisst et al. (2020) reported the dust temperatures measured for four main-sequence galaxies at $z \sim 5.5$. The measured dust temperatures are $5-10$ K below what would be predicted by extrapolating the T_{dust}-z relations derived at $z < 4$ (see Figure 1.17). This could suggests a change in the dust properties at high-z, for example the dust could be more optically thin at $z > 4$. However, the number of galaxies with good FIR SED coverage at $z > 4$ is still very limited.

1.5 This Thesis

To improve our understanding of galaxy evolution processes, we look into various questions relating to star-formation and the properties of the ISM. Specifically, this Thesis explores different methods of measuring molecular gas masses in galaxies, and their applicability as a function of global galaxy properties, redshift, and presence of an active galactic nucleus (AGN).

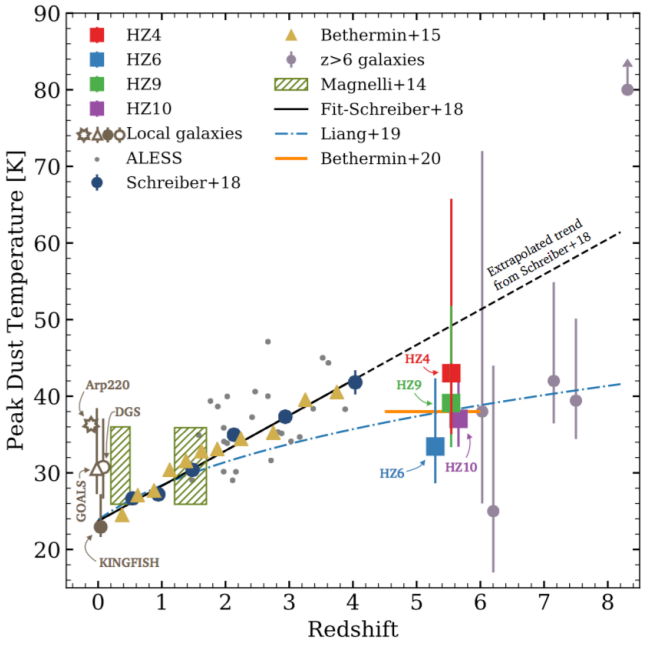

Figure 1.17. Figure from Faisst et al. (2020). Evolution of dust temperature T_{dust} with redshift. Squares show the $z \sim 5.5$ galaxies from Faisst et al. (2020). The plot shows also the galaxy samples at $z = 0$ from KINGFISH (dark grey circle, Skibba et al. 2011), DGS (dark grey open circle, Kennicutt et al. 2011), and GOALS (dark gray open triangle, Madden et al. 2013); galaxies at $z = 0.2-4$ from ALESS (gray small circles, Smail & Walter 2014; Schreiber et al. 2018), Béthermin et al. (2015 , yellow triangles) and Magnelli et al. (2014 , hatched rectangles); and galaxies at $z > 6$ (Knudsen et al. 2016; Hashimoto et al. 2019; Bakx et al. 2020 , light purple circles). The fit to the Schreiber et al. (2018) data is shown in black (dashed when it is extrapolated), together with the expectation from hydrodynamic simulations (blue dot-dashed, Liang et al. 2019; Ma et al. 2019), and the temperature derived from an average template for ALPINE galaxies (orange line, Béthermin et al. 2020).

The most commonly used tracer of molecular hydrogen is the CO molecule. While CO(1-0) is most often used for nearby galaxies, higher transitions such as CO(3-2) are more readily accessible for high redshift galaxies. In order to connect high-z and low-z studies we need to understand how the r_{31} =CO(3-2)/CO(1-0) line luminosity ratio changes. In Chapter 2, we confirm a trend for r_{31} to increase as a function of star-formation efficiency (SFE=SFR/M(H_2)) in the local Universe, using a sample of $\sim$ 100 nearby star-forming galaxies and AGN. Using a photon-dissociation region (PDR) code (`UCL-PDR`), we find that the gas density is the main parameter regulating r_{31}. This suggests a connection between the gas density and the star-formation efficiency. Additionally, we investigate whether the

presence of an AGN can have an impact on the r_{31} line ratio. From our study, we find that there is no difference in the r_{31} between star-forming galaxies and AGN hosts when they are matched in SSFR. This suggests that CO(3-2) can be used to reliably measure molecular gas masses also for moderately luminous AGN, similarly as CO(1-0).

Another possible way to measure the molecular gas content is by using dust emission. To do that, it is important to know how dust properties vary within the galaxy population and to quantify the uncertainties in measuring the dust masses. In Chapter 3, we study how the dust properties (in particular dust mass, dust temperature and emissivity index) vary in a sample of ~ 500 nearby ($z < 0.05$) galaxies from the JINGLE and HRS surveys, and derive scaling relations between the dust properties and other general galaxy properties. We find that the dust temperature (T) correlates with SFR, SSFR and SFR divided by dust mass, and that the emissivity index β correlates with stellar mass surface density, metallicity and anti-correlates with the HI mass fraction (M_{HI}/M_*). These scaling relations may be used to estimate T and β for galaxies that lack a good FIR photometric coverage.

In Chapter 4, we focus on the evolution with redshift of the dust properties using data from the A^{3}COSMOS catalogue. We confirm the trend of the dust temperature increasing with redshift, as has already been reported in the literature, but we find lower T compared to previous studies. This may be due to the different methods used and to the different sample selection. Understanding the variation of dust temperatures with galaxy properties at high-z will be important to characterize the dust content of galaxies in the early Universe.

The FIR observations can also be used to trace dust obscured star-formation. This is particularly useful in the case of AGN, where other star-formation tracers suffer more heavily from the contamination by AGN emission. In Chapter 5, we use FIR continuum observations combined with spatially resolved observations of the ionized gas to investigate the impact of AGN outflows on star-formation at $z \sim 2$. We do not find evidence of suppression of dust-obscured star-formation in the regions where the outflows are located. However, we do not have a spatially-resolved map of a good tracer of recent star-formation, thus we can not rule out that the outflows are affecting star-formation on short time-scales.

Finally, in the Conclusions and Future Work chapter of this Thesis we present a summary of the main results of this thesis and an outlook into future works that are needed to address some the remaining open questions related to the ISM and galaxy evolution.

Throughout this Thesis, we assume a cosmological model with $\Omega_\lambda = 0.7$, $\Omega_\mathrm{M} = 0.3$, and $H_0 = 70$ km s^{-1} Mpc^{-1}.

Acknowledgments of telescopes, surveys and softwares

This work is based on observations carried out with the IRAM 30m telescope. IRAM is supported by INSU/CNRS (France), MPG (Germany) and IGN (Spain). The James Clerk Maxwell Telescope is operated by the East Asian Observatory on behalf of The National Astronomical Observatory of Japan; Academia Sinica Institute of Astronomy and Astrophysics; the Korea Astronomy and Space Science Institute; the Operation, Maintenance and Upgrading Fund for Astronomical Telescopes and Facility Instruments, budgeted from the Ministry of Finance (MOF) of China and administrated by the Chinese Academy of Sciences (CAS), as well as the National Key R& D Program of China (No. 2017YFA0402700). Additional funding support is provided by the Science and Technology Facilities Council of the United Kingdom and participating universities in the United Kingdom and Canada. The Pan-STARRS1 Surveys (PS1) and the PS1 public science archive have been made possible through contributions by the Institute for Astronomy, the University of Hawaii, the Pan-STARRS Project Office, the Max-Planck Society and its participating institutes, the Max Planck Institute for Astronomy, Heidelberg and the Max Planck Institute for Extraterrestrial Physics, Garching, The Johns Hopkins University, Durham University, the University of Edinburgh, the Queen's University Belfast, the Harvard-Smithsonian Center for Astrophysics, the Las Cumbres Observatory Global Telescope Network Incorporated, the National Central University of Taiwan, the Space Telescope Science Institute, the National Aeronautics and Space Administration under Grant No. NNX08AR22G issued through the Planetary Science Division of the NASA Science Mission Directorate, the National Science Foundation Grant No. AST-1238877, the University of Maryland, Eotvos Lorand University (ELTE), the Los Alamos National Laboratory, and the Gordon and Betty Moore Foundation. Funding for the SDSS and SDSS-II has been provided by the Alfred P. Sloan Foundation, the Participating Institutions, the National Science Foundation, the U.S. Department of Energy, the National Aeronautics and Space Administration, the Japanese Monbukagakusho, the Max Planck Society, and the Higher Education Funding Council for England. The SDSS Web Site is http://www.sdss.org/. The SDSS is managed by the Astrophysical Research Consortium for the Participating Institutions. The Participating Institutions are the American Museum of Natural History, Astrophysical Institute Potsdam, University of Basel, University of Cambridge, Case Western Reserve University, University of Chicago, Drexel University, Fermilab, the Institute for Advanced Study, the Japan Participation Group, Johns Hopkins Univer-

sity, the Joint Institute for Nuclear Astrophysics, the Kavli Institute for Particle Astrophysics and Cosmology, the Korean Scientist Group, the Chinese Academy of Sciences (LAMOST), Los Alamos National Laboratory, the Max-Planck-Institute for Astronomy (MPIA), the Max-Planck-Institute for Astrophysics (MPA), New Mexico State University, Ohio State University, University of Pittsburgh, University of Portsmouth, Princeton University, the United States Naval Observatory, and the University of Washington. This research has made use of data from HRS project. HRS is a Herschel Key Programme utilising Guaranteed Time from the SPIRE instrument team, ESAC scientists and a mission scientist. The HRS data was accessed through the Herschel Database in Marseille (HeDaM - http://hedam.lam.fr) operated by CeSAM and hosted by the Laboratoire d'Astrophysique de Marseille. This research made use of data from the A^{3}COSMOS project. A^{3}COSMOS is a joint project between the astronomical research groups of Argelander-Institut für Astronomie, Universität Bonn (AIfA group) and Max-Planck-Institut für Astronomie (MPIA group) for the full exploration of the Atacama Large Millimeter/submillimeter Array (ALMA) observations toward millions of galaxies in the COSMOS two square degree sky. This research makes use of the following ALMA data: ADS/JAO.ALMA#2018.1.00992.S. ALMA is a partnership of ESO (representing its member states), NSF (USA) and NINS (Japan), together with NRC (Canada), MOST and ASIAA (Taiwan), and KASI (Republic of Korea), in cooperation with the Republic of Chile. The Joint ALMA Observatory is operated by ESO, AUI/NRAO and NAOJ. Based on observations collected at the European organisation for Astronomical Research in the Southern Hemisphere under ESO program 196.A-0377. Based in part on data products produced by TERAPIX and the Cambridge Astronomy Survey Unit on behalf of the UltraVISTA consortium. Based on observations obtained as part of the VISTA Hemisphere Survey, ESO Progam, 179.A-2010 (PI: McMahon) This work has made use of data from the European Space Agency (ESA) mission *Gaia* (`https://www.cosmos.esa.int/gaia`), processed by the *Gaia* Data Processing and Analysis Consortium (DPAC, `https://www.cosmos.esa.int/web/gaia/dpac/consortium`). Funding for the DPAC has been provided by national institutions, in particular the institutions participating in the *Gaia* Multilateral Agreement.

The `Starlink` software (Currie et al. 2014) is currently supported by the East Asian Observatory. This research has made use of the NASA/IPAC Extragalactic Database (NED) which is operated by the Jet Propulsion Laboratory, California Institute of Technology, under contract with the National Aeronautics and Space Administration. This research made use of Astropy, a community-developed core Python package for Astronomy (The Astropy Collaboration et al. 2013), `Matplotlib` (Hunter 2007) and `NumPy` (Van Der Walt et al. 2011). This research made use of `APLpy`, an open-source plotting package for Python (Robitaille & Bressert 2012). This research used the `TOPCAT` tool for catalogue cross-matching (Taylor 2005). This research used the `Stan` interface for Python `PyStan` (Stan Development Team 2018). This research used the `CORNER` Python package (Foreman-Mackey 2016).

This page was intentionally left blank

Chapter 2

The CO(3-2)/CO(1-0) luminosity line ratio in nearby star-forming galaxies and AGN

The work described throughout this chapter has been published in **Lamperti et al. (2020)** *"The CO(3-2)/CO(1-0) luminosity line ratio in nearby star-forming galaxies and AGN from xCOLD GASS, BASS and SLUGS".*

Star formation in galaxies is closely related to their gas content. This has been found in the correlation between the star-formation rate (SFR) surface density and gas mass surface density (Kennicutt-Schmidt (KS) relation, Kennicutt 1998). The relation between SFR and molecular gas content is stronger than with the total gas content (Bigiel et al. 2008; Leroy et al. 2008; Saintonge et al. 2017). However, there is some scatter in this relation: the SFR surface density can vary by an order of magnitude for the same molecular gas mass surface density, measured from the CO(1-0) luminosity (Saintonge et al. 2012). A possible explanation is that CO(1-0) is a good tracer of the total molecular gas in massive galaxies, but it does not accurately trace the amount of gas located in the dense molecular cores where the formation of stars takes place (e.g., Solomon et al. 1992; Kohno et al. 2002; Shibatsuka et al. 2003). Since stars form in dense molecular clouds, it is reasonable to expect the SFR to correlate better with the amount of dense molecular gas than with

the total (dense and diffuse) molecular gas. Commonly used tracers of dense gas are HCN, HCO+ or CS (e.g., Tan et al. 2018; Gao & Solomon 2004a,b; Wu et al. 2010; Zhang et al. 2014).

Observations have shown that the HCN(1-0)/CO(1-0) ratio is enhanced in galaxies with high star-formation efficiency (SFE = SFR/$M(H_2)$), like Luminous Infra-Red Galaxies (LIRGs; Gao & Solomon 2004a; Gracia-Carpio et al. 2008; García-Burillo et al. 2012). However, the HCN(1-0) line flux is usually fainter than CO by more than an order of magnitude, making surveys of large samples of normal star-forming galaxies very time consuming. Another option is to use higher CO transitions to trace the mass of dense molecular gas. The ideal transition is CO(3-2): it does not trace low density gas (critical density $n_{crit} = 3.6 \cdot 10^4$ cm^{-3}, calculated under the optically thin assumption, Carilli & Walter 2013) like the CO(1-0) and CO(2-1) transitions, and at the same time it does not require high temperatures to populate it (the minimum gas temperature needed for significant excitation is $T_{min} = 33$ K; Mauersberger et al. 1999; Yao et al. 2003; Wilson et al. 2009). If the gas density is the key quantity regulating the relation between molecular gas mass and SFR, then we expect to see a correlation between the SFE and the r_{31}= $L'_{\rm CO(3\text{-}2)}/L'_{\rm CO(1\text{-}0)}$ luminosity line ratio, that can be interpreted as an indicator of the gas density.

The r_{31} value has been measured in samples of luminous infrared galaxies (Leech et al. 2010; Papadopoulos et al. 2012), in the central regions of nearby galaxies (Mauersberger et al. 1999; Mao et al. 2010), in sub-millimeter galaxies (SMGs, Harris et al. 2010), and in nearby galaxies (Wilson et al. 2012). Yao et al. (2003) and Leech et al. (2010) found a trend for r_{31} to increase with increasing star formation efficiency in samples of infrared luminous galaxies and LIRGs. This trend has also been found in spatially resolved observations of M 83, NGC 3627, and NGC 5055 (Muraoka et al. 2007; Morokuma-Matsui & Muraoka 2017). Sharon et al. (2016) found a similar trend in a sample of sub-millimeter galaxies and AGN-hosts at redshift $z = 2 - 3$. Most studies of the r_{31} line ratio focused on extreme objects, like LIRGs, or are limited to small samples. In this chapter, we collect CO observations for a homogeneous sample of main-sequence galaxies to investigate the r_{31} line ratio in more 'normal' star-forming galaxies.

We also analyse a sample of galaxies hosting active galactic nuclei (AGN), to investigate if the AGN has an effect on the r_{31} line ratio of its host galaxy. Several studies of the CO Spectral Line Energy Distribution (SLED) of AGN focused on the high-J rotational

transition levels. For instance, Lu et al. (2017) studied the CO SLED in the GOALS sample (The Great Observatories All-Sky LIRG Survey Armus et al. 2009) and found that the presence of an AGN influences only the very high J levels (J > 10). Mashian et al. (2015) find that the CO SLED is not the same in all AGN and that the shape of the CO SLED of a galaxy is more related to the content of warm and dense molecular gas than to the excitation mechanism. Rosenberg et al. (2015) analyse the CO ladder of 29 objects from the *Herschel* Comprehensive ULIRG Emission Survey (HerCULES). They find that in objects with a large AGN contribution the CO ladder peaks at higher J levels, which means that in these objects the CO excitation is influenced by harder radiation sources (X-rays or cosmic rays). These studies focus mostly on the high J levels (J > 4). Rosario et al. (2018) studied the molecular gas properties, traced by CO(2-1), of a sample of 20 nearby (z < 0.01) hard X-ray selected AGN hosts from the LLAMA survey and compare it with a control sample of star-forming galaxies. They found similar molecular gas fraction and SFE in the central region of AGN and in the control galaxies. Also Sharon et al. (2016) compared the r_{31} values of 15 SMGs and 13 AGN host galaxies at redshift $z = 2 - 3$ and did not find a significant difference.

In this chapter, we study the r_{31}= $L'_{\rm CO(3\text{-}2)}/L'_{\rm CO(1\text{-}0)}$ luminosity line ratio in a sample of nearby (z < 0.05) star-forming galaxies and AGN. In Sections 2.1 and 2.2 we describe the sample and the CO observations. In Section 2.3 we present the r_{31} values and analyse the correlation with SFR, SSFR and SFE. We also compare the r_{31} values for AGN and star-forming galaxies. In Section 2.4 we use modelling of the line ratio using a PDR (photo-dissociation region) code to test which parameters regulate the CO line ratios. Finally in Section 2.5 we compare the Kennicutt-Schmidt relation with molecular gas masses derived using the CO(1-0) and CO(3-2) line emission.

2.1 Sample

2.1.1 Star-forming galaxies: xCOLD GASS

The xCOLD GASS survey (Saintonge et al. 2011a, 2017) was designed to observe the CO(1-0) emission for ∼ 500 galaxies in order to establish the first unbiased scaling relations between the cold gas (atomic and molecular) contents of galaxies and their stellar, structural, and chemical properties. A sample of 25 galaxies from xCOLD GASS also has observations of the CO(3-2) emission line taken with the James Clerk Maxwell Telescope

(JCMT). The sample was selected based on the following criteria:

- good detection of the CO(1-0) line (signal-to-noise of the line > 3);
- CO(3-2) luminosity high enough to require less than two hours of integration time with the JCMT in band 3 (opacity $\tau_{225\mathrm{GHz}} = 0.08 - 0.12$). Assuming r_{31}= 0.5, this requirement corresponds to CO(1-0) luminosities $L'_{\mathrm{CO(1\text{-}0)}} > 10^8$ K km s^{-1} pc^2.
- the targets were selected to span a broad range of specific star-formation rate (SSFR = SFR/M_*, $-10.5 < \log \mathrm{SSFR/yr}^{-1} < -8.5$) and star-formation efficiency (SFE = SFR/$M(H_2)$, $-9.5 < \log \mathrm{SFE/yr}^{-1} < -8$).

The galaxies in the sample are in the redshift interval $0.026 < z < 0.049$. They have stellar masses in the range $10 < \log M_*/M_\odot < 11$ and star-formation rates in the range $-0.05 < \log \mathrm{SFR}/[\mathrm{M}_\odot\ \mathrm{yr}^{-1}] < 1.54$.

All the galaxy properties are taken from the xCOLD GASS catalogue (Saintonge et al. 2017). In particular, star-formation rates are calculated by combining the IR and UV based SFR components obtained from WISE and GALEX photometry, as described in Janowiecki et al. (2017). Stellar masses come from the SDSS DR7 MPA/JHU catalogue[1]. The 25 galaxies with CO(3-2) observations are not classified as AGN by the optical emission line diagnostics BPT diagram (Baldwin et al. 1981; Kewley et al. 2001; Kauffmann et al. 2003). Four objects are classified as composite, one as LINER, and the remaining galaxies are classified as star-forming. The properties of the sample are summarized in Table 7.1 in Appendix A.

2.1.2 Active galactic nuclei: BASS

We include in our study a sample of AGN selected in the hard X-ray from the *Swift*/BAT 70 Month survey (Baumgartner et al. 2013). We have CO(3-2) observations of 46 BAT AGN at redshift < 0.04. In our analysis we focus on sources for which we also have observations of the CO(2-1) transition. Additionally, we discard from our sample three AGN for which *Herschel* FIR observations are not available and thus we cannot infer their SFRs. Thus, the final AGN sample that we use in our analysis consists of 36 objects. These sources are part of the BAT AGN Spectroscopic Survey (BASS[2]), for which ancillary

[1] http://home.strw.leidenuniv.nl/~jarle/SDSS/
[2] www.bass-survey.com

information from optical and X-ray spectroscopic analysis is available (Koss et al. 2017; Ricci et al. 2017). The AGN are in the redshift range $0.002 < z < 0.040$.

The SFR is inferred from the total ($8 - 1000$ μm) infrared (IR) luminosity due to star-formation given in Shimizu et al. (2017), which was measured by decomposing the infrared SED in the AGN and host galaxy component. We use the following conversion from total infrared luminosity ($3-1100$ μm range) to SFR , calculated assuming a Kroupa IMF (Hao et al. 2011; Murphy et al. 2011; Kennicutt & Evans 2012):

$$SFR = 3.89 \cdot 10^{-44} \cdot L_{\rm IR}, \tag{2.1}$$

where the SFR is in units of [$M_\odot$ yr^{-1}], and $L_{\rm IR}$ is the total infrared luminosity in [erg s^{-1}].

We use stellar masses measured for BAT AGN host galaxies from Secrest et al. (in prep.). They are derived by spectrally de-convolving the AGN emission from stellar emission via SED decomposition, combining near-IR data from 2MASS, which is more sensitive to stellar emission, with mid-IR data from the AllWISE catalog (Wright et al. 2010), which is more sensitive to AGN emission. The galaxies in the sample have stellar masses in the range $9.7 < \log M_*/M_\odot < 11.1$ and SFR in the range $-0.83 < \log {\rm SFR}/[M_\odot\ {\rm yr}^{-1}] < 1.75$. Table 7.3 in Appendix A lists the properties of this sample.

2.1.3 Infrared luminous galaxies: SLUGS

We also include in our analysis a sample of infrared luminous galaxies ($L_{\rm FIR} > 10^{10}\ L_\odot$) from the SCUBA Local Universe Galaxy Survey (SLUGS, Dunne et al. 2000). We include this sample in order to extend the parameter range to galaxies with higher SFR. We chose this sample over other samples available in the literature because it has beam-matched observations and information about how to scale the total SFR to the SFR within the beam.

We select the 38 SLUGS galaxies with observations of both CO(3-2) and CO(1-0) available in Yao et al. (2003). These galaxies are in the redshift range $0.006 < z < 0.048$. Stellar masses from the SDSS DR7 MPA/JHU catalogue are available for only 22 galaxies of this sample and are in the range $9.6 < \log M_*/M_\odot < 11.4$.

We use the optical emission line diagnostic (Baldwin et al. 1981; Kewley et al. 2001; Kauffmann et al. 2003) from SDSS DR12 to distinguish between AGN and SFGs. Of the 22 galaxies with stellar masses from SDSS, two are classified as Seyferts (IRAS 10173+0828

and Arp 220), seven as Composite and 13 as star-forming galaxies. We include the galaxies classified as Composite in the star-forming galaxies sample.

The total SFR are derived from the total infrared luminosities $L_{\rm IR}$ using eq. (2.1). We measure $L_{\rm IR}$ by integrating the SED, approximated by a modified black-body, in the range $8 - 1000\mu$m. The parameters of the modified black-body (MBB) model are given in Dunne et al. (2000). We calculate the uncertainties on $L_{\rm IR}$ by propagating the uncertainties on the MBB parameters given in Dunne et al. (2000). The SFRs are in the range $0.18 < \log {\rm SFR}/[{\rm M}_\odot\ {\rm yr}^{-1}] < 2.15$. Yao et al. (2003) also provide the FIR luminosity and SFR corresponding to the 15" central part of the galaxy (equivalent to the size of the CO beam), obtained by applying a scale factor to the total FIR luminosity. This factor is derived from the original 850 μm SCUBA-2 images. To calculate the SFE, we use the SFR in the 15" central part of the galaxy, since it matches the beam size of the CO observations.

We note that for this sample the molecular gas mass $M(H_2)$, and consequently also the star-formation efficiency (SFE), represents only the value in the central 15" region of the galaxy, since no correction has been applied to extrapolate from the beam area to the total $M(H_2)$.

2.1.4 Samples in the SFR-M$_*$ plane

Figure 2.1 shows the distribution of the xCOLD GASS, BASS and SLUGS samples in the SFR-M_* plane. The position of the star formation main sequence (Saintonge et al. 2016) is shown by the dashed line, and the dotted lines show the 0.4 dex dispersion. The 'full xCOLD GASS' sample is shown by the grey points for reference. The three samples cover a similar range in stellar masses. All galaxies from the xCOLD GASS sample are on the main sequence or above, while the infrared luminous galaxies from the SLUGs sample are mostly above the main sequence. The BASS sample spans a broad range of SSFR, with ∼8 AGN below the main sequence and the rest of the sample overlapping in the parameter space with the xCOLD GASS galaxies.

The right panel of Fig. 2.1 shows the SSFR versus the star-formation efficiency SFE. The three samples span a similar range of SSFR ($-11 < \log {\rm SSFR}/[{\rm yr}^{-1}] < -8.5$). The galaxies of the xCOLD GASS sample have slightly higher SFE at the same SSFR than the BASS galaxies, but there is a good overlap with the BASS sample. The infrared luminous galaxies from SLUGS have in general high SSFR and high SFE.

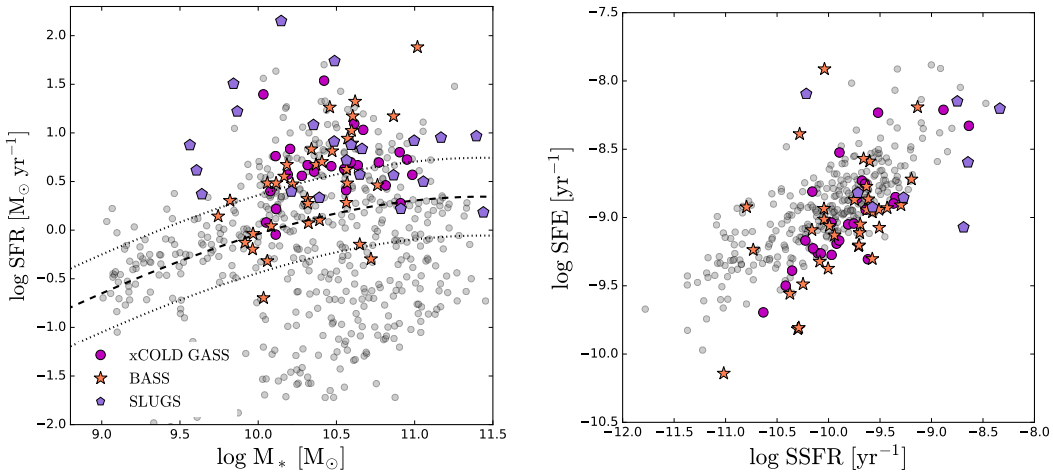

Figure 2.1. *Left:* Distribution of the xCOLD GASS, BASS and SLUGS samples in the SFR-M_* plane. The position of the star formation main sequence (Saintonge et al. 2016) is shown by the dashed line, the 0.4 dex dispersion is shown by dotted lines. The full xCOLD GASS sample is shown by the grey points, while the sub-sample with CO(3-2) observations is shown in magenta. *Right:* SSFR versus star-formation efficiency (SFE = SFR/$M(H_2)$). Galaxies from the BASS sample have in general lower SFE than the xCOLD GASS galaxies at the same SSFR. For the SLUGS sample, we plot only the galaxies with angular diameter $D < 100$", since their SFE is measured within the beam, while the SSFR is the total value.

2.2 CO data, observations and data reduction

2.2.1 xCOLD GASS

xCOLD GASS: CO(1-0) data from the literature

The CO(1-0) line luminosities $L'_{\rm CO(1\text{-}0)}$ are taken from the xCOLD GASS catalogue (Saintonge et al. 2017). The CO(1-0) line fluxes are observed with the IRAM 30m telescope (beam size: 22"). The 25 galaxies from xCOLD GASS selected for the CO(3-2) observations all have S/N$>$ 3 in CO(1-0). We refer to Saintonge et al. (2017) for information about the observations and data reduction.

xCOLD GASS: CO(3-2) observations

The CO(3-2) observations are taken with the HARP instrument (Heterodyne Array Receiver Program, beam size: 14", Buckle et al. 2009) on the JCMT (observing program M14AU21, PI: A. Saintonge). These observations took place between January and June 2014.

Each CO(3-2) spectrum was observed in a single HARP pointing in 'hybrid' mode, which produces two spectra for every scan (in two spectral windows). The spectra were reduced using the `Starlink` software (Currie et al. 2014). First the two spectra within each scan were combined, after correcting for any baseline difference, and then all scans were combined together. A linear fit to the continuum was used to remove the baseline and then the spectrum was binned to a resolution of 40 km s^{-1}.

The HARP instrument has 4×4 receptors (pixels), each one with a half power beam width of 14". We extract the CO(3-2) spectrum only from the pixel which is centred on the galaxy. The technique used to measure the flux from the reduced spectrum is the same used for the main xCOLD GASS survey (Saintonge et al. 2017). We convert the antenna temperature to flux units by applying the point source sensitivity factor 30 Jy/K recommended for HARP[3]. We measure the velocity-integrated line flux $S_{\rm CO}$ in [Jy km s^{-1}] by adding the signal within a spectral window. We initially set the width of the spectral window ($W_{\rm CO}$) equal to the FWHM of the CO(1-0) given in the xCOLD GASS catalog. In case the CO(3-2) line is clearly wider, we extend $W_{\rm CO}$ to cover the total line emission. We determine the center of the line based on the SDSS spectroscopic redshift. In two cases where the CO(3-2) is clearly shifted with respect to the position determined from the SDSS redshift, we use the redshift of the CO(1-0) line, which is shifted in the same direction of the CO(3-2) line, to center the CO(3-2) line. We measure the baseline rms noise of the line-free channels ($\sigma_{\rm CO}$) per 40 km s^{-1} channel in the spectral regions around the CO line.

The beam-integrated CO(3-2) line luminosity in units of K km s^{-1} pc^2 is defined following Solomon et al. (1997) as:

$$L'_{\rm CO} = 3.25 \cdot 10^7 S_{\rm CO} \nu_{\rm obs}^{-2} D_L^2 (1+z)^{-3}, \tag{2.2}$$

where $S_{\rm CO}$ is the velocity-integrated CO(3-2) line flux within the HARP beam in units of Jy km s^{-1}, $\nu_{\rm obs}$ is the observed frequency of the CO(3-2) line in GHz, and D_L is the luminosity distance in Mpc. The error on the line flux is defined as:

$$\epsilon_{\rm obs} = \frac{\sigma_{\rm CO} W_{\rm CO}}{\sqrt{W_{\rm CO} \Delta w_{ch}^{-1}}}, \tag{2.3}$$

[3] www.eaobservatory.org/jcmt/instrumentation/heterodyne/harp/, www.eaobservatory.org/jcmt/instrumentation/heterodyne/calibration/

where $\sigma_{\rm CO}$ is the rms noise achieved around the CO(3-2) line in spectral channels with width $\Delta w_{ch} = 40$ km s^{-1}, and $W_{\rm CO}$ the width (in km s^{-1}) of the spectral window where we integrate the CO(3-2) line flux.

We use a detection threshold of signal-to-noise S/N$>$ 3, defined as S/N $= S_{\rm CO}/\epsilon_{\rm obs}$, which is the same adopted for the main xCOLD GASS catalogue. In 7/25 galaxies the CO(3-2) line is not detected and we use conservative upper limits equal to five times the error: $S_{\rm CO(3-2),limit} = 5 \cdot \epsilon_{\rm CO(3-2),obs}$. The 5σ upper limits correspond to a 'false negative' fraction of 2%, which is the probability that a source with 'true' flux higher than this upper limit is not detected. To calculate $\epsilon_{\rm CO(3\text{-}2),\mathit{obs}}$ we use the FWHM of the CO(1-0) line as an approximation for the width of the CO(3-2) line ($W_{\rm CO}$). The CO(3-2) spectra from xCOLD GASS are shown in Fig. 2.2 and the measured line properties in Table 7.2 (Appendix A).

2.2.2 BASS

Both the CO(2-1) and CO(3-2) lines have been observed at the JCMT: the CO(3-2) with HARP and the CO(2-1) with the RxA instrument (beam size: 20"). The HARP observations took place in weather bands $3-4$ (corresponding to an opacity $\tau_{225\rm GHz} = 0.07-0.21$), while the RxA observations took place in weather band 5 ($\tau_{225\rm GHz} = 0.20-0.32$). The observations and data reduction of the CO(2-1) line emission is explained in detail in Koss et al. (2020).

The CO(3-2) observations were taken between February 2011 and November 2012 in programs M11AH42C (P.I: E. Treister) and M12BH03E (PI: M. Koss). Additionally, we also include 13 spectra from archival observations. Each galaxy was initially observed for 30 minutes. For weak detections, additional observations were obtained up to no more than two hours. The individual scans for a single galaxy were first-order baseline-subtracted and then co-added. We extract the CO(3-2) spectrum only from the pixel centred on the galaxy. We measure the CO(3-2) and CO(2-1) line fluxes using the same method as for the xCOLD GASS sample, for consistency. We measure the $S_{\rm CO}$ line flux in [Jy km s^{-1}] by adding the signal within a spectral range that covers the entire width of the line. In Appendix A, we show the CO(3-2) spectra from BASS, in which we highlight the spectral regions where we integrate the fluxes. All BASS objects have good detections (i.e. S/N$>$ 3) of the CO(2-1) lines, while we have non-detections (i.e. S/N$<$ 3) in the CO(3-2) line for 3/36 galaxies. For these galaxies we use upper limits equal to five times the flux

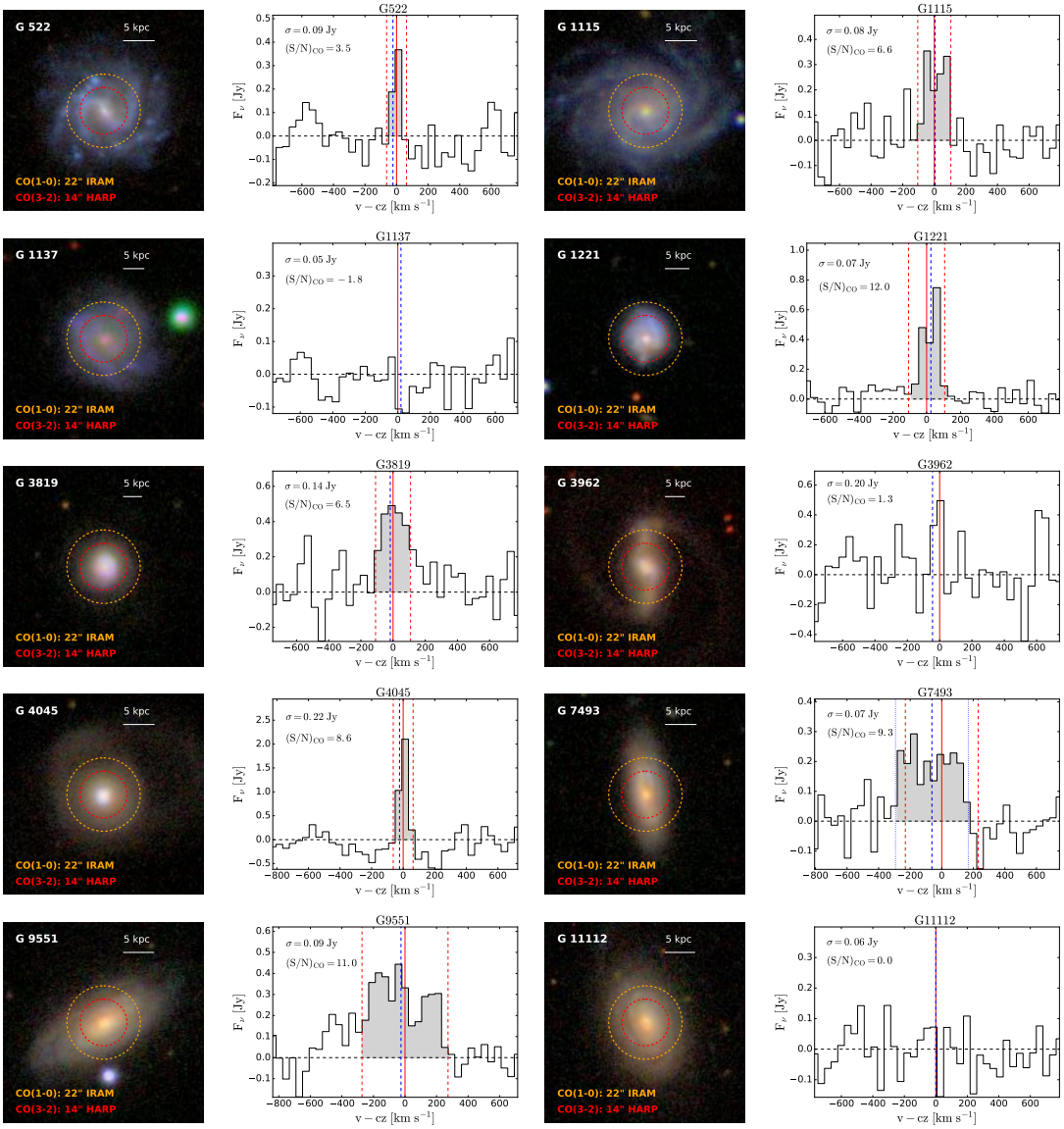

Figure 2.2. *First and third columns*: SDSS *gri* images of the xCOLD GASS sample. Every image has dimension 60" × 60" ($1' \times 1'$) and shows the the size of the IRAM-30m and JCMT HARP beams. *Second and fourth columns*: CO(3-2) spectra of the xCOLD GASS sample taken with HARP on the JCMT. The spectra are centred at the position of the CO(3-2) line. The solid red line is the central velocity of the line based on the spectroscopic redshift from SDSS and the dashed red lines indicate the interval where the CO(3-2) flux was integrated, based on the FWHM of the CO(1-0) line. The blue solid line indicates the central velocity of the CO(1-0) line. For the two galaxies (G7493 and G2527) where the CO(3-2) line flux was measured based on the position of the CO(1-0) line, the blue dotted line shows the interval where the CO(3-2) flux was integrated. Additional figures showing the remaining 15 galaxies of the xCOLDGASS sample and the full sample of 46 BASS objects are shown in Appendix A.

error: $S_{\mathrm{CO,limit}} = 5 \cdot \epsilon_{\mathrm{CO,obs}}$.

Our set of observations is not homogeneous since for the xCOLD GASS and SLUGS samples we compare the CO(3-2) to the CO(1-0) line, but for the BASS sample we have to estimate CO(1-0) from the CO(2-1) line. Therefore we need to assume a value for the ratio $r_{21} = L'_{\mathrm{CO(2\text{-}1)}}/L'_{\mathrm{CO(1\text{-}0)}}$. The typical value observed for normal spiral galaxies is $r_{21} = 0.8$ (Leroy et al. 2009; Saintonge et al. 2017). Leroy et al. (2009) studied a sample of ten nearby spiral galaxies and found r_{21} values between 0.48 and 1.06, with most values in the range $0.6 - 1.0$. They found an average of 0.81. For the xCOLD GASS survey, Saintonge et al. (2017) found a mean value of $r_{21} = 0.79 \pm 0.03$ using a sample of 28 galaxies.

Some of the AGN in our sample (12/36) have recently been observed with the IRAM 30m telescope as part of a programme to measure CO(1-0) line luminosity for 133 BAT AGN (P.I: T. Shimizu). We compute the r_{21} line ratios for these 12 objects using the values from Shimizu et al. (in prep.). Since the difference in beam size is very small (IRAM: 22", JCMT RxA: 20"), we did not apply any beam corrections. The r_{21} line ratios for these 12 objects are in the range 0.4-2.1, with a median $r_{21} = 0.72$. We obtain a robust standard deviation by computing the median absolute deviation $MAD = 0.17$. The robust standard deviation, under the assumption of a normal distribution, is given by $\sigma = 1.4826 \cdot MAD = 0.26$ (Hoaglin et al. 1983). For the 12 objects with CO(1-0) observations, we use the CO(1-0) luminosities from Shimizu et al. (in prep.) to compute the r_{31} line ratio. For the remaining AGN, we use a constant r_{21}= 0.72, and we assume an uncertainty of 0.26 on this value. The CO line fluxes for this sample are shown in Table 7.4 in Appendix A.

2.2.3 SLUGS

The CO(1-0) observations were taken with the Nobeyama Radio Observatory (NRO) 45 m telescope (beam size: 14.6") and the CO(3-2) observations with the HARP instrument on the JCMT. We take the CO line luminosities and line ratios from Yao et al. (2003) and we refer to that paper for information about the observations and data reduction.

2.2.4 Beam corrections

We calculate beam corrections for two purposes: 1) to correct for the different beam sizes of the CO(3-2), CO(2-1), and CO(1-0) observations and 2) to extrapolate the CO luminosity measured within the beam to the total CO luminosity of the galaxy.

1) Corrections for the different beam sizes:

For the SLUGs sample the beam sizes are similar (14.6" for the CO(1-0) line and 14" for the CO(3-2) line), therefore the line luminosities can be directly compared without applying any corrections for the beam size. For the xCOLD GASS and BASS samples instead, the beam sizes of the telescopes used for the CO(3-2), CO(2-1) and CO(1-0) observations vary between 14" and 22", thus we need to apply beam corrections. In order to compare the CO emission from different lines, we need first to ensure that we are comparing fluxes coming from the same part of the galaxy. To estimate the amount of flux that is missing in the observation done with the smaller beam, we use the following approach. Under the assumption that the dust emission in the infrared is a good tracer of the cold molecular gas distribution (e.g. Leroy et al. 2008), we can estimate the flux that would be observed from beams of different sizes by measuring the flux within different apertures in the infrared images. After that, we apply an additional correction to take into account the fact that the infrared images have a point-spread function (PSF) that causes the observed flux to appear more extended than the intrinsic emission.

To calculate the beam corrections from the infrared images, we apply the following procedure. We multiply the infrared image by a 2D Gaussian centred on the galaxy centre and with FWHM equal to the beam size, to mimic the effect of the beam sensitivity of the telescope that took the CO observations. Then we measure the total flux from the image multiplied by the 2D Gaussian. We repeat this measurement for the two beams, and we take the ratio of the fluxes:

$$C_{IR} = \frac{F(\text{inside the larger beam})}{F(\text{inside the smaller beam})} = \frac{F(\text{inside the CO(1-0) or CO(2-1) beam})}{F(\text{inside the CO(3-2) beam})}. \quad (2.4)$$

For the xCOLD GASS sample, we use the 22 μm images from the WISE survey. Specifically, we use the co-added images from 'unWISE' [4] which have been systematically produced without blurring, retaining the intrinsic resolution of the data (Lang 2014; Meisner et al. 2016). For 36 galaxies in our BASS sample there are *Herschel*/PACS observations at 70 μm and 160 μm available (Meléndez et al. 2014; Shimizu et al. 2017). We decide to use the PACS 160 μm images because the longer wavelength is less likely to be contaminated by AGN emission, which can still contribute for a significant fraction of the 70 μm emission (Shimizu et al. 2017).

[4] http://unwise.me/

The point-spread-functions (PSF) of the WISE 22 μm and PACS 160 μm images are rather large (12") when compared with the size of the CO beams (14"-22"), and can therefore affect the measurement of the beam corrections. The images that we are using to trace the distribution of the FIR emission are not maps of the 'true' distribution, instead they are maps of the 'true' distribution convolved with the PSF of the FIR telescope. To correct for the effect of the PSF, we use a simulated galaxy gas profile, following the procedure described in Saintonge et al. (2012). For each galaxy, we create a model galaxy simulating a molecular gas disk following an exponential profile, with a scale length equivalent to its half-light radius. Then, the profile is tilted according to the inclination of the galaxy and we measure the amount of flux that would be observed from this model galaxy, using an aperture corresponding to the size of the beam (F_{sim}). Then, we convolve the galaxy profile with a 2D Gaussian with the FWHM equal to the size of the PSF of the image and we measure again the flux within the beam radius ($F_{sim,PSF}$). By taking the ratio of these two measurements, we estimate how much the flux changes due to the effect of the PSF:

$$C_{PSF} = \frac{F_{sim,PSF}}{F_{sim}}. \tag{2.5}$$

This correction is in the range $1.04 - 1.27$. We apply this PSF correction to the beam correction obtained from the infrared images:

$$C_{IR,PSF} = \frac{C_{IR}}{C_{PSF}}. \tag{2.6}$$

We finally apply this factor to the r_{31} ratios:

$$r_{31,corr} = r_{31} \cdot C_{IR,PSF}. \tag{2.7}$$

The final beam corrections ($C_{IR,PSF}$) for the BASS sample are in the range $1.05-1.70$, with a mean value of 1.27. For the xCOLD GASS sample they span a similar range between 1.08 and 1.80, with a mean of 1.31. The corrections for the xCOLD GASS samples are larger because of the larger difference between the two beams (22" for the CO(1-0) beam vs. 14" for the CO(3-2) beam), compared to the BASS sample (20" for the CO(2-1) beam vs. 14" for the CO(3-2) beam). In order to check that the beam corrections do not have an effect on our analysis, we look at the relation between r_{31} and galaxy angular size or the beam corrections value. We do not find any dependence of the r_{31} on the beam

corrections or on the angular size of the galaxies (see Section 2.3.3).

We note that the line ratios presented in this work are measured in the central region of the galaxies, and may not be representative of the line ratio of the entire galaxy. Resolved studies of the CO line ratios in nearby galaxies find that the excitation tend to be higher in the central part than at larger radii (Leroy et al. 2009; Wilson et al. 2009). With the beam corrections, we want to correct for the fact that the beams of the two transitions have different sizes, but they still represent only the central part of the galaxy.

2) Beam-to-total luminosity corrections:

To calculate the total CO(1-0) emission and molecular gas mass, we need to apply a correction to extrapolate the CO(1-0) emission within the beam to the total CO(1-0) luminosity. For the xCOLD GASS sample, we retrieve these values from the xCOLD GASS catalogue (Saintonge et al. 2017). They are in the range $1.02-1.95$. For the BASS sample, we use the method described above to estimate the total amount of CO emission.We measure the total infrared 160 μm emission of the galaxy within a radius big enough to include the entire galaxy, paying attention not to include any emission not related to the galaxy. We determine the radius until which we integrate the flux based on the curve of growth of the galaxy profile. For compact sources the radius extends until ~ 60", while for the more extended and nearby galaxies, we measure the flux within a radius up to 140".

Then,we take the ratio between the flux from the map multiplied by the CO(2-1) beam sensitivity, measured as explained above, and the total infrared flux and we use this value to extrapolate the total CO(2-1) flux. The beam corrections for BASS are in the range $1.46-15.66$. For the analysis in Section 2.3, we use only galaxies with angular diameter $D < 100$", for which the beam corrections are < 2.4, to avoid galaxies for which the CO emission within the beam is not representative of the total CO emission. For the angular size D of xCOLD GASS and SLUGS we use $D = D_{25}$, i.e. the optical diameter derived from SDSS g-band. For BASS we use $D = 2 \times R_{k20}$, where R_{k20} is the isophotal radius at 20 mag arcsec^{-2} in the K-band. We expect the sizes measured in the g-band and in the K-band to be similar (Casasola et al. 2017). The beam correction values can be found in Tables 7.2 and 7.4 in Appendix A.

2.2.5 Total molecular gas mass

We use two different CO-to-H_2 conversion factors: for normal star-forming galaxies we adopt a Galactic conversion factor $\alpha_{CO} = 4.3$ $M_\odot/(K\ km\ s^{-1}\ pc^2)$ (Strong & Mattox 1996; Abdo et al. 2010; Bolatto et al. 2013) and for "ULIRGs-type" galaxies we use $\alpha_{CO} = 1$ $M_\odot/(K\ km\ s^{-1}\ pc^2)$ (Bolatto et al. 2013). To distinguish between normal SFGs and "ULIRGs-type" galaxies, we apply the selection criterion described in Saintonge et al. (2012), which is based on the FIR luminosity and on the dust temperature. According to this criterion, we apply the "ULIRGs-type" conversion factor to galaxies with $\log L_{\rm FIR}/L_\odot > 11.0$ and $S_{60\mu m}/S_{100\mu m} > 0.5$. For the other galaxies, we use the Galactic conversion factor. For the BASS sample, we also need to apply a conversion from CO(2-1) to CO(1-0) line luminosity, which is explained in Section 2.2.2.

2.3 CO line ratios

2.3.1 r_{31} and star-formation

In this section we look at the r_{31} distribution for AGN and SFGs and investigate the relation between r_{31} and galaxy global properties. For this part of the analysis, we exclude from the sample the galaxies with large angular size (diameter $D > 100$"), in order to avoid galaxies for which the luminosity measured within the beam is not representative of its total emission. The sample used in this section consists of 25 galaxies from xCOLD GASS, 20 from BASS, and 8 from SLUGS.

The r_{31} values in the xCOLD GASS sample are in the range $0.25 - 1.15$ and the mean value is 0.55 ± 0.05, with a standard deviation of 0.22. This value is consistent with observations of low redshift galaxies. Mao et al. (2010) found a mean value $r_{31} = 0.61 \pm 0.16$ in their sample of normal SFGs. Papadopoulos et al. (2012) found a higher mean value $r_{31} = 0.67$ in a sample of nearby LIRGs, which are expected to have higher r_{31} given their higher SSFR and SFE. Also, Yao et al. (2003) found a higher mean value $r_{31} = 0.66$ in their sample of infrared luminous galaxies. The r_{31} values in the BASS AGN sample span a very similar range to the xCOLD GASS sample $0.22 - 1.23$, with a mean value 0.53 ± 0.06 (standard deviation 0.25). For the SLUGS sample, the r_{31} values are in the range $0.32 - 0.89$ with a mean value 0.58 ± 0.07 (standard deviation 0.20). The mean value of the total sample is $< r_{31} >= 0.55 \pm 0.03$ (standard deviation 0.23).

We investigate how the ratio r_{31} evolves as a function of SFR, SSFR and SFE (Fig. 2.3). We find a general trend for r_{31} to increase as these quantities increase (Pearson correlation coefficients $R = 0.26 - 0.60$). To illustrate the evolution of r_{31}, we divide the total sample in bins of 0.5 dex according to the quantity on the x-axis (SFR, SSFR, or SFE), and calculate the mean values of r_{31} in these bins. The mean values are shown as black points in the plots, with the error bars showing the standard errors on the mean values. For bins that contain less than three objects we do not show the mean values.

In order to properly take into account the upper limits on the r_{31} values, we apply the principles of survival analysis (Feigelson & Nelson 1985). We perform the Kendall's rank correlation test for censored data (i.e. data with upper limits) as given in Brown et al. (1974). The test gives p-value $= 9.1 \cdot 10^{-4}, 1.2 \cdot 10^{-2}, 5.4 \cdot 10^{-5}$ for the relation of r_{31} with SFR, SSFR and SFE, respectively. The p-values of the correlation with SFR and SFE are < 0.05, meaning that we can reject the null hypothesis that there is no association between the two quantities. The strongest relation is the one with the SFE (largest Pearson correlation coeff. $R = 0.6$). The correlation of r_{31} with SFE is significantly different from the correlation of r_{31} with SFR and SSFR, according to the Fisher Z-test (p-value=0.03 and p-value $= 9.6 \cdot 10^{-5}$, respectively). This trend has already been reported by Yao et al. (2003) and Leech et al. (2010) for samples of infrared luminous galaxies and LIRGs. If we consider the r_{31} ratio to be a proxy for the ratio of relatively dense to very diffuse molecular gas, the correlation between r_{31} and SFE suggests that galaxies with a higher fraction of dense molecular gas tend to have higher SFE. The connection between r_{31} and gas density is investigated further in Section 2.4. We find that the r_{31} ratio tends to increase with SFE, but there is a large scatter in the relation. It is then likely that other factors contribute to regulate the r_{31} ratio.

2.3.2 Comparison of star-forming galaxies and AGN

We divide the sample into AGN (20 BASS objects and one AGN from SLUGS) and star-forming galaxies (25 xCOLD GASS galaxies and the remaining 7 SLUGS galaxies), to investigate whether we see any difference in the r_{31} values between these two classes of objects. The two samples have different distributions of specific-star formation rate (SSFR= SFR/M$_*$): the AGN host galaxies have lower values of SSFR ($-10.8 < \log \mathrm{SSFR}/[\mathrm{yr}^{-1}] < -8.8$) than the star-forming galaxies ($-10.6 < \log \mathrm{SSFR}/[\mathrm{yr}^{-1}] < -8.3$). To remove the effect of the different SSFR in the two samples, we match the samples in SSFR, and we

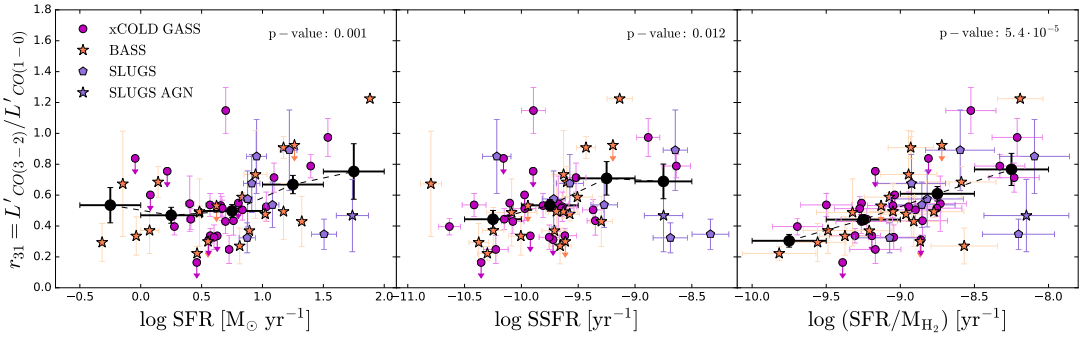

Figure 2.3. Ratio r_{31}= $L'_{\rm CO(3\text{-}2)}$/ $L'_{\rm CO(1\text{-}0)}$ as a function of star-formation rate (SFR), specific star formation rate (SSFR = SFR/M$_*$) and star-formation efficiency (SFE = SFR/$M(H_2)$) for the xCOLD GASS, BASS and SLUGS samples. The black points show the mean values of the total sample in bins of 0.5 dex, with the error bars showing the standard errors on the mean values. The dashed line connects the mean values to help to visualize the trends. In each plot, we show the p-value of the null hypothesis that there is no correlation, calculated using the Kendall's rank correlation test for censored data.

look again at the distribution of r_{31} in SFGs and AGN. This is important because of the correlation between SSFR and SFE (Saintonge et al. 2011b, 2016). We pair every SFG with the AGN host galaxy which has the most similar value of SSFR. The results are shown in Fig. 2.4. The mean r_{31} for the matched samples are consistent with each other: r_{31}= 0.52 ± 0.04 for SFGs and 0.53 ± 0.06 for AGN. To test whether the two samples have different r_{31} distributions at the same SSFR, we do a Two Sample test using the survival analysis package ASURV (Feigelson & Nelson 1985), which allows to take into account upper limits. We find that the two samples are not significantly different according to the Gehan's, Logrank and Peto-Prentice's Two Sample Tests (p-value=0.57-0.79). So our results suggest that there is no clear difference in the r_{31} values due to the AGN contribution.

Mao et al. (2010) find a higher $r_{31} = 0.78 \pm 0.08$ in AGN than in normal star-forming galaxies ($r_{31} = 0.61 \pm 0.16$). They however do not control for the SSFR, so it is possible that the difference in r_{31} is partly due to differences in SSFR between the two samples and not to the effect of the AGN. They also find higher r_{31} values in starbursts ($r_{31} = 0.89 \pm 0.11$) and in ULIRGs ($r_{31} = 0.96 \pm 0.14$) than in AGN. Additionally, most of the galaxies in their sample have rather large angular size (optical diameter $D_{25} > 100$") and thus the CO beam is sampling a smaller region around the nucleus. Therefore it is reasonable to expect that the AGN could have a large impact on the observed r_{31} line ratio.

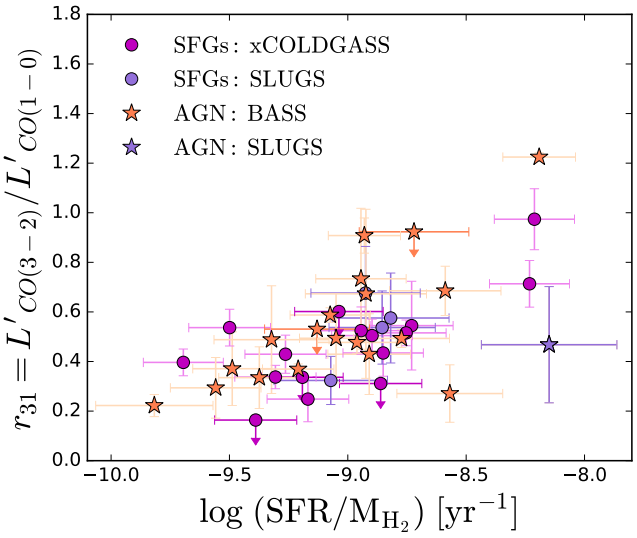

Figure 2.4. Ratio r_{31}= $L'_{\mathrm{CO(3\text{-}2)}}$/ $L'_{\mathrm{CO(1\text{-}0)}}$ as a function of star-formation efficiency (SFE = SFR/M(H_2)) for SFGs (circles) and AGN (stars). The SFG and AGN samples are matched in SSFR: at every SFG corresponds the AGN host galaxy with the most similar value of SSFR.

We look at the relation between r_{31} and hard X-ray luminosity (14-195 keV) for the BASS sample, but we do not find a clear trend between the two quantities ($R = 0.33$, see Figure 2.5), which suggests that the X-ray flux is not the main parameter affecting this line ratio. Even though the X-ray radiation may contribute to enhance the r_{31} ratio in the nuclear region, as is shown later in Section 2.4.2, it is probably not enough to regulate the CO excitation in the entire galaxy.

We conclude that there is no significant difference between the values of r_{31} of AGN and SFGs.

2.3.3 r_{31} dependence on galaxy size and beam corrections

In order to check that the beam corrections and beam sizes do not have an effect on our analysis, we investigate if there is any relation between r_{31} and galaxy angular size. For the angular size of xCOLD GASS and SLUGS we use $D = D_{25}$, i.e. the optical diameter from SDSS g-band. For BASS we use $D = 2 \times R_{k20}$, where R_{k20} is the isophotal radius at 20mag arcsec^{-2} in the K-band. If there is a correlation between r_{31} and the galaxy angular size, that could mean that the part of the galaxy that we are sampling is affecting the r_{31} measurements (i.e. the difference in the CO(1-0) and CO(3-2) beam sizes are affecting the r_{31} measurements.) For galaxies with large angular size, the telescope beam is only

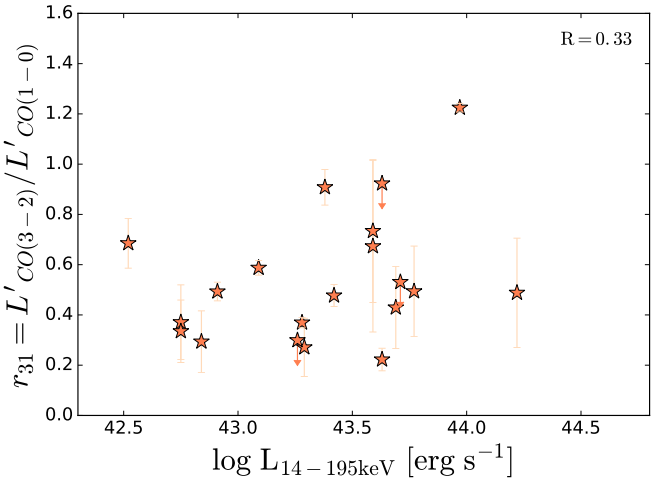

Figure 2.5. Ratio r_{31}= $L'_{\rm CO(3\text{-}2)}$/ $L'_{\rm CO(1\text{-}0)}$as a function of hard X-ray luminosity measured in the 14-195 keV band for the BASS sample.

sampling a small part of the galaxy. If the gas is denser in the central part of the galaxy, r_{31} will be higher, and thus we expect to observe a higher r_{31} for galaxies with large angular sizes. On the other hand, if the region of the galaxy included in the beam is large enough, we would not find this trend. The left panel of Fig. 2.6 shows r_{31} as a function of galaxy angular size. We do not find any trend of r_{31} increasing or decreasing with angular size ($R = -0.03$). Thus we can rule out the possibility that the angular size plays a significant role in the r_{31} variations. We note that BASS objects have in general larger angular size that the xCOLD GASS galaxies, due to their lower redshift (most objects in the BASS sample have $z < 0.025$ with respect to $z = 0.026 - 0.05$ for xCOLD GASS). We also look at the distribution of r_{31} with respect to the beam correction factor $C_{IR,PSF}$ (right panel of Figure 2.6), and we do not see any evidence of r_{31} increasing with the beam correction factor. Thus, we conclude that the beam corrections are not affecting our results.

2.4 Modelling: UCL-PDR

In order to better understand which physical parameters influence the line ratios r_{21} and r_{31}, we model the CO emission lines using a photon-dissociation region (PDR) code. Our goal is to test which are the physical quantities that have the largest effect on the CO line ratios, and which values of these quantities can reproduce our observations.

We employ the 1D UCL-PDR code, developed by Bell et al. (2005, 2006) and upgraded by Bayet et al. (2011). The latest version of the code is presented in Priestley et al. (2017).

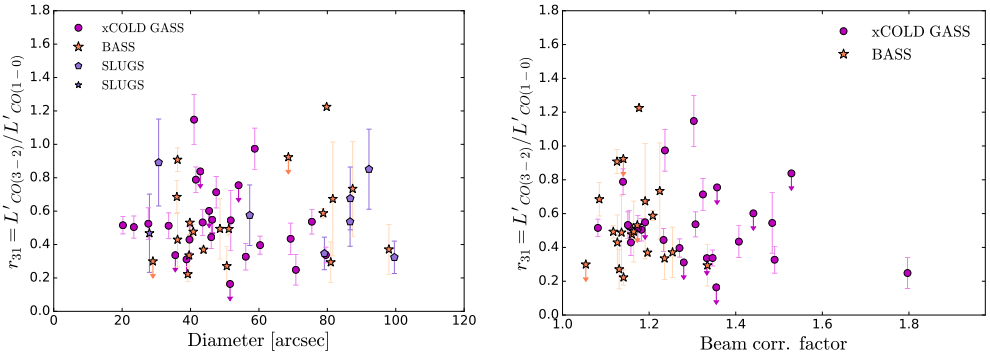

Figure 2.6. *Left:* Ratio $r_{31} = L'_{\mathrm{CO(3\text{-}2)}}/L'_{\mathrm{CO(1\text{-}0)}}$ as a function of galaxy angular diameter. For the angular diameter of xCOLD GASS and SLUGS we use $D = D_{25}$, i.e. the optical diameter from SDSS g-band. For the angular diameter of BASS we use $D = 2 \times R_{k20}$, where R_{k20} is the isophotal radius at 20 mag arcsec^{-2} in the K-band. *Right:* Ratio r_{31} as a function of the beam correction applied to account for the different beam sizes of the CO(3-2) and CO(1-0) beams. The beam corrections extrapolate the CO(3-2) flux to the area of the CO(1-0) beam.

The code models the gas cloud as a semi-infinite slab with a constant density, illuminated from one side by a far-ultraviolet (FUV) radiation field. At each depth point in the slab, the code calculates the chemistry and thermal balance of the gas self-consistently and returns, for every element, the gas chemical abundances, emission line strengths and gas temperature. Surface reactions on dust grains are not included. The FUV radiation field is modelled as the standard Draine field (Draine 1978; Bell et al. 2006). The unit of 1 Draine field corresponds to the integrated energy-intensity of the radiation field defined by Draine (1978) in the wavelength range $912 - 2000$ Å.

The gas is cooled by the emission from collisionally excited atoms and molecules and by the interactions with the cooler dust grains (Bell et al. 2006). We include in our model the cooling from the following lines: Lyman α, ^{12}C+, ^{12}C, ^{16}O, ^{12}CO, and the para and ortho H_2 and H_2O states. Table 2.1 shows the elements included in the chemical network and their initial abundances relative to hydrogen, where depletion in the dust by some elements is already taken into consideration. For the values of the initial elemental abundances we follow Bell et al. (2006). We set $n(H_2)/n_H = 0.4$ (where n_H is the volume density of hydrogen nuclei $n_H = n(H) + 2 \cdot n(H_2)$) following Bell et al. (2005).

We calculate the integrated line intensity of the CO emission lines as described in Bell et al. (2006). The opacity is included in the calculation of each coolant transition along each path (Bell et al. 2006; Banerji et al. 2009). The intensity I in units of erg s^{-1} cm^{-2}

Table 2.1. Initial elemental abundances used in the UCL-PDR code relative to the hydrogen nuclei.

Element	Abundance
He	$7.50 \cdot 10^{-2}$
O	$3.19 \cdot 10^{-4}$
C+	$1.42 \cdot 10^{-4}$
N	$6.50 \cdot 10^{-5}$
Mg(+)	$5.12 \cdot 10^{-6}$
S(+)	$1.43 \cdot 10^{-6}$

sr^{-1} is calculated by integrating the line emissivity Λ over the depth into the cloud L:

$$I = \frac{1}{2\pi} \int \Lambda(L) dL, \tag{2.8}$$

where Λ has units of erg s^{-1} cm^{-3}, and the factor of 2π takes into account the fact that the photons only emerge from the edge of the cloud/slab.

The velocity-integrated antenna temperature in units of K km s^{-1} is calculated from the intensity as:

$$T_{int} = \int T dv = \frac{c^3}{2 k_B \nu^3} I, \tag{2.9}$$

where c is the speed of light, ν the frequency of the line, and k_B is the Boltzmann constant.

The model is computed from $A_V = 0$ to $A_V = 10$. We choose the maximum A_V value to be representative of the average visual extinction measured in dark molecular clouds. At these A_V, the temperature is already ≤ 10 K and the gas enters the dense molecular cloud regime, where the freeze out starts to be efficient and it can not be considered a PDR anymore (Bergin & Tafalla 2007).

We define the r_{31} line ratio as the ratio between the integrated antenna temperatures:

$$r_{31} = \frac{T_{int,\mathrm{CO(3\text{-}2)}}}{T_{int,\mathrm{CO(1\text{-}0)}}} = \left(\frac{\nu_{\mathrm{CO(3\text{-}2)}}}{\nu_{\mathrm{CO(1\text{-}0)}}} \right)^{-3} \frac{I_{\mathrm{CO(3\text{-}2)}}}{I_{\mathrm{CO(1\text{-}0)}}}, \tag{2.10}$$

where ν is the frequency of the line. In an analogous way we calculated r_{21}. This ratio is equivalent to the observed L'_{CO} luminosity ratio that we studied in the previous section.

2.4.1 CO line ratios from modelling

We define a grid of models, varying three parameters: the volume density of hydrogen nuclei ($n_{\mathrm{H}} = n(\mathrm{H}) + 2 \cdot n(\mathrm{H_2})$), the FUV radiation field, and the cosmic ray ionization

Table 2.2. Parameters used in the grid of UCL-PDR models. (*a*) The FUV radiation is defined by the standard Draine field (Draine 1978; Bell et al. 2006). 1 Draine = $9.41 \cdot 10^{-4}$ erg s^{-1} cm^{-2} . (*b*) Standard Galactic value (Shaw et al. 2008).

Gas density ($n_{\rm H}$) [cm^{-3}]	FUV radiation field (FUV) [Draine$^{(a)}$]	cosmic ray ionization rate (*c.r.*) [10^{-17} s^{-1}]
10^2	10	2.5 $^{(b)}$
10^3	10^2	25
10^4	10^3	250
10^5		

rate (*c.r.*). The values assumed in our models are summarized in Table 2.2. The standard Galactic value of the cosmic ray ionization rate is $2.5 \cdot 10^{-17}$ s^{-1} (Shaw et al. 2008). We select a range up to two orders of magnitude higher, to take into account the fact that in AGN the cosmic ray density is higher (George et al. 2008 and references therein).

Recent studies found that cosmic ray ionization rates can be up to 100 times the Galactic value in particular regions of the interstellar medium (Indriolo & McCall 2012; Indriolo et al. 2015; Bisbas et al. 2015, 2017). Even though these extreme conditions may happen close to the source of cosmic rays, i.e. the AGN, the cosmic ray ionization rate will decrease quickly with increasing H_2 column density (Padovani et al. 2009; Schlickeiser et al. 2016). Since we are studying integrated CO fluxes within a beam that has a minimum size of $\sim$ 2 kpc, we do not expect to have an average cosmic ray ionization rates higher than 10 times the Galactic value in the region covered by the CO beam.

We note that a limitation of our approach is the degeneracy of the low-J CO line ratios to the average state of the ISM (Aalto et al. 1995). Using only two low-J CO line ratios to derive physical properties of the gas can lead to large uncertainties. Additionally, it is possible that models with line ratios that match the observations have individual intensities that are unrealistic. We compare the individual line intensities from the UCL-PDR models which match the observed r_{31} line ratios, with the observed line intensities (both for CO(3-2) and for CO(1-0)). For all galaxies, we find that the line intensities from the models are higher than the observed line intensities (by a factor that varies between 1.7 and 124). This can be explained by beam dilution effects. The UCL-PDR models assume a 100% filling factor. The observed PDR regions typically do not fill the entire beam and thus the emission from the PDR regions is diluted when averaging over the beam. As a result, the observed intensities are lower than the ones predicted from the models. Even given these

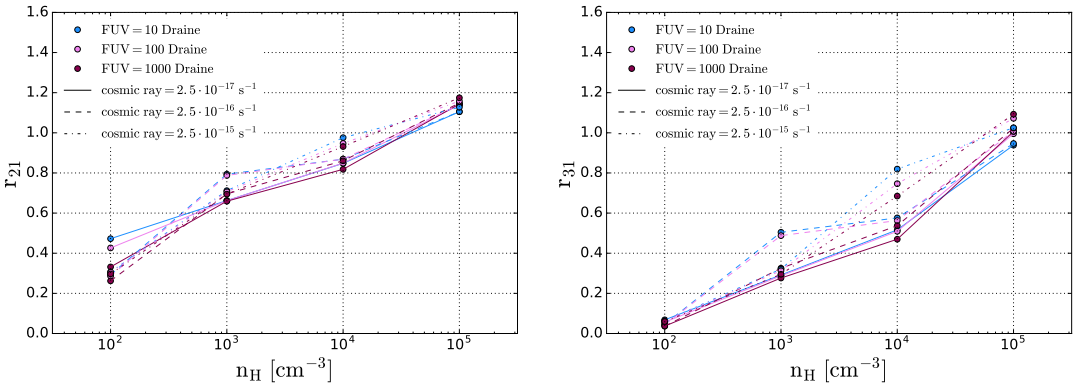

Figure 2.7. CO line ratios $r_{21} = L'_{\mathrm{CO(2\text{-}1)}}/L'_{\mathrm{CO(1\text{-}0)}}$ (left) and $r_{31} = L'_{\mathrm{CO(3\text{-}2)}}/L'_{\mathrm{CO(1\text{-}0)}}$ (right) predicted from UCL-PDR as a function of gas density n_{H}. The colors indicate models with different FUV values: 10^1 Draine (blue), 10^2 Draine (orange), 10^3 Draine (magenta). The line styles indicate models with different cosmic ray ionization rate: $2.5{\cdot}10^{-17}$ s^{-1} (full line), $2.5{\cdot}10^{-16}$ s^{-1}(dashed line), $2.5 \cdot 10^{-15}$ s^{-1} (dotted-dashed line).

limitations, qualitatively the UCL-PDR models can provide an indication of which physical parameters have the highest impact in regulating the CO line ratios.

Figure 2.7 shows the modelled line ratios r_{21} (left) and r_{31} (right) as a function of n_{H}. The colors indicate different values of the FUV radiation field and different line types correspond to different cosmic ray ionization rates. The parameter that has the largest effect on the line ratios is the density n_{H}. As expected, there is a clear increase in both line ratios with n_{H}. The r_{21} values are in the range $0.3 - 1.1$. The r_{31} value goes from 0.01 at n_{H}= 10^2 cm^{-3} to 1 at n_{H}= 10^5 cm^{-3}.

The FUV radiation field has very little effect on the line ratio. The only visible difference is for the r_{21} ratio: at n_{H}= 10^2 cm^{-3} it decreases from ~ 0.45 for FUV = 10 Draine[5] to ~ 0.3 for FUV = 1000 Draine. At low density, the high FUV field suppresses the CO emission in all J-levels. This is due to the fact that a stronger FUV field will increase the photo-dissociation of CO and consequently the CO abundance will decrease. The $J = 2-1$ level is slightly more suppressed that the $J = 1-0$ level, causing a decrease in the r_{21} line ratio.

We note also that the cosmic ray ionization rate does not have a big impact on the CO line ratios. We see an effect only at n_{H}= 10^4 cm^{-3}, where there is an enhancement of ~ 0.2 in both line ratios when the cosmic ray ionization rate is two order of magnitude

[5] 1 Draine = $9.41 \cdot 10^{-4}$ erg s^{-1} cm^{-2}. The FUV radiation is defined by the standard Draine field (Draine 1978; Bell et al. 2006).

above the Galactic value ($2.5 \cdot 10^{-15}$ s^{-1}).

So we conclude that both CO line ratios are mainly tracing the gas density. The range of variation of r_{21} is smaller than the range of r_{31}, but it is still significant.

The mean r_{31} line ratio in the combined xCOLD GASS, BASS and SLUGS samples is 0.55, which corresponds to a density of $n_{\rm H} \sim 10^4$ cm^{-3}. We note that this value should be interpreted as the average gas density of the gas traced by CO, and not as the average gas density of the ISM in giant molecular clouds. The r_{21} value at that density from UCL-PDR model is 0.8, which is consistent with the mean values reported by Saintonge et al. (2017) and Leroy et al. (2009).

One possible caveat of our analysis is that the FUV radiation field is modelled as the standard Draine field in the range $912 - 2000$ Å, but the shape and intensity of the SED in the UV is different in AGN and in SFGs. This effect is not considered in our current model. However, we consider a wide range for the strength of the FUV field, in order to take into account the stronger UV field due to the accretion disk of AGN.

2.4.2 Effect of the X-rays

We consider also the effect of the X-rays on the observed CO line ratios. AGN can be a strong source of X-rays and this could potentially affect the excitation of the CO molecules. The BASS sample is selected in the hard X-rays, and therefore we know that our sources are strong X-ray emitters.

The X-ray chemistry and physics are implemented in the latest version of the UCL-PDR code following Meijerink & Spaans (2005) and Stäuber et al. (2005). The shape and intensity of the X-ray spectrum can be defined to describe the spectrum of an AGN or of a young stellar object (Priestley et al. 2017). In the case of an AGN, the X-ray spectrum is modelled in the range 1-10 keV as a black-body with a temperature of $1.16 \cdot 10^7$ K, corresponding to an energy $kT = 1$ keV. The intensity of the X-rays can be specified.

We estimate the X-rays flux that would be observed at a distance of 1 kpc from the AGN, based on the observed fluxes measured in the 2-10 keV energy band from Ricci et al. (2017). For our sample, this flux ranges from 10^{-4} to 3×10^{-1} erg s^{-1} cm^{-2}, with a median of 10^{-2} erg s^{-1} cm^{-2}.

Figure 2.8 shows the modelled CO ratios r_{21} and r_{31} as a function of X-ray flux. For X-ray flux $< 10^{-2}$ erg s^{-1} cm^{-2} the effect on the CO ratios is negligible. This flux corresponds to an X-ray luminosity of $\sim 10^{42}$ erg s^{-1} in the 2-10 keV band, assuming

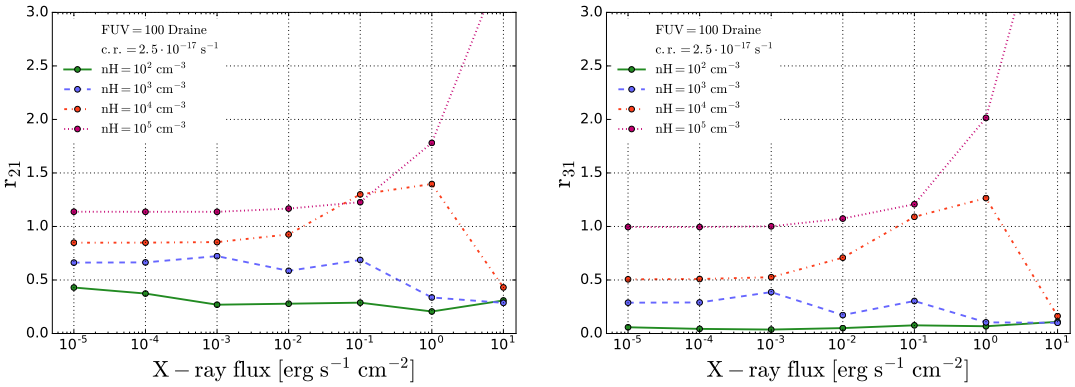

Figure 2.8. CO line ratios $r_{21} = L'_{\mathrm{CO(2\text{-}1)}}/L'_{\mathrm{CO(1\text{-}0)}}$ (left) and $r_{31} = L'_{\mathrm{CO(3\text{-}2)}}/L'_{\mathrm{CO(1\text{-}0)}}$ (right) predicted from UCL-PDR as a function of X-ray flux. The colors indicate models with different gas density values: n_{H}=10^2 cm^{-3} (green solid line), 10^3 cm^{-3} (blue dashed line), 10^4 cm^{-3} (red dotted-dashed line), and 10^5 cm^{-3} (magenta dotted line). For all models the FUV radiation field is set at 100 Draine and the cosmic ray ionization rate is set at the standard Galactic value $2.5 \cdot 10^{-17}$ s^{-1}.

that the flux is observed at 1 kpc from the nucleus. For higher X-ray fluxes in the range from 10^{-2} to 1 erg s^{-1} cm^{-2}, both r_{21} and r_{31} are enhanced if they are combined with high densities ($n_{\mathrm{H}} = 10^4 - 10^5$ cm^{-3}). If instead they are combined with lower densities ($n_{\mathrm{H}} = 10^2 - 10^3$ cm^{-3}), the ratios stay constant or decrease.

If we consider an even higher X-ray flux of 10 erg s^{-1} cm^{-2} (corresponding to an X-ray luminosity of $\sim 10^{45}$ erg s^{-1}), then the behaviour is clearly different for high and low densities. For $n_{\mathrm{H}} < 10^5$ cm^{-3}, both line ratios decrease to $r_{21} < 0.5$ and $r_{31} < 0.3$. For the highest density considered $n_{\mathrm{H}} = 10^5$ cm^{-3}, both line ratios increase to very high values (> 3). This can be explained by the fact that for low density gas the high X-ray flux reduces the CO abundance, due to photo-dissociation of CO. Thus the overall CO emission is weak and the CO ladder peaks at J=1. Only when the density is high enough can the X-rays start to excite the higher CO levels, causing the r_{21} and r_{31} levels to increase.

We conclude that the X-rays can affect the CO line ratios only for very high density and high X-ray flux. This is likely to occur only in a region very close to the active nucleus, but not in the rest of the galaxy. Thus if we consider the total CO emission of a galaxy, we do not expect to see a difference due to the presence of an AGN.

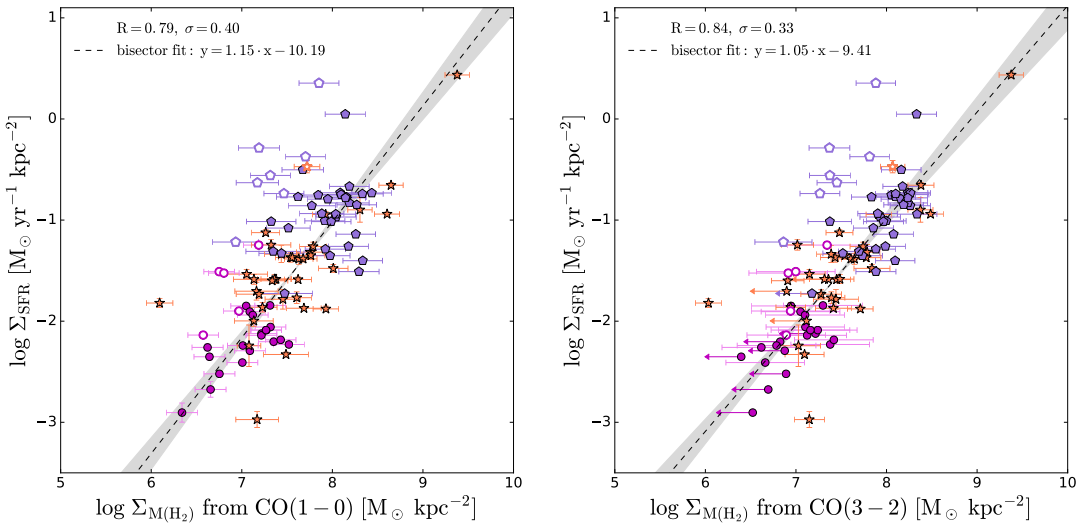

Figure 2.9. Kennicutt-Schmidt relation for the molecular gas measured from the CO(1-0) luminosity (left), and the molecular gas measured from the CO(3-2) luminosity (right). The CO(3-2) luminosities have been converted to CO(1-0) luminosities using a constant $r_{31} = 0.55$, before applying the same CO-to-H_2 conversion factor (α_{CO}) as used for the CO(1-0) lines. The surface densities are calculated for the quantities within the telescope beams. The dashed line shows the ordinary least-squares bisector fit taking into account the upper limits. Circles are xCOLD GASS galaxies, the star symbol is used for AGN from BASS, and pentagons are galaxies from SLUGS. The empty symbols are the sources for which the "ULIRG-type" CO-to-H_2 conversion factor (α_{CO}) was used and which are not included in the fit.

2.5 Molecular Kennicutt-Schmidt relation

In this section we investigate how the relation between the SFR and the molecular gas mass changes when the latter is derived from the CO(3-2) luminosity instead of from the CO(1-0) luminosity. Since CO(3-2) is tracing only the denser gas, we expect that the Kennicutt-Schmidt (KS) relation (Kennicutt 1998) measured from CO(3-2) will be tighter. Past studies found that the CO(3-2) emission correlates more strongly than the CO(1-0) emission with SFR (Muraoka et al. 2007; Komugi et al. 2007; Wilson et al. 2009).

For this analysis we consider all properties measured within the beam, applying inverse beam corrections to scale the total SFR to the SFR measured within the beam. In this way we can include also the galaxies with large angular size ($D > 100$").

Figure 2.9 shows the KS relation with the total molecular gas mass measured from the CO(1-0) luminosity and the mass of the 'dense' molecular mass measured from the CO(3-2) luminosity. The CO(3-2) luminosities have been converted to CO(1-0) luminosities using

a constant r_{31}=0.55, before applying the same CO-to-H_2 conversion factor (α_{CO}) used for the CO(1-0) luminosities. We did not include in the fit the galaxies for which we used the "ULIRGs-type" α_{CO} conversion factor (empty symbols in Fig. 2.9). By assigning to them a different conversion factor, we implicitly assume that they have a different star-formation mechanism and do not follow the same relation between the amount of molecular gas and the SFR. The correlation of SFR surface density with the molecular gas mass derived from CO(3-2) (measured by the Pearson correlation coefficient $R = 0.84$) is only slightly higher than the correlation with the molecular gas mass measured from CO(1-0) ($R = 0.79$). The two correlation coefficients are not significantly different, according to the Fisher Z-test (p-value = 0.06).

We fit the KS relation $\log \Sigma_{SFR} = a \cdot \log \Sigma_{M(H_2)} + b$ using the ordinary least-squares bisector fit (Isobe et al. 1990) taking into account the upper limits and including an intrinsic scatter. The fit to the molecular gas derived by CO(1-0) has a slope $a = 1.15 \pm 0.10$ with an intrinsic scatter of 0.48, while the fit to the molecular gas derived by CO(3-2) gives a slightly lower value $a = 1.05 \pm 0.09$ with intrinsic scatter 0.42. The two slopes are consistent with each other, within the uncertainties. We find that the KS relation becomes tighter when we consider only the dense molecular gas traced by the CO(3-2) transition. The intrinsic scatter decreases from 0.40 to 0.33, but it is still quite large also for the dense molecular gas. Thus, the fact that CO(1-0) is also tracing the diffuse molecular gas is probably not the only cause of the scatter in the KS relation.

The CO(3-2) emission line is commonly used to measure the molecular gas content of galaxies at redshift $z > 1$, for which observations of the CO(1-0) line are more time consuming. Despite the fact that CO(3-2) is tracing denser gas than CO(1-0), the KS relations obtained from CO(3-2) and from CO(1-0) are similar, with slopes that are consistent with each other and similar scatters. It is important to note that we have excluded from this analysis the 'ULIRGs'-type of galaxies. The similar KS slope of CO(3-2) and CO(1-0) suggests that there is no systematic trend in SFE along the KS relation for 'normal' star-forming galaxies in the parameter space studied in this work. This result may not hold for objects above the main-sequence (ULIRGs, starbursts), that have higher SFE with respect to MS galaxies. For 'normal' star-forming galaxies (with $\log \mathrm{SFR} < 1$), we do not observe a systematic variation of the mean r_{31} line ratio as a function of SFR (Fig. 2.3). Thus we do not expect systematic variations in the relation between the emission of 'dense' and 'total' molecular gas in these galaxies. Therefore the KS relation derived from CO(3-2)

can be directly compared to the KS relation derived from CO(1-0), once a constant offset due to the r_{31} line ratio is taken into account.

For galaxies with higher SFR ($\log \mathrm{SFR} > 1$), the r_{31} ratio increases as a function of SFR. Thus for galaxies above the main sequence, the systematic increase of the r_{31} values with SFR will cause the KS relation for CO(3-2) to be different from the CO(1-0) KS relation. Since we have excluded the ULIRG-type of galaxies from our analysis, this effect is not present in our result.

We also note the that SFE measured in our samples is similar to the SFE of main-sequence galaxies at higher redshift ($z \sim 1-3$). For example Aravena et al. (2019) find a typical depletion time of 1 Gyr ($\log \mathrm{SFE} = -9$) in galaxies with $\log \mathrm{SFR} = 1 - 1.5$, and Tacconi et al. (2013) find a mean depletion time of 0.7 Gyr, in a sample of galaxies at $z \sim 1-2$.

Our result suggests that the CO(3-2) line can be used to study the relation between SFR and molecular gas for high-redshift 'main-sequence' galaxies, and to compare it with studies of low-redshift galaxies.

2.6 Summary and conclusions

In this work, we study the ratio between the CO(1-0) and CO(3-2) emission of star-forming galaxies and AGN using observations and modelling.

Simulations from `UCL-PDR` show that the main parameter regulating the r_{31} ratio is the gas density. The FUV radiation field and X-rays play only a secondary role.

We find a relation between the r_{31} line ratio and the star-formation efficiency using data from the xCOLD GASS, BASS and SLUGS survey. This relation was already reported for the full SLUGS sample by Yao et al. (2003), and in spatially resolved observations of M83, NGC 3627, and NGC 5055 (Muraoka et al. 2007; Morokuma-Matsui & Muraoka 2017). If the CO(1-0) emission traces the total molecular gas and the CO(3-2) emission traces the denser gas, then r_{31} can be interpreted as a measure of the fraction of molecular gas which is in the dense star-forming molecular clouds. If this fraction is higher, then the efficiency of a galaxy in forming stars will be higher. The same effect is reflected in the tightening of the Kennicutt-Schmidt relation when we consider only the dense molecular gas, traced by CO(3-2), instead of the total molecular gas, traced by CO(1-0).

We have shown that the SFE is related to the amount of molecular gas which is in the

dense phase, but we do not know which factors cause the variation of the dense molecular gas fraction. The presence of spiral arms and bars may be connected to higher fraction of dense molecular gas (e.g. Sakamoto et al. 1999; Sheth et al. 2005). The presence of a bulge may also have an impact, with SFE that may be different in bulge or disk-dominated galaxies (Martig et al. 2009; Saintonge et al. 2012). However, we do not see a relation between r_{31} and the concentration index of the galaxies.

We also compare the r_{31} values in star-forming galaxies and active galaxies, to test whether the presence of an AGN has an impact on the r_{31} ratio. We do not see a difference in the distribution of the r_{31} values of AGN and SFGs. This is not surprising, as the effect of the AGN is expected to become relevant at higher J-levels (J > 10; Lu et al. 2017). The `UCL-PDR` models show that the X-rays emitted from an AGN can have an impact on the r_{31} values at higher gas density. However, the X-ray flux needs to be high ($> 10^{-1}$ erg s^{-1} cm^{-2}) and thus the X-rays can affect the condition of the ISM only close to the nucleus. This explains why we do not see this effect if we consider the total CO emission of the host galaxy. This can be different at high redshift, where we can find both more luminous quasars (with bolometric luminosities $L_{bol} > 10^{45}$ erg s^{-1}) and higher fraction of dense gas. In these conditions, the presence of an active nucleus could significantly impact the r_{31} line ratio.

We do not find large variations in the r_{31} line ratio in our sample of 'normal' star-forming galaxies. However, based on our modelling, we expect to observe higher r_{31} values in galaxies with a larger fraction of dense gas, as for example in starburst galaxies, ULIRGs, or in sub-millimeter galaxies at high redshift (e.g. Gao & Solomon 2004a; Carilli & Walter 2013; Riechers et al. 2013; Casey et al. 2014). If we were to study the r_{31} ratio in a sample of starbursts or ULIRGs, we would probably find different results. Indeed Mao et al. (2010) found higher r_{31} in starburst and ULIRGs (0.89 ± 0.11 and 0.96 ± 0.14 respectively) than in normal star-forming galaxies (0.61 ± 0.16).

In summary, the main conclusions of this work are:

- The mean value of the r_{31} ratio in our sample is $r_{31} = 0.55 \pm 0.03$. There is no significant difference in the r_{31} values of star-forming galaxies and AGN.

- We model the r_{31} using the `UCL-PDR` code and find that the main parameter regulating the r_{31} ratio is the gas density. The mean value $r_{31} = 0.55$ corresponds to a volume density of hydrogen nuclei $n_{\rm H} \sim 10^4$ cm^{-3}.

- There is a trend for the r_{31} ratio to increase with SFE (p-value=$5.4 \cdot 10^{-5}$). We find that the correlation with SFE is stronger than with SFR and SSFR.

- The correlation of the Kennicutt-Schmidt relation increases when we consider molecular gas mass traced by CO(3-2) ($R = 0.84$), instead of the molecular gas mass traced by CO(1-0) ($R = 0.79$). However, the difference is not statistically significant ($p = 0.06$). This suggests that the CO(3-2) emission line can be used to study the relation between SFR and molecular gas for 'normal' star-forming galaxies at high redshift, and to compare it with studies of low-redshift galaxies.

Chapter 3

Dust properties of nearby galaxies from the JINGLE survey

The work described throughout this chapter has been published in **Lamperti et al. (2019)** *"JINGLE V: Dust properties of nearby galaxies derived from hierarchical Bayesian SED fitting".*

In order to understand how the dust content and the dust properties of galaxies change within the galaxy population and with cosmic time, it is the necessary to have tools to accurately measure the dust content of nearby and distant galaxies and have a good understanding of the uncertainties on these measurements. This is the question this chapter tackles.

Dust masses are measured by fitting the spectral energy distribution (SED) of galaxies in the far-infrared/sub-millimeter spectral range. The standard model used is a modified black-body function (MBB), which depends on the dust mass, temperature (T) and emissivity index β. An anti-correlation between temperature and β has been observed in galactic sources and luminous infrared galaxies (Dupac et al. 2003; Désert et al. 2008; Yang & Phillips 2007). However, it has been shown that noise in the data can introduce an artificial anti-correlation between T and β (e.g. Shetty et al. 2009a,b). An incorrect estimate of T and β would consequently bias the measurement of the dust mass. A way to overcome this problem and break the $T - \beta$ degeneracy is to use a hierarchical Bayesian approach

(Kelly et al. 2012; Juvela et al. 2013; Veneziani et al. 2013; Galliano 2018). The hierarchical approach uses the information from the parameter distribution of the entire sample of galaxies to better constrain temperature and β for each single galaxy. The hierarchical method has the advantage that it does not require knowing the prior distribution of the parameters before the fitting, but can infer the parameters describing the prior directly during the fitting procedure, after assuming the shape of the distribution. The limitation of this is that the prior is only valid for the sample of galaxies under consideration, i.e. the prior depends on the population that one is considering.

The JINGLE (JCMT dust and gas In Nearby Galaxies Legacy Exploration) survey is a large program on the James Clerk Maxwell Telescope (JCMT) which aims to characterize the dust and molecular gas in nearby galaxies and study the relation between the two (Saintonge et al. 2018). JINGLE combines dust observations from the SCUBA-2 camera on the JCMT (and from *Herschel*), with the cold gas measurements obtained with the JCMT RxA instrument. With both measurements of the dust and cold gas properties for a statistical sample of nearby galaxies, we will be able to study the variations in the dust-to-gas mass ratio as a function of galaxy and dust properties.

One of the objectives of the survey is to benchmark dust scaling relations with other galaxy properties such as stellar mass, metallicity, and star-formation rate. These relations can be used to estimate the dust temperature and dust emissivity index in galaxies for which there are not enough photometric data available to measure them directly through SED fitting. This can be useful especially for high redshift galaxies.

An excess of emission at wavelengths $\geq 500\mu$m with respect to the modified blackbody model has been observed in numerous dwarf galaxies (e.g. Galametz et al. 2011; Rémy-Ruyer et al. 2013, 2015), in late-type galaxies (Dumke et al. 2004; Bendo et al. 2006; Galametz et al. 2009), in the Magellanic Clouds (Israel et al. 2010; Bot et al. 2010), and in M33 (Hermelo et al. 2016; Relaño et al. 2018). The origin of this 'submm' excess is still an open question. The SCUBA-2 observations at 850 μm can help to place better constraints on the submm slope and investigate the presence of this excess in the JINGLE sample.

In this chapter, we take advantage of the large and homogeneous JINGLE sample and by applying a hierarchical Bayesian approach, we reduce the $T-\beta$ degeneracy and obtain more accurate measurements of the dust parameters. The hierarchical approach is crucial to disentangle dust temperature T and emissivity index β and allows us for the first time

to study the independent relations of these two dust quantities with other galaxy global properties.

This chapter is organised as follows. In Section 3.1 we present the sample and the data used in this work. Then, we describe the classical and hierarchical Bayesian SED fitting methods and compare the two methods using simulated SEDs (Section 3.2). Section 3.3 illustrates the results of the SED fitting of the JINGLE sample, the T-β relation, and comparison of different modified black-body models. In Section 3.3.5 we derive scaling relations between dust quantities and other global galaxy properties. Finally, in Section 3.4 we summarize the main results and our conclusions.

3.1 Sample and data

3.1.1 JINGLE sample

The 192 galaxies in the JINGLE sample have stellar masses in the range $\log M_*/M_\odot = 9 - 11.3$ and are in the redshift range $0.01 < z < 0.05$. The targets were selected from the H-ATLAS survey (Eales et al. 2010; Maddox et al. 2018) with the requirement to have a detection $\geq 3\sigma$ in the 250 μm and 350 μm SPIRE bands. Additionally, they have been selected to have a flat logarithmic stellar mass distribution. Due to these requirements, they are mainly main-sequence star-forming galaxies with $-1.5 < \log \mathrm{SFR}/[\mathrm{M}_\odot\ \mathrm{yr}^{-1}] < 1.5$ (see Figure 3.1). A detailed description of the selection criteria is provided in Saintonge et al. (2018). Most of the JINGLE objects are late-type galaxies, with only seven classified as early-type galaxies (Saintonge et al. 2018).

Properties of the JINGLE galaxies used in this work (such as SFR, metallicity, distances,...) are taken from the JINGLE catalog (Saintonge et al. 2018). In particular, we use the star-formation rates and stellar masses measured with `MAGPHYS` (da Cunha et al. 2008). In this work, we refer to JINGLE galaxies using their corresponding JINGLE ID, as described in the JINGLE catalog (Saintonge et al. 2018).

3.1.2 HRS sample

To extend our analysis to a larger range in galaxy properties, we include in our analysis also galaxies from the *Herschel* Reference Survey (HRS, Boselli et al. 2010a). The HRS is a volume-limited sample (15 Mpc $\leq D \leq$ 25 Mpc) of 323 galaxies, with flux limits in the K-band to minimize selection effects due to dust and young high-mass stars. A large

fraction of HRS galaxies lie in clusters, with 47% of the HRS galaxies listed in the Virgo Cluster Catalogue alone. They have stellar masses in the range $\log M_*/M_\odot = 8.4 - 11.3$. Galaxies from the HRS have been observed in the five *Herschel* bands (at 100, 160, 250, 350, and 500 μm), but do not have observations at 850 μm. In our analysis we use the SFR and stellar masses measured with `MAGPHYS` by De Vis et al. (2017), to be consistent with the JINGLE measurements.

Figure 3.1 shows the JINGLE and HRS galaxies on the SFR-M_* plane. With respect to the JINGLE galaxies, the HRS sample includes galaxies which are less massive ($\log M_* < 9$) and with lower SFR ($-2 < \log$ (SFR/[M$_\odot$ yr^{-1}]) < 0.6, mean $\log$ (SFR/[M$_\odot$ yr^{-1}]) $= -0.71$) compared to JINGLE, which has a mean $\log$(SFR/[M$_\odot$ yr^{-1}]) $= 0.04$. HRS galaxies are also less dusty than JINGLE targets (De Looze et al. 2020), since contrary to JINGLE they have not been selected based on detection in the infrared bands. The HRS sample includes also a large number of early-type galaxies (62/323, Smith et al. 2012a), which are not well represented in the JINGLE sample (7/192). Therefore, by including this sample in our analysis, we can test whether the dust scaling relations that we find with the JINGLE sample hold also for other types of galaxies. Additionally, increasing the dynamical range of galaxy properties will help to constrain better the dust scaling relations.

3.1.3 Data

JINGLE survey: Our data set consists of photometric points at 22 μm (WISE), 60 μm (IRAS), 100 μm, 160 μm (*Herschel*/PACS), 250 μm, 350 μm, 500 μm (*Herschel*/SPIRE), and 850 μm (SCUBA-2). A detailed description of the JINGLE photometric data set is given in Smith et al. (2019) and De Looze et al. (in prep.). Here we summarize the most important points. The fluxes of the WISE, *Herschel*, and SCUBA-2 bands have been extracted from matched apertures based on the SPIRE 250 μm band. The flux extraction is described in detail by Smith et al. (2019). One galaxy (JINGLE 62) has been removed from the sample since it is not detected in the 250 μm band and therefore it is not listed in the release version of the *H*-ATLAS DR2 catalogue (Maddox et al. 2018). Thus, the sample analysed in this work consists of 192 galaxies.

We consider upper limits for fluxes with peak signal-to-noise ratio S/N < 3. Since the CO(3-2) 345.79 GHz line emits in the 850 μm band, we correct the SCUBA-2 flux by subtracting the estimated contribution of the CO(3-2) line (for details see Smith et al. 2019). After subtracting the CO(3-2) emission, some of the fluxes become negative, due

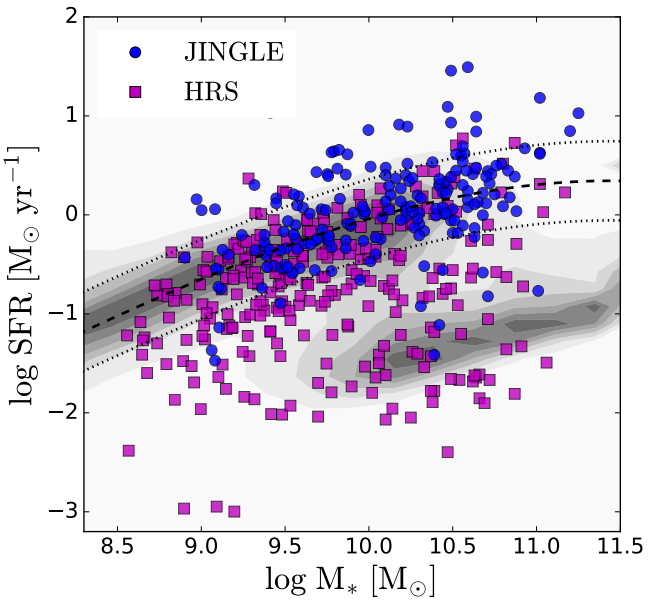

Figure 3.1. Distribution of the JINGLE and HRS sample in the SFR-M_* plane. The position of the star formation main sequence (Saintonge et al. 2016) is shown as a dashed line, the 0.4 dex dispersion is shown by dotted lines. The grey contours show the distribution of SDSS galaxies at redshift $z < 0.05$.

to the uncertainties in the 850 μm fluxes and in the CO(3-2) predictions. These fluxes are consistent with zero within the uncertainties and are considered as upper limits. In our sample, there are 66 galaxies with peak S/N < 3 and additionally 4 galaxies have negative 850 μm flux, even though their peak S/N > 3 before subtraction of the CO(3-2) contribution. For all these cases, we use conservative upper limits equal to five times the flux uncertainty in that band.

The IRAS 60 μm fluxes are derived using the Scan Processing and Integration Tool (SCANPI[1]), following the strategy of Sanders et al. (2003). In our sample, 69/192 galaxies have 5σ upper limits for the 60 μm flux and 22/192 do not have IRAS 60 μm observations.

HSR survey: For the HRS sample, we have flux measurements in the *Herschel*/PACS (Cortese et al. 2014) and *Herschel*/SPIRE bands (Ciesla et al. 2012), from 100 μm to 500 μm. We note that, contrary to JINGLE, this sample does not have observations at 850 μm, therefore the long-wavelength slope of the SED can be constrained only by the 500 μm point. In the case of non-detections, we consider upper limits equal to five times the flux uncertainties as we do for the JINGLE sample.

[1]http://irsa.ipac.caltech.edu/applications/Scanpi/

We exclude from the sample 39 galaxies which are not detected in all of the *Herschel* bands, and therefore do not have constraints on their dust properties. We also exclude four galaxies which do not have SFR and stellar mass measurements from De Vis et al. (2017). They were excluded from the sample because their SEDs show signs of contamination from dust heated by an active galactic nucleus or a hot X-ray halo or from synchrotron radiation emission (Eales et al. 2017). The final sample consists of 41 early-type and 239 late-type galaxies, for a total of 280 galaxies.

3.2 Method

3.2.1 Models

To describe the far-infrared and sub-millimeter spectral energy distribution (SED) we adopt the three models employed by Gordon et al. (2014) for the SED fit of the Magellanic Clouds: single modified black-body (SMBB), broken emissivity law modified black-body (BMBB), and two modified black-bodies (TMBB). We describe below the analytic functions and the parameters used for the three models:

- **SMBB:** The single modified black-body model describes the dust emission F_λ (in units of W m^{-2} Hz^{-1} sr^{-1}) at each wavelength λ in the following way (Hildebrand 1983):

$$F_\lambda = \frac{M_{\rm dust}}{D^2}\kappa_\lambda B_\lambda(T), \tag{3.1}$$

  where $M_{\rm dust}$ is the dust mass in the galaxy and D is the distance of the galaxy. $B_\lambda(T)$ is the Planck function for the emission of a black-body with a dust temperature T given by:

$$B_\lambda(T) = \frac{2hc^2}{\lambda^5}\frac{1}{\exp\left(\frac{hc}{k_B T\lambda}\right) - 1}. \tag{3.2}$$

  The dust mass absorption coefficient κ describes which dust mass gives rise to an observed luminosity. The value of κ depends on the physical properties of the dust, such as the mass density of the constituent materials, the efficiency with which they emit, the grain surface-to-volume ratio, and the grain size distribution (Köhler et al. 2015; Ysard et al. 2018). The SMBB applies a dust emissivity power law to

characterise the behaviour of κ as a function of wavelength:

$$\kappa_\lambda = \kappa_0 \left(\frac{\lambda_0}{\lambda}\right)^\beta \tag{3.3}$$

where κ_0 is the reference dust mass absorption coefficient. Laboratory studies found that the absorption coefficient depends also on the dust temperature and dust emissivity index β, with higher κ values observed for higher temperatures and lower β values (Coupeaud et al. 2011). For simplicity, here we assume a constant value κ_0= $\kappa(500\mu\text{m}) = 0.051$ m^2 kg^{-1} from Clark et al. (2016).

This model has three free parameters (M_{dust}, T, and β), and assumes that the dust emission can be described by a dust component with a single temperature. At wavelengths shorter than 100 μm, a second warmer dust component can contribute to the FIR emission (e.g. Relaño et al. 2018). Therefore, we use only the flux bands with wavelengths $\geq$ 100 μm for this model . Additionally, we use the 60μm point as an upper limit, in order to better constrain the dust temperature.

- **BMBB:** When fitting the FIR SED with a SMBB model, some galaxies show an excess in the flux at wavelengths $\geq$ 500 μm, called 'sub-millimeter' excess (Lisenfeld et al. 2002; Galliano et al. 2003; Dumke et al. 2004; Bendo et al. 2006; Galametz et al. 2009; Israel et al. 2010; Bot et al. 2010; Hermelo et al. 2016). The broken emissivity law modified black-body (BMBB) model assumes that the submm excess is due to variations in the wavelength dependence of the dust emissivity law. These variations are parametrized by a broken power law:

$$\kappa_\lambda = \begin{cases} \kappa_0 \left(\frac{\lambda_0}{\lambda}\right)^{\beta_1} & \text{if } \lambda < \lambda_b \\ \kappa_0 \left(\frac{\lambda_0}{\lambda_b}\right)^{\beta_1} \left(\frac{\lambda_b}{\lambda}\right)^{\beta_2} & \text{if } \lambda > \lambda_b \end{cases} \tag{3.4}$$

where λ_b is the wavelength of the break. This model has five free parameters: M_{dust}, T, β_1, β_2, and λ_b. Also for this model, we use only the flux bands with wavelengths $\geq$ 100 μm. In order to have good constraints on the fitting parameters, it is crucial to have a detection of the 850 μm flux. If the SCUBA-2 point is not detected, an upper limit is not enough to constrain the parameters of this model. Without the 850 μm flux point, the 500 μm flux point is the only one that can be used to deter-

mine β_2 and λ_b, leading to large uncertainties on their values.

- **TMBB:** The two modified black-body model assumes that the FIR SED is emitted by two dust populations with different temperatures. The dust emission is parametrized by two modified black-bodies: one for the cold dust (indicatively $T < 40$ K) and one for the warm dust (indicatively $T > 40$ K):

$$F_\lambda = F_\lambda^{\mathrm{SMBB}_{cold}} + F_\lambda^{\mathrm{SMBB}_{warm}} \tag{3.5}$$

  where the two SMBB components are defined as above. In order to reduce the number of free parameters, we fix the β value of the warm component to 1.5 (Coupeaud et al. 2011; Boselli et al. 2012), while we leave the β value of the cold component as a free parameter. So in this model we have five free parameters: M_{cold}, T_{cold}, β_{cold}, M_{warm}, and T_{warm}. For the fitting, we use the fluxes in all available bands from 22 to 850 μm.

All these models assume that dust grains are optically thin. According to dust models, this assumption holds for wavelengths ≥ 100 μm, while at shorter wavelengths it is possible that dust is optically thick (Draine & Li 2007). Casey (2012) modelled the SED of 65 luminous infrared galaxies from the GOALS survey (Armus et al. 2009) and found that even if the dust is optically thick, the difference in the SED shape at 22 μm would be small. Utomo et al. (2019) studied the dust emission at resolved scales in four nearby galaxies (Small and Large Magellanic Clouds, M31, and M33) and found that most of the dust emitting at wavelengths longer than 100 μm is optically thin. They observe that at wavelengths ~ 20 μm some regions of the galaxies become optically thick, but on global galaxy scales we do not expect these regions to dominate the emission.

We apply the SMBB model to both the JINGLE and HRS sample, while we apply the BMBB and TMBB models only to the JINGLE sample. We make this decision because for the HRS sample we do not have the 850 μm flux point, and therefore we do not have enough flux points for models with a large number of free parameters. Additionally, for the BMBB model it is very important to have the 850 μm point to constrain the emissivity index β_2 after the break. Fig. 3.2 shows an example of the SED fitting of one galaxy from the JINGLE sample using the three models.

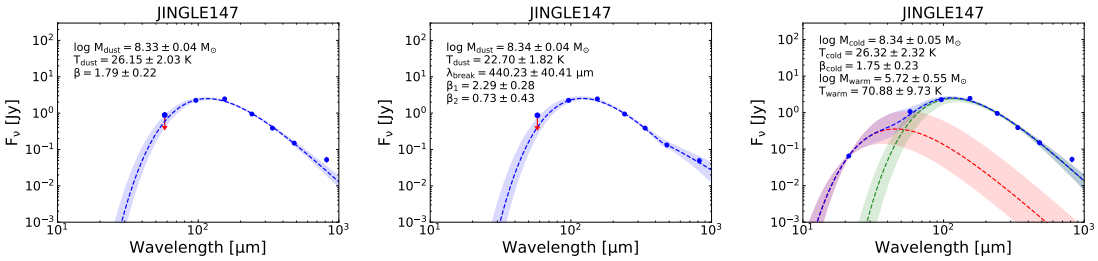

Figure 3.2. Example of FIR SED of one galaxy from the JINGLE sample, fitted with the non-hierarchical approach using the three models: single modified black-body (SMBB, left panel), broken emissivity law modified black-body (BMBB, middle panel) and two modified black-bodies (TMBB, right panel). The shaded regions show the lower and upper 1-σ uncertainties on the SED models, defined by taking the maximum and minimum flux values of the models with likelihood values in the highest 68th percentile.

3.2.2 Introduction to the Bayesian SED fitting method

In this section we briefly describe the Bayesian approach used for the SED fitting (we follow the same notation as in Galliano 2018). Readers who are less interested in the statistical methods may wish to go directly to the results presented in Section 3.3. The observed SED of a galaxy (F^{obs}) can be described in the following way:

$$F^{obs}(\lambda_j) = F^{mod}(\lambda_j, \vec{\theta}) + \epsilon(\lambda_j) \cdot F^{err}(\lambda_j) \tag{3.6}$$

where $F^{obs}(\lambda_j)$ is the flux observed at the wavelength λ_j and $F^{mod}(\lambda_j, \vec{\theta})$ is the flux described by our model with parameters $\vec{\theta}$. The last term describes the deviation of the observed flux from the model due to random noise: $F^{err}(\lambda_j)$ is the amplitude of the noise and $\epsilon(\lambda_j)$ is a random variable with mean $< \epsilon >= 0$ and standard deviation $\sigma(\epsilon) = 1$. We can reverse the previous formula to express $\epsilon(\lambda_j)$ as a function of the other quantities:

$$\epsilon(\lambda_j) = \frac{F^{obs}(\lambda_j) - F^{mod}(\lambda_j, \vec{\theta})}{F^{err}(\lambda_j)}. \tag{3.7}$$

The goal is to find the best parameters to fit the data by minimising the offset between the model and the data. From a Bayesian point of view, this is equivalent to maximising the likelihood of the model, given the data. The probability of the data given the model

parameters $\vec{\theta}$ can be expressed as:

$$p(\vec{F}^{obs}|\vec{\theta}) = \prod_{j=1}^{m} p(\epsilon(\lambda_j, \vec{\theta})) \tag{3.8}$$

where $\vec{F}^{obs} = \left(F^{obs}(\lambda_1), ..., F^{obs}(\lambda_m)\right)$ is the vector containing the flux emission at each waveband $j = 1, ..., m$. We are interested in the probability of the model parameters, knowing the observations. Thus, we can use the Bayes' theorem to write the expression:

$$p(\vec{\theta}|\vec{F}^{obs}) = \frac{p(\vec{F}^{obs}|\vec{\theta}) \cdot p(\vec{\theta})}{p(\vec{F}^{obs})} \propto p(\vec{F}^{obs}|\vec{\theta}) \cdot p(\vec{\theta}), \tag{3.9}$$

where $p(\vec{\theta})$ is the 'prior' distribution, and $p(\vec{\theta}|\vec{F}_{obs})$ is the 'posterior' distribution. The denominator $p(\vec{F}^{obs})$ can be neglected since it is constant for a given set of observed fluxes. By sampling the posterior distribution in the parameter space we can construct the posterior probability density function (PDF). Examples of PDFs are shown in Fig. 3.3. The figure shows the PDFs obtained from the SED fit of one galaxy using the SMBB, BMBB, and TMBB models.

3.2.3 Hierarchical Bayesian method

The difference between the classical and hierarchical Bayesian method is that in the former the prior distribution is an assumption and in the latter it is defined by the data sample (e.g. Gelman et al. 2004; Galliano 2018). Hierarchical methods require therefore a population of objects, which are used to define the prior distributions. In the case of SED fitting, the sample can be formed by multiple spatially resolved regions of the same galaxy or by a sample of galaxies with similar properties. The entire sample is then fitted simultaneously, in order to extract both the information about the prior distribution of the sample and the posterior distribution of the single elements of the sample.

Kelly et al. (2012) showed that the hierarchical method can be used to reduce the degeneracy between T and β. This approach has subsequently been used in other studies to reduce the T-β degeneracy (Juvela et al. 2013; Veneziani et al. 2013; Galliano 2018). The key assumption behind the hierarchical approach is that the dust parameters of our sample of galaxies follow a common distribution. In our case we assume that they follow a Student's t-distribution. Thanks to this assumption, we are able to better constrain model parameters, especially for galaxies with low S/N, where a large range of combinations of T

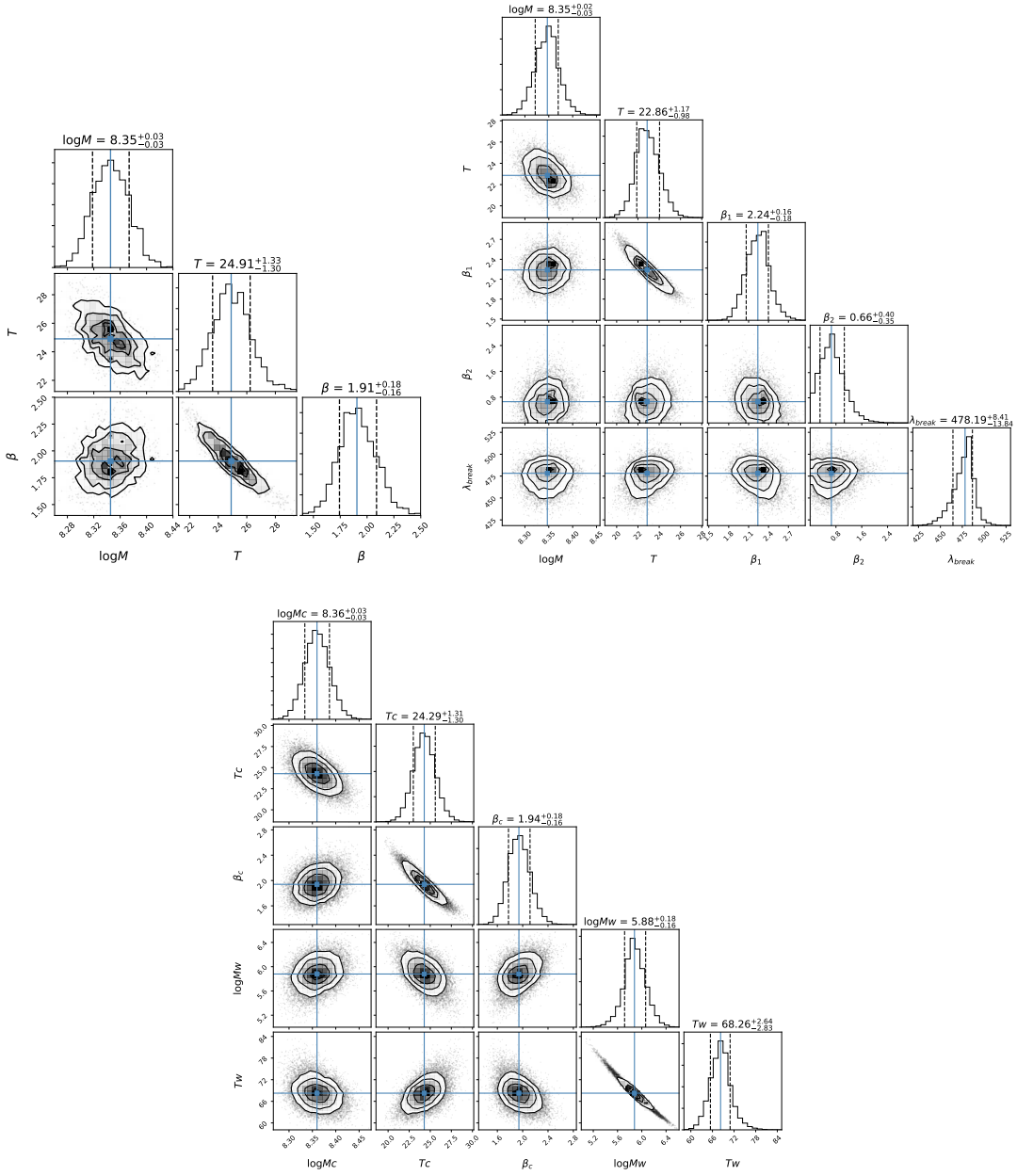

Figure 3.3. Example of the posterior probability density functions (PDFs) of the model parameters obtained using the hierarchical method for the fit of one galaxy (JINGLE 147). The three panels show the results of fit using the SMBB (upper left), BMBB (upper right) and TMBB (bottom) models. The blue line indicates the median values, the dotted lines show the 16th and 84th percentiles, that indicate the one-sigma uncertainties on the parameters.

and β provide reasonably good fits to the data. In those cases, the prior helps to constrain the range of possible T and β. The key point of the hierarchical approach is that we do not need to specify the mean and standard deviation of the prior distribution before doing the fit, but they can be inferred from the data.

The new parameters describing the prior distributions of the parameters $\vec{\theta}$ are called *hyper-parameters*. The commonly used hyper-parameters are:

- $\vec{\mu}$: the average of the parameter vector $\vec{\theta}$;
- Σ: the covariance matrix describing the standard deviation and correlation of $\vec{\theta}$.

Using this formalism, the posterior distribution of the parameters given the data $p(\vec{\theta}|\vec{F}_{obs})$ for the i-th galaxy in the sample becomes:

$$p(\vec{\theta_i}|\vec{F_i}^{obs}, \vec{\mu}, \Sigma) \propto p(\vec{F_i}^{obs}|\vec{\theta_i}) \cdot p(\vec{\theta_i}|\vec{\mu}, \Sigma). \tag{3.10}$$

This is the hierarchical equivalent of eq. (3.9). The posterior distribution of the parameters and hyper-parameters for the entire sample of n galaxies is:

$$\begin{aligned} p(\vec{\theta_1}, ..., \vec{\theta_n}, \vec{\mu}, \Sigma|\vec{F_1}^{obs}, ..., \vec{F_n}^{obs}) &\propto \prod_{i=1}^{n} p(\vec{\theta_i}|\vec{F_i}^{obs}, \vec{\mu}, \Sigma) \cdot p(\vec{\mu}) \cdot p(\Sigma) \\ &\propto \prod_{i=1}^{n} p(\vec{F_i}^{obs}|\vec{\theta_i}) \cdot p(\vec{\theta_i}|\vec{\mu}, \Sigma) \cdot p(\vec{\mu}) \cdot p(\Sigma), \end{aligned} \tag{3.11}$$

where $p(\vec{\mu})$ and $p(\Sigma)$ are the prior distributions of the hyper-parameters. When compared to the classical Bayesian method, the hierarchical method is able to recover the distribution of parameters with better precision, especially if the noise in the data is high (Kelly et al. 2012; Galliano 2018). In that case, the hierarchical approach uses the information about the parameter distribution obtained from the rest of the sample to better constrain the parameters for the particular objects where the quality of the data is low. The hierarchical method will not necessarily perform better in measuring the parameters of a single object, but it will be less biased when measuring the distribution of parameters of the entire population.

3.2.4 Noise distribution

In this section we describe the functions used to model the noise distribution for both the non-hierarchical and hierarchical approaches. The noise is usually modelled with

a normal distribution or a Student's t-distribution. The Student's t-distribution has a higher probability in the tails with respect to the normal distribution, allowing for more outliers. Its shape is described by the number of degrees of freedom f: as f decreases, more probability will be in the tails of the distribution. The normal distribution is a special case of the t-distribution with the number of the degrees of freedom that goes to infinity, $f \to \infty$.

The probability density of a normal distribution is defined as:

$$\text{Normal}(y|\mu,\sigma) = \frac{1}{\sqrt{2\pi}\sigma} \exp\left(-\frac{1}{2}\left(\frac{y-\mu}{\sigma}\right)^2\right), \tag{3.12}$$

where μ is the mean and σ is the standard deviation. The multivariate normal distribution is the generalization of the one-dimensional normal distribution to a higher dimension m:

$$\text{MultiNormal}(\vec{y}|\vec{\mu},\Sigma) = \frac{1}{(2\pi)^{m/2}} \frac{1}{\sqrt{|\Sigma|}} \exp\left(-\frac{1}{2}(\vec{y}-\vec{\mu})^T\Sigma^{-1}(\vec{y}-\vec{\mu})\right), \tag{3.13}$$

where m is the dimension of the vector $\vec{y}$, Σ is the $m \times m$ covariance matrix, and $(\vec{y}-\vec{\mu})^T$ indicates the transpose of the vector $(\vec{y}-\vec{\mu})$.

The Student's t-distribution is defined as:

$$\text{Student}(y|\mu,\sigma,f) = \frac{\Gamma((f+1)/2)}{\Gamma(f/2)} \frac{1}{\sqrt{f\pi}\sigma} \left(1+\frac{1}{f}\left(\frac{y-\mu}{\sigma}\right)^2\right)^{-\frac{f+1}{2}}, \tag{3.14}$$

where f is the number of degrees of freedom. The multivariate Student's t-distribution is the generalization of the one-dimensional distribution to a higher dimension m:

$$\text{MultiStudent}(\vec{y}|\vec{\mu},\Sigma,f) = \frac{\Gamma((f+m)/2)}{\Gamma(f/2)} \frac{1}{(f\pi)^{m/2}} \frac{1}{\sqrt{|\Sigma|}} \left(1+\frac{1}{f}(\vec{y}-\vec{\mu})^T\Sigma^{-1}(\vec{y}-\vec{\mu})\right)^{-\frac{f+m}{2}}, \tag{3.15}$$

where m is the dimension of the vector $\vec{y}$.

We expect to observe a flux excess at 850 μm for some galaxies, given the fact that the submm excess has been reported in numerous studies (e.g. Galametz et al. 2011; Rémy-Ruyer et al. 2013, 2015; Hermelo et al. 2016). Since the 850 μm fluxes have usually larger uncertainties than the other points, if we use a Student's t-distribution, the SMBB model will assume that every change in slope at 850 μm is due to the error being underestimated,

rather than to a physical effect. The model will then 'ignore' the 850 μm point, and produce a fit considering only the *Herschel* points. Since we believe that there is information in the longer wavelength points, we decide to use a normal distribution for the error. In Section 8.1 of the appendix we compare the results obtained using the Student and normal distribution.

In both the non-hierarchical and hierarchical case, we model the noise as:

$$p(\vec{F}^{obs}|\vec{F}^{mod}(\vec{\theta}), C) = \text{MultiNormal}(\vec{F}^{obs}|\vec{F}^{mod}(\vec{\theta}), C), \tag{3.16}$$

where C is the covariance matrix, which describes the uncertainties associated with the flux densities in the different wavebands (see Section 3.2.6 for the definition of the covariance matrix).

3.2.5 Prior distributions

In this section we describe the prior distributions assumed for the hierarchical and non-hierarchical method.

Non-hierarchical: For the prior distribution of the parameters $\vec{\theta}$, we assume uniformly distributed ("flat") priors, i.e. $p(\theta) = 1$, in the ranges described in Table 3.1.

Hierarchical: For the definition of the prior distributions in the hierarchical framework, we follow Kelly et al. (2012), Galliano (2018) and the `Stan` manual (Stan Development Team 2017).

- *parameters*: for the definition of the prior distributions of the parameters given the hyper-parameters, we follow Kelly et al. (2012) and Galliano (2018). We assume a multivariate Student's t distribution with $f = 8$ degrees of freedom:

$$p(\vec{\theta_i}|\vec{\mu}, \Sigma) = \text{MultiStudent}(\vec{\theta_i}|\vec{\mu}, \Sigma, f = 8). \tag{3.17}$$

  We also tried to vary the number of degrees of freedom and did not see any differences in the results. Assuming a Student's t-distribution allows one to have more galaxies with dust parameters which are 'outliers' from the mean of the sample. In this way, we make sure that our assumption that the galaxies belong to the same population

is not too stringent. We note that the parameters $\vec{\theta_i}$ are not constrained within a certain range but they are allowed to take any value. Their distribution is described by the prior distribution and we set some constraints on the allowed range of the hyper-priors (mean and standard deviation) that determine the shape of the priors (see next point).

- *hyper-parameters*: For the mean $\vec{\mu}$ of the parameters, we assume a uniform prior with a large parameter range. In this way we ensure that the prior is proper (i.e $\int p(\theta)d\theta < \infty$), and at the same time we maintain the prior vague enough to not constrain the results (Tak et al. 2018; Gelman & Hill 2007). The prior ranges for $\vec{\mu}$ are shown in Table 3.2. We note that we set the prior range of $\mu(T_{warm})$ to be > 50 K, because we want the distribution of warm temperatures to be well separated from the distribution of cold temperatures. For the covariance matrix Σ, we use the *separation strategy* from Barnard et al. (2000). This formalism ensures that the prior distributions of the correlations between parameters are uniform over the range $[-1, 1]$, meaning that all values of the correlations are equally likely. The separation strategy breaks down the covariance matrix in:

$$\Sigma = SRS \ , \tag{3.18}$$

where S is a diagonal matrix with the values of the standard deviation, and R is the correlation matrix. Both S and R have dimension $q \times q$, where q is the number of free parameters in the model. The prior distribution of the hyper-parameters is then:

$$p(\vec{\mu}) \cdot p(\Sigma) \propto p(\vec{\mu}) \cdot p(S) \cdot p(R) \ . \tag{3.19}$$

For the priors on the S and R we follow the recommendations given by the `Stan` manual (Stan Development Team 2017). For the priors on the diagonal elements of S, we use a weakly informative prior, parametrized by a half-Cauchy distribution with a small scale $\sigma = 2.5$ (Stan Development Team 2017):

$$p(S_{k,k}) = \text{Cauchy}(0, \sigma) = \frac{1}{\pi\sigma} \frac{1}{1 + \left(\frac{S_{k,k}}{\sigma}\right)^2}, \tag{3.20}$$

where $S_{k,k} > 0$, for $k = 1, .., q$. For the priors on the correlation matrix R, we use a

Table 3.1. Prior parameter ranges assumed for the Bayesian non-hierarchical SED modelling using the SMBB function.

Parameter	Range
$\log M_{dust}/M_{\odot}$	(5, 9)
T [K]	(5, 50)
β	(0.1, 3)

Table 3.2. Ranges of the priors on the hyper-parameter $\vec{\mu}$ (sample mean) for the Bayesian hierarchical SED fit using the SMBB, BMBB and TMBB models.

Hyper-parameter	Range
SMBB	
$\mu(\log M_{dust}/M_{\odot})$	(6, 9)
$\mu(T)$ [K]	(15, 50)
$\mu(\beta)$	(0.5, 3)
BMBB	
$\mu(\log M_{dust}/M_{\odot})$	(5, 9)
$\mu(T)$ [K]	(5, 50)
$\mu(\beta_1)$	(0, 5)
$\mu(\beta_2)$	(0, 5)
$\mu(\lambda_b)$ [μm]	(420, 500)
TMBB	
$\mu(\log M_{\rm cold}/M_{\odot})$	(6, 10)
$\mu(T_{\rm cold})$ [K]	(5, 40)
$\mu(\beta_{\rm cold})$	(0.5, 5)
$\mu(\log M_{\rm warm}/M_{\odot})$	(2, 7)
$\mu(T_{\rm warm})$ [K]	(50, 90)

LKJ correlation distribution with shape $\nu = 2$:

$$p(R) = \text{LKJ Corr}(R, \nu) \propto \det(R)^{\nu-1} \tag{3.21}$$

(see Lewandowski et al. (2009) for definitions). The basic idea of the LKJ correlation distribution is that as ν increases, the prior increasingly concentrates around the identity matrix.

3.2.6 Covariance matrix, beam and filter corrections

In order to perform an accurate fit, it is important to take into account correctly the uncertainties associated with each flux measurement as well as the correlation between these uncertainties. The covariance matrix C describes the uncertainties associated with the

Table 3.3. Percentage of correlated and uncorrelated uncertainties for the different instruments.

Instrument	Waveband [μm]	Correlated uncertainty	Uncorrelated uncertainty	Reference
WISE	22	-	5.7 %	Jarrett et al. (2011)
IRAS	60	-	20 %	Sanders et al. (2003) Miville-Deschênes & Lagache (2005)
PACS	100, 160	5 %	2 %	Balog et al. (2014), Decin & Eriksson (2007)
SPIRE	250, 350, 500	4 %	1.5 %	Bendo et al. (2013)
SCUBA	850	-	10 %	Smith et al. (2019)

flux densities in the different wave bands, and includes both calibration and measurement uncertainties. Calibration uncertainties can be correlated between bands observed with the same instrument. For the definition of the covariance matrix, we follow Gordon et al. (2014). The calibration covariance matrix is defined as:

$$C^{cal}_{j,k} = [A_{cor,j,k} + A_{uncor,j,k}] = [\sigma^2_{cor,j,k} + \delta_{j,k}\sigma^2_{uncor,j,k}] \tag{3.22}$$

where A_{cor} is the matrix of the noise correlated between bands, A_{uncor} is the diagonal matrix of repeatability that is uncorrelated between bands. $\sigma_{cor,j,k}$ and $\sigma_{uncor,j,k}$ are the percentage of correlated and uncorrelated uncertainties, respectively, between the j-th and k-th band, and $\delta_{j,k}$ is one for $j = k$ and zero otherwise. The calibration uncertainty values that we use are reported in Table 3.3, given in percentage of the flux.

The total covariance matrix C is a combination of the calibration and measurement uncertainties:

$$C_{j,k} = C^{cal}_{j,k} \cdot F_j \cdot F_k + F^{err}_j \cdot F^{err}_k \tag{3.23}$$

where F_j and F_k are the fluxes in the j-th and k-th waveband, and F^{err}_j and F^{err}_k are the corresponding measurement uncertainties.

The colour and beam corrections applied to our data are described in detail in De Looze et al. (in prep.).

Non-hierarchical: The filter corrections are applied to the model SED by convolving the model flux points with the appropriate filter response curve in each band. The *Herschel*/SPIRE fluxes were corrected also for the effective beam area, which depends on the shape of the spectrum due to the absolute SPIRE calibration in units of flux density per

beam. The SED shape is described by the dust temperature T and the emissivity index β. At each step of the Markov chain Monte Carlo (MCMC) algorithm, the *Herschel*/SPIRE fluxes are corrected according to the two model parameters, before comparing them to the fluxes of the SED model. For the BMBB model, we applied the beam and color corrections using β_1 or β_2 depending on the wavelength position of the break λ_b. For the TMBB model, we calculate which of the two components (warm or cold) contribute the most to the flux in every band. Then we calculate the corrections using the temperature T and β values of the dominant component in each band.

Hierarchical: The beam and filter corrections make it more difficult for the code to converge, since in every MCMC step the fluxes are slightly modified. This is more problematic for the hierarchical approach, because it has a larger number of free parameters. Therefore, in order to achieve convergence in a reasonable amount of time, we apply a slightly different approach to implement the beam and filter corrections in the hierarchical case. We first do the hierarchical fit without beam and filter corrections. Then we apply the beam and filter corrections on the fluxes based on the values of T and β measured from the fit with no corrections, and finally we repeat the hierarchical fit using the 'corrected' fluxes. The beam and filter corrections are generally small compared to the flux uncertainties, therefore this approximation of the corrections does not affect the results significantly.

3.2.7 Implementation of the SED fitting

Non-hierarchical method: For the implementation of the classical Bayesian SED fitting method, we employ the affine-invariant ensemble sampler for Markov Chain Monte Carlo (MCMC, Metropolis et al. 1953) code `emcee` (Goodman & Weare 2010; Foreman-Mackey et al. 2013). The MCMC algorithm is designed to sample the posterior distribution of the unknown parameters, i.e. the probability of the parameters given the data. The values of the parameters with the corresponding uncertainties can then be inferred from the posterior distribution. We consider as results the median values of the marginalized posterior probability distributions, and we estimate the uncertainties from the values corresponding to the 16th and 84th percentiles.

To monitor the convergence, we look at the effective sample size (N_{eff}), which is defined as the number of iterations divided by the integrated autocorrelation time $N_{eff} =$

N_{iter}/τ_{int}. The autocorrelation time τ_{int} measures the number of steps after which the drawings are truly independent (Foreman-Mackey et al. 2013). It is recommended to have at least $N_{eff} > 10$, to ensure that the sequence has converged (Gelman et al. 2004).

Hierarchical method: For the implementation of the hierarchical Bayesian fitting we use `Stan` (Carpenter et al. 2017 http://mc-stan.org/), a software for Bayesian inference which employs the No-U-Turn sampler (NUTS), a variant of Hamiltonian Monte Carlo sampler. The Hamiltonian Monte Carlo (HMC) sampling (Duane et al. 1987; Neal 1994, 2011) is a form of MCMC sampling which uses the gradient of the logarithmic probability function to accelerate the parameter exploration and the convergence to the stationary distribution (Stan Development Team 2017). The HMC algorithm is more efficient than other MCMC algorithms (as for example the Metropolis-Hastings algorithm) in sampling the parameter space and in finding the region of high likelihood, because it samples the probability distribution with fewer samples. Therefore, it is particularly well suited for problems with high dimension, as is the case for hierarchical models. For example, for the hierarchical fit of 100 galaxies using the SMBB model, which has three free parameters, the dimension is of the order ~ 300. Another advantage of `Stan` is that it can sample simultaneously the posterior distribution of parameters and hyper-parameters. `Stan` allows to define the model by specifying the probability distribution of each parameter (or hyper-parameter) independently, without the need of computing the full posterior distribution. For the practical implementation, we used `PyStan`[2], which is the Python interface to `Stan` (Stan Development Team 2018).

The recommended method for monitoring the convergence of the MCMC chains in `Stan` is computing the potential scale reduction statistics $\hat{R}$ (Gelman & Rubin 1992), which gives an estimate of the factor by which the scale of the posterior distribution may be reduced as the number of iterations goes to infinity. If $\hat{R}$ is large, it means that increasing the number of iterations is likely to improve the inference. If $\hat{R} \sim 1$, then we can be confident that the number of iterations that we are using is large enough. Thus, we set the requirement that for our runs $\hat{R} < 1.15$. We also check that the effective sample size N_{eff} is always larger than 10.

[2]http://pystan.readthedocs.io/en/latest/
http://mc-stan.org

3.2.8 Validation of the method with simulations of mock SEDs

We test our fitting methods using simulated FIR SEDs. For the mock SEDs, we know the input parameter values, thus, we can assess how well our fitting procedure is able to recover them. The simulation code takes as input parameters the dust mass ($\log M_{dust}$), temperature T, and emissivity index β, and it uses these parameters to generate an SED assuming a single modified black-body (SMBB) model. Then it extracts the flux density in the selected wavebands and it adds random noise at each flux point. We assume the noise to be Gaussian distributed around zero, with amplitude equal to the noise level. We assume a different noise level in every band. For the wavebands (100, 160, 250, 350, 500, 850) μm, we use the following noise levels, given as percentages of the flux: (20, 10, 5, 10, 20, 25)%, respectively. We estimate these values by taking the mean of the error fraction in each band from our data.

The goal of the test is to assess how well the non-hierarchical Bayesian approach can measure the values of temperature and β. We simulate 100 SEDs with the same input parameters ($\log M_{dust} = 8$ M$_\odot$, $T = 30$ K, $\beta = 1.5$), adding to every SED random noise in every band as explained above. Figure 3.4 shows the results in the T-β plane. As we can see from the figure, an artificial anti-correlation is generated only from the effect of adding noise to the fluxes. This suggests that the non-hierarchical Bayesian approach will always measure a T-β anti-correlation, even if it is not present in the data. Thus, in order to asses if the T-β anti-correlation is indeed present in our sample, we need a more sophisticated fitting method.

We run the same simulation, but this time we use the hierarchical code to fit the SEDs. The results are in better agreement with the input value, and do not show any artificial correlation or anti-correlation between T and β. The non-hierarchical method measures a large range of temperatures ($T = 22-42$ K) and β values ($\beta = 0.8-2.3$). The hierarchical method measures smaller ranges of $T = 27-30$ K and $\beta = 1.50-1.55$, which are closer to the input values. Consequently, also the dust masses are better measured with the hierarchical method. The dust masses measured with the non-hierarchical method are in the range $\log M_{dust}/M_\odot = 7.87-8.23$, with typical uncertainties of ~ 0.13 dex, while the ones measured with the hierarchical method are in the range $\log M_{dust}/M_\odot = 8.06-8.09$, with typical uncertainties 0.02 dex.

We also test whether the codes can recover a positive or negative T-β correlation. In

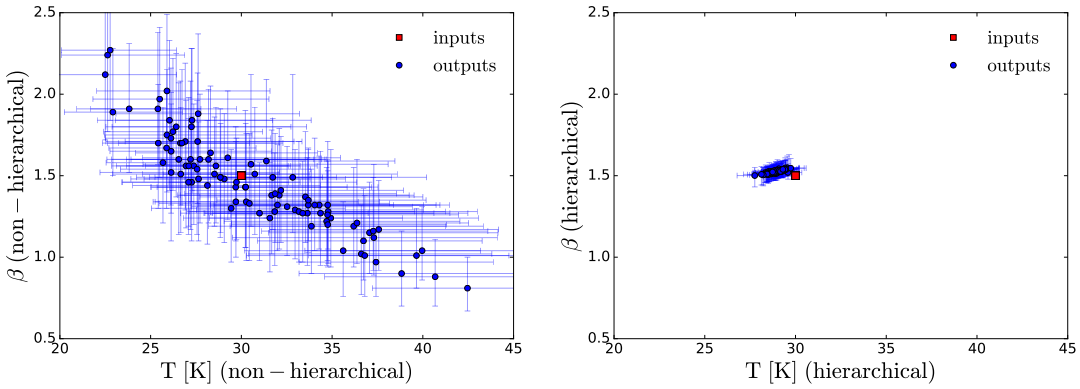

Figure 3.4. Results of temperature and β from the fit of 100 simulated SMBB SEDs with the same input parameters ($\log M_{dust}/M_{\odot} = 8$, $T = 30$ K, and $\beta = 1.5$) and 10% added noise. The output values are derived with the non-hierarchical (left panel) and hierarchical (right panel) SED fitting method. In red is shown the input value and in blue are the measured values.

both cases, the hierarchical method perform equally or better than the non-hierarchical code. Details of these simulations can be found in Appendix B (Section 8.3).

3.3 Results

3.3.1 JINGLE sample: non-hierarchical vs. hierarchical results

In the previous section we have demonstrated, using simulated SEDs, that the hierarchical method works better than the non-hierarchical approach. Here we apply both methods to the 192 galaxies of the JINGLE sample and we show the advantages of using the hierarchical method.

We start by using the simplest model, the single modified black-body (SMBB). Figure 3.5 shows the comparison of the dust masses, dust temperatures and β derived with the two approaches. In general, dust masses agree quite well between the two methods (median difference = 0.07 dex). The dust masses derived using the hierarchical method are slightly smaller, and this is probably due to the variations in dust temperatures. For a given constant flux, higher dust temperatures correspond to lower dust masses. In the range $15 - 25$ K the dust temperatures from the hierarchical approach are indeed slightly higher. At high temperatures, the differences between the two methods are larger and the non-hierarchical method measures much higher temperatures ($T >$ 30 K) than the hierarchical method. This is because as the dust temperature increases, the peak of

the SED moves to shorter wavelengths. If the SED peaks at wavelengths shorter than 100 μm, it is not sampled by the flux bands considered in the fit, since for the SMBB we are considering the 60 μm point as an upper limit. Therefore, it is more difficult to constrain the temperature. If we were to include flux points at shorter wavelengths we would need to consider a second MBB component with a warmer temperature, because the assumption of a single temperature MBB does not hold over such a large wavelength range. Instead, in the hierarchical framework, the code uses the information from the temperature distribution of the galaxy population to constrain T, and it will consider more likely for the galaxy to have a temperature close to the population mean temperature than an extreme value. Therefore, the hierarchical method can better constrain the dust temperature.

The range of temperatures is smaller in the hierarchical case ($T = 17 - 30$ K), than in the non-hierarchical case ($T = 15 - 48$ K). The same is true for the range of β: in the hierarchical case $\beta = 0.6 - 2.2$, while in the non-hierarchical case $\beta = 0.0 - 2.5$. In the hierarchical approach, we assume that the population follows a common distribution, thus the fitting is less likely to return extreme values of β. However, the hierarchical code can accommodate some outliers, since we do not define a priori the standard deviation of the prior distribution. Thus, if the data require it, the standard deviation can be large, allowing for more 'extreme' values of β. But if the extreme objects have large noise on the flux values, then the hierarchical method considers more likely that they are not 'true outliers', but that their extreme SED shape is only due to the noise in the data points. If we believe that the hierarchical approach gives more accurate results for the cases with high noise level, we conclude that the extreme values found with the non-hierarchical approach are likely not reliable, but only due to the noise in the data. The results of the hierarchical fit using the SMBB model are given in Table 8.1 in Appendix B.

3.3.2 T-β relation in the JINGLE sample

We use the results of the SED fitting using the SMBB model to investigate whether there is a relation between dust temperature and β in our sample of galaxies. An anti-correlation between T and β has been observed in many studies (e.g. Dupac et al. 2003; Désert et al. 2008), but it has been demonstrated that it can be attributed to the degeneracy between the two parameters and the effect of noise on the data (Shetty et al. 2009a,b).

Figure 3.6 shows the results from the non-hierarchical and hierarchical approach applied to our sample of 192 galaxies. The results from the non-hierarchical method show

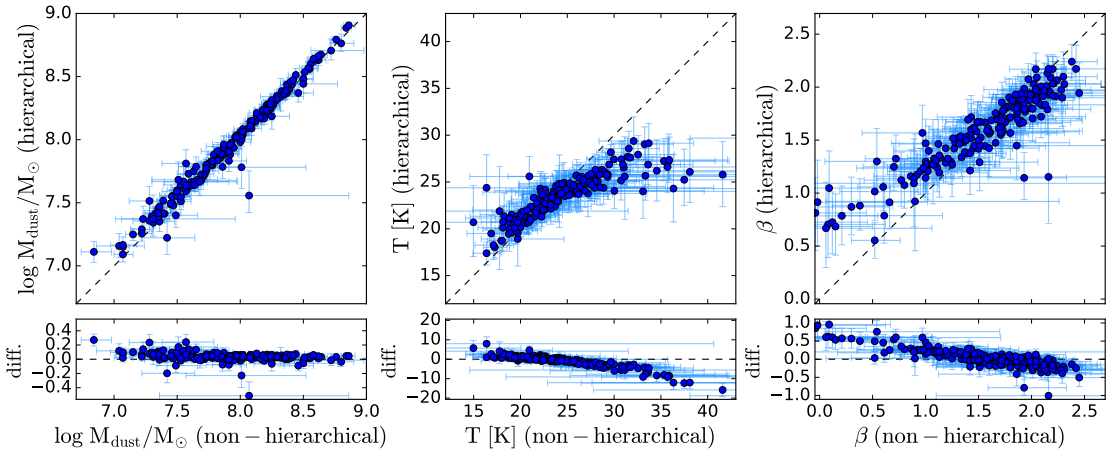

Figure 3.5. Comparison of dust properties of the JINGLE sample obtained through the fit of a single modified black-body (SMBB) using the non-hierarchical and hierarchical approaches. The lower panels show the difference between the hierarchical and non-hierarchical fit in each of the derived properties.

a significant anti-correlation between T and β. The Pearson correlation coefficient is $R_{pear} = -0.79$ (p-value $= 1.19 \cdot 10^{-41}$). The results from the hierarchical method shows a weaker anti-correlation ($R_{pear} = -0.52$, p-value $= 9.79 \cdot 10^{-15}$). This shows that the choice of the method used is really important and can deeply influence the results. This result confirms previous findings (Shetty et al. 2009a,b; Kelly et al. 2012; Veneziani et al. 2013; Juvela et al. 2013) that the observed $T - \beta$ anti-correlation is mainly driven by the fact that they are degenerate parameters, and by the noise on the data. There is still an anti-correlation between T and β even using the hierarchical approach ($R_{pear} = -0.52$). This could mean that there is indeed a physical relation between these two quantities. However, it is also possible that the hierarchical method is not able to remove completely the $T - \beta$ degeneracy, leaving a residual anti-correlation. With our current data we are not able to distinguish whether the observed relation is a physical effect or whether it is due to a residual degeneracy.

We also compare the results obtained with and without including the 850 μm flux point in the fit using the hierarchical approach (see Figure 3.7). In general, the emissivity indices β measured with the 850 μm flux point are equal or lower than the ones measured without the 850 μm point. This means that without the SCUBA-2 flux, the fits of the *Herschel* points alone have steeper slopes. This suggests that there is indeed a 'submm' excess visible at 850 μm, at least in some galaxies. This is visible especially for low values

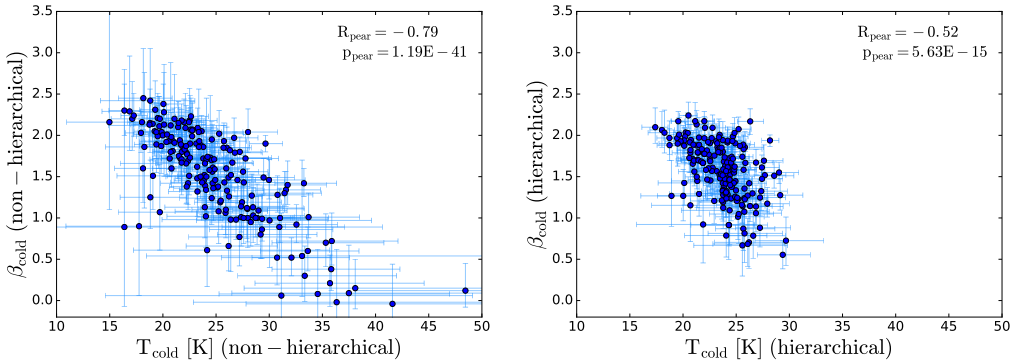

Figure 3.6. Relation between the dust temperature and dust emissivity index (T-β relation) for the JINGLE sample derived with non-hierarchical (left panel) and hierarchical (right panel) Bayesian methods. In both cases, we fit the SED using a single modified black-body (SMBB) model and we include the 850 μm flux point in the fit.

of $\beta < 1$. We note that not all galaxies show this behaviour: for some galaxies the β values measured with and without SCUBA-2 flux are in good agreement, or they show a small deficit at 850 μm. Consequently, the dust temperatures show the opposite trend: they are in general larger when the 850 μm point is included in the fit, because they have to compensate for the lower β values.

The mass measurements are only slightly affected by the presence of the SCUBA-2 flux point (median difference: 0.002 dex). The largest difference in the dust masses measured with and without the SCUBA-2 flux point is 0.07 dex. The fact that the dust masses do not show a larger variation depends on the fact that we assumed a constant absorption coefficient κ_0. Laboratory studies show that κ changes with dust temperature T and β (Coupeaud et al. 2011; Demyk et al. 2017a,b). Therefore, by keeping κ constant we erase the difference in dust masses that would arise from the different temperature and β values. A certain value of κ_0 will give an accurate dust mass only if the β value used for the fit is the same that was used to measure κ_0 (Bianchi 2013). However, a recent laboratory study by Demyk et al. (2017a) shows that variations in κ_0 are more prominent for high temperatures ($T > 30$ K) than for low temperatures. For the temperature range considered in this study ($10 - 30$ K) they do not observe variations in κ_0. A possible approach to account for variations in κ_0 would be to change the value of κ_0 according to the value of T and β used for the fitting in an iterative way. We plan to investigate this in the future.

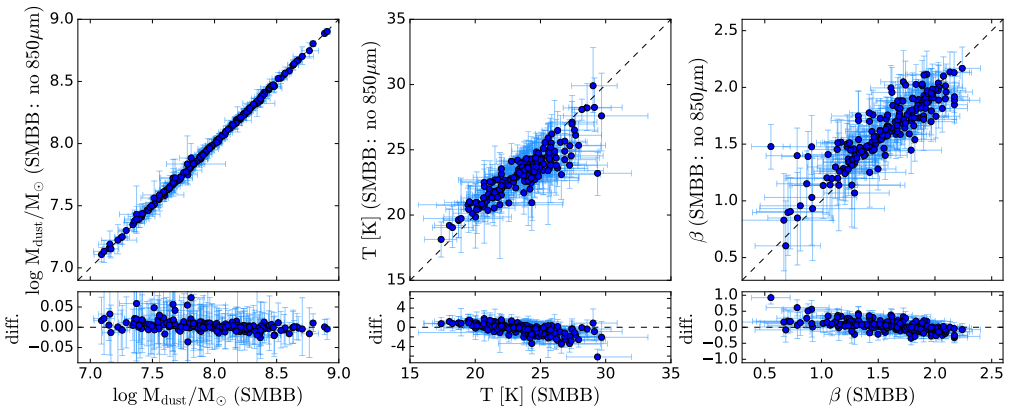

Figure 3.7. Comparison of the dust masses, temperatures and emissivity indices obtained through the fit of a single modified black-body (SMBB) using the hierarchical approach, with and without the SCUBA-2 flux point at 850 μm. The lower panels show the difference between fit with and without the SCUBA-2 flux in each of the derived properties.

3.3.3 Comparison of models: SMBB, BMBB, TMBB

In many cases, the SMBB model is not enough to fit the FIR/submm SED accurately. Especially at long wavelengths, the SED often shows a change in the slope. Therefore, we consider also two other models: the broken emissivity law modified black-body (BMBB) and the two modified black-bodies (TMBB) models, described in Section 3.2.1. In this section we compare the results obtained applying these models to the SED fit of the JINGLE sample. The results of the hierarchical fit using the BMBB and TMBB models are given in Tables 8.2 and 8.3 in Appendix B.

BMBB: The broken emissivity law modified black-body model (BMBB, Gordon et al. 2014) allows for a variation in the wavelength dependence of the dust emissivity law, to account for a submm excess. This is parametrized by using two emissivity indices for shorter and longer wavelengths. The break wavelength is a free parameter in our model. For the JINGLE sample we find values in the range $480 - 488$ μm. The emissivity index at wavelengths shorter than λ_{break} (β_1) is in the range $0.6 - 2.2$. The range of the second emissivity index at wavelengths $> \lambda_{break}$ (β_2) is larger ($0.1 - 3.3$).

We compare the results obtained using the BMBB model with the results from the SMBB model in Figure 3.8 (upper panels). The dust masses measured with the BMBB model are in agreement with the ones measured with the SMBB model, with a maximum

difference of 0.1 dex. The BMBB model measures generally slightly lower temperatures than the SMBB model (median difference of 1 K). In the case of a shallower slope of the submm SED, the SMBB model fits it by using a lower value of β and a higher T. The BMBB can correct using a smaller value of β_2, without affecting the temperature measurement. Thus, T does not depend anymore on the longer wavelength points and can have a lower value. We compare also the emissivity index β from the SMBB model, with the parameter β_1 which describes the slope of the BMBB model before the break. β_1 tends to be larger than β from the SMBB for low values of β. This is due to the fact that any excess at longer wavelength can be modelled by a second index β_2, while in the case of the SMBB the excess needs to be taken into account by β.

The results from the BMBB model are more similar to the SMBB fit without the 850 μm point. This is due to the fact that the BMBB model fits the fluxes at longer wavelengths (500 μm and 850 μm point) using a second emissivity index β_2, thus, the measurements of T and β_1 are not sensitive to the flux measurement at 500 μm and 850 μm. Figure 3.9 shows an example of the SMBB and BMBB fit of one galaxy for which the difference in temperature is more evident (JINGLE 1). This model is especially useful to quantify the possible sub-mm excess, given by the difference between the two emissivity indices β_1 and β_2. Further discussion on the submm excess is presented in Section 3.3.7.

TMBB: The bottom panels of Figure 3.8 show the comparison of the SMBB and TMBB models. The dust masses are in good agreement, with the cold dust masses derived from the TMBB being slightly higher (median offset: 0.03 dex).

The dust temperatures of the cold component obtained with the TMBB model tend to be lower than the ones measured from the SMBB model by about 3% (or 0.8 K). This is expected, since the warm component is contributing to the fit of the 100 μm flux, allowing the cold component to shift to longer wavelengths, corresponding to colder temperatures. Consequently, the β_{cold} values from the TMBB are also slightly higher (median offset: 0.05). The outlier is JINGLE 33 (Fig. 3.10). This galaxy has a high 60 μm flux, compared to the 100 μm flux, which results in the warm dust component (with $T_{warm} = 52.3$ K) reproducing most of the emission, and skewing the cold dust component to a lower temperature ($T_{cold} = 17.2$ K) and a higher dust mass.

The warm dust component does not contribute much to the entire dust mass. Warm dust masses are in the range $10^{3.4} - 10^{6.6}$ $M_\odot$, which correspond to only $0.01 - 4.4\%$ of

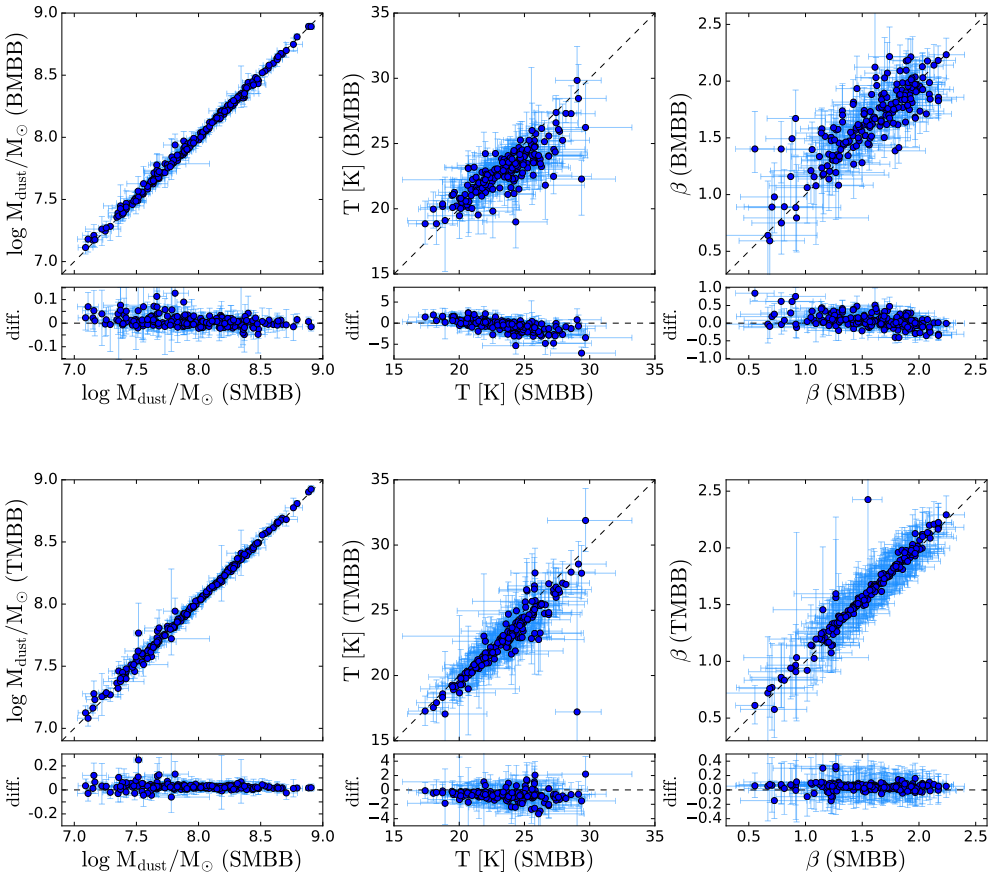

Figure 3.8. *Upper panels*: Comparison of the cold dust masses, temperatures and emissivity index obtained through the fit of a single modified black-body (SMBB) and a broken emissivity power law MBB model (BMBB). For the BMBB model, the β value shown in the plot is β_1, i.e. the emissivity index at wavelength $< \lambda_{break}$. The lower sub-panels show the difference between the two models in each of the derived properties. *Bottom panels:* Comparison of the results from the SMBB and two modified black-bodies (TMBB) model. For the TMBB model, the values shown in the plot are the parameters of the cold component (log M_{cold}, T_{cold}, β_{cold}).

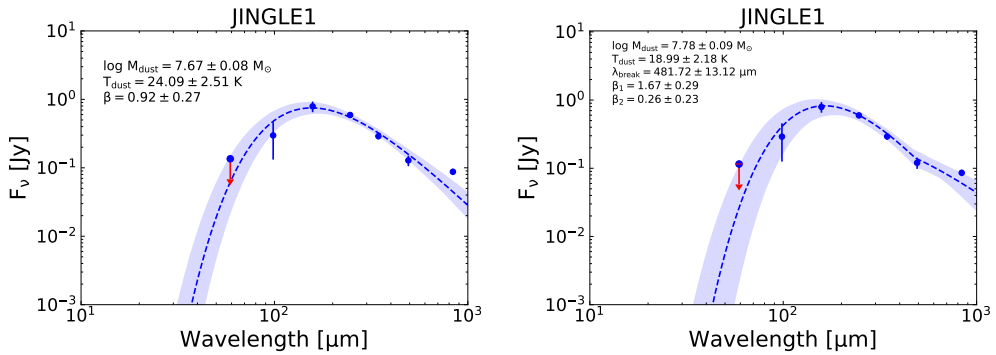

Figure 3.9. SMBB and BMBB fit for the galaxy JINGLE 1, where there is a clear difference in the dust temperature measured with the two different models.

the total dust mass of the galaxies. Nevertheless, it is important to take into account this component because, as we have shown, it can affect the measurement of the temperature and emissivity β of the cold component. The temperatures of the warm component are in the range $66 - 76$ K, with the exception of JINGLE 33 which has a lower temperature (52.3 K).

If we compare the total dust masses ($M_{dust,tot} = M_{cold} + M_{warm}$) from the TMBB with the cold dust masses M_{cold} from the SMBB, the latter are smaller by 10% ($\sim$ 0.08 dex) on average. Other studies found that fitting the SED using the TMBB model will result in higher cold dust masses. For example Gordon et al. (2014) found that the dust masses of the Small and Large Magellanic Clouds are 6-15 times larger when estimated using a TMBB model instead of the SMBB model. Clark et al. (2015) found that the warm dust mass can contribute up to 38% of the total dust mass of galaxies in the *Herschel*-ATLAS survey. The disagreement with our findings is probably due the fact that these studies do not include the 22 μm flux point in their fit. Consequently, their warm component is shifted to longer wavelength and has lower temperature than ours, thus contributing more to the total dust mass. The cold dust temperature of the TMBB will also be lower than in the SMBB case, thus resulting in higher cold dust masses.

3.3.4 Model comparison with information criterion

In order to decide which of the models provides a better fit to the data, we applied a criterion based on the comparison of the likelihoods. We consider the Bayesian Information Criterion (BIC) (Schwarz 1978) which takes into account not only the likelihood of the

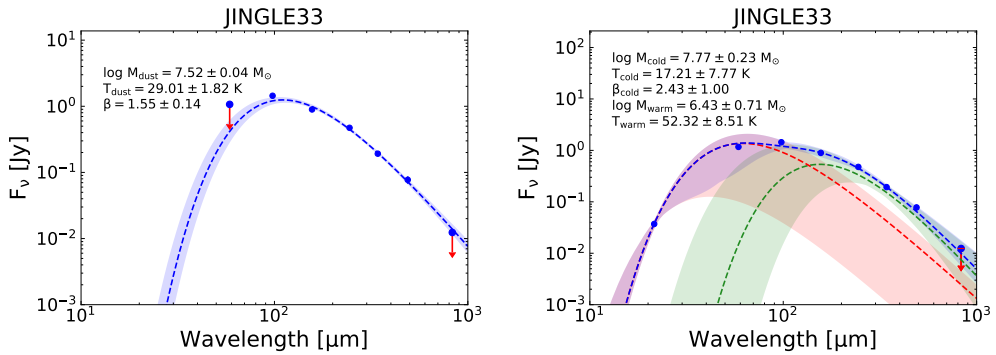

Figure 3.10. SMBB and TMBB fit for the galaxy JINGLE 33, which shows a clear difference in the cold dust mass measured with the two different methods. The warm component has a large contribution to the total dust emission in this galaxy.

fit, but also the number of free parameters of the models. The latter point is important, since increasing the number of free parameters would generally lead to better fits. The Bayesian Information Criterion (BIC) (Schwarz 1978) is defined as:

$$BIC = -2 \cdot \ln(L) + q \cdot \ln(m) \tag{3.24}$$

where L is the likelihood (i.e. the probability of the data given the parameter $p(\vec{F}|\vec{\theta})$), q is the number of free parameters of the model, and m is the number of data points (wavebands). The model with the lowest BIC value is the preferred model according to this criterion. To calculate the likelihood L_i for the i-th galaxy we consider the product of the likelihood $p(F_{i,j}^{obs}|\vec{\theta_i}, F_{i,j}^{err}, \delta_j)$ in all wavebands $j = 1, ..., m$.

$$L_i = \prod_{j=1}^{m} p(F_{i,j}^{obs}|\vec{\theta_i}, F_{i,j}^{err}, \delta_j) \tag{3.25}$$

Figure 3.11 shows the BIC values for the BMBB and TMBB models compared to the SMBB model. For most of the galaxies (180/192, 94%), the TMBB model is preferred. This is probably due to the fact that the additional warm component can help to improve the fit at 100 μm, without affecting the fit of the points at longer wavelengths.

For seven galaxies the preferred model is the BMBB model (JINGLE ID: 35, 56, 77, 101, 118, 133, and 147). In all these galaxies there is a clear submm excess at 850 μm. The BIC criterion does not identify all galaxies for which the 850 μm flux is enhanced

with respect to the SMBB model, but selects the ones for which the discrepancy can not be attributed to flux uncertainties or uncertainties in the model.

There are five galaxies which are best modelled with the SMBB model (JINGLE ID 83, 110, 142, 159, and 186). The TMBB model is not able to fit well the 60 μm and 100 μm flux points of these galaxies. For JINGLE 83 and JINGLE 159, the 60 μm flux is too low and is not well fitted by the TMBB model. For JINGLE 110, the 60 μm flux is instead too high compared to the 100 μm flux. For JINGLE 186, the uncertainty on the 60 μm flux is very small, and therefore even a small deviation from the perfect fit of that data point results in a low likelihood. In JINGLE 142, the 500 μm point is enhanced with respect to the 350 μm flux point and the 850 μm upper limit. In general neither the SMBB and TMBB models are able to produce a good fit for this galaxy. The SED fits with the BMBB and TMBB models for all galaxies are shown in Figure 8.6 in Appendix B.

We conclude that the TMBB model produces the best fit of the FIR SED for most of the galaxies. Additionally, the comparison of the BIC of the SMBB and BMBB model can be used to identify galaxies which show a strong submm excess or deficit.

3.3.5 Relation between dust properties and galaxy properties

In this section, we investigate how dust properties correlate with global galaxy properties. We use the results obtained using the SMBB model, even though the TMBB model is preferred according to the Bayesian information criterion. We decide to use the SMBB model because one of the goals of this analysis is to provide prescriptions to estimate T and β from other galaxy quantities. These prescriptions can be useful in those cases where only a few photometric data points are available and in such cases it is preferred to use the model with the smallest number of free parameter (i.e. the SMBB model). Additionally, as we have shown in the previous section, the differences in T and β derived from the SMBB and the TMBB models are not very large and they are mainly systematic shifts, that can be accounted for.

We include in this analysis also the galaxies from the *Herschel* Reference Survey (HRS, Boselli et al. 2010a), which allow us to extend the parameter range to lower SFR and lower specific SFR (SSFR), since a large fraction of the HRS sample are galaxies which lie below the star-formation main-sequence (see Fig. 3.1). In this case, the total sample of galaxies consists of two populations: star-forming galaxies (main-sequence galaxies) and

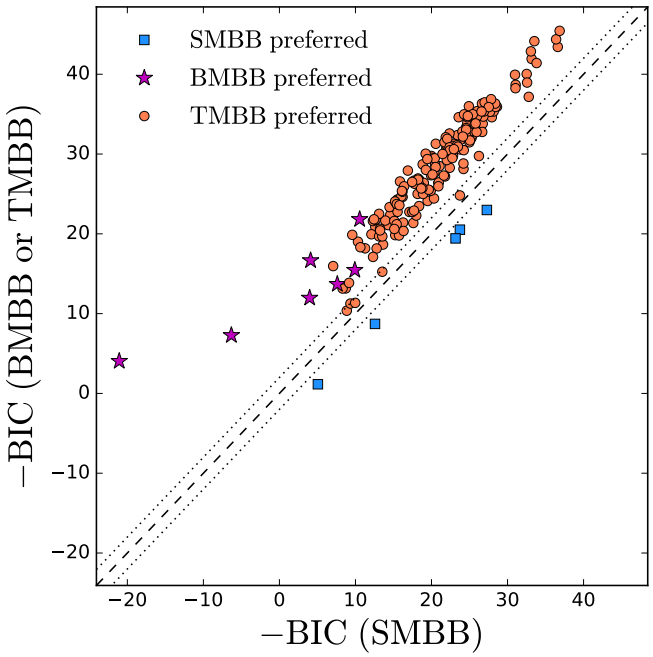

Figure 3.11. Comparison of the negative Bayesian Information Criterion (-BIC) for the fit using the three models: SMBB, BMBB, TMBB. The model with the largest value of -BIC is the preferred model. If the difference between the BICs is smaller than two (shown by the dotted lines) there is little evidence to prefer one model over an other.

passive galaxies (below main-sequence). Therefore, the basic assumption for the use of the hierarchical method that all galaxies belong to the same population does not hold any more. Therefore, we divide the 'total' sample (JINGLE+HRS) into two sub-samples according to their position in the SFR-M_* plane and fit each separately. In this way, the assumption that the galaxies in one sub-sample belong to the same population is still valid. We define the two sub-samples as follows:

- *main-sequence galaxies/ star-forming sample*: galaxies belonging to the SF main-sequence or laying above it. This sample consists of all galaxies which fall above the lower limit of the SF main-sequence, defined as 0.4 dex below the SF main-sequence definition from Saintonge et al. (2016).

- *below main-sequence sample/passive sample*: galaxies laying below the SF main sequence. These are the galaxies which lie more than 0.4 dex below the SF main-sequence defined by Saintonge et al. (2016).

The star-forming sample consists of 313 galaxies (177 from JINGLE and 136 from

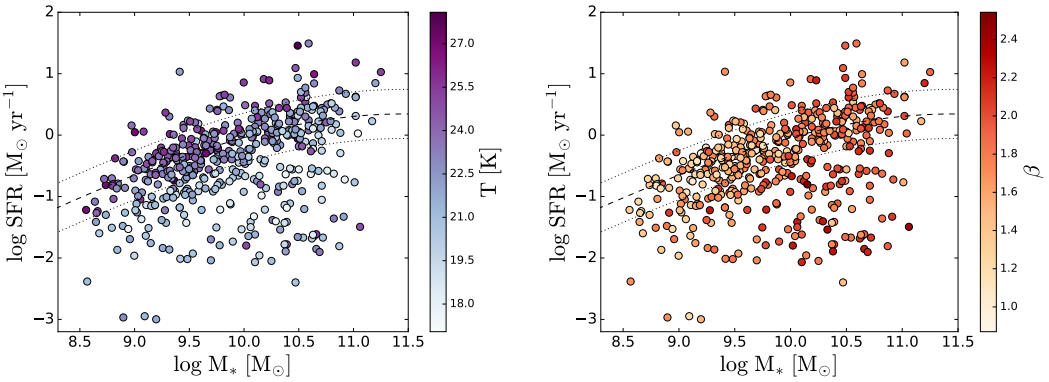

Figure 3.12. Distribution of the JINGLE and HRS sample in the SFR-M_* plane, color coded by dust temperature (left) and emissivity index β (right). Dust temperatures and β are measured using the SMBB model and the hierarchical SED fitting approach. The position of the star formation main sequence (Saintonge et al. 2016) is shown as a dashed lines, the 0.4 dex dispersion is shown by dotted lines.

HRS) and the passive sample of 159 galaxies (15 from JINGLE and 144 from HRS). We did a test fitting galaxies belonging to the two sub-samples together. This test confirms that it is necessary to separate the sample in two, to avoid to force the two sub-samples to move toward a common mean, introducing systematic biases in the results.

Figure 3.12 shows the galaxies on the SFR-M_* plane, color-coded by dust temperature T and emissivity index β. The dust temperature increases when moving from the bottom-right corner (high M_*, low SFR) to the upper-left corner (low M_*, high SFR). The emissivity β instead tends to increase with M_*. From this figure we can already see that T and β are related to different galaxy properties, with T varying depending on the SSFR and β on the stellar mass.

We quantify the strength of these relations by calculating the correlation coefficients between T, β and the following quantities: stellar mass, stellar mass surface density ($\mu_* = M_*/(2\pi R_{50}^2)$, where R_{50} is the optical half-light radius in the i band from SDSS), metallicity (12+log(O/H), using the O3N2 calibration of Pettini & Pagel 2004), HI mass fraction ($M_{\rm HI}/M_*$), star-formation rate (SFR), specific SFR (SSFR), SFR surface density ($\Sigma_{\rm SFR}$), and SFR divided by dust mass. We consider all quantities in log space. The comparison of T and β with these quantities are shown in Figure 3.13.

We calculate the Pearson correlation coefficient R and perform a linear fit when the absolute value of the correlation coefficient is higher than 0.4, both for the total sample

Table 3.4. The table shows the Pearson correlation coefficient R between dust properties (dust emissivity index β and dust temperature T) and global galaxy properties. If $|R|>0.4$ we provide the best fit relation (slope and intercept) between the selected galaxy property (p) and T (or β).

Properties p	correlation with β			correlation with T		
	R	slope	intercept	R	slope	intercept
$\log M_*$	0.58	0.23 ± 0.02	-0.60 ± 0.22	-0.29		
$\log \mu_*$	0.62	0.30 ± 0.03	-0.84 ± 0.27	-0.19		
12+log(O/H)	0.58	0.95 ± 0.13	-6.64 ± 1.16	-0.19		
$\log M_{HI}/M_*$	-0.65	-0.25 ± 0.04	1.56 ± 0.02	0.41	0.38 ± 0.23	23.07 ± 0.15
log SFR	0.20			0.21		
log SSFR	-0.40			0.54	1.83 ± 0.19	41.02 ± 1.90
$\log \Sigma_{\rm SFR}$	0.13			0.49	2.49 ± 0.23	26.74 ± 0.38
$\log {\rm SFR}/M_{dust}$	-0.15			0.73	3.40 ± 0.29	49.52 ± 2.32

and for the JINGLE and HRS samples separately. We did the fit also for the two samples separately to see whether there are differences in the correlations derived using JINGLE or HRS. We apply a correction to account for the fact that the stellar mass distribution of our sample does not exactly represent the stellar mass distribution in the local Universe, using the method developed for the xCOLD GASS survey (Saintonge et al. 2017). We compare the mass distribution of our sample, in bins of 0.1 dex in $\log M_*$, to the expected mass distribution of a volume-limited sample based on the stellar mass function from Baldry et al. (2012). For each mass bin, we calculate the ratio between the normalized number of galaxies in our sample and in the mass distribution from Baldry et al. (2012). We apply this ratio as a statistical weight when we fit the dust scaling relations. The correlation coefficients and parameters of the linear fits are summarized in Table 3.4.

We find that the emissivity β shows a positive correlation with $\log M_*$ (Pearson correlation coefficient $R = 0.58$), $\log \mu_*$ ($R = 0.62$), and metallicity ($R = 0.58$). Since these galaxy properties are all correlated with each other, it is not surprising that they all correlate with β. These trends were already observed by Cortese et al. (2014) in the HRS sample. They also observed negative correlations of these quantities with dust temperature T, due to the fact that they used a non-hierarchical method for the fitting and therefore they could not break the degeneracy between T and β. Thus, they were not able to distinguish whether the fundamental physical correlations were driven by the temperature or by the emissivity index. In our analysis, these three quantities do not show a strong anti-correlation with temperature ($-0.29 \leq R \leq -0.19$). We note that for the JINGLE galaxies the metallicities are measured from the SDSS fibre spectra and there-

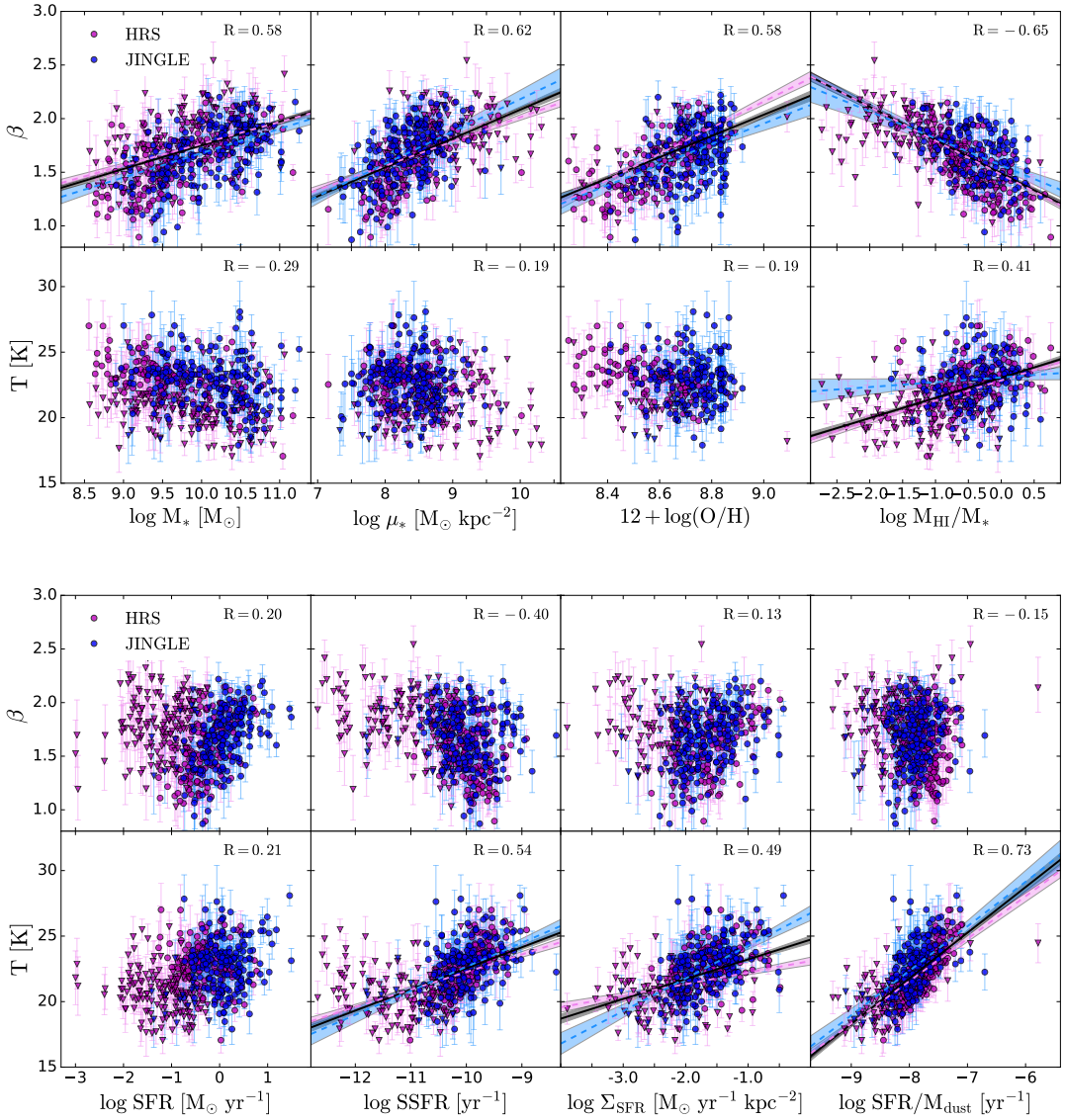

Figure 3.13. Dust scaling relations: correlation of dust temperature T and effective β with other global galaxy properties: stellar mass (M_*), stellar mass surface density ($\mu_* = M_*/(2\pi R_{50}^2)$, where R_{50}^2 is the optical half-light radius in the i band from SDSS in kpc), metallicity (12+log(O/H), O3N2 calibration of Pettini & Pagel 2004), HI mass fraction (M_{HI}/M_*), star-formation rate (SFR), specific SFR (SSFR), SFR surface density ($\Sigma_{\rm SFR}$), and SFR over dust mass (SFR/$\rm M_{dust}$). Dust temperatures and β are measured using the SMBB model and the hierarchical SED fitting approach. The JINGLE sample is shown in blue and the HRS sample in magenta. Galaxies of the 'main-sequence' sample are shown with circles and galaxies of the 'below main-sequence' sample are shown with triangles. In every panel we show the Pearson correlation coefficient R. For the cases where $R > 0.4$, the plot shows the linear fit to the JINGLE sample (in blue), to the HRS sample (in magenta), and to the two samples together (in black).

fore represent only the metallicities in the central 3 arcsec of the galaxies. For the HRS sample, metallicities are measured from long-slit integrated optical spectra (Boselli et al. 2013; Hughes et al. 2013), and thus represent better the global metallicities of the galaxies. Indeed, we find that the correlation between β and metallicity is higher ($R = 0.67$) if we consider only the HRS sample. We also find an anti-correlation between β and the HI mass fraction ($R = -0.65$), that was already observed in Cortese et al. (2014). In this case, the HI mass fraction shows a weaker correlation with dust temperature ($R = 0.41$). The HI mass fraction is known to correlate with the inverse of the stellar mass surface density and with SSFR (Catinella et al. 2013). Thus, it is expected to see an anti-correlation with β and a positive correlation with T, due to the correlation of SSFR with T.

The dust temperature correlates with log SSFR ($R = 0.54$), log Σ_{SFR} ($R = 0.49$), and log SFR/M_{dust} ($R = 0.73$). These correlations have already been observed by Clemens et al. (2013) and Cortese et al. (2014). As stated in Clemens et al. (2013), the fact the cold dust temperature correlates with SFR surface density but not with stellar mass surface density suggests that the cold dust is heated more by ongoing star-formation or by young stars. Also Kirkpatrick et al. (2014) observed a correlation between cold dust temperature and SFR normalized by the 500 μm luminosity, that is a proxy for the dust mass, on spatially resolved scales in galaxies from the KINGFISH sample (Kennicutt et al. 2011). According to their work, this correlation suggests that the number of photons from young stars relative to the amount of dust has an important heating effect on the diffuse cold dust component. Moreover, Galametz et al. (2012) studied a sub-sample of galaxies from the KINGFISH sample and observed that the higher dust temperatures coincide with the center of star-forming regions, showing a connection between dust temperature and star-formation.

The temperature of the dust is regulated by the radiation from star-formation, weighted by the amount of dust present in the galaxy. The relation between T and SSFR shows more scatter at low SSFR. This may be related in part to the fact that SFR measurements are less accurate for low SSFR (log SSFR< -10.6, Hunt et al. 2019). Also it is likely that the contribution of the older stellar population to the dust heating is higher in low SSFR galaxies, since the star-formation is weak and the contribution from old stars can be more significant.

3.3.6 Primary correlation analysis

In this section we investigate which are the primary parameters driving the correlation with dust properties. This analysis has two goals: 1) to provide prescriptions to estimate the temperature T and the emissivity index β of the dust from other galaxy properties, 2) to understand which are the physical quantities that influence and set T and β in a galaxy.

We perform a Bayesian inference analysis to find the best combination of parameters that can be used to estimate the dust properties. We consider the galaxy parameters which, alone or combined, show some correlation with β and T: stellar mass M_*, star-formation rate, dust mass, metallicity, and surface area ($A = 2\pi R_{50}^2$, where R_{50}^2 is the optical half-light radius in the i band from SDSS in kpc). The surface area is used to calculate for example the SFR and stellar mass 'surface density'. We fit first-order polynomial models with a different number of parameters, exploring all possible combinations of parameters. The number of possible combination of k parameters selected from a total sample of n parameters is $C_{n,k} = \frac{n!}{k!(n-k)!}$. We use a first-order polynomial model in log space:

$$Q_{model}(x_1, ..., x_k) = \sum_{j=1}^{k} a_j \log(x_j) + b, \tag{3.26}$$

where k is the number of galaxy properties x_j considered, and Q_{model} is the value of the dust quantity (T or β) approximated by the model. We use a Bayesian inference method to determine the optimal number of parameters needed to fit the data and the best fitting relations. We model the probability of observing our data, given the model and the uncertainties, as a normal distribution:

$$p(Q_i|Q_{model,i}(x_{1,i}, ..., x_{k,i}), Q_{err,i}) = w_i \cdot \text{Normal}(Q_{model,i}, Q_{err,i}), \tag{3.27}$$

for each galaxy i in our sample, where w_i is the weight correcting for the flat M_* distribution (see Sec. 3.3.5). We consider only the uncertainties on the dust quantity Q_i, but not on the galaxy properties $x_{j,i}$. We make this choice because we want to minimise the difference between Q_i and $Q_{model,i}$, given the quantities $x_{j,i}$. We perform a MCMC fit using `Stan` to find the best fitting parameters and measure the likelihood of the different models. Then we apply the Bayesian Information Criterion (BIC) to find the optimal number of parameters and the best model.

Table 3.5. Increase in R^2 when the parameter is added to a model that already contains the other parameters.

	β	T
Parameter	increase in ΔR^2 (%)	increase in ΔR^2 (%)
$\log M_*$	11.2	0.5
log SFR	5.0	80.0
log Area	8.0	2.4
12+log(O/H)	7.1	1.5
$\log M_{dust}$	0.5	13.6
$\log M_{HI}$	5.7	0.5

We consider first the models to estimate β. According to the BIC, the preferred model has five parameters: stellar mass, surface area, metallicity, star-formation rate, and HI mass. The best fit relation is given by:

$$\beta_{model} = 0.26^{+0.03}_{-0.03} \cdot \log M_* - 0.27^{+0.03}_{-0.03} \cdot \log Area + 0.60^{+0.09}_{-0.09} \cdot [12 + \log(O/H)] + 0.18^{+0.03}_{-0.03} \cdot logSFR - 0.23^{+0.03}_{-0.03} \cdot logM_{HI} - 3.54^{+0.82}_{-0.84}. \quad (3.28)$$

This model includes five parameters, several of which are known to be correlated, therefore, it is difficult to know which one is more fundamentally related to β. To assess this, we measure the increase in R^2 that each parameter produces when it is added to a model that contains already all other parameters. This change represents the amount of variance that can be explained by each parameter and that is not explained by the other variables. We measure R^2 ($0 < R^2 < 1$) as the squared Pearson correlation coefficient between the dust parameter (β or T) and the 'modelled' parameter (β_{model}, T_{model}), i.e. the parameter estimated by the linear combination of galaxy properties. Table 3.5 shows the results.

From the analysis of the increase of the R^2, we can see that the most fundamental parameter determining β is the stellar mass (increase in R^2: $\Delta R^2 = 11.2\%$). The second one is the surface area ($\Delta R^2 = 8.0\%$). Since they have opposite coefficients in the fit with almost the same magnitude (0.26 ± 0.03 for M_* and -0.27 ± 0.03 for the surface area), this can be interpreted as the stellar mass surface density correlating with β. If we consider stellar mass and surface area combined as a single parameter in the analysis, the increase in R^2 due to stellar mass surface density is $\Delta R^2 = 17.9\%$. The following parameter in order of importance is the metallicity ($\Delta R^2 = 7.1\%$). SFR and HI mass cause a smaller

increase in R^2 ($\Delta R^2 = 5.0\%$ and 5.7% respectively), and the dust mass has a negligible contribution ($\Delta R^2 = 0.5\%$).

Smith et al. (2012b) studied the variation of β in M31 (Andromeda). They found that β decreases with galactocentric radius. Since the stellar mass surface density (μ_*) in M31 also decreases with radius (Tamm et al. 2012), their result is consistent with a correlation between β and μ_*. Köhler et al. (2015) found that the emissivity index of grains evolve from lower to higher β values when transitioning from diffuse to denser inter-stellar medium (ISM) due to grain coagulations. If the stellar mass density is related to the density of the ISM, this could explain the relation between β and the stellar mass surface density.

As we have seen in the previous section, β correlates also with metallicity and with the inverse of the HI mass fraction. This indicates a relation between β and the state of evolution of a galaxy: more evolved galaxies tend to have higher metallicity and lower HI fraction. A possible interpretation of the variation of β with metallicity and HI mass fraction is related to the structure and composition of dust grains. Crystalline or carbonaceous dust is characterized by a lower β with respect to amorphous or silicate dust (Désert et al. 1990; Jones et al. 2013). We expect less evolved (metal-poor) galaxies undergoing an elevated period of star formation activity to produce a lot of dust in stars (Zhukovska 2014), and this dust has a more crystalline structure at the beginning (Waters et al. 1996; Waelkens et al. 1996; de Vries et al. 2010) and tends to become more 'amorphous' with time (e.g. Demyk et al. 2001). Therefore, more evolved galaxies can be expected to have more amorphous dust and higher β. Additionally, silicate dust is thought to survive for a longer time compared to carbon dust (e.g. Jones & Nuth 2011). Thus, we expect dust in a more evolved galaxy to have a larger fraction of silicate grains that are associated with higher values of β. Another possible explanation for the relation between β and metallicity is the observation that the abundance of carbon stars, which produce carbon dust, decreases at high metallicities (Boyer et al. 2019). Thus, we can expect high-metallicity galaxies to have less carbonaceous dust and consequently a higher β.

Another possibility is that the low β values are due to temperature mixing. In our analysis we are not measuring directly the emissivity of dust grains but we are measuring an 'effective β', which includes both the actual emissivity of the dust and the effect of temperature mixing (e.g. Hunt et al. 2015). It has been shown that variations of the dust temperatures along the line-of-sight can broaden the SED and mimic the effect of a low

β value (Shetty et al. 2009a). Rémy-Ruyer et al. (2015) find the SEDs of low-metallicity dwarf galaxies to be broader than the one of higher metallicity galaxies, consistent with our finding of lower β in low-metallicity galaxies. They explain this effect with the fact that dwarf galaxies have a clumpier ISM that produces a wider distribution of dust temperatures.

Since the preferred relation to approximate β needs a large number of parameters, we also provide the best relation with two parameters (stellar mass and surface area) and with three parameters (stellar mass, surface area, and metallicity), that are more practical to use:

$$\beta_{model} = 0.42^{+0.02}_{-0.02} \cdot \log M_* - 0.37^{+0.03}_{-0.03} \cdot \log Area - 1.97^{+0.18}_{-0.18}. \tag{3.29}$$

$$\beta_{model} = 0.28^{+0.03}_{-0.03} \cdot \log M_* - 0.38^{+0.03}_{-0.03} \cdot \log Area + 0.80^{+0.09}_{-0.09} \cdot [12 + \log(\mathrm{O/H})] - 7.48^{+0.64}_{-0.67}. \tag{3.30}$$

A summary with the best relations for every number k of parameters can be found in Table 3.6.

We perform a similar analysis to investigate which combination of parameters gives the better approximation of the dust temperature T. According to the BIC, the preferred model has three parameters: SFR, dust mass, and metallicity (BIC= 848.8). Also the two-parameter model with SFR and dust mass has a similar BIC (BIC= 849.6), meaning that adding the metallicity parameter has only a small effect on improving the correlation. This confirms our previous finding that dust temperature correlates strongly with SFR per unit dust mass. The R^2 analysis gives the same result: the most important parameter is clearly the SFR ($\Delta R^2 = 87.9\%$), with a secondary dependence on the dust mass ($\Delta R^2 = 16.6\%$). The other four parameters have a very small effect ($\Delta R^2 < 3\%$). This relation is however of limited practical interest since it requires prior knowledge of the dust mass. Therefore, we consider also the two-parameter model with the best BIC that do not include $\log M_{dust}$ as a parameter. The two-parameter model uses SFR and stellar mass ($R = 0.50$):

$$T_{model} = 2.50^{+0.22}_{-0.22} \cdot \log SFR - 2.14^{+0.20}_{-0.19} \cdot \log M_* + 44.24^{+1.93}_{-2.02}. \tag{3.31}$$

Tables for T and β with all the relations with two or three parameters are shown in Appendix B (Tables 8.4 and 8.5).

Table 3.6. Results of the correlation analysis to derive an expression to approximate the emissivity β and the dust temperature using global galaxy properties. The table shows the coefficients a_j of the best polynomial expression ($Q_{model}(x_1, ..., x_k) = \sum_{j=1}^{k} a_j \log(x_j) + b$) to estimate β and T using a different number of parameters k. The table also shows the Baysian Information Criterion (BIC) and the Pearson correlation coefficient R between the dust parameter (β or T) and the 'modelled' parameter (β_{model}, T_{model}), i.e. the parameter estimated by the linear combination of galaxy properties.

emissivity index β									
Parameters	$\log M_*$ [$M_\odot$]	log SFR [$M_\odot$ yr^{-1}]	log Area [kpc^2]	12+log(O/H)	$\log M_{dust}$ [$M_\odot$]	$\log M_{HI}$ [$M_\odot$]	intercept	BIC	R
$k = 1$				0.98 ± 0.06			-6.77 ± 0.59	170.56	0.61
$k = 2$	0.42 ± 0.02		-0.37 ± 0.03				-1.97 ± 0.18	53.19	0.64
$k = 3$	0.28 ± 0.03		-0.38 ± 0.03	0.80 ± 0.09			-7.48 ± 0.64	-14.37	0.70
$k = 4$	0.33 ± 0.03		-0.29 ± 0.03	0.69 ± 0.10		-0.13 ± 0.03	-5.92 ± 0.69	-27.87	0.71
$k = 5$	0.26 ± 0.03	0.18 ± 0.03	-0.27 ± 0.03	0.60 ± 0.09		-0.23 ± 0.03	-3.54 ± 0.82	-54.40	0.73
$k = 6$	0.31 ± 0.04	0.23 ± 0.04	-0.25 ± 0.04	0.66 ± 0.10	-0.13 ± 0.08	-0.20 ± 0.04	-3.84 ± 0.89	-51.19	0.73
Temperature									
Parameters	$\log M_*$ [$M_\odot$]	log SFR [$M_\odot$ yr^{-1}]	log Area [kpc^2]	12+log(O/H)	$\log M_{dust}$ [$M_\odot$]	$\log M_{HI}$ [$M_\odot$]	intercept	BIC	R
$k = 1$		0.65 ± 0.13					22.93 ± 0.08	1024.78	0.15
$k = 2$		4.19 ± 0.29			-3.73 ± 0.30		51.88 ± 2.20	849.60	0.68
$k = 3$		4.06 ± 0.29		-1.85 ± 0.75	-3.31 ± 0.31		64.7 ± 5.44	848.76	0.68
$k = 4$		3.93 ± 0.31	-0.66 ± 0.28	-2.24 ± 0.79	-2.71 ± 0.41		64.13 ± 5.67	849.08	0.69
$k = 5$	0.36 ± 0.35	3.99 ± 0.32	-0.63 ± 0.29	-2.36 ± 0.76	-3.08 ± 0.57		64.86 ± 5.82	853.77	0.69
$k = 6$	0.29 ± 0.39	4.01 ± 0.33	-0.58 ± 0.30	-2.59 ± 0.81	-2.86 ± 0.64	-0.23 ± 0.29	67.87 ± 7.28	859.06	0.70

3.3.7 Submm excess

In this section we discuss the behaviour of the SED at long wavelengths ($\lambda > 500$ μm). In particular, we are interested in galaxies which show a so-called 'submm excess'. An excess at submm wavelength has been observed in dwarf galaxies (Lisenfeld et al. 2002; Galliano et al. 2003), in late-type galaxies (Dumke et al. 2004; Bendo et al. 2006; Galametz et al. 2009), and in the Magellanic Clouds (Israel et al. 2010; Bot et al. 2010). The most significant excesses can not be explained by contribution from synchrotron, free-free or molecular line emission (e.g. Galliano et al. 2003). Different explanations proposed to explain this phenomenon are for example the presence of a very cold dust component, a temperature-dependent emissivity (Meny et al. 2007), and the presence of rotating or magnetic grains (Draine & Hensley 2012).

We identify the galaxies with an excess at 850 μm with respect to the SMBB model, taking into account uncertainties on the SCUBA-2 fluxes and on the SMBB model:

$$F^{obs} - F^{model} > F^{obs}_{err} + F^{model}_{err}. \tag{3.32}$$

There are 27/192 (14%) galaxies which satisfy this criterion. If we adopt a more stringent criterion, requiring the galaxy to have an excess above 2σ (i.e. $(F^{obs} - F^{model}) > 2 \cdot F^{obs}_{err}$), we find that 24 galaxies (12%) satisfy this criterion. From a normal distribution, we would expect to find only 2.5% of the galaxies with an excess above 2σ, thus we think that it is a statistically significant result. The galaxies with submm excess do not appear to be in a particular region of the SFR-M_* plane (see Fig. 3.14). There also some galaxies which show a deficit at 850 μm.

A weak point of this analysis is that the submm excess is determined only by a single point, the 850 μm SCUBA-2 flux. Therefore, the presence of an excess can also be due to a number of factors including measurement errors, uncertainties on the apertures, contamination by other sources, and uncertainties on the CO(3-2) contribution. In order to better characterise and quantify the submm excess, additional flux points at longer wavelengths are needed. We plan to investigate this in the future. We have an accepted proposal to observe 18 JINGLE targets at 1mm and 2mm with NIKA-2 on the IRAM-30m telescope. With two additional flux points we will be able to characterize better the submm excess and to test different models proposed to account for it.

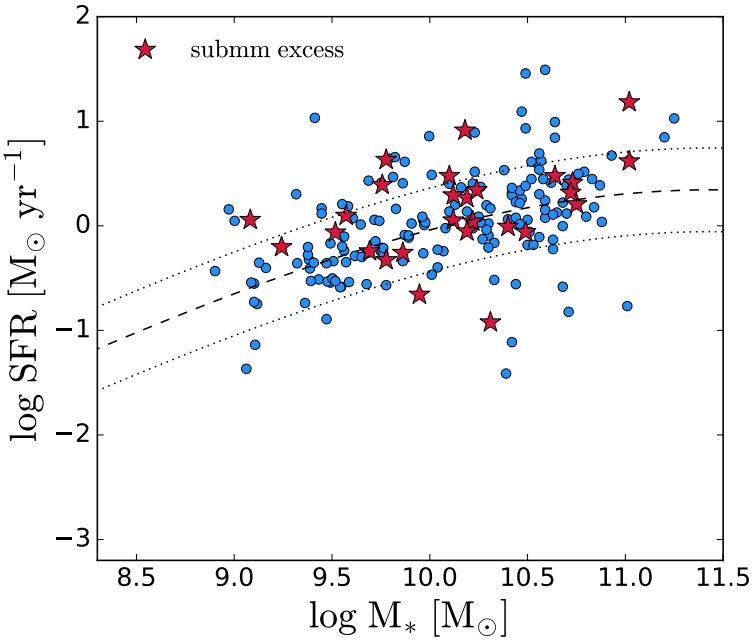

Figure 3.14. JINGLE galaxies in the SFR-M_* plane: galaxies with a submm excess are shown by red stars symbols, while the rest of the JINGLE sample is shown in light blue. The position of the star formation main sequence (Saintonge et al. 2016) is shown as a dashed lines, the 0.4 dex dispersion is shown by dotted lines.

3.4 Conclusions

In this work, we analyse a sample of 192 star-forming galaxies from the JINGLE survey. We also include in the analysis 323 galaxies from the Herschel Reference Survey (HRS) to expand our analysis to galaxies with lower specific star-formation rate. We fit their far-infrared/submm SED with modified black-body (MBB) models using a hierarchical Bayesian approach that allows to reduce the degeneracy between parameters, especially between dust temperature and emissivity index β. We consider three models: single modified black-body (SMBB), two modified black-bodies (TMBB), and MBB with a broken emissivity law (BMBB).

The main results of our study are:

- *Dust masses*: the choice of the model (SMBB, BMBB or TMBB) has only a small effect on the dust mass estimates. The cold dust masses measured with the TMBB are larger than the ones measured by the SMBB by only 0.04 dex on average, and the dust masses measured with the BMBB model agree very well with the SMBB

results.

- T-β relation: the use of the hierarchical Bayesian approach to fit the FIR SED is crucial to infer the intrinsic relation between dust temperature and dust emissivity index β. In the JINGLE sample, the anti-correlation between T and β is reduced when we use the hierarchical approach ($R = -0.52$) with respect to the non-hierarchical result ($R = -0.79$). Using the hierarchical approach, both T and β span smaller ranges (17 K $< T <$ 30 K, $0.6 < \beta < 2.2$) with fewer outliers.

- *Dust scaling relations:* the hierarchical approach is able to reduce the degeneracy between T and β and to separate their relations with other galaxy properties. We find that the dust emissivity index β correlates with stellar mass surface density, metallicity and anti-correlates with HI mass fraction (M_{HI}/M_*). The strongest relation is with stellar mass surface density. The dust temperature correlates with HI mass fraction, SSFR, SFR surface density and SFR per unit dust mass. The strongest relation is with SFR per unit dust mass. These relations can be used to estimate the dust temperature or emissivity index in galaxies where insufficient data prevents determining them directly through SED fitting.

- *Submm excess*: we observe an excess at 850 μm with respect to the flux predicted from the SMBB fit in 26/192 (14%) galaxies, but we do not find these galaxies to lie in a particular region of the SFR-M_* plane. Additional flux points at longer wavelengths are needed to better characterize the submm excess and to investigate its origin.

The dust scaling relations derived in this work based on low-redshift galaxies show that dust properties correlate with global galaxy properties. After calibrating these relations with data at higher redshift, they could be applied to the study of high-redshift galaxies. Thanks to ALMA it is now possible to detect dust emission in galaxies at redshifts as high as $z > 7$ (e.g. Watson et al. 2015; Laporte et al. 2017), but the measurement of dust masses in these objects is difficult due to the scarcity of photometric points. The possibility to use scaling relations to predict what dust properties to apply in the SED modelling will increase the precision of the dust mass measurements in the early Universe, and consequently will help our understanding of dust evolution over cosmic time.

This page was intentionally left blank

Chapter 4

Evolution of dust properties with cosmic time

In the previous chapter, we derive scaling relations between dust properties (temperature T and emissivity index β) and other global galaxy properties. These relations can be useful to measure the dust mass of galaxies with poor coverage of the FIR SED, for which it is necessary to make an assumption about T or β. In order to apply these relations at high redshift, we need to know if and how these relations evolve with cosmic time. Several studies investigated the evolution of T with cosmic time (e.g, Magnelli et al. 2014; Béthermin et al. 2015; Schreiber et al. 2018), finding that T increases with redshift. Most studies used stacking techniques, and focused mainly on the dust temperature. The hierarchical Bayesian approach offers the possibility to investigate simultaneously variations of T and β with redshift.

In this chapter, we apply the hierarchical Bayesian SED fitting code developed for JINGLE to study the dust properties in galaxies at high redshift ($z \sim 1 - 3$). The main goals are:

- test the performance of the hierarchical approach on a sample of high-redshift galaxies;
- study the evolution of dust temperature and dust emissivity β with redshift;

- compare dust scaling relations at high redshift with the scaling relations derived at low-z from JINGLE and HRS.

4.1 Sample

For this work, we use photometric data from the recently published A^{3}COSMOS catalogue[1] (Automated mining of the ALMA Archive in COSMOS, Liu et al. 2019a). The COSMOS field covers an area of two square degrees, which contains about 1.3 million detected galaxies (Scoville et al. 2007). The A^{3}COSMOS project aims to exploit the ALMA archive to better understand the FIR and submm properties of galaxies in this field.

The COSMOS field has been covered by the *Herschel* Space Telescope (Lutz et al. 2011; Oliver et al. 2012), providing a good photometric coverage of the SED in the range $100 - 500$ μm. However, when moving to high-redshift, the rest-frame wavelength range covered by *Herschel* shifts to lower values and it becomes more difficult to characterize the long-wavelength part of the FIR SED. Adding long-wavelength data-points from ALMA, it is possible to overcome this problem. For example, Berta et al. (2016) calculated that combining ALMA fluxes with *Herschel* data can reduce the uncertainties on the dust masses to $< 30\%$.

The COSMOS field has a rich set of multi-wavelength data (from X-rays to radio) that can be used to characterize the sources in the field. Liu et al. (2019a) use the ancillary multi-wavelength observations and redshift catalogues to derive information about the redshift, stellar mass and SFR of COSMOS targets observed by ALMA. Starting from a parent sample of 823 galaxies with at least one ALMA detection, they produce a galaxy catalogue consisting of 676 galaxies with reliable stellar mass and SFR measurements. They derive SFRs and stellar masses from SED fitting using the `MAGPHYS` code (da Cunha et al. 2008, 2015) assuming a Chabrier (2003) IMF. For the SED fit, they use as a prior the redshift from the literature (either photometric or spectroscopic redshift) and then derive a 'best redshift' from the 'best fit' SED.

To select our sample from the A^{3}COSMOS catalogue, we apply the following additional criteria:

- Galaxies are required to have redshift, SFR and stellar mass measurements from the galaxy catalogue of Liu et al. (2019a). We need this information to be able to

[1] https://sites.google.com/view/a3cosmos

study scaling relations and define the position of the galaxies with respect to the main-sequence.

- We select galaxies with at least five detected (S/N> 3) photometric points in the FIR (observed wavelength 100 μm to ∼3000 μm), to be able to derive accurate dust properties.

- We require each galaxy to lie within 0.4 dex from the main-sequence at the redshift of the galaxy. We use the redshift-dependent MS definition by Schreiber et al. (2015). We select only MS galaxies to make sure that the galaxies belong to the same population, which is a requirement for the hierarchical approach. In the future, we plan to investigate also the dust properties of the populations of galaxies above and below the MS.

We divide the sample in redshift bins of width $\Delta z = 0.5$. We start by considering only the redshift bins with the largest number of galaxies, i.e. between $z = 1$ and $z = 3.5$. Our total sample consists of 110 galaxies, with the five redshift bins ($z = 1 - 1.5, 1.5 - 2, 2 - 2.5, 2.5 - 3, 3 - 3.5$,) containing 30, 20, 29, 21 and 10 galaxies, respectively. Figure 4.1 shows the sample in the SFR-M_* plane, divided in five redshift bins. The redshift-dependent MS definition by Schreiber et al. (2015) is also shown. The galaxies that satisfy our selection criteria are shown in red. Due to the FIR selection, galaxies in the A^{3}COSMOS sample tend to have high SFRs (SFR $\geq$ 50 M$_\odot$ yr^{-1}) and high stellar masses ($M_* = 10^{10.5} - 10^{12}$ M$_\odot$).

4.2 Models

Measuring the cold dust temperature for galaxies at different redshifts using a SMBB model poses some challenges. Photometric data at wavelength < 100 μm need to be discarded, to avoid including the 'warm dust component' in the fit (see TMBB model in Chapter 3). However, when moving to high-redshift, this would imply discarding some of the few precious photometric data points available. Additionally, this sharp cut in wavelength used in the fit could potentially introduce a redshift-dependent bias in the measured dust temperatures (see discussion in Magnelli et al. 2014). One possibility to overcome this problem is to fit the SED using a set of templates, and then assign a dust temperature to each template, for example by fitting the template with a SMBB model,

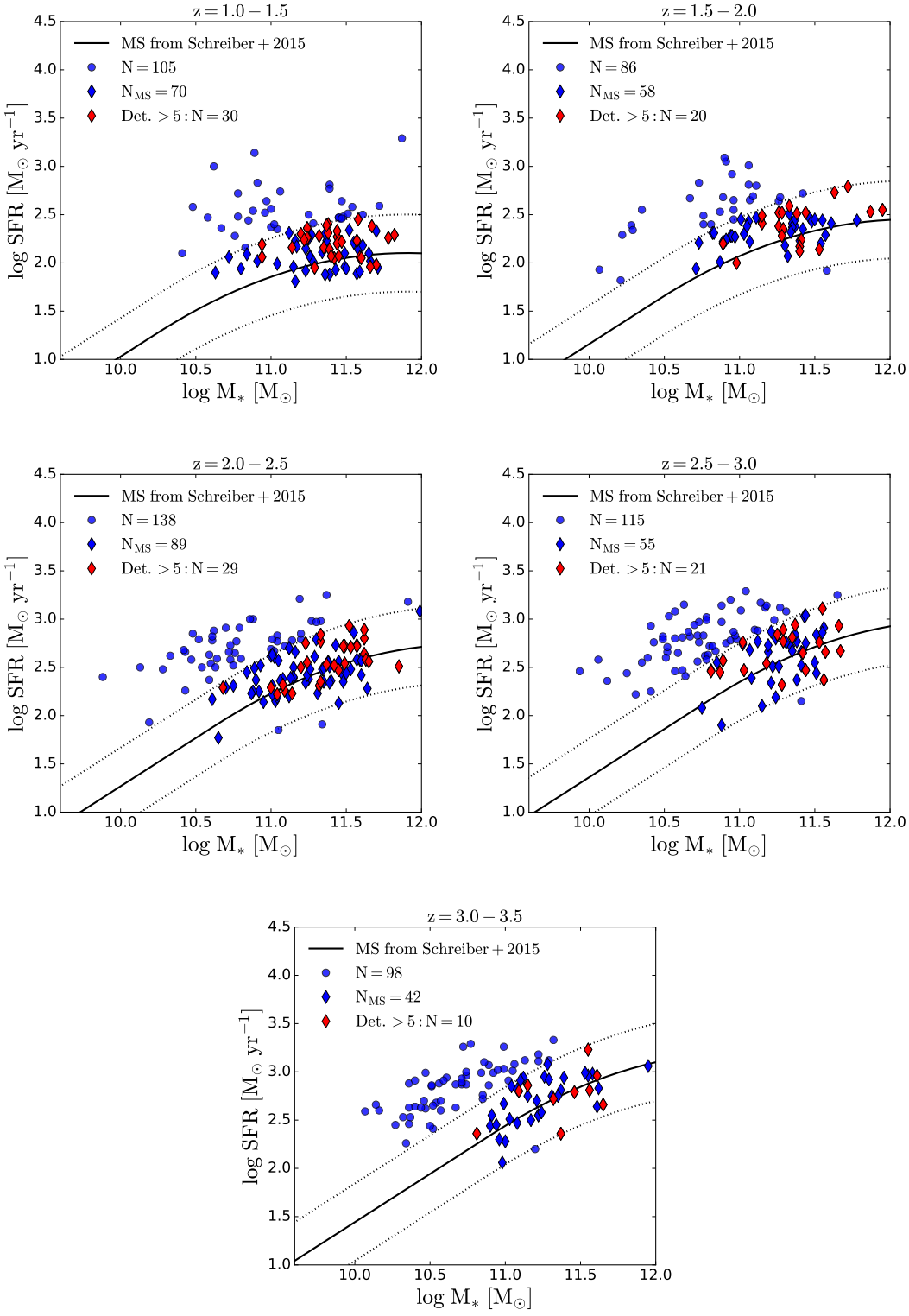

Figure 4.1. A^{3}COSMOS sample on the SFR-M_* plane divided in five redshift intervals from $z = 1$ to $z = 3.5$. The black solid curve shows the main-sequence (MS) definition by Schreiber et al. (2015) at the mean redshift of each interval. We consider for our fit the objects within 0.4 dex from the MS (shown by the dashed curves) with at at least five detections (red diamonds).

as was done by Magnelli et al. (2014).

We prefer to use a model that can incorporate into the fit also the warm dust component, even though this implies adding some additional free parameters. We consider two models:

- **TMBB** (two modified black-bodies): This model was already described in detail in the previous chapter (Section 3.2), where it was applied to fit $z \sim 0$ galaxies from the JINGLE survey. We remind the reader that this model has five free parameters: three for the cold dust component (M_{cold}, T_{cold}, β_{cold}) and two for the warm component (M_{warm} and T_{warm}), since we fix $\beta_{warm} = 1.5$.

  When moving to high-z, the photometric points move to shorter rest-frame wavelengths. To fit the shortest wavelength point, the warm component will shift to higher temperature. This is an artificial effect, and therefore we cannot consider the warm temperature T_{warm} as a reliable measurements. However, this effect should affect only the warm component and not the cold component. We will test this in Section 4.3 using simulations.

- **SMBB+PL** (single modified blackbody plus power law): This model was proposed by Casey (2012) and has been applied to the fit of high-z galaxies and AGN (e.g., Ramasawmy et al. 2019; Carvajal et al. 2020; Faisst et al. 2020). The model combines a SMBB with a power-law (PL) to fit the MIR emission. The emission in the MIR ($\leq$ 50 μm) is due to a combination of warm dust components from clumpy hot star-forming regions or from AGN heating. Additionally, PAH emission or silicate absorption at 9.7 μm can contribute to the SED shape in the MIR. However, the effect of these components on the integrated SED is $<$ 10% in most of the cases (Casey 2012). This model is defined as the sum of a SMBB and a power law ($F_\lambda = F_{SMBB,\lambda} + F_{PL,\lambda}$). The power-law component is defined as:

$$F_{PL,\lambda} = N_{PL} \cdot \lambda^{\alpha} e^{-(\lambda/\lambda_c)^2}, \tag{4.1}$$

  where $F_{PL,\lambda}$ is the flux density in Jy at wavelength λ; N_{PL} is a normalization constant; α is the slope of the power-law; and λ_c is the wavelength where the MIR power law turns over and no longer dominates the emission. The power-law component dominates in the MIR, at wavelengths $\lesssim 50\mu$m.

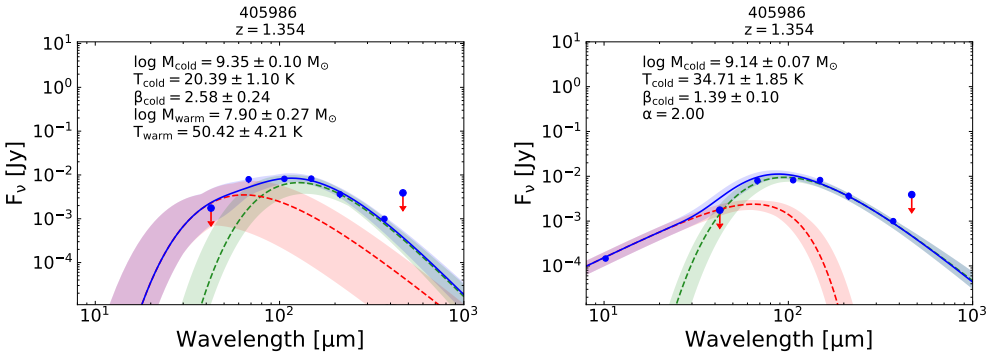

Figure 4.2. Example SED fit of a galaxy from the A^{3}COSMOS sample with the TMBB (left) and SMBB+PL (right) model. The shaded regions show the 1σ uncertainties on the SED models. The red arrows show upper limits equal to 5 times the flux uncertainties.

This model has six free parameters: three for the SMBB (M_{dust}, T_{dust}, β) and three for the PL component (N_{PL}, α, λ_c). To reduce the number of free parameters, both N_{PL} and λ_c can be tied to the best fitting values of the SMBB parameters and to the slope α. Following Casey (2012), we define the turnover wavelength as:

$$\lambda_c = [T \cdot (a_1 + a_2\alpha)]^{-1}, \tag{4.2}$$

where $a_1 = 26.68$ and $a_2 = 6.246$. The normalization of the power-law is tied to the normalization of the SMBB as:

$$N_{PL} = \frac{F_{SMBB,\lambda_c}}{\lambda_c^{\alpha}}. \tag{4.3}$$

Since we only have few (one or two) flux points that can be used to fit the power-law slope at wavelengths $10 - 50\mu$m, we fix $\alpha = 2$ following Casey (2012).

Figure 4.2 shows as an example SED of one galaxy at $z = 1.3$ from A^{3}COSMOS, fitted with both the TMBB and the SMBB+PL model.

4.2.1 Effect of the CMB on the FIR SED

The temperature of the cosmic microwave background (CMB) evolves with redshift as $T_{CMB}(z) = T(z = 0) \cdot (1 + z)$, where $T(z = 0) = 2.725$ K. This means that when moving to high-z the CMB temperature starts to become comparable to the cold dust temperature

and needs to be taken into account. We follow the theoretical description from da Cunha et al. (2013), as implemented in Carniani et al. (2019) and Jones et al. (2020). First, the CMB temperature heats the dust, resulting in a higher observed temperature:

$$T_{dust,obs} = \left[T_{dust}^{4+\beta} + T_{CMB}(z=0)^{4+\beta}\left((1+z)^{4+\beta} - 1\right)\right]^{\frac{1}{4+\beta}}, \tag{4.4}$$

where T_{dust} is the true dust temperature, $T_{dust,obs}$ is the effective observed dust temperature, and β is the dust emissivity spectral index. This effect is illustrated in Figure 4.3. In the redshift range that we are interested in ($z \sim 1-3$), this effect is significant only at observed dust temperatures < 15 K.

Additionally, the CMB provides a background against which the observations are made. This contribution can be taken into account with the formula (da Cunha et al. 2013):

$$F_\lambda = SMBB_\lambda(M_{dust}, T_{dust}, \beta) - SMBB_\lambda(M_{dust}, T_{CMB}(z), \beta). \tag{4.5}$$

The right panel of Figure 4.3 shows the effect of the CMB background on the observed SED. Taking into account this effect is important to derive correctly the slope of the long-wavelength part of the FIR SED, and in particular to measure accurately the dust emissivity index β.

4.2.2 Optically thin or optically thick dust

For our models, we assume optically thin dust emission. If the dust is instead optically thick into the far-infrared, the optically thin model will underestimate the dust temperature (e.g., Riechers et al. 2013). Cortzen et al. (2020) studied a starburst galaxy at $z \sim 4$ and found evidence that an optically thick dust model is more appropriate. They show that assuming optically thick dust shifts the dust temperature of their target from 33 K to 52 K. However, it is not clear whether this applies only to starburst galaxies or more generally to 'normal' main-sequence galaxies at high-z.

Using an analytical and physically-motivated model, Sommovigo et al. (2020) show that the dust in high-z, star-forming giant molecular clouds dominates the observed FIR luminosity and it is optically thin at the wavelength of the peak emission. Higher pressure values than the ones considered in their model are needed for dust to be optically thick to FIR emission (e.g. Conley et al. 2011; da Cunha et al. 2015).

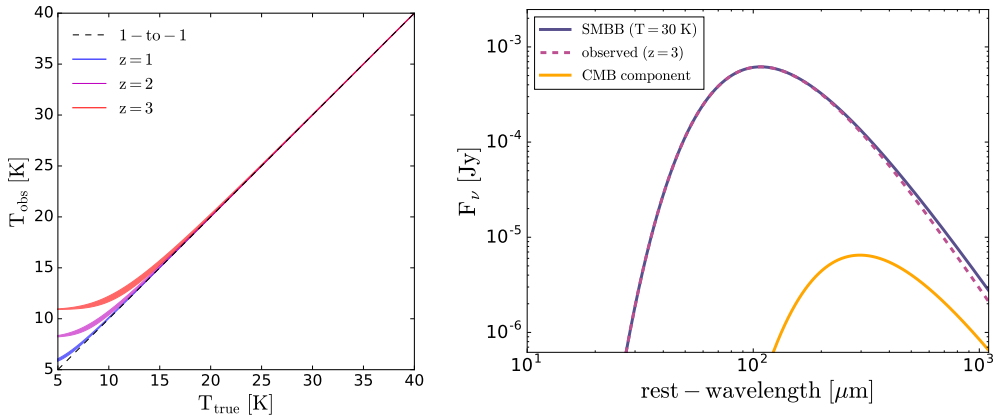

Figure 4.3. Illustration of the effect of CMB heating on the dust temperature. *Left*: The dust temperature (T_{true}) is heated by the CMB to the observed temperature (T_{obs}) according to Eq. 4.4. The curves show the relation for different redshifts. As T_{CMB} increases with redshift, the effect become more important. The breadth of curves shows the range of T_{obs} for a range of values of the emissivity index $\beta = 0.5 - 2.5$. *Right*: effect of the CMB background on the observed SED. The dark-violet solid curve shows the intrinsic SED of a SMBB with temperature $T = 30$ K. The dashed curve illustrates the observed SED at $z = 3$ with the effect of the CMB background (shown in orange), according to Eq. 4.5.

For the moment, we use the optically thin model, but we plan to investigate how the assumption of an optically thick model will affect our results in the future.

4.3 Simulations of mock SEDs

The photometric bands sample the SEDs at the same observed wavelengths, which correspond to different rest-frame wavelengths for galaxies at different redshifts. The different sampling of the SEDs could potentially introduce some biases in the measured dust properties. For example, with increasing redshift the shortest wavelength point moves to shorter rest-frame wavelengths. To compensate for this, the warm temperature parameter of the TMBB model will tend to increase, and could potentially also affect the measurement of the temperature of the cold component. We use simulated SEDs to test whether the different wavelength coverage at different redshifts may introduce biases in the measured dust properties.

In this section, we use mock SEDs to assess how well our hierarchical Bayesian SED fitting code can recover the input dust parameters. In particular, we are interested in testing how well the code can measure the cold dust temperature T_{cold} and recover possible

Table 4.1. Mean and standard deviation (σ) of the normal distribution used to generate the input parameters of the simulations.

Parameter	Mean	σ
$\log M_{cold}/M_{\odot}$	9.5	0.5
β_{cold}	1.8	0.5
$\log M_{warm}/M_{\odot}$	7.5	0.3
T_{warm}	60 K	2.5 K

trends between T_{cold} and redshift.

We run two sets of simulations, varying the distribution of the input cold dust temperature, while the other four input parameters ($\log M_{cold}$, β_{cold}, $\log M_{warm}$, T_{warm}) remain the same. For these four input parameters, we generate the inputs by sampling from normal distributions. The mean and standard deviation of the distributions are reported in Table 4.1. For the parameter T_{cold}, we consider two options:

1. T_{cold} *normal distributed*: We set the mean of the distribution at 25 K and the standard deviation to be 2.5 K;

2. T_{cold} *increasing with redshift*: We sample T_{cold} from a normal distribution with mean given by $T_{cold} = 20 + 2.5 \cdot z$ and standard deviation 1 K. We choose this distribution arbitrarily to have a sequence of T_{cold} increasing between $\sim 20 - 30$ K.

We simulate the SEDs according to the input parameters and redshifts. The mock photometric data are generated by extracting the flux densities at the following wavelengths: 100, 160, 250, 350, 500, 870, 1000, 2000 μm. For the SMBB+PL model, we add the 24 μm wavelength point, since the power law component can model the SED also in the MIR regime. Then, we add random noise, sampled from a normal distribution with a standard deviation equal to 25% of the flux. The 25% level was chosen because it is similar to the noise level in the A^{3}COSMOS catalogue. If the signal-to-noise ratio (S/N) of a flux point is < 3, we convert the mock photometric flux point to an upper limit equal to five times the flux error ($5 \times F_{err}$).

We simulate 100 galaxies in the redshift range $z = 1 - 3$. We assign to each galaxy a redshift according to a uniform distribution in this range. We ran two sets of SED fitting using the hierarchical Bayesian fitting code by:

- i) fitting all galaxies together;

- ii) separating the galaxies in four redshift bins and running the hierarchical code on each redshift bin separately.

With these two methods, we want to test whether considering all galaxies together, i.e. assuming that they belong to a single population, can introduce any biases in the measured temperatures.

We decide to use a Student's t-distribution to model the flux noise instead of a Gaussian distribution. We note that some galaxies from A^{3}COSMOS show some flux points that seem to be outliers compared to the rest of the SED, especially from the ALMA bands. In some cases, measurements at very similar wavelengths show quite different fluxes (see examples in Figure 4.12). This can be due to emission lines that have not been properly taken into account or to background galaxies that may contaminate the fluxes. To account for outliers, we decide to use a Student's t-distribution to model the noise, since this distribution can accommodate more outliers in the 'tails' of the distribution with respect to a Gaussian.

4.3.1 TMBB model

We first test the TMBB model. We ran the two simulations with T_{cold} normal distributed and with T_{cold} increasing with redshift. We are mostly interested in the properties of the cold component, and in particular in measuring accurately the cold dust temperature T_{cold}. Thus, in the following we focus mainly on the cold dust properties.

1) T_{cold} ***normal distributed***: We start with the simulation with T_{cold} normal distributed with no redshift dependence. The upper left panel of Figure 4.4 shows the input distribution of T_{cold} versus redshift. We compare the input parameters with the results of the fit with i) all galaxies fitted together (Figure 4.4) and ii) the galaxies divided in four redshift bins fitted independently (Figure 4.5).

We first analyse the results of the fit of all galaxies together. The measured temperatures have a flat distribution with respect to the redshift, but the range of temperatures is smaller than the input range. This effect is probably due to the assumption of the hierarchical method that all galaxies belong to the same population, with the parameters following a common distribution. Thus, the more extreme temperatures are pulled towards the mean values by the hierarchical assumption. We observe a similar effect also for β, but

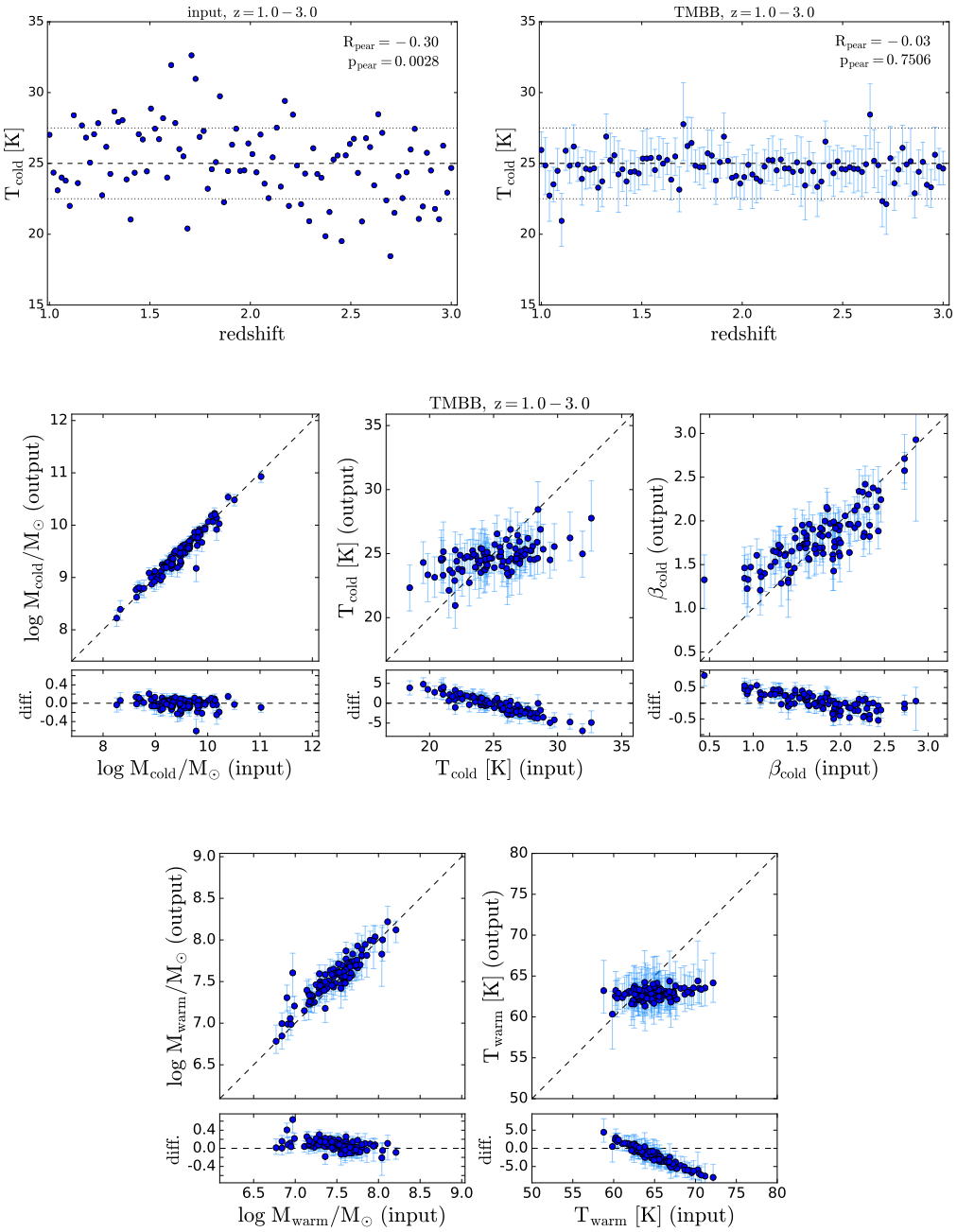

Figure 4.4. Results of the TMBB simulations with (1) temperature normal distributed independent of redshift and (i) the SEDs fitted all together. *Upper row*: input cold dust temperature (left) and measured cold dust temperature (right) as a function of redshift. The lines show the mean (25 K, dashed line) and standard deviation (2.5 K, dotted lines) of the input T_{cold} distribution. *Middle and bottom row*: comparison of input and measured (output) dust parameters: cold dust mass (log M_{cold}), cold dust temperature (T_{cold}), emissivity index of the cold component (β_{cold}), warm dust mass (log M_{warm}), and warm dust temperature (T_{warm}).

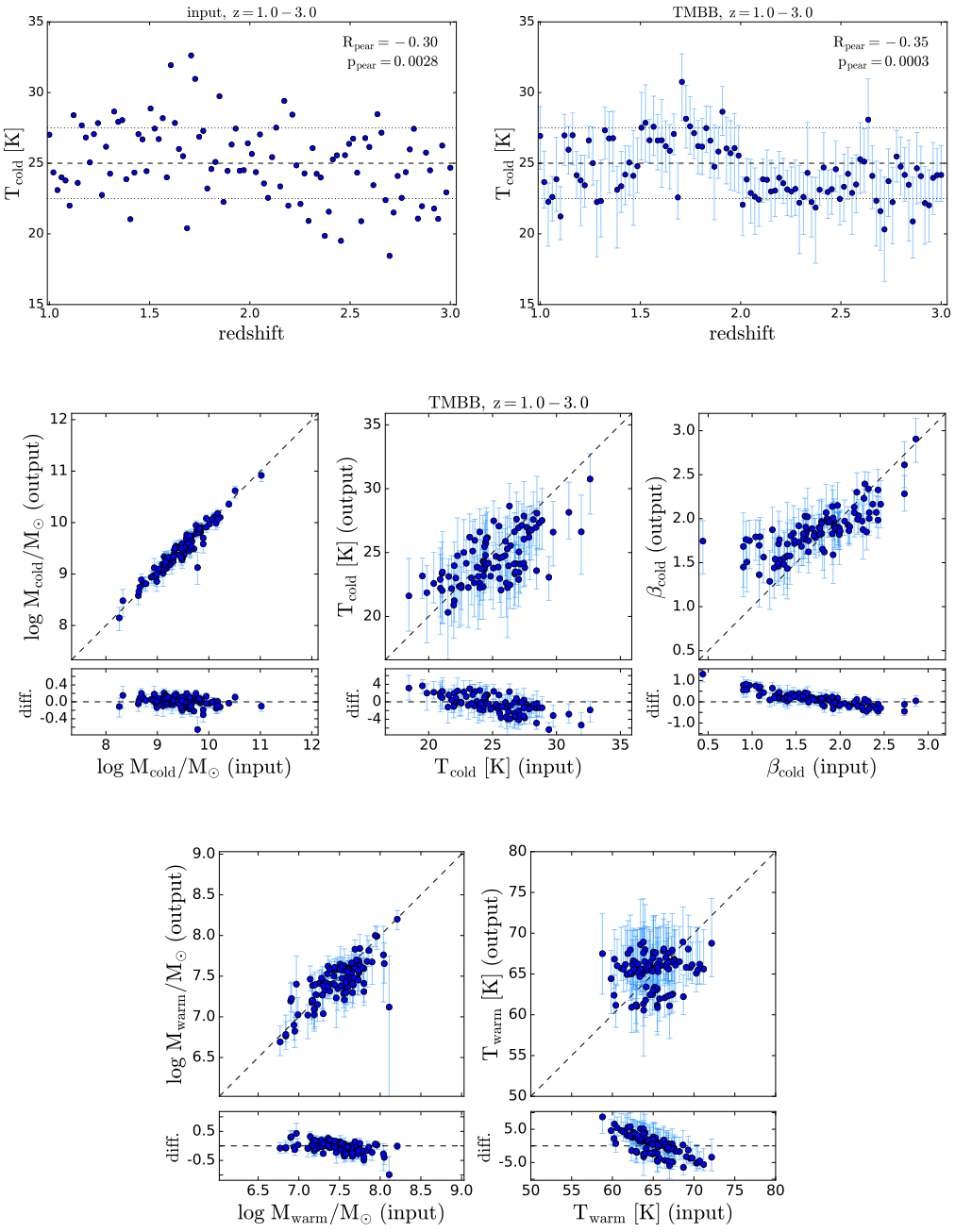

Figure 4.5. Results of the TMBB simulations with (1) temperature normal distributed independent of redshift and (ii) the mock SEDs fitted divided in four redshift bins. *Upper row*: input temperature (left) and measured temperature (right) as a function of redshift. The lines show the mean (25 K, dashed line) and standard deviation (2.5 K, dotted lines) of the input T_{cold} distribution. *Middle and bottom row*: comparison of input and measured (output) dust parameters.

the trend is less strong than the one observed for the temperatures. Even though there is a bias in the temperatures, the dust masses are recovered quite well with differences between input and output < 0.2 dex.

In the fit divided by redshift bins (Figure 4.5), the input temperatures are recovered better and the range of measured temperatures is larger. We note that low β values are difficult to recover, probably because there are not many points at long wavelengths to constrain the slope of the SED.

In both cases, the warm dust temperature (T_{warm}) is not well constrained. The output T_{warm} are clustered around a single value. The output warm dust masses show some differences with respect to the input values (up ~ 0.4 dex), but the difference is not systematic.

2) T_{cold} ***increasing with redshift***: In Figure 4.6 we compare the input parameters for the simulation of T_{cold} increasing with redshift with the results of fitting all galaxies together. The code is not able to recover the trend of increasing T_{cold} with redshift. Instead, the measured T_{cold} are almost constant, distributed around ~ 24 K. Even though T_{cold} is not well recovered, the measured M_{dust} and β are mostly in agreement, within the uncertainties, with the input values.

Figure 4.7 shows the results of the fit of the galaxies divided in four redshift bins. In this case, the code is able to recover the trend of T_{cold} increasing with redshift. For each redshift bin, the distribution of T_{cold} is almost flat, but the mean T_{cold} of the bins increases with redshift. Thanks to the fact that the sample is split in bins, we can recover the general trend between T_{cold} and z. The measured M_{dust} and β are also in general agreement with the input values. As in the case i), the code struggles to measure low values of β.

4.3.2 SMBB+PL model

1) T_{cold} ***normal distributed***: The results of the simulations with T_{cold} proportional to z, fitted with all galaxies together or divided in redshift bins are shown in Figures 4.8 and 4.9, respectively. In the first case, the measured temperatures follow a normal distribution, but they are overestimated by about 4 K on average. As a consequence, the dust masses are slightly underestimated (0.11 dex on average). The high input values of β (> 2) also tend to be underestimated.

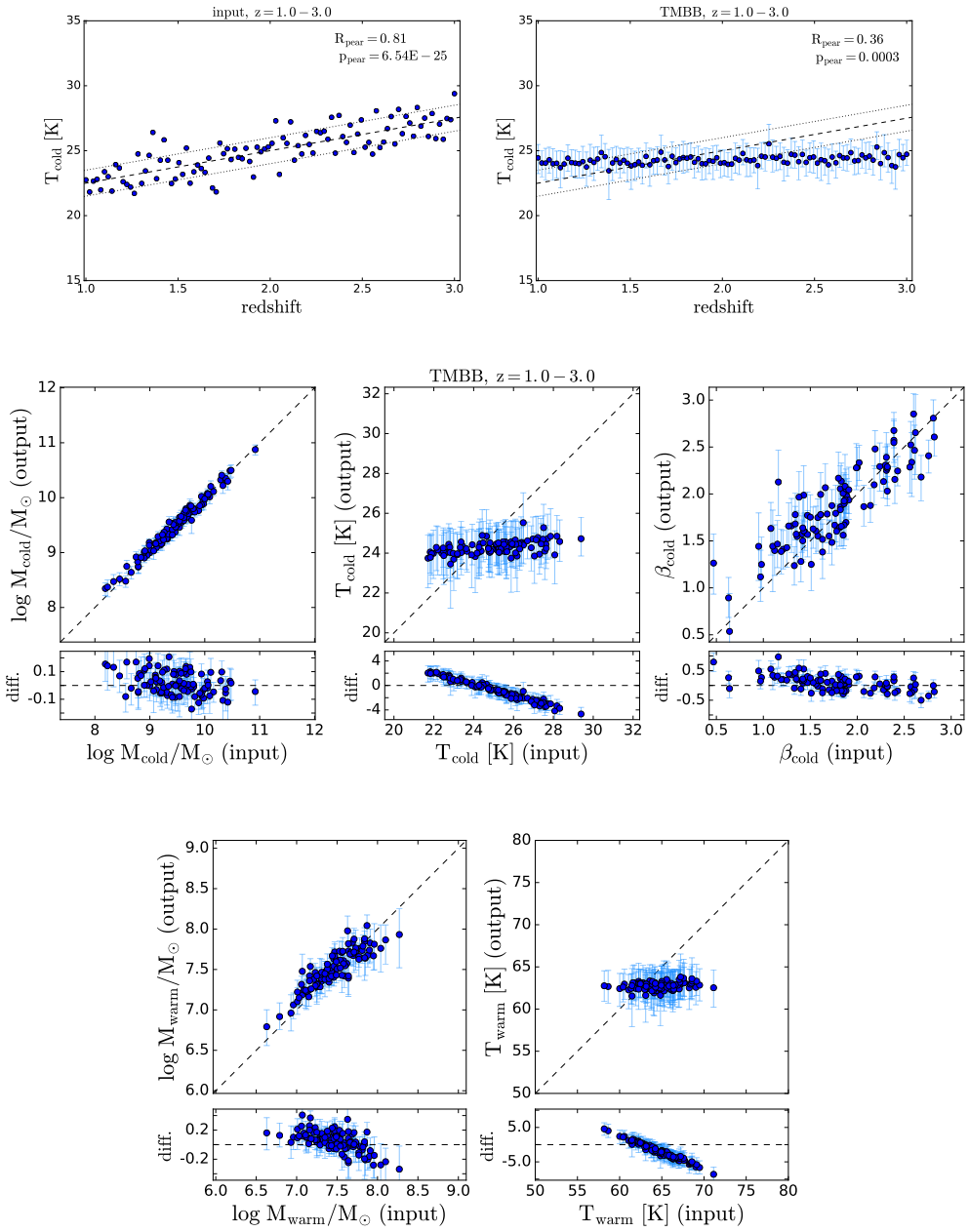

Figure 4.6. Results of the TMBB simulations with (2) temperature increasing with redshift and (i) the mock SEDs fitted all together. *Upper row*: input temperature (left) and measured temperature (right) as a function of redshift.The lines show the mean (dashed line) and standard deviation (1 K, dotted lines) of the input T_{cold} distribution. *Bottom row*: comparison of input and measured (output) dust parameters.

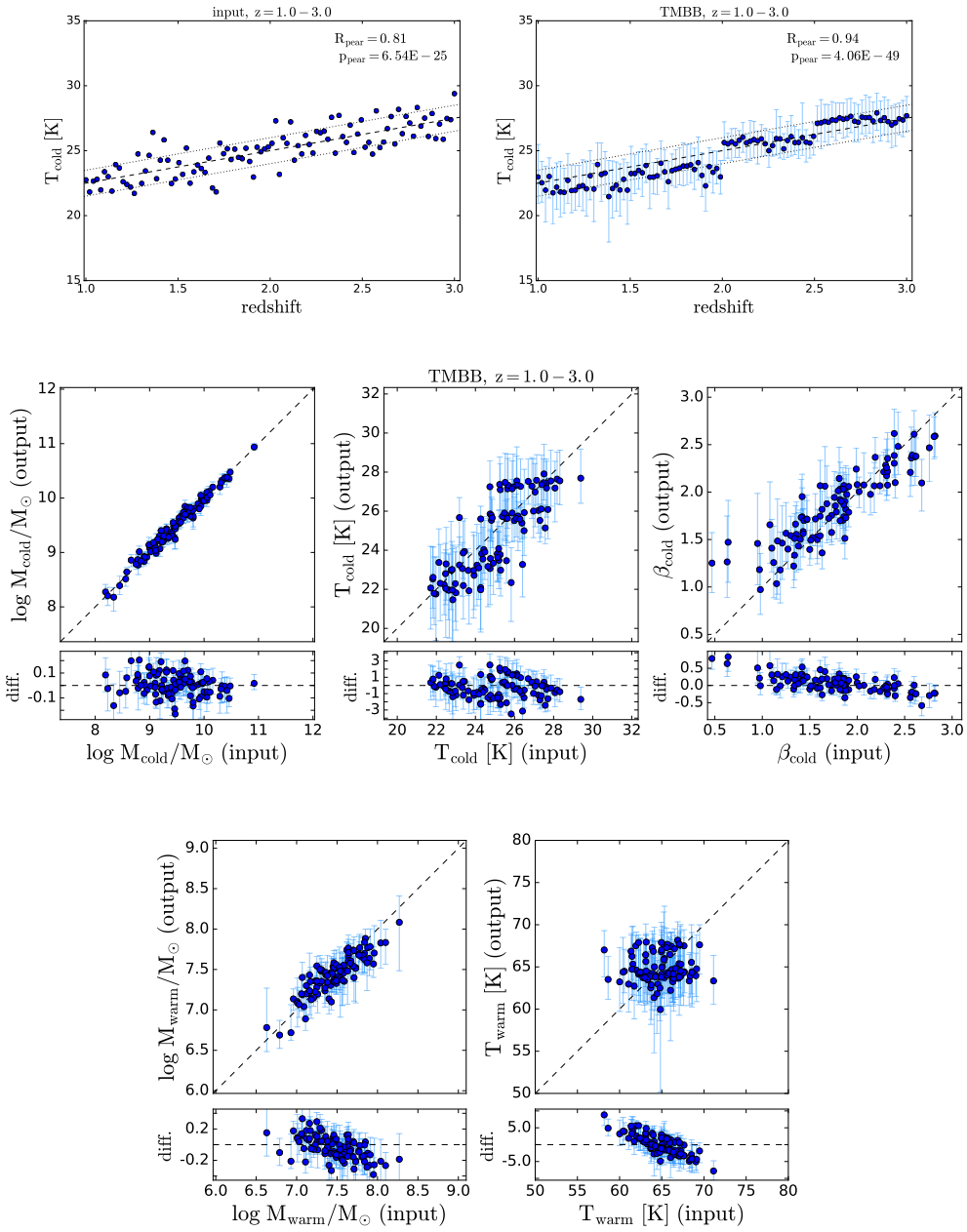

Figure 4.7. Results of the TMBB simulations with (2) temperature increasing with redshift and (ii) the mock SEDs fitted divided in four redshift bins. *Upper row*: input temperature (left) and measured temperature (right) as a function of redshift. The lines show the mean (dashed line) and standard deviation (1 K, dotted lines) of the input T_{cold} distribution. *Bottom row*: comparison of input and measured (output) dust parameters.

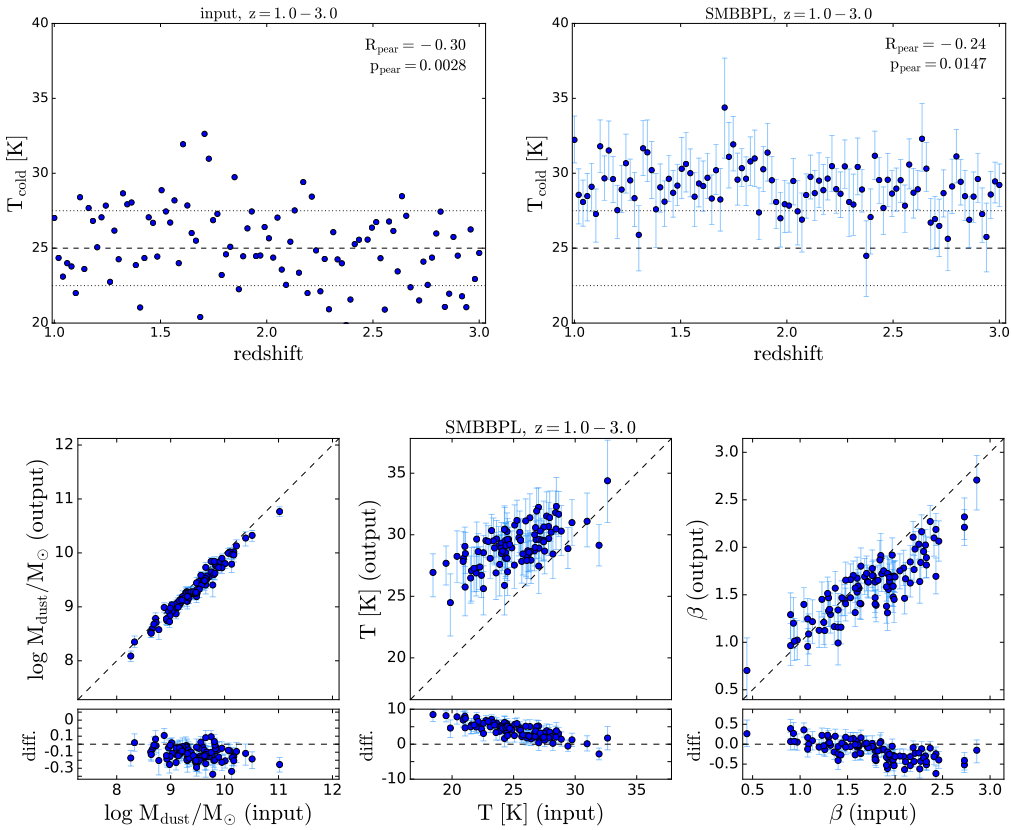

Figure 4.8. Results of the SMBB+PL simulations with (1) temperatures normal distributed and (i) the mock SEDs fitted all together. *Upper row*: input temperature (left) and measured temperature (right) as a function of redshift. The lines show the mean (25 K, dashed line) and standard deviation (2.5 K, dotted lines) of the input T_{cold} distribution. *Bottom row*: comparison of input and measured (output) dust parameters.

The fit of the galaxies divided in redshift bins overestimates the dust temperatures as well. The measured dust temperatures are in the range $25-30$ K and span a narrow range in each redshift bin.

2) T_{cold} ***increasing with redshift***: Figures 4.10 and 4.11 show the results of the simulations with T_{cold} proportional to z, with the fitting of all galaxies together or divided in redshift bins, respectively. In the first case, the code measures almost the same temperatures for all simulated SEDs which is higher than the input range ($\sim$ 30 K). In the second cases, the trend of T_{cold} increasing with z is recovered, but the temperatures are systematically overestimated by $\sim$ 3 K. As a consequence of the higher T_{cold}, the dust masses are slightly underestimated in both cases by $\sim$ 0.2 dex.

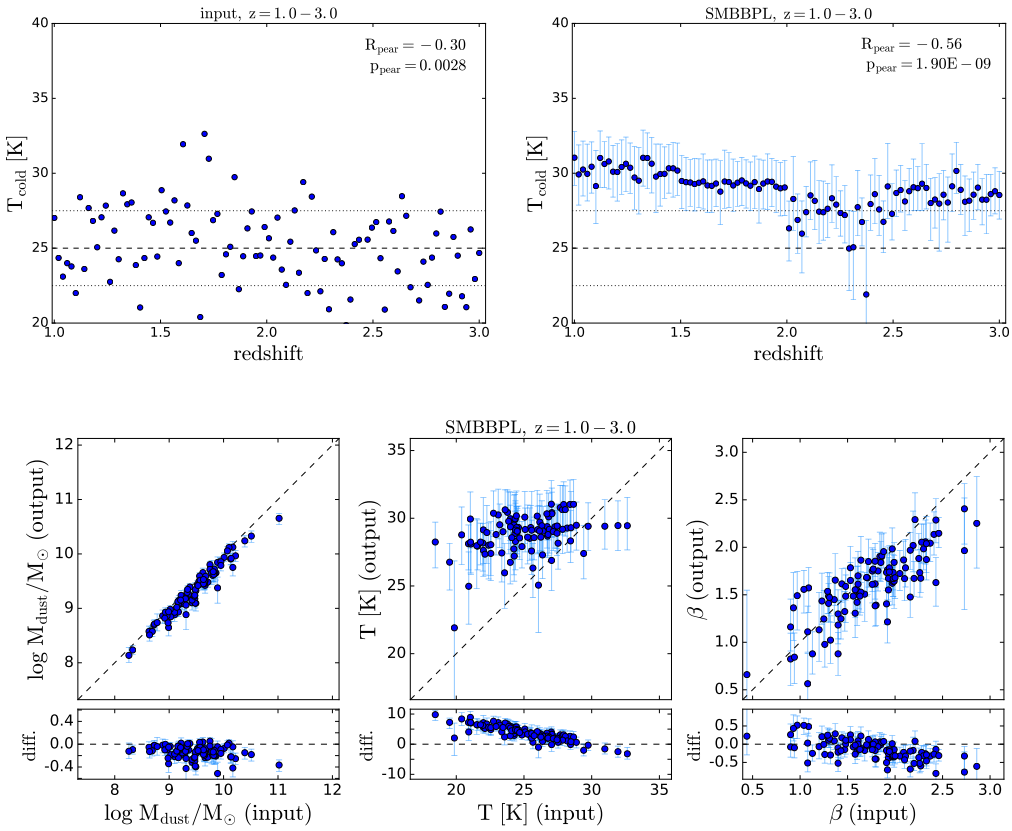

Figure 4.9. Results of the SMBB+PL simulations with (1) temperatures normal distributed and (ii) the mock SEDs fitted divided in four redshift bins. *Upper row*: input temperature (left) and measured temperature (right) as a function of redshift. The lines show the mean (25 K, dashed line) and standard deviation (2.5 K, dotted lines) of the input T_{cold} distribution. *Bottom row*: comparison of input and measured (output) dust parameters.

In this model, the position of the peak is given by the dust temperature T_{cold} and the cutoff wavelength of the power law component. It is possible that the overestimation of T_{cold} is due to a degeneracy between T_{cold} and λ_c.

In summary, the simulations with mock SEDs show that the TMBB model can recover the input dust temperatures, but only if the sample is divided in small redshift bins. On the other hand, the SMBB+PL model overestimates the dust temperatures in all simulations. We will investigate the cause of this in the future, but for the moment we focus on the TMBB model.

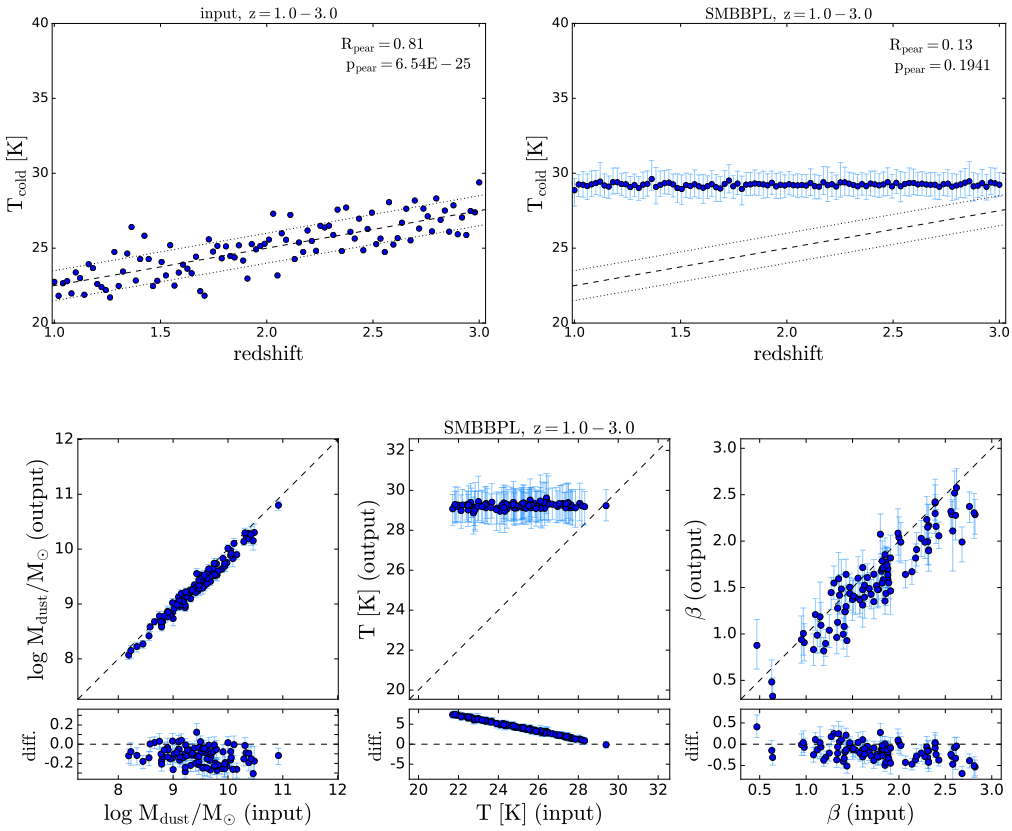

Figure 4.10. Results of the SMBB+PL simulations with (2) temperature increasing with redshift and (i) the mock SEDs fitted all together. *Upper row*: input temperature (left) and measured temperature (right) as a function of redshift. The lines show the mean (dashed line) and standard deviation (1 K, dotted lines) of the input T_{cold} distribution. *Bottom row*: comparison of input and measured (output) dust parameters.

4.4 Results

In this section, we present the results of the SED fitting of main-sequence galaxies in the A^{3}COSMOS sample. Following the results of the simulations, we decide to apply the TMBB model and to split the sample in five redshift bins between $z = 1.0-3.5$, fitting each bin independently with the hierarchical Bayesian method. Figure 4.12 shows examples of the SEDs of five A^{3}COSMOS galaxies, one for each redshift bin, with the fitted TMBB model. The parameters inferred from the fit are presented in Appendix C.

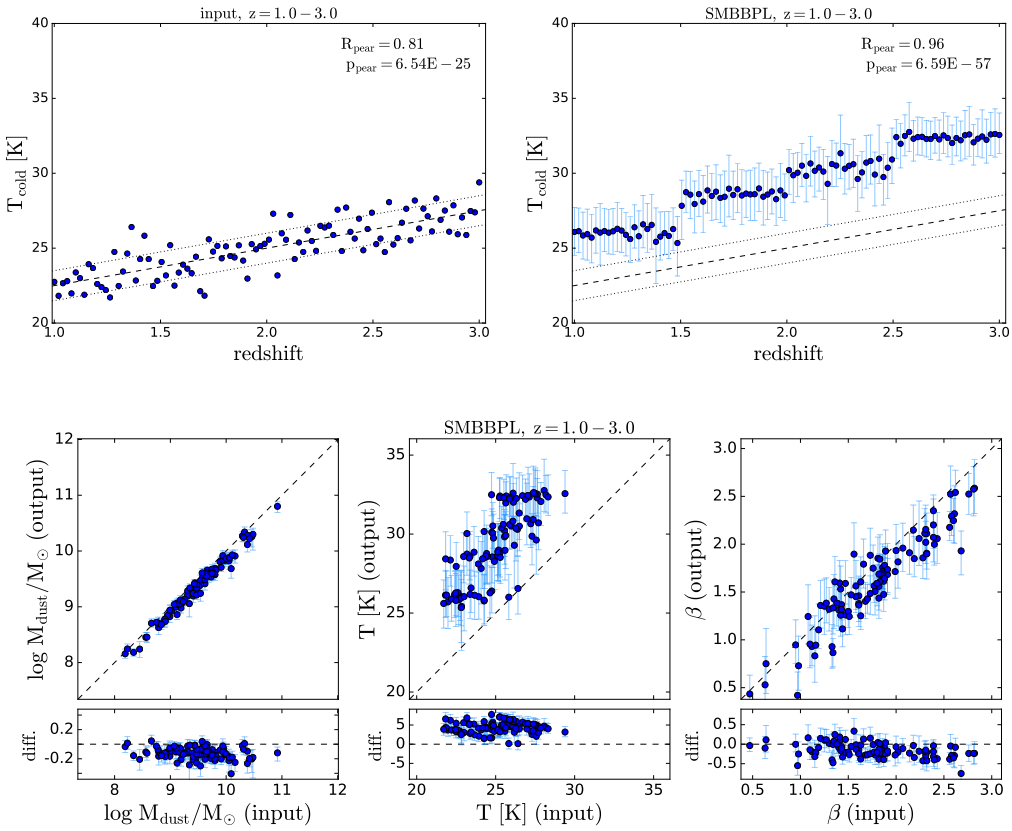

Figure 4.11. Results of the SMBB+PL simulations with (2) temperature increasing with redshift and (ii) the mock SEDs fitted divided in four redshift bins. *Upper row*: input temperature (left) and measured temperature (right) as a function of redshift. The lines show the mean (dashed line) and standard deviation (1 K, dotted lines) of the input T_{cold} distribution. *Bottom row*: comparison of input and measured (output) dust parameters.

4.4.1 Evolution of dust properties with redshift

We first look at the distribution of dust temperature as a function of redshift (upper left panel of Figure 4.13). We find that the dust temperatures increase from ~ 20 K at $z = 1$ to ~ 32 K at $z = 3.5$. The scatter in the dust temperatures also increases with redshift. The small scatter in the lower redshift bins may be due to the fact that the short-wavelength part of the SED is not very well constrained: the shortest wavelength covered at $z = 1$ is at $100/(1+z) = 50$ μm, while at $z = 3$ it is at 25 μm. Therefore, in the lowest redshift bin the code has difficulties in determining both the cold temperature T_{cold} and the warm temperature (T_{warm}) for the single galaxies. In this case, the hierarchical code pushes the T_{cold} values toward a single 'mean' temperature, while it allows T_{warm} to vary by ~ 5 K

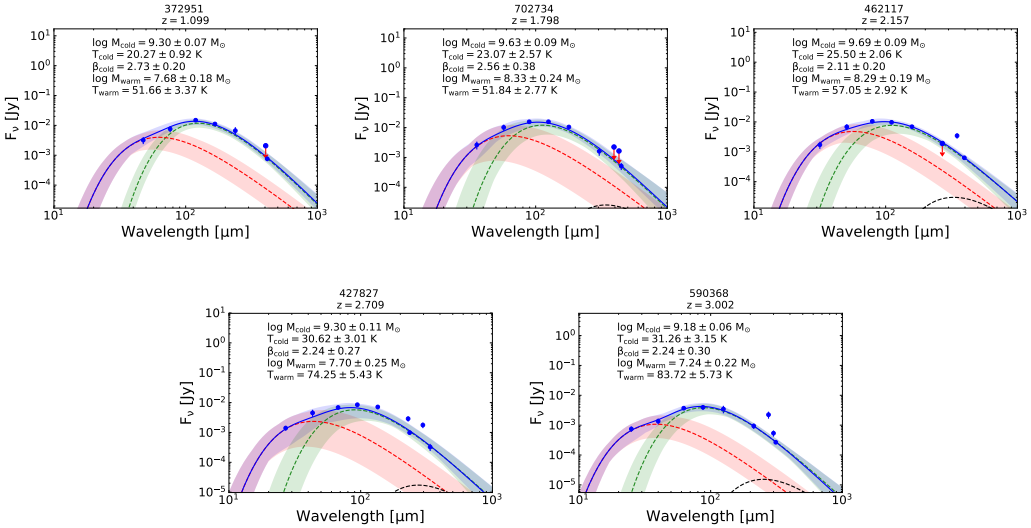

Figure 4.12. Example of galaxy SEDs at different redshifts (one SED for redshift bin), fitted with the TMBB model. The cold component, warm component and total fit are shown with blue, red and green curves, respectively. The contribution from the CMB component is shown with a black dashed line. The shaded regions show the lower and upper 1-σ uncertainties on the SED models, defined by taking the maximum and minimum flux values of the models with likelihood values in the highest 68th percentile. These plots show how the peak of the SED shift to shorter wavelengths, implying a shift towards higher temperatures.

to fit the different SED shapes.

In Figure 4.13, we also plot the emissivity index β against redshift (upper right panel). The lowest redshift bin shows higher β values $(2.5-3.0)$ compared to the other redshift bins ($\beta = 1.8-2.5$). It is not clear whether this result is physical or whether it is related to the issue with accurately measuring T_{cold} at low redshift. In the first redshift bin, the code measures the same T_{cold} for all galaxies and this may affect the β measurements as well. In our set of simulations, we assume a normal distribution for β. Additional simulations with β varying as a function of redshift are needed to assess the capability of the code to recover β.

The bottom left panel of Figure 4.13 shows the dust temperature versus β. There is no clear relation between T_{cold} and β, even though in some redshift bins there is a hint of a positive correlation. Overall, our results are not affected by the intrinsic $T-\beta$ degeneracy of the modified black-body models (see Chapter 3).

The temperature of the warm component (T_{warm}) increases with redshift (similarly to T_{cold}) from $\sim$ 52 K at $z = 1$ to $\sim$ 84 K at $z = 3.5$. It is possible that this effect is

related to the shortest wavelength point (the 100 μm point) shifting to shorter rest-frame wavelengths with increasing redshift, rather than to a physical effect. We note that in each redshift bin, the warm temperatures occupy a rather small range. This means that T_{warm} is not well constrained for the single galaxies and the values tend to cluster near the 'mean' T_{warm}. We note that in the lowest redshift bin, T_{warm} spans a larger range ($50-55$ K) than T_{cold}, which is clustered around 20 K. In the $z = 1.5-2.0, z = 2.5-3.0$ and $z = 3.0-3.5$ redshift bins, there is the opposite trend. It seems that the code is not able to simultaneously constrain T_{cold} and T_{warm} for the single galaxies. We do not want to give too much emphasis on the interpretation of the measured T_{warm}, because we know that in the $20-50$ μm range we can have other physical processes at play, as for example dust heated by AGN. The main reason we are including the warm component in the fit is to improve the measurements of the cold dust properties.

In Figure 4.13 (upper left panel), we compare our dust temperature measurements with previous works. We choose as comparison the relations derived by Magnelli et al. (2014) in the redshift range $z = 0-2.3$ and by Schreiber et al. (2018) in the range $z = 0-4$. These two relations predict higher mean dust temperatures than our measurements at any given redshift. The slope of the Schreiber et al. (2018) relation appears to be similar to the increase of our T_{cold} measurements, despite the offset of about 8 K. The slope from the Magnelli et al. (2014) relation is instead shallower.

For this comparison, it is important to consider the different methods used for the SED fitting and the approaches used to define the dust temperatures. Both Magnelli et al. (2014) and Schreiber et al. (2018) use stacking to derive the typical dust temperatures across the SFR-M_*-z space.

Magnelli et al. (2014) fit the stacked SED using the templates by Dale & Helou (2002). Then, they fit the Dale & Helou (2002) templates with a SMBB model to assign a dust temperature to each template. Thus, their approach is more similar to a SMBB fit. We use two modified black-bodies to fit the SED, and consider the temperature of the cold component in our comparison. Therefore, it is not surprising that we measure lower dust temperatures.

Schreiber et al. (2018) derive a new library of dust spectral SEDs to fit their sample, based on the templates from Galliano et al. (2011). The SEDs of their library are characterized by only three parameters: dust mass, dust temperature and the mid-to-total infrared color. They compute the dust temperature by applying Wien's displacement law

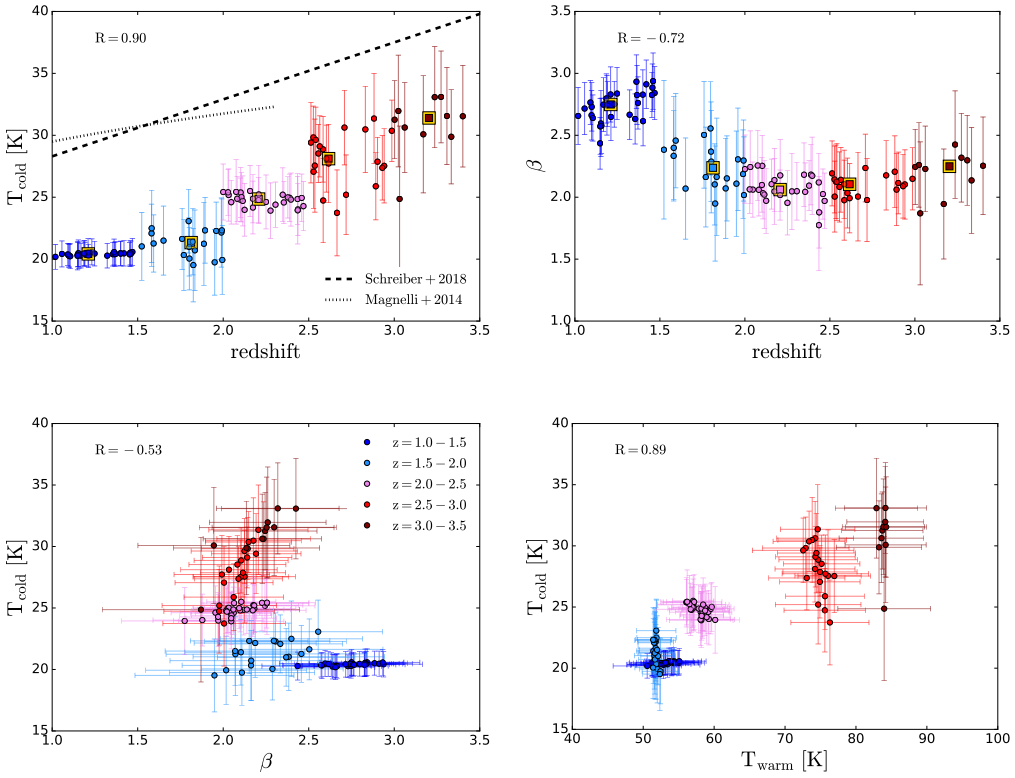

Figure 4.13. *Upper row:* Cold dust temperature (T_{cold}) and emissivity index β as a function of redshift for the A^{3}COSMOS sample considered here. The points are color coded according to the redshift bins. The yellow squares show the mean temperature for each redshift bin. In the left plot, the dashed and dashed-dotted curve show the relations between dust temperature and redshift from Schreiber et al. (2018) and Magnelli et al. (2014), respectively. *Lower row:* Cold dust temperature (T_{cold}) versus β and the temperature of the warm component (T_{warm}). The Pearson correlation coefficient R is shown in each panel.

to the Galliano et al. (2011) templates:

$$T_{peak}[\mathrm{K}] = \frac{2.898 \cdot 10^3 [\mu\mathrm{K}]}{\lambda_{peak}[\mu\mathrm{m}]}, \tag{4.6}$$

where λ_{peak} is the wavelength corresponding to the peak of $\lambda^{\beta} L_{\nu}$. The term λ^{β} takes into account the effective emissivity of the templates which have $\beta \sim 1.5$. In our TMBB fitting, we find higher β values ($\beta = 1.8 - 3$). If we were to assume a fix $\beta = 1.5$, we would probably measure higher dust temperatures to compensate for the lower β. We still need to test whether the change in β can account for the discrepancy between our mean T_{cold} values and the $T_{cold}-z$ relation from Schreiber et al. (2018). We compute the peak temperatures (T_{peak}) for our sample, by measuring the wavelength corresponding to

the peak of the best fitted TMBB model and applying Eq. 4.6. The values of T_{peak} are higher than T_{cold}, as expected, but they still lie below the T-z relation from Schreiber et al. (2018) by ~ 5 K.

An additional difference is the fact that we limit our sample to 'main-sequence galaxies', while Magnelli et al. (2014) and Schreiber et al. (2018) include also galaxies above or below the main-sequence. The presence of starburst galaxies in their sample could contribute to increase the mean T_{cold} in their sample, since T_{cold} scales with SSFR (see Section 3.3.5).

This comparison highlights the fact that comparing dust temperatures measured with different methods and with different definitions of T_{cold} is difficult. When assuming a dust temperature to derive dust masses, one needs to be careful in using dust temperatures measured exactly with the same method and defined in the same way.

4.4.2 Relations between dust temperature and SFR

In this section, we investigate the relations between the cold dust temperature and quantities related to the SFR. We have seen in the previous chapter that at $z = 0$ there is a positive correlation between T_{cold} and SFR, SSFR and SFR divided by dust mass (SFR/M$_{dust}$).

Figure 4.14 shows T_{cold} as a function of SFR, SSFR and SFR/M$_{dust}$ for the A^{3}COSMOS sample. We observe positive correlations between T_{cold} and these quantities, with Pearson correlation coefficients in the range $0.65 - 0.76$. The strongest correlation is with SFR/M$_{dust}$, as we found also for the JINGLE+HRS galaxies at $z = 0$.

On Figure 4.14, we also show the extrapolation of the linear relations (T_{cold} versus SSR and SFR/M$_{dust}$) at $z \sim 0$ derived from the combined JINGLE and HRS samples. The relation between T_{cold} and SFR is not provided because it has a lower significance for the JINGLE+HRS sample (Pearson correlation coefficient$R = 0.21$). We note that T_{cold} for JINGLE+HRS was measured using a SMBB model, but at redshift $z = 0$ the cold dust temperatures derived with the SMBB agree well with the results of the fit with TMBB model (see Section 3.3.3). The data from A^{3}COSMOS seem to show steeper trends compared to the extrapolation of the relations derived from JINGLE+HRS.

In the previous section we showed how T_{cold} increases with redshift. The normalization of the main-sequence increases with redshift as well, consequently the mean SFR of our samples increases with redshift. Thus, the increase of T_{cold} with z could be related to the increase of the mean SFR with z in our redshift bin.

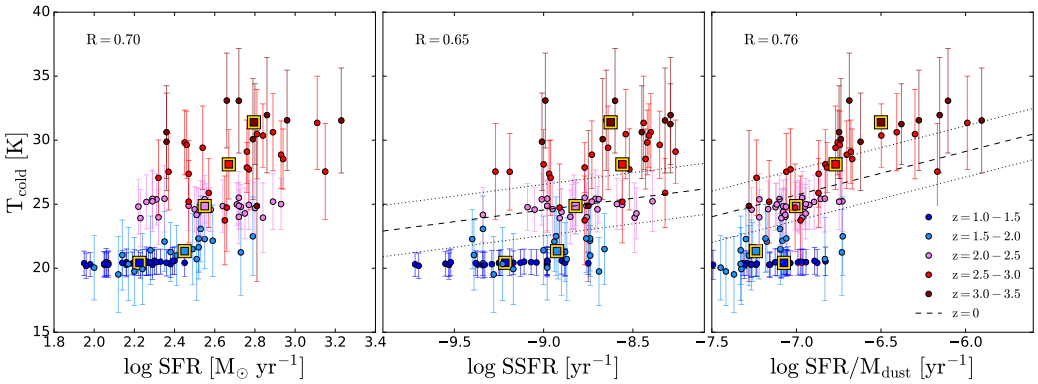

Figure 4.14. Cold dust temperature (T_{cold}) as a function of SFR (left), SSFR (middle) and SFR divided by M_{dust} (right). The yellow squares show the mean temperature for each redshift bin. The dashed line shows the extrapolation of the best fit relations derived for $z = 0$ galaxies from JINGLE and HRS (Lamperti et al. 2019). The dotted lines illustrate the 1σ dispersion of the JINGLE and HRS sample around the best fit relations.

To test this, we look at the relation between dust temperature and distance from the main sequence (defined as difference between the SFR of a galaxy and the SFR of a galaxy of the same stellar mass and redshift on the main-sequence). We find no relation between T_{cold} and distance from the main-sequence ($R = -0.06$). We note that we selected only galaxies lying within 0.4 dex from the main-sequence, thus the dynamic range of the distance from the MS is small. From this analysis, it seems that the absolute SFR is more important that the distance from the main-sequence in determining T_{cold}. We note that at fixed SFR, galaxies at high redshift have higher T_{cold} (see left panel of Figure 4.14). This suggests that the SFR alone can not explain the dust temperatures observed, but there is also an additional increase of T_{cold} with redshift.

4.5 Conclusions

In this chapter, we applied the hierarchical SED fitting code that we developed for the JINGLE+HRS sample to a sample of main-sequence galaxies at $z = 1 - 3.5$ from the A^{3}COSMOS sample. The main conclusions of this work are:

- We use simulated SEDs to test the ability of the hierarchical Bayesian SED fitting code in recovering the dust properties at different redshifts, focusing in particular on the cold dust temperature. We find that the SMBB+PL model systematically

overestimates T_{cold}, while the TMBB model performs better. We obtain better results by dividing the sample in redshift bins and fitting each bin separately, rather than fitting the entire sample together.

- We apply the TMBB model on main-sequence galaxies in the range $z = 1 - 3.5$. We confirm the trend of T_{cold} increasing with redshift, as has been reported in the literature. We measure lower dust temperatures (by ~ 8 K) compared with previous works by Magnelli et al. (2014) and Schreiber et al. (2018). The difference could be explained by the different methods used to measure T_{cold} and by the different sample selection.

- We find a positive correlation of T_{cold} with SFR, SSFR and SFR/M$_{dust}$, confirming the trend that we found at redshift $z = 0$ from JINGLE and HRS.

In the future, we would like to expand the sample, including galaxies with less detections (to increase the number statistics) and including galaxies above and below the main-sequence. Moreover, we plan to apply the optically-thick assumption to test whether it provides a better fit to the data and to investigate how the dust temperatures will change with this assumption. Finally, while in this chapter we focus our analysis on T_{cold}, we also plan to investigate the possible relations between the dust emissivity index β and other galaxy properties.

This page was intentionally left blank

Chapter 5

Resolved FIR observations of z∼2 AGN and connection to ionized outflows properties

The impact of AGN on star-formation can be particularly important at redshift $z \sim 2$, which corresponds to the peak of star-formation and AGN activity in the Universe (e.g., Shankar et al. 2009; Madau & Dickinson 2014; Tacconi et al. 2020).

To study AGN feedback on star-formation, one possibility is to use spatially resolved observations to map the distribution of both the outflows and the star-forming regions and look for spatial correlations or anti-correlations, that can indicate signatures of star-formation suppression ('negative feedback') or enhancement ('positive feedback') (Cresci & Maiolino 2018 and references therein). Using Integral Field Unit (IFU) spectroscopy, several studies investigate the impact of ionized outflows, traced by [O III], on star-formation in AGN host galaxies and found evidence of both positive and negative feedback (e.g. Cano-Díaz et al. 2012; Cresci et al. 2015b; Carniani et al. 2016; Maiolino et al. 2017; Gallagher et al. 2019; Perna et al. 2020), although the interpretation of some of these observations may not be trivial (see Scholtz et al. 2020).

Assessing the impact of outflows on star-formation can be complicated by the fact that common SFR tracers (as for example the Hα emission line) are affected by dust obscuration (Madau et al. 1996; Casey et al. 2014; Whitaker et al. 2014). In some objects, the UV

and Hα emission could be completely hidden by the dust (e.g., Hodge et al. 2016; Chen et al. 2017). Thus, to have a complete view of the star-formation happening in the host galaxy it is crucial to also have information about the dust-obscured star-formation traced by the far-infrared (FIR) emission (e.g., Whitaker et al. 2014; Brusa et al. 2018; Scholtz et al. 2020). In this chapter, we combine IFU observations, to map the Hα emission and [O III] outflows, with matched-resolution observations of the rest-frame FIR emission, to map the dust-obscured star formation.

High-resolution observations from the Atacama Large Millimeter/submillimeter Array (ALMA) have been used to measure the FIR sizes of high-redshift star-forming galaxies (e.g. Ikarashi et al. 2015; Simpson et al. 2015; Hodge et al. 2016; Gullberg et al. 2019). Several studies found the rest-frame FIR sizes of star-forming galaxies at $z > 1$ to be smaller than the rest-frame optical sizes (e.g., Chen et al. 2015; Barro et al. 2016; Tadaki et al. 2017; Fujimoto et al. 2017, 2018; Elbaz et al. 2018; Lang et al. 2019). A possible interpretation is that the central compact dusty star-forming component is related to the formation of the bulge (Fujimoto et al. 2017). It is still unclear whether the presence of an AGN can affect the FIR size of the host galaxy. For example, Chang et al. (2020) studied a sample of seven AGN and 20 non-AGN at $z \sim 1$ and found that obscured IR-selected AGN have smaller FIR sizes (median size $R_e = 0.76 \pm 0.48$ kpc) than non-AGN (median size $R_e = 1.62 \pm 0.50$ kpc) at the same redshift and stellar mass. On the other hand, Harrison et al. (2016b) measured the FIR sizes of a sample of five X-ray selected AGN at $z \sim 1.5 - 4.5$ and found that their FIR sizes (FWHM size $1 - 3$ kpc, median 1.8 kpc) are comparable to the sizes of sub-millimetre galaxies (SMGs) at the same redshift (median FWHM size 2.4 ± 0.2 kpc).

This work is part of a series of papers from SUPER[1] (SINFONI Survey for Unveiling the Physics and Effects of Radiative feedback, Circosta et al. 2018), a large program which aims to investigate the outflows properties of $z \sim 2$ AGN. The high resolution ($\sim 0.2''$, corresponding to ~ 2 kpc) of the IFU SINFONI observations is critical to resolve the morphology of the ionized outflow (Kakkad et al. 2020) and connect it with the star-formation properties of the host galaxy. The SUPER sample consists of 39 X-ray selected AGN in the redshift range $z = 2 - 2.5$, spanning a wide range of AGN bolometric luminosities ($\sim 10^{44} - 10^{48}$ erg s^{-1}).

Here we present high-resolution (~ 0.2") ALMA FIR maps for a sub-sample of eight

[1] http://www.super-survey.org

AGN from SUPER. With these data, we investigate the impact of AGN outflows on star-formation, taking into account both obscured and unobscured star-formation.

This chapter is organized as follows. In Section 5.1 we describe the selection criteria and the general properties of the sample. In Section 5.2 we present the ALMA data and the analysis to extract the information about the FIR sizes and flux densities. Section 5.3 describes the SINFONI Hα and [O III] data. In Section 5.4 we present our results. First, we investigate the origin of the FIR emission in our targets (Sec. 5.4.1). Then, we compare the FIR sizes with other samples from the literature (Sec. 5.4.2). Finally, we compare the spatial distribution of the FIR continuum with the Hα and [O III] emission, as well as with the ionized outflows (Sec. 5.4.3 and 5.4.4). In Section 5.5 we summarize the main results and our conclusions.

5.1 Sample

The sample studied in this paper consists of eight AGN with ALMA Band 7 continuum observations, which have been selected from the SUPER parent sample. The sample selection of SUPER is described in detail in Circosta et al. (2018). In brief, SUPER targets were selected in the X-rays from various surveys, by adopting as a threshold an absorption-corrected X-ray luminosity of $L_X \geq 10^{42}$ erg s^{-1}, to exclude sources where the X-ray emission may come from star-formation (Aird et al. 2017). To select the sub-sample to be observed with ALMA, we consider all the SUPER objects with photometric detections in the FIR (i.e. > 24 μm), to be able to properly assess the emission process at 870 μm, and with [O III] detections in the completed IFU data at the time of the proposal (April 2018), to be able to investigate the impact of [O III] outflows on the dust-obscured star-formation. Eight SUPER targets satisfied these criteria and were selected for the ALMA observations.

Our sample includes five AGN from the COSMOS-Legacy survey (Civano et al. 2016; Marchesi et al. 2016), two from the *Chandra* Deep Field South (CDF-S, Luo et al. 2017), and one from the wide-area XMM-Newton XXL survey (Pierre et al. 2016). A summary of the sample characteristics is provided in Table 5.1.

Table 5.1. Properties of the sample. All quantities are taken from Circosta et al. (2018). (1) Field where the targets are located; (2) Source identification number from the catalogues corresponding to each field; (3) RA and (4) Dec of the optical counterpart; (5) Spectroscopic redshift; (6) AGN classification as broad line (BL) or narrow line (NL) objects according to the optical spectra; (7) Host galaxy stellar mass and 1σ error; (8) SFR from the FIR luminosity and 1σ error; (9) AGN bolometric luminosity and 1σ error, derived from SED fitting; (10) Absorption-corrected X-ray luminosity in the hard band ($2-10$ keV) and 90% confidence level error; (11) Absorbing hydrogen column density and 90% confidence level error.

Field	ID	RA [deg]	Dec [deg]	z	AGN type	log M_* [log $M_\odot$]	SFR [$M_\odot$ yr^{-1}]	log L_{bol} [erg s^{-1}]	log $L_{2\text{-}10keV}$ [erg s^{-1}]	log N_H [cm^{-2}]
(1)	(2)	(3)	(4)	(5)	(6)	(7)	(8)	(9)	(10)	(11)
XMM-XXL	X_N_81_44	34.378942	-4.306572	2.311	BL	11.04±0.37	229±103	46.80±0.03	$44.77^{+0.07}_{-0.09}$	< 21.86
CDF-S	XID36	52.961556	-27.784281	2.259	NL	10.68±0.07	184±9	45.70±0.06	$43.84^{+0.31}_{-0.63}$	> 24.10
CDF-S	XID419	53.097649	-27.715270	2.145	NL	10.89±0.02	44±2[a]	45.54±0.05	$43.84^{+0.29}_{-0.44}$	$24.28^{+0.19}_{-0.31}$
COSMOS	cid_1057	149.812485	2.111014	2.214	NL	10.84±0.07	85±4	45.91±0.06	$44.53^{+0.26}_{-0.30}$	$23.98^{+0.24}_{-0.28}$
COSMOS	cid_346	149.930878	2.118734	2.219	BL	11.01±0.22	362±49	46.66±0.02	$44.47^{+0.08}_{-0.09}$	$23.05^{+0.17}_{-0.19}$
COSMOS	cid_451	150.002533	2.258629	2.450	NL	11.20±0.05	48±19[b]	46.44±0.07	$45.18^{+0.23}_{-0.19}$	$23.87^{+0.19}_{-0.15}$
COSMOS	cid_1205	150.010696	2.332968	2.255	BL[c]	11.20±0.10	384±33	45.75±0.17	$44.25^{+0.21}_{-0.23}$	$23.50^{+0.27}_{-0.27}$
COSMOS	cid_1143	150.036819	2.257776	2.492	NL	10.40±0.17	108±18	44.85±0.12	$44.83^{+0.43}_{-0.36}$	$24.01^{+0.77}_{-0.29}$

[a] For XID419, we updated the SFR from Circosta et al. (2018), see text in Section 5.1. [b] For cid_451, we updated the SFR from Circosta et al. (2018), after removing the contribution from synchrotron emission. The value from Circosta et al. (2018) was an upper limit of 125 $M_\odot$ yr^{-1}. [c] cid_1205 was previously reported as a NL target in Circosta et al. (2018), but it is now classified as a BL target based on the presence of BLR emission in the Hα line in the K-band SINFONI spectrum (Kakkad et al. 2020).

Given the selection criteria based on the FIR and [O III] detections, it is important to consider how representative of the parent population these targets are. Figure 5.1 shows the 2−10 keV absorption corrected X-ray luminosities (L_X) and hydrogen column densities (N_H) for the total SUPER sample, with the ALMA targets highlighted in orange. X-ray luminosities and N_H are derived from the analysis of the X-ray spectra (for more details see Circosta et al. 2018).

The ALMA targets have X-ray luminosities in the range $\log L_X/(\mathrm{erg\ s^{-1}}) = 43.8-45.2$, with median $\log L_X/(\mathrm{erg\ s^{-1}}) = 44.5$. In terms of X-ray luminosity, the ALMA sample is representative of the parent SUPER sample, which has median $\log L_X/(\mathrm{erg\ s^{-1}}) = 44.7$ and interquartile range $\log L_X/(\mathrm{erg\ s^{-1}}) = 44.1 - 44.8$.

Most of the ALMA targets have relatively high N_H ($\log N_H/\mathrm{cm^{-2}} = 23.0 - 24.3$), with the exception of X_N_81_44 ($\log N_H/\mathrm{cm^{-2}} < 21.9$). The three ALMA targets with the lowest N_H are classified as optical broad line (Type 1) AGN. Our ALMA sample includes 7/8 (88%) obscured sources (based on $\log N_H/\mathrm{cm^{-2}} > 22$; Mainieri et al. 2002; Szokoly et al. 2004), compared to 54% in the parent sample, and 5/8 (63%) optical Type 2 (narrow line) AGN, compared to 41% in the parent sample. The fact that our targets tend to be more obscured and to have high N_H values compared to the parent SUPER sample could be due to our FIR selection. If this is the case, it would suggest that part of the obscuration measured by N_H is due to dust in the host galaxies. For example, Circosta et al. (2019) studied a sample of seven AGN at $z > 2.5$ and found that a significant part of the obscuration measured from the X-ray spectral analysis is due to the dense ISM in the host galaxy. A similar result was reported by D'Amato et al. (2020). In summary, although our sample has X-ray luminosities which are representative of the parent sample, we are biased towards heavily obscured (high N_H) and Type 2 targets.

The right panel of Figure 5.1 shows the parent SUPER sample and the ALMA targets in the star-formation rate (SFR) versus stellar mass (M_*) plane. Stellar masses are derived from the panchromatic (UV-to-FIR) spectral energy distribution (SED) fitting performed by Circosta et al. (2018), using the Code Investigating GALaxy Emission (`CIGALE`; Burgarella et al. 2005; Noll et al. 2009; Boquien et al. 2019). This code takes into account the energy balance between the absorption by dust in the UV-optical and the corresponding re-emission in the FIR. The SED model includes three emission components: i) stellar emission; ii) emission by cold dust heated by star-formation; iii) AGN emission, consisting in direct emission from the accretion disk in the UV-optical range and emission from the

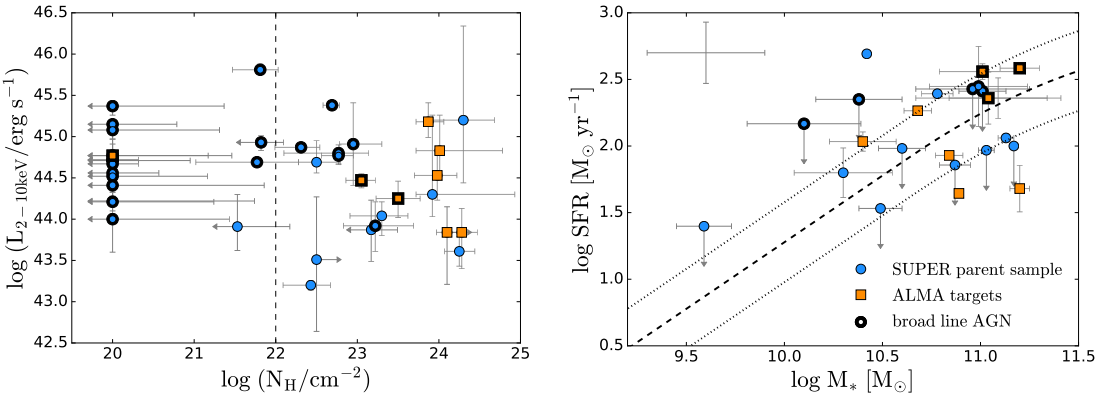

Figure 5.1. *Left:* X-ray luminosity in the $2-10$ keV band versus hydrogen column density (N_H) for the SUPER sample. ALMA targets for this work are marked with orange squares. Targets classified as broad line AGN in the optical are marked with black contours. The dashed line at $\log(N_H/\mathrm{cm}^{-2}) = 22$ marks the separation between X-ray unobscured and obscured AGN. *Right:* SUPER sample in the star-formation vs. stellar mass plane. Only the 24/39 objects with star formation and stellar mass constraints are shown. The size of the systematic uncertainties is shown on the top left corner. The black dashed curve shows the main sequence (MS) of star-forming galaxies from Schreiber et al. (2015) at the average redshift of our target sample (z∼2.3), the 0.3 dex dispersion is showed by dotted lines. Most of the ALMA targets are consistent with being on the main-sequence, with the exception of XID419 and cid_451, which lie slightly below the MS.

dusty torus peaking in the MIR. For more details on the SED fitting method we refer the reader to Circosta et al. (2018).

The SFRs are estimated from the infra-red (IR) luminosity, obtained by integrating the best-fit template SED in the rest-frame wavelength range $8-1000$ μm, after removing the AGN contribution. The IR luminosity is converted to SFR using the Kennicutt (1998) calibration, converted from a Salpeter IMF to a Chabrier (2003) IMF by subtracting 0.23 dex (Bolzonella et al. 2010)[2].

We update the SFRs of two targets (XID419 and cid_451) with respect to the measurements reported in Circosta et al. (2018). For XID419, we re-calculate the SFR after correcting a mistake that was made in Circosta et al. (2018) in assigning the flux values at 870 μm and 1 mm. This correction results in a small increase of the SFR (5%), which is of the order of the uncertainties. For cid_451, only an upper limit on the SFR (< 125 $M_\odot$ yr^{-1}) was reported in Circosta et al. (2018) due to the possible high contamination from

[2]Systematic uncertainties on the stellar masses are around 0.3 dex and can be larger for SFRs (e.g. Mancini et al. 2011; Santini et al. 2015). These uncertainties are due to the models used, degeneracies between parameters, a priori assumptions and the discrete coverage of the parameter space.

synchrotron emission to the FIR fluxes. This target is classified as a radio-loud source based on the comparison between infrared and radio luminosity. Thanks to a new flux measurement at 1 mm from C. Circosta et al. (2020, submitted), we are able to better constrain the synchrotron contribution to the FIR fluxes (see Sec. 5.4.1). We re-measure the SFR after subtracting the synchrotron contribution from the FIR fluxes and obtain SFR$= 48 \pm 19$ M$_\odot$ yr^{-1}.

The ALMA targets have stellar masses in the range $\log M_*/M_\odot = 10.4 - 11.2$, with a median $\log M_*/M_\odot = 11.0$. The SUPER parent sample has a similar median $\log M_*/M_\odot = 10.9$, and an interquartile range $\log M_*/M_\odot = 10.5 - 11.0$. The SFRs of the ALMA sample are in the range SFR$= 44 - 384$ M$_\odot$ yr^{-1}, with a median SFR $= 146$ M$_\odot$ yr^{-1}. The SUPER parent sample has a median SFR $= 131$ M$_\odot$ yr^{-1} and interquartile range SFR $= 81 - 250$ M$_\odot$ yr^{-1}. We note that only 24/39 of the SUPER targets have SFR and stellar mass measurements, and ten of these have only upper limits on the SFR. The ALMA targets have similar SFRs and stellar masses to the objects with SFR and stellar mass measurements in the parent SUPER sample. However, given the presence of many SFR upper limits in the parent sample, our targets are likely to represent the upper end of the SFR distribution of the SUPER sample.

On the SFR-M_* plane, we show also the main-sequence definition of Schreiber et al. (2015) at the average redshift of our sample ($z \sim 2.3$). Most of our sample lies within 0.3 dex of the main-sequence[3]. The exceptions are XID419 and cid_451 that lie slightly below the main-sequence.

In summary, despite the pre-selection of FIR detections, our ALMA targets are mainly main-sequence galaxies. However, SUPER primarily consists of moderate luminosity X-ray AGN which, as a population, tend to have SFR distributions slightly below the main-sequence (e.g. Mullaney et al. 2015; Grimmett et al. 2020). Thus, our sample is likely to have a distribution of SFRs skewed to higher values compared with the parent population of X-ray AGN.

[3]We note that the main-sequence from Schreiber et al. (2015) is derived assuming a Salpeter IMF (Salpeter 1955), while we assume a Chabrier IMF (Chabrier 2003). However, assuming a different IMF would systematically shift both M_* and SFRs by approximately the same amount (Brinchmann et al. 2004; Elbaz et al. 2007), and therefore would not affect the shape of the main-sequence.

5.2 ALMA observations and analyses

We use FIR continuum observations from ALMA with the goal of tracing the dust obscured star-formation at the same resolution (∼2 kpc) of the [O III] and Hα emission line maps extracted from our SINFONI IFU data.

The ALMA Band 7 continuum observations used in this work belong to the Cycle 6 observing programme ID 2018.1.00992.S (P.I: C. M. Harrison). Observations were taken between 18 October and 5 November 2018. The integration time on source for each target is between 14 and 70 minutes. The observations were performed with $45 - 49$ antennas, with baselines in the range $15.1 - 2500$ m. The Band 7 870 μm continuum observations correspond to rest-frame $250 - 270$ μm for our sources. The requested angular resolution was $0.15 - 0.30$", to match the resolution of the SINFONI observations. The maximum recoverable scales are in the range $1.2 - 1.9$".

5.2.1 Data reduction and imaging

We reduce the data using the Common Astronomy Software Application (`CASA`) version 5.4.0. The calibrated measurement sets are created using the standard ALMA pipeline provided with the raw data in the ALMA archive. We use the `CASA` task `fixvis` to phase-center the calibrated measurement set on the central position of the source, determined by fitting a 2D Gaussian profile on the reduced image provided by the ALMA data-reduction pipeline.

We produce an image of the calibrated measurement sets using the `CASA` task `tclean` We measure the RMS (root mean square) noise of the dirty image in an annulus around the source (with inner radius 1" and outer radius 2"). The inner radius is selected large enough to exclude emission from the source and the outer radius small enough so that the selected region has similar noise properties to the center of the map. We set the cleaning threshold of `tclean` to 2·RMS and the pixel size to be one fifth of the beam size.

One of our aims is to make a comparison of positions, sizes and morphologies between the FIR emission, measured from the ALMA maps, and the ionized gas emission, measured with SINFONI. Thus, we want to create ALMA maps with a similar resolution to the SINFONI IFU maps (FWHM PSF$\sim$ 0.3"). We generate the maps using the Briggs weighting scheme with robust parameter = 2 (corresponding to natural weighting).

Table 5.2. Properties of the ALMA maps and measurement of FIR sizes and 870 μm flux densities. (1) Synthesized beam size (FWHM) of the ALMA maps created with Briggs weighting with robust=2. (2) RMS noise. (3) Peak signal-to-noise in the ALMA map. (4) Best fit model to the *uv*-visibility data, according to the Bayesian Information Criterion (BIC). (*) If the peak $S/N < 8$ in the ALMA maps, we do not consider the size measurements to be reliable. (5) Flux density at 870 μm, measured from the *uv*-visibilities using the best model. (6) Half-light radius in arcsec measured from the *uv*-visibilities using the best model. (7) Half-light radius in kpc. (8) Axial ratio measured using `uvmodelfit`. Axial ratios significantly different from one are marked with *. (9) Position angle (P.A.) measured using `uvmodelfit` for the objects with axial ratios significantly different from one. The P.A. measures the angle of the major axis with respect to the North in anti-clockwise direction. (10) AGN contribution to the 870 μm flux estimated from the SED fit. (11) Contribution from synchrotron emission to the 870 μm flux estimated from the SED fit. We model the synchrotron emission as a power law with a spectral index α_r. (12) Spectral index α_r used to estimate the synchrotron contribution. In the cases where we could not constrain α_r with the available data, we assume $\alpha_r = 0$ which gives a conservative upper limit on f_{sync} (see Sec. 5.4.1).

ID	Beam size [arcsec^2] (1)	RMS [μJy beam^{-1}] (2)	S/N (3)	best model (4)	F(870 μm) [mJy] (5)	R$_e$ [arcsec] (6)	R$_e$ [kpc] (7)	axial ratio (8)	P.A. [deg.] (9)	f_{AGN} % (10)	f_{sync} % (11)	α_r (12)
X_N_81_44	0.23×0.22	39.40	22.8	exp.	1.13±0.16	0.10±0.01	0.83±0.10	1.00±0.11	-	< 1	< 5	0
XID36	0.22×0.21	31.27	21.1	exp.	1.05±0.13	0.12±0.01	1.00±0.10	1.22±0.12	-	5	< 1	-1.25
XID419	0.22×0.21	26.65	9.4	Gaussian	0.43±0.05	0.10±0.01	0.79±0.12	2.88±0.80*	88±5	5	< 11	0
cid_1057	0.18×0.16	18.67	3.5*	point	0.06±0.02	< 0.08	< 1.40	1.16±0.41	-	< 1	< 3	0
cid_346	0.27×0.22	41.14	28.5	Gauss.+point	2.58±0.14	0.19±0.01	1.61±0.09	1.31±0.06*	2±5	< 1	< 1	-0.98
cid_451	0.26×0.23	20.70	5.5*	exp.	0.29±0.09	0.24±0.07	1.98±0.55	3.15±0.83*	-58±5	6	23	-0.98
cid_1205	0.25×0.25	18.36	16.2	point	0.27±0.02	< 0.12	< 2.06	1.00±1.00	-	< 1	2	0
cid_1143	0.25×0.23	16.13	12.0	exp.	0.50±0.10	0.26±0.04	2.13±0.36	4.60±0.70*	23±2	< 1	< 1	0

The beam sizes obtained using natural weighting are in the range $0.17 - 0.25$" and match closely the resolution of the SINFONI maps. We also created maps using the Briggs weighting scheme with robust = 0.5 (higher resolution, beam size $0.16 - 0.20$") and we find no appreciable difference in the morphology and size of the FIR emission that would affect our conclusions. Therefore we decide to use the maps obtained with natural weighting for the rest of the analysis. We show these final ALMA maps in Figure 5.2.

The ALMA maps have an RMS in the range $0.02 - 0.04$ mJy beam^{-1}. We measure peak signal-to-noise (S/N) of the sources by dividing the peak flux density by the RMS. The S/N values vary between 3.5 and 22. Two of the targets (cid_1057 and cid_451) have S/N < 8, and therefore we cannot derive reliable size measurements for these objects. We highlight these two targets with low S/N in all the relevant figures. The beam size, RMS, and peak signal-to-noise of the ALMA images are summarized in Table 5.2.

5.2.2 Modelling the 870 μm data: sizes and flux densities

In this section, we describe how we measure the sizes and flux densities of the 870 μm emission. In particular, we are interested in comparing the 870 μm sizes with FIR sizes of literature samples and with the sizes of the optical emission-line regions (Hα and [O III]).

We test models describing different morphologies (e.g., point source, exponential disk profile) to extract reliable size and flux density measurements. We measure the sizes both from the visibilities and in the image plane. Measuring the sizes directly from the *uv*-visibilities has the advantage that it is not dependent on the choices made to create the images. All the size measurements using the different methods are shown in the appendix in Tables 10.1 and 10.2.

First we use the `CASA` routine `uvmodelfit` to fit a model directly to the visibilities. The models available with `uvmodelfit` are a point source, a 2D Gaussian and an elliptical disk. We run `uvmodelfit` on the phase-centred calibrated measurement sets using 20 iterations assuming a 2D Gaussian model. The results from `uvmodelfit` also provide the information on the ratio of the major and minor axis (see Table 5.2).

We also perform a fit on the collapsed visibilities using python outside of `CASA`, which gives us more freedom in the choice of models. We extract the visibility amplitudes from the phase-centred calibrated measurements sets. Then, we bin the data in *uv*-distance intervals of 50 kλ. We measure the average of the visibilities at each *uv*-distance, weighted by the corresponding uncertainties. The uncertainty on each mean visibility is given by the

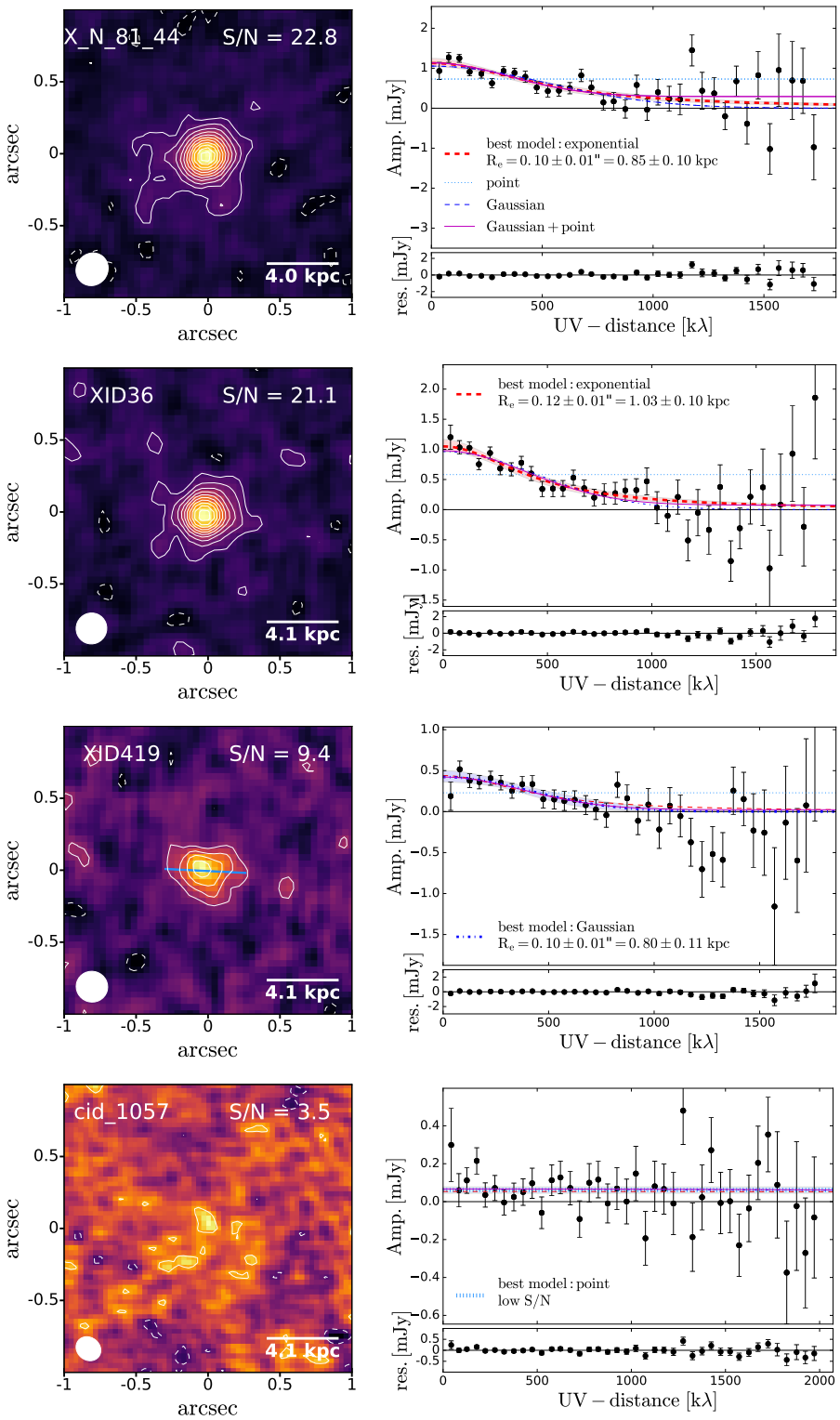

Figure 5.2. *Left column:* Maps of the ALMA continuum created with a Briggs weighting scheme with robust parameter=2. The white ellipse represents the ALMA beam. The peak S/N is also shown. Contours start at 2σ and increase at intervals of 2σ. Dashed contours are negative contours at -2σ. The lightblue bar indicates the position angle along the major axis of the FIR emission, when it can be reliably determined (see Section 5.2.3). *Right column:* Visibility versus *uv*-distance. The overlaid straight and curved lines show the fit using different models: point source (dotted lightblue line), exponential profile (dashed red curve), Gaussian profile (dashed-dotted blue curve), and Gaussian plus point source (solid magenta curve). The best model according to the Bayesian Information Criterion (BIC) is labelled in each case. The shaded area shows the 1σ uncertainties on the best model. The lower panel shows the residuals with respect to the best model.

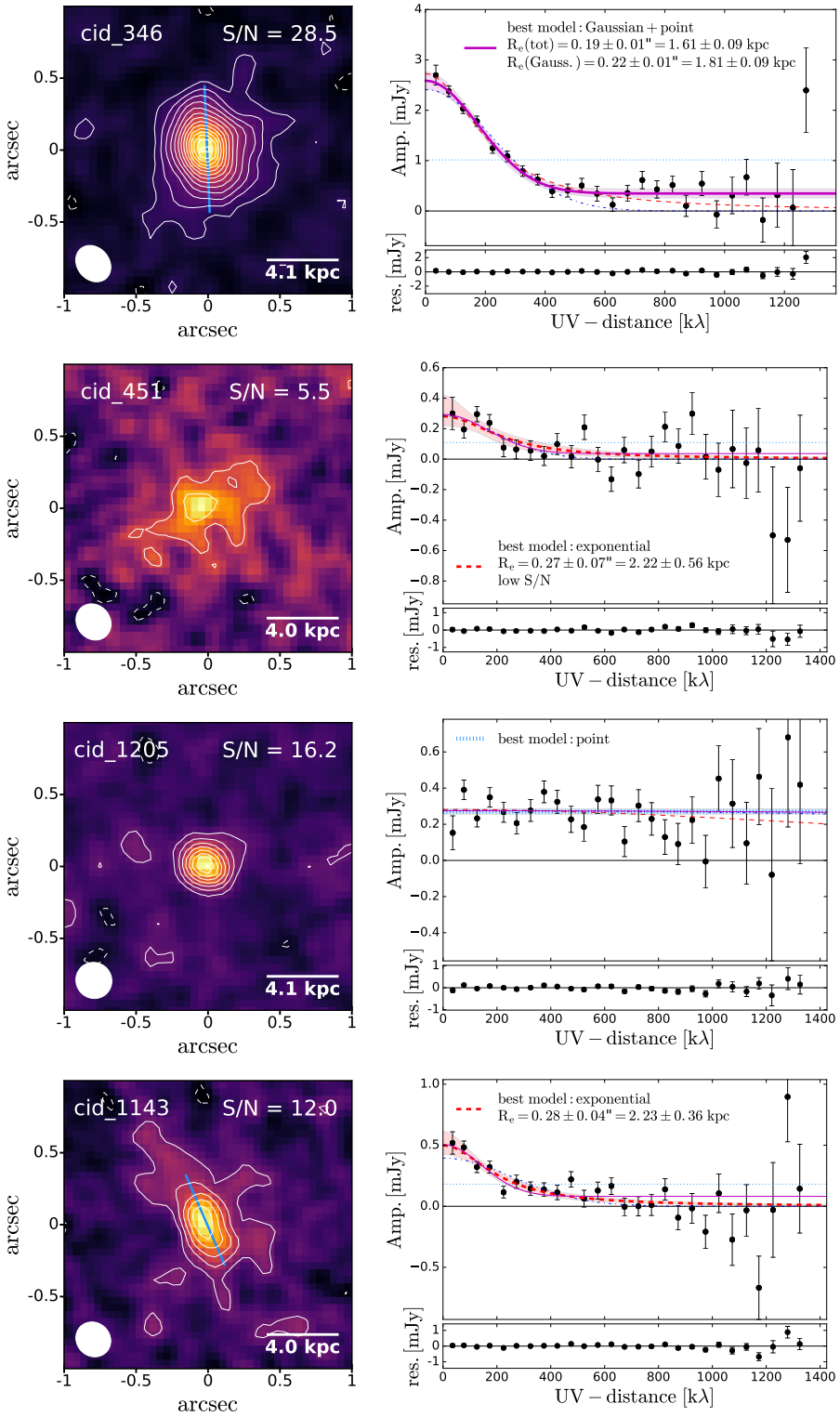

Figure 5.2. – continued.

standard deviation of the mean divided by the square root of the number of visibility points in that bin. In Figure 5.2 we show the visibility amplitudes as a function of uv-distance for our sample.

For simplicity, we only consider symmetrical models, i.e. an axial ratio of one. We test the following models: point source, 2D Gaussian, 2D Gaussian plus a point source, and exponential profile (equivalent to a Sérsic profile with index $n = 1$). To fit the visibilities versus uv-distances, we use the Markov Chain Monte Carlo (MCMC) program `Stan`[4] (Carpenter et al. 2017), which allows us to accurately estimate the uncertainties on the derived parameters. Specifically, we employ `PyStan`[5], the python interface to `Stan`. We assume a Gaussian likelihood and use uniform priors, allowing the free parameters to vary in a large parameter range (the prior ranges are tabulated in Table 10.3 in Appendix D.).

We derive the best fit parameters by taking the median values from the marginal posterior distributions. The uncertainties are given as the 16th and 84th percentiles of the posterior distributions. We express all sizes in terms of half-light radius (also known as effective radius) R_e. For a 2D Gaussian, R_e is equivalent to 0.5× FWHM. For the exponential profile $I(R) = \exp(-R/a)$, where a is the scale parameter, R_e is given by $1.6783 \cdot a$. For the model with Gaussian plus point source, we calculate the radius that contains half of the light based on the total profile derived from the fit (R_e(tot)). We also report the value of R_e for the Gaussian component only (R_e(Gauss.)).

The results from our fit on the visibilities using a Gaussian model are consistent within the uncertainties with the results from `uvmodelfit` both in terms of sizes and flux densities. Therefore, for the rest of this work we use the flux densities and size measurements from our analysis of the collapsed visibility amplitude versus uv-distance performed in python.

To assess the preferred model to fit our data, we use the Bayesian Information Criterion (BIC; Schwarz 1978):

$$BIC = -2 \cdot \ln L + q \cdot \ln(m), \tag{5.1}$$

where L is the likelihood (i.e. the probability of the data given the parameters), q is the number of free parameters of the model, and m is the number of data points. The BIC considers the likelihood of the model and penalizes models with a larger number of parameters. The model with the smallest BIC is the preferred model. Figure 5.2 shows the visibilities versus uv-distances data with the curves showing the different models fitted.

[4] http://mc-stan.org/
[5] http://pystan.readthedocs.io/en/latest/

The preferred model is highlighted with a thicker line.

At least a S/N≥ 10 is required to obtain reliable size measurements (Simpson et al. 2015). cid_1057 and cid_451 have very low S/N (3.6 and 5.5, respectively), therefore we do not consider the size measurements of these two targets to be reliable. However, for completeness we show their values throughout the figures, and we highlight them as unreliable. XID419 has S/N= 9.4 and is therefore a borderline case. Given the good agreement in the size measured with different methods for this source, we consider the size measurements to be reliable.

We verify that we obtain consistent results by performing the analysis also in the image plane. We fit a 2D Gaussian to the ALMA maps using the python routine `scipy.optimize.curve_fit`, and we derive the size of the emission as well as the centroid of the emission. We perform the fitting also using the 2D Gaussian fitting routine available using the `CASA viewer` and we find consistent results within the 1σ uncertainties. The sizes and flux densities measured in the image plane are in agreement with the measurements done in the *uv*-plane using the Gaussian model. For more details on the comparison between different methods, see Section 10.1 of Appendix D.

The sizes and flux densities measured with the different methods are reported in Tables 10.1 and 10.2 in Appendix D. We consider as our 'best measurements' the FIR sizes and flux densities derived from the fit of the *uv*-visibilities with the 'preferred model' (reported in Table 5.2). Given the general agreement between the different methods, the choice of the method does not affect our results.

5.2.3 870 μm sizes, morphologies and flux densities

FIR sizes and morphologies

The effective radii derived from the 'best fit' models for our sample are in the range $0.80 - 2.13$ kpc, with a median of 1.31 ± 0.23 kpc. There is a general agreement between the sizes derived using the different models (see Figure 10.1 in Appendix D). The sizes measured from the fit with an exponential profile are larger than the sizes derived assuming a Gaussian profile by a factor of 1.38 on average (for the extended sources). This is by construction, since the exponential profile does not go rapidly to zero at larger radii and therefore there is a larger fraction of flux at large distances.

Half of the sources with reliable size measurements (3/6) are best described by an

exponential profile according to the BIC. One source (cid_1205) is better described by a point source and one source (XID419) by a Gaussian. The preferred model for cid_346 is a Gaussian plus a point source. The point source accounts for 13.5% of the total flux density, according to the results of our fit. For this source, we also test a model consisting of an exponential profile plus a point source. This model gives a point source contribution to the total flux of 4.1%, but it is not preferred over the 'Gaussian plus point source' or the 'exponential profile' model, according to the BIC. From our SED fitting decomposition, the AGN component contributes 0.15% to the total 870 μm flux. Thus, the exact contribution from the point source is uncertain. The point source could be due to the emission from the AGN or from a compact starburst, but we are not able to distinguish between these two scenarios.

The ratios between the major and minor axis derived using `uvmodelfit` for the 6/8 sources with high S/N are in the range $1 - 4.6$. For two sources (X_N_81_44 and cid_1205) the axial ratio is consistent with one. For XID_419, cid_346, and cid_1143 the difference in the sizes of the major and minor axes show that the emission is significantly elongated in one direction (axial ratio > 1.3). For these three sources, we are able to determine the position angle (tabulated in Table 5.2) with an uncertainty ≤ 5 degrees.

Flux densities

The flux densities measured with the different methods we explore to model the data are in agreement within the uncertainties (see Figure 10.1). The only exception is cid_346, for which the `uvmodelfit` Gaussian fit gives a slightly smaller flux (8%) than the other methods. This is probably because the Gaussian model cannot well describe the point source emission in the center, and therefore misses part of the flux.

Our high resolution ALMA images are probably missing some of the more diffuse emission, and therefore the measured flux densities cannot be considered as 'total' flux densities. For example, Harrison et al. (2016b) found a drop in peak flux of $18 - 44\%$ between a resolution of 0.8" and 0.3". To assess how much flux we are potentially missing in our ALMA data, we compare our flux measurements with other 870 μm flux measurements from lower resolution data from the ALMA Archive (compiled by Circosta et al. 2018) and from Scholtz et al. (2020). XID419 has an upper limit from Scholtz et al. (2020), that is consistent with our measurement. For cid_451 and cid_1205, our flux density measurements are smaller than the 870 μm flux densities from the ALMA Archive by 28%

and 23%, respectively.

We also compare our flux density measurements with the ones predicted from the SED fitting. The SED fitting is performed on the UV-to-FIR photometry, excluding our ALMA measurements. Figure 10.2 in Appendix D shows the SEDs with the results from the SED fitting, and the measured 870 μm flux densities. The ratio between the measured flux densities and the ones predicted from the SED fit vary between 12-150%, for the 6/8 targets with high S/N in the ALMA data. We note that unfortunately the SED fitting code does not provide the uncertainties on the predicted flux densities. However, for some of the targets, the predictions from SED fitting must be highly uncertain due to many upper limits at long wavelengths ($>$ 100 μm) that do not allow us to constrain well the shape of the SED.

5.3 Hα and [OIII] observations

5.3.1 SINFONI observations and data reduction

The SINFONI Adaptive Optics (AO) assisted observations and data reduction are described in detail in Kakkad et al. (2020), for the Type 1s, and in M. Perna et al. (in prep.), for the Type 2s. Here we summarize the main information. The SINFONI observations took place between November 2015 and December 2018 (ESO large program 196.A-0377). We observe the H-band ($1.45 - 1.85$ μm), which includes the rest frame optical lines Hβ and [O III]$\lambda\lambda$4959, 5007, and the K-band ($1.95 - 2.45$ μm), which includes the [N II]$\lambda\lambda$6584,6548, Hα and [S II]$\lambda\lambda$6716, 6731 lines. The average spectral resolution in the H-band and K-band is $\sim$3000 and $\sim$4000 respectively, corresponding to a channel width of $\sim$ 2 Å and $\sim$ 2.5 Å, respectively. The PSF sizes of the H-band and K-band are in the range $0.27 - 0.52$" and $0.15 - 0.46$", respectively (the PSF sizes for each target are listed Table 5.3). We note that cid_1057 is not detected in Hα, thus for this target we only show the [O III] (i.e., H-band) data.

5.3.2 Astrometry registration

Since one of our main goals is to compare the spatial distribution of the FIR continuum and ionized gas emission, we need to have reliable astrometry for both ALMA and the SINFONI maps. The absolute position of the SINFONI cubes, as derived from the SINFONI pipeline, is not sufficiently accurate for our purposes. Given the small field of view of the SINFONI

Table 5.3. Information about the SINFONI maps. PSF of the H and K-band SINFONI images and line fluxes measured from the integrated spectra. If the S/N of a line is smaller than 3, we report a 5σ upper limit. For cid_1057, the S/N of the K-band image is too low to derive any information about the Hα and [N II] emission. (4) redshift derived from the narrow component of the [O III] line. (5) Ratio of the fluxes of [O III]λ5007 and Hβ narrow emission lines. For Type 1 AGN, this is the flux of the narrow component, i.e. the BLR component is not included. (6) Ratio of the fluxes of [N II]λ6548 and Hα narrow emission lines. For Type 1 AGN, this is the flux of the narrow component, i.e. the BLR component is not included. (7) Half-light radius (R_e) of the [O III] systemic emission ([-300,300] km s^{-1} range), deconvolved from the PSF. If R_e is smaller than the PSF, we give the size of the PSF as an upper limit. (8) Half-light radius (R_e) of the Hα systemic emission ([-300,300] km s^{-1} range), deconvolved from the PSF.

ID	H-band PSF [arcsec^2]	K-band PSF [arcsec^2]	$z_{[O\,III]}$	F([O III])/F(Hβ)	F([N II])/F(Hα)	Re([O III]) [kpc]	Re(Hα) [kpc]
(1)	(2)	(3)	(4)	(5)	(6)	(7)	(8)
X_N_81_44	0.27×0.27	0.24×0.24	2.3180	> 8.00	-	< 1.11	1.35±0.03
XID36	0.35×0.35	0.15×0.15	2.2591	> 1.57	1.18±0.07	1.06±0.01	1.57±0.01
XID419	0.52×0.47	0.24×0.22	2.1430	> 0.61	0.90±0.28	< 2.07	1.42±0.02
cid_1057	0.32×0.30	0.46×0.43	2.2103	4.70±0.92	-	1.36±0.01	-
cid_346	0.30×0.30	0.30×0.30	2.2170	1.67±0.20	-	1.99±0.03	3.23±0.04
cid_451	0.30×0.28	0.28×0.27	2.4434	> 1.38	0.60±0.09	0.78±0.00	0.67±0.01
cid_1205	0.30×0.30	0.30×0.30	2.2555	> 1.66	-	0.99±0.02	1.33±0.09
cid_1143	0.41×0.38	0.30×0.30	2.4418	> 0.97	0.51±0.14	< 1.62	0.92±0.02

images (3×3 arcsec^2), we cannot correct the astrometry using nearby stars, since usually the target is the only visible source in the field of view. Thus, we need to rely on coordinates derived from other images.

We align our SINFONI data-cubes to broadband H- and K-band images of the same field from VLT/VISTA and VLT/ISAAC. To do this, we first align the H/K-band images to *Gaia* astrometry (Gaia Collaboration et al. 2016, 2018) using several stars across the fields. We then make broad-band images from the SINFONI data-cubes by collapsing them over the same wavelength range as the archival H/K-band images. We find the centroids of the images from the data-cubes and align these to the positions of the corresponding source in the near-infrared (H/K-band) images[6]. For the uncertainties on these positions, we combine in quadrature the uncertainties from: (1) the *Gaia* coordinates ($<$ 4 mas), (2) the alignment of the H/K-band images with *Gaia* (75-130 mas), (3) the PSF of the VLT/VISTA or VLT/ISAAC K-band images (3-40 mas), (4) the 2D Gaussian fit to determine the position of sources in the VLT images (1-49 mas), and (5) the centroid position of the collapsed data-cubes ($\sim$25 mas). This results in uncertainties on the astrometry in our SINFONI cubes of $0.03 - 0.14$". More details about the coordinate registration are provided in Appendix D (Section 10.3).

The ALMA astrometry has an absolute accuracy of 2% of the synthesized beam (ALMA Cycle 6 Technical Handbook[7]), which corresponds to $\sim 3 - 6$ mas for our observations and it is small enough compared to the other uncertainties.

5.3.3 Spectral line fitting

We aim to use the spatially integrated spectra to derive narrow line flux ratios and investigate the main source of ionization in our objects. We need therefore to measure the fluxes of the Hα, [N II], Hβ, and [O III] emission lines. The integrated SINFONI spectra of the Hα+ [N II] and Hβ+[O III] spectral regions for our targets are shown in Figure 5.3.

The line fluxes of the Type 1 AGN have been already measured by Kakkad et al. (2020), doing a careful decomposition of the line components belonging to the narrow and broad line region. Thus, we use the results of the emission line fitting performed by Kakkad et al. (2020) for our analysis. They extracted the spectra from a circular aperture centred on the targets. The diameter of the aperture was defined to include at least $\sim$ 95%

[6]For two of the Type 1 sources (X_N_81_44 and cid_346) we use the more accurate *Gaia* position and for XID419 we use more accurate coordinates from *HST*/WFC3, see appendix 10.3.

[7]https://almascience.eso.org/documents-and-tools/cycle6/alma-technical-handbook

of the emission and it is in the range $0.3 - 0.9$" for the three Type 1 AGN considered in this work.

To measure the line fluxes for the Type 2 AGN in our sample, we follow an approach as similar as possible to the fitting method used for the Type 1s. We create a map of the Hα emission by integrating the data cube on a 200 km s^{-1} wide channel centred on the central wavelength of Hα, after first removing the continuum and [N II] emission. We measure the central position and size of the Hα emission by fitting a 2D Gaussian using the python routine `scipy.optimize.curve_fit`. We finally extract the K-band spectrum from a circular aperture centred on the position of the Hα emission and with diameter equal to the major axis derived by the 2D Gaussian fit. We extract also the H-band spectrum from the same region, so that we can measure the line fluxes consistently. We note that the Hα and [O III] emission are broadly co-spatial (see Section 5.4.3). We tested the effect of the choice of the aperture on the line ratios, by extracting the spectra from a region equal to 1×PSF or 2×PSF. The line ratios are only marginally affected by the choice of aperture and our conclusions on the source of ionization do not change.

We perform the emission line fitting using `PySpeckit` (Ginsburg & Mirocha 2011). We first fit the continuum-subtracted H-band spectra in the wavelength range 4700-5100 Å. We model the three emission lines (Hβ, [O III]$\lambda\lambda$4959, 5007) using single or double Gaussians. For the single Gaussian fit, we tie together the width of the lines and their relative wavelength positions. For the double Gaussian fit, we also tie together the width and relative positions of the lines, separately for each of the two components. In order to decide if a second Gaussian component is needed, we calculate the reduced χ^2 value for the single Gaussian and double Gaussian models and we select the model with the smaller reduced χ^2 value. Based on this criterion, we use the double Gaussian fit only for two objects (cid_1143 and cid_451). We note that using the BIC criterion instead of the reduced χ^2 would give the same result. For the single Gaussian fit, we use the wavelength position of the [O III]λ5007 line to determine the systemic redshift of the source. In the case of the double Gaussian fit, we use the wavelength position of the 'narrower' component of the [O III]λ5007 line.

We then perform the fitting of the continuum-subtracted K-band spectra in the wavelength range 6200-6700 Å. We model the three emission lines (Hα, [N II]$\lambda\lambda$6584,6548) with single Gaussians. Given the lower S/N of the K-band spectra, we prefer to use single Gaussians instead of double Gaussians for all targets. However, since we are mostly in-

terested in the [N II]/Ha line ratio, we check that the fit with single and double Gaussians gives consistent line ratios, although the fluxes measured with the double Gaussian fit have larger uncertainties because of the additional free parameters. We fix the position and width of the three lines based on the redshift and width of the [O III]λ5007 line. We also fix the ratio of the [N II] lines ([N II]λ6584/[N II]λ6548 = 3, according to their atomic parameters) to minimise the number of free parameters in the fit. The H and K-band spectra with the corresponding emission line fits are shown in Figure 5.3.

We estimate the uncertainties on the lines with a Monte Carlo approach, following the same method used by Kakkad et al. (2020). We create mock spectra by adding to the model spectrum random noise proportional to the dispersion that we measured in the line-free regions of the spectrum. Then, we perform the fit on the mock spectra. We repeat this procedure 100 times and take the standard deviation of the 100 flux measurements as the uncertainty on the line flux (F_{err}).

We define a line as detected if it has a S/N=$F/F_{err} \geq 3$. If a line is not detected, we calculate a conservative upper limit equal to the flux of a Gaussian emission line with amplitude five times the noise level (measured in a line-free region of the spectrum) and with the same width as the other detected emission lines. The 5σ upper limit corresponds to a 'false negative' fraction of 2%, which is the probability that a source with 'true' flux higher than this upper limit is not detected.

We note that we did not correct the line fluxes for obscuration. In most of the cases we are not able to calculate the Balmer decrement, because the Hβ line is not detected. Additionally, given the different spatial location of the ionized gas and FIR emission (see Section 5.4.3), the obscuration derived from the Balmer decrement would not be representative of the total dust obscuration in the galaxies. Moreover, we are only interested in emission line ratios, which are negligibly affected by obscuration.

5.3.4 Hα and [OIII] maps

In this section we describe how we create the maps of the narrow Hα (i.e. without Broad Line Region) and [O III] emission.

In this paper, we consider a W_{80} (i.e. the width containing 80% of the line emission) value > 600 km s^{-1} as a conservative signature of an AGN-driven outflow (Kakkad et al. 2020). Following this definition, we consider the velocity range $< |300|$ km s^{-1} as systemic (non-outflowing) emission. We choose this definition because we want a consistent, model-

independent definition across all targets and for both emission lines (Hα and [O III]). For the two targets with two component fit to the [O III] emission line, this definition covers the bulk of the narrower component and excludes the broader, blue-shifted component.

To create the maps, we use the continuum-subtracted data-cubes. For the Hα map, we also subtract the [N II] components. For the Type 1 AGN, the Hα line was fitted with one Gaussian component for the BLR and two additional Gaussian components, tracing the systemic and outflowing gas. To create the narrow Hα maps, we remove the BLR component and the 'broader' of the two Gaussian components from the data-cubes. The second 'broader' component is tracing outflowing gas, that we do not want to include in our maps. We set the zero velocity at the wavelength position of the center of the [O III]λ5007 line (or Hα line, respectively). In case of fits with two components, we use the center of the 'narrower' Gaussian component to set the zero velocity (see Sec. 5.3.3). We create the [O III] and Hα maps by collapsing the spectra over the selected velocity channels for each spaxel.

Figure 5.3 shows the contours of the Hα and [O III] emission in the central 600 km s^{-1} channels. For every map, we measure the size and the centroid ('peak position') of the emission by fitting a 2D Gaussian using the python package `scipy.optimize.curve_fit`. We use these measurements in Sec. 5.4.3, where we compare the sizes and positions of the Hα and [O III] emissions with the location of the FIR emission. The uncertainties on the positions are calculated by adding in quadrature the uncertainties on the coordinate registration (see Section 5.3.2) and the uncertainties due to the 2D Gaussian fit (mean uncertainty $\sim$ 2 mas). The uncertainties on the position are in the range $0.04 - 0.15$".

5.4 Results and Discussion

In this Section, we first investigate the origin of the 870μm emission in our targets, to know what are the physical processes responsible for the FIR emission in our sample (Section 5.4.1). Then, we compare the FIR size of our sample with other AGN hosts and non-AGN galaxies at similar redshift from the literature, to test whether our sample has similar sizes to the general population of $z \sim 2$ galaxies (Section 5.4.2). Finally, we compare the spatial distribution of the FIR emission with the ionized gas distribution (Section 5.4.3), as well as with the position of the ionized outflow (Section 5.4.4).

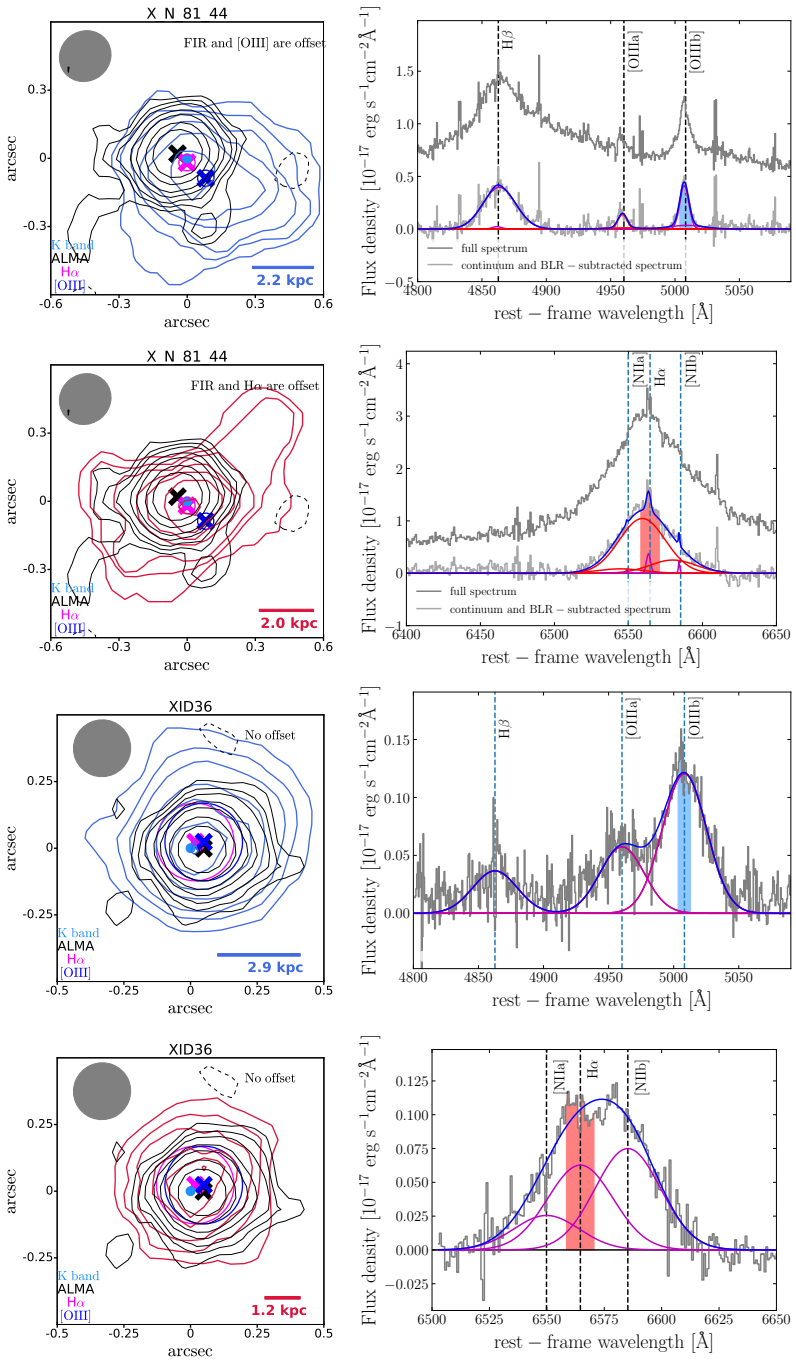

Figure 5.3. [O III] and Hα continuum-subtracted maps (where available), with the corresponding spectra. For the Type 1 AGN (X_N_81_44, cid_346 and cid_1205), we subtracted also the broad line region component and we show the total spectrum, before subtracting the continuum and broad line emission. The [O III] and Hα maps were created by integrating the spectrum over the [-300, 300] km s^{-1} velocity range, with respect to the center of the line (see shaded regions on the spectra). The FIR (black), [O III] (lightblue), and Hα (red) emission contours show the 2, 3, 4, 6, 8, 12, and 16σ levels. Dashed lines indicate the negative -2σ contours. The centroids of the optical continuum (lightblue point), FIR (black cross), [O III] (blue cross), Hα (magenta cross), are shown with the respective uncertainties (circles). The grey ellipses show the size of the ALMA beam, the scale-bars give the size of the PSF of the line emission maps. The grey bar shows the position angle along the major axis of the FIR emission, when it can be reliably determined (see Section 5.2.3). On the continuum subtracted spectra, the blue curve shows the total fit to the emission lines. The magenta curves show the individual narrow Gaussian components. In the cases where two Gaussian components are used in the fit, the second component is shown in red.

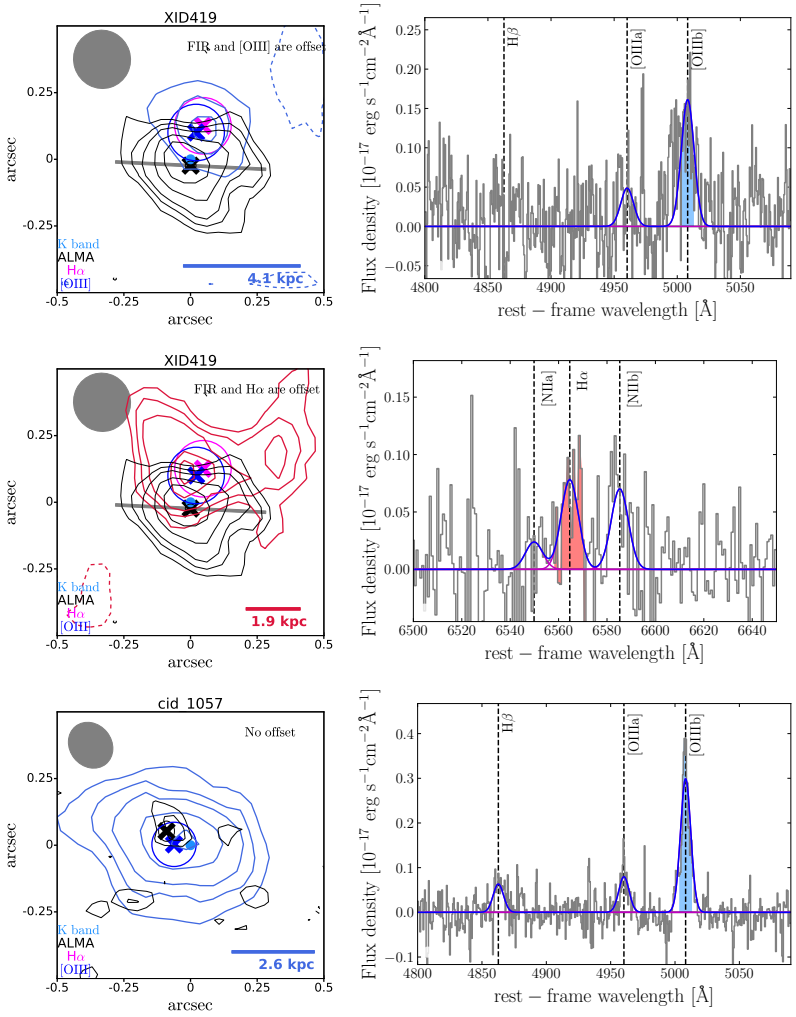

Figure 5.3. – continued.

5.4.1 Origin of the 870 μm emission

We aim at comparing the distribution of dust-obscured star-formation with the distribution of ionized gas and corresponding ionized outflows in our targets. For this goal, we use the rest-frame FIR images from our ALMA 870 μm maps. However, it is important to first assess the physical processes that are responsible for the 870 μm emission in our sample.

The observed 870 μm emission (corresponding to rest-frame $\sim$ 250 μm emission) can have different origins. The three main sources of emission are: 1) dust heated by star-formation/young stars, 2) dust heated by the AGN, and 3) synchrotron emission (e.g. Falkendal et al. 2019). The observed emission is likely a combination of the three processes above, nevertheless in this section we attempt to estimate their fractional contribution,

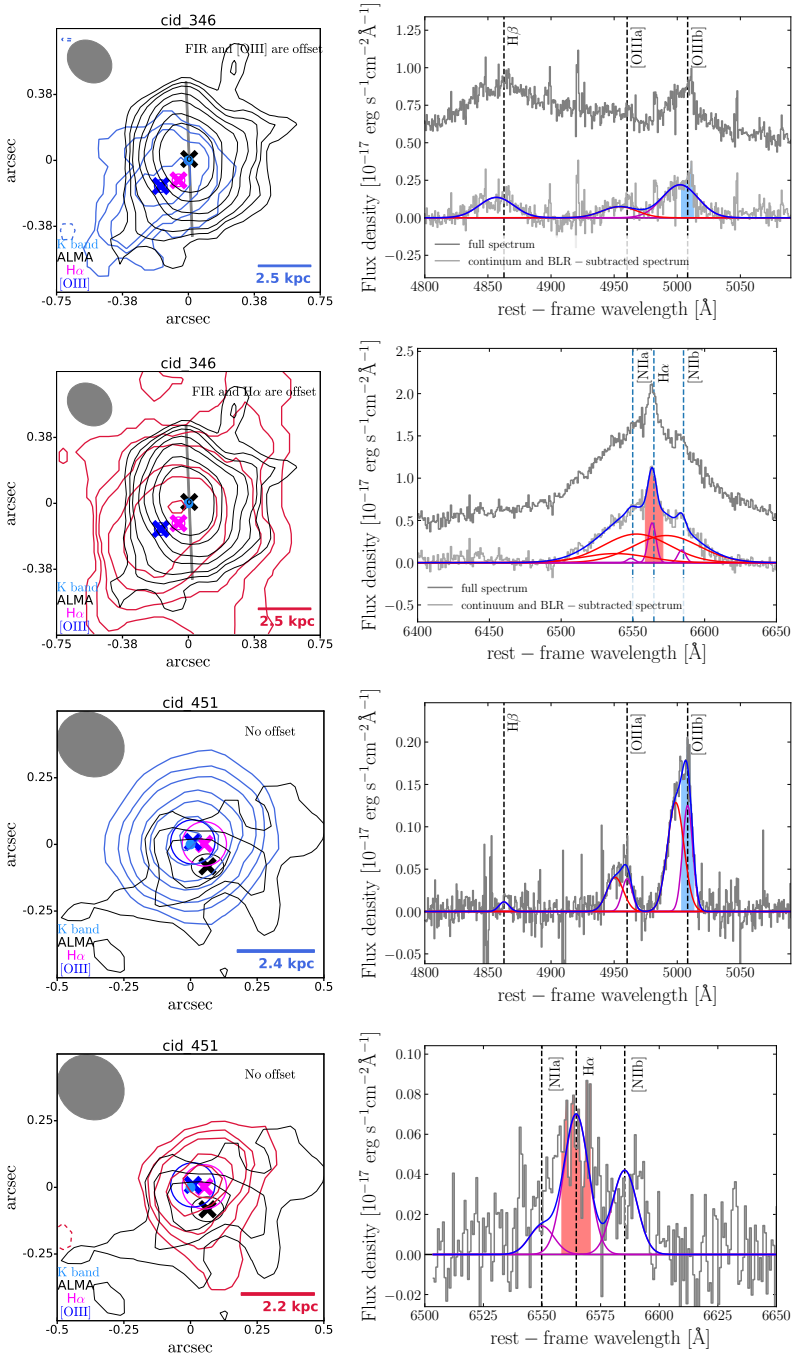

Figure 5.3. – continued.

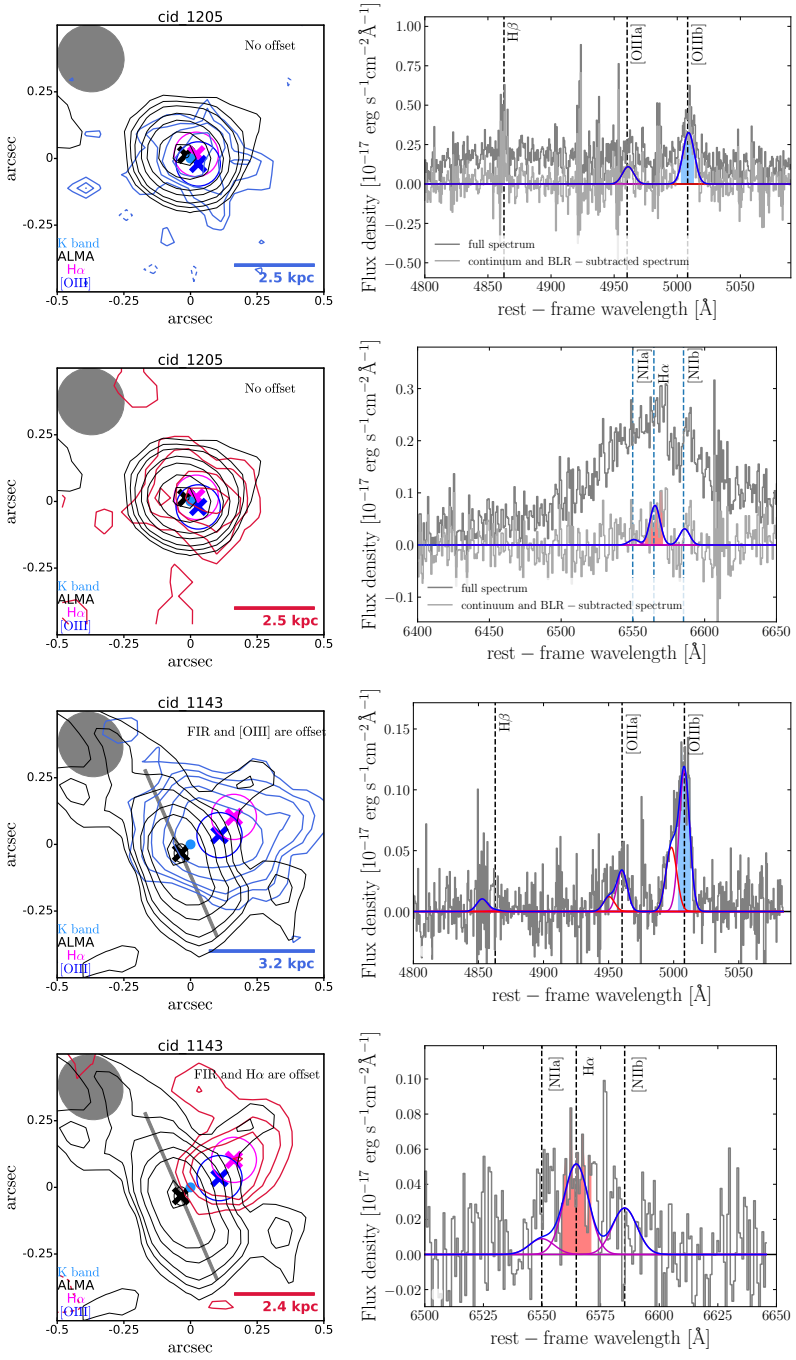

Figure 5.3. – continued.

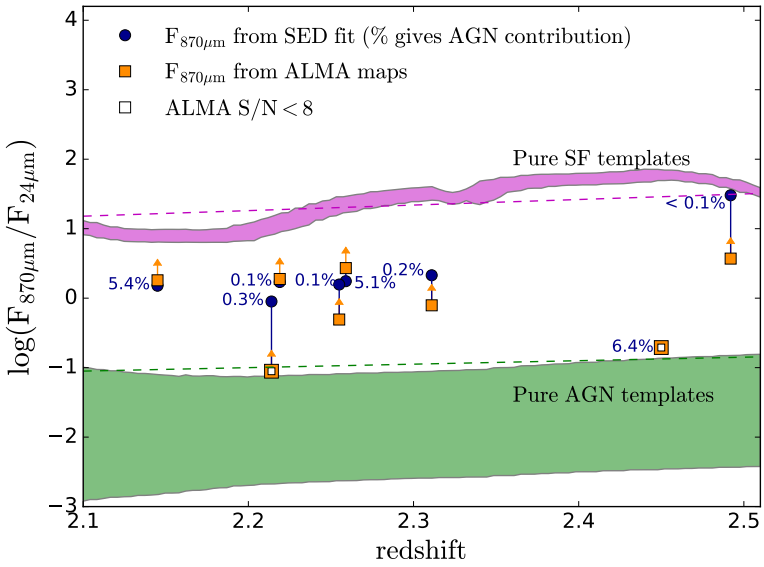

Figure 5.4. Ratio of 870 μm to 24 μm flux as a function of redshift for our targets. In orange we show the ratios calculated using the measured $F_{870\mu m}$ from the ALMA maps and in blue the ratios calculated using the $F_{870\mu m}$ from the best model SED fit. The ALMA points are marked as lower limits because it is possible that part of the 870 μm flux is resolved out in our high-resolution observations (see discussion in Sec 5.4.1). The two sources with peak S/N$<$ 8 in the ALMA maps are marked with empty symbols (cid_1057 and cid_451). The numbers show the percentage AGN contribution at 870 μm estimated by taking the ratio of the AGN component 870 μm flux to the total 870 μm flux of the modelled SED. The dashed lines show the median flux ratio as a function of redshift for SF templates (magenta) and AGN templates (green) from Stanley et al. (2018). The shaded areas show the range of flux ratios obtained from the SF (magenta) and AGN (green) templates used to fit our ALMA targets.

and to determine the dominant source of emission.

We consider first a diagnostic to estimate the AGN contribution in the FIR that does not rely directly on our specific SED fits. Following Stanley et al. (2018), this method focuses on the ratio of FIR (870 μm) to MIR (24 μm) flux (observed wavelengths). AGN have a stronger MIR emission compared to star-forming galaxies, due to emission from hot dust in the torus. Therefore, looking at the flux ratio $F_{870\mu m}/F_{24\mu m}$, it is possible to assess whether the SED is dominated by AGN emission in the $24-870$ μm regime. In Figure 5.4, we show the $F_{870\mu m}/F_{24\mu m}$ flux ratios as a function of redshift for our sample. To compute the flux ratios, we use the 24 μm *Spitzer*/MIPS fluxes from the photometric catalog by Circosta et al. (2018) and our measurements of the 870 μm fluxes. Our high-resolution ALMA observations cannot recover the more diffuse, extended flux, therefore it is likely

that the 'total' flux of our targets is higher than the measured flux (see Section 5.2.3). Thus, we should consider the $F_{870\mu m}/F_{24\mu m}$ values as lower limits. We also show the flux ratios obtained using the $F_{870\mu m}$ inferred from the best SED fit model, which in some cases may provide a better estimate of the 'total' flux. We note that for the targets with the measured $F_{870\mu m}$ larger than the prediction from the SED fit (by $\sim 10-50\%$), we can probably consider the measured ALMA flux to be the total flux. On the figure, we show the curves corresponding to the average star-formation (SF) only template and the average AGN only template from Stanley et al. (2018). They use AGN templates from Mullaney et al. (2011) and SF templates from Mullaney et al. (2011) and Silva et al. (1998). We also show the range of flux ratios obtained from the SED fit of our objects by Circosta et al. (2018) using AGN models from Fritz et al. (2006) and SF templates from Dale et al. (2014).

All our targets are in the region between the SF and AGN templates, suggesting that the $24-870$ μm emission is produced by a mixture of star formation and AGN. The only two targets which are close to the AGN-dominated region of this diagram are cid_1057 and cid_451. These two targets are those with low SNRs in the 870 μm data (S/N$<$ 8). This is probably reflecting the uncertainty in the measured $F_{870\mu m}$ fluxes and the higher fraction of flux that is resolved out in the ALMA observations, rather than suggesting a higher AGN contribution. In particular for cid_1057, the $F_{870\mu m}/F_{24\mu m}$ flux ratio inferred from the SED fit is a factor of ten higher.

To provide a more quantitative estimate of the contribution of the different physical processes to the 870 μm flux, we also analyse the results of the UV-to-FIR SED fitting from Circosta et al. (2018). We gave a description of the SED fitting method in Section 5.1. The MIR to FIR spectral range is modelled with two main components: emission by cold dust heated by star-formation and AGN emission due to the dusty torus peaking in the MIR. To estimate the AGN contribution to the 870 μm flux, we consider the ratio between the AGN component and the cold dust emission due to star-formation at 870 μm. In Figure 5.5, we show as an example the SED of one target (XID36). The SEDs of the other targets are shown in Figure 10.2 in Appendix D. The AGN contribution to the total flux ranges from 0.001% (for cid_1143) to 6.4% (for cid_451), with a mean of 2%. Therefore the results of the SED fitting decomposition suggest that most of the emission at 870 μm is due to star-formation rather than heating from the AGN. For the two targets with low SNRs in the 870 μm data (cid_1057 and cid_451), which are close to the AGN-dominated

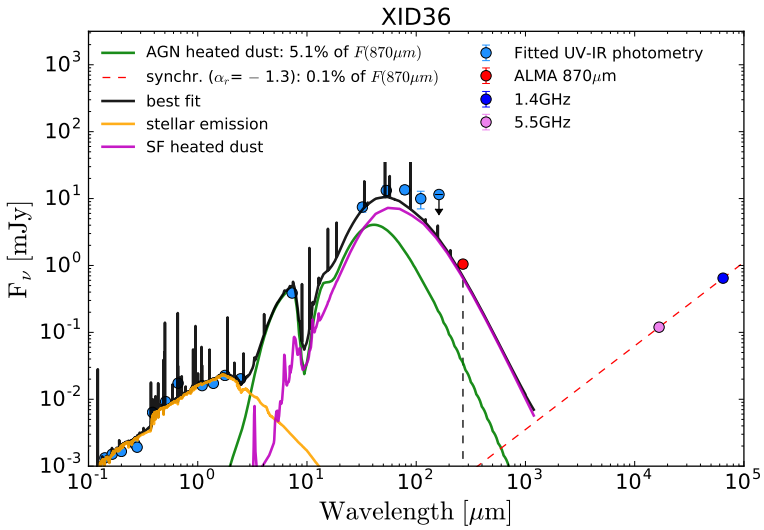

Figure 5.5. Example rest-frame spectral energy distribution (SED) of one of our targets (XID36). The light blue data points represent the UV-IR photometry that was used for the SED fitting Circosta et al. (2018). The arrows indicate 3σ upper limits. The red point shows our ALMA Band 7 flux measurement, which has not been used for the SED fit. The blue and pink points show the radio fluxes at 1.4 and 5.5 GHz, respectively. The solid curves show the results of the SED fitting with `CIGALE`: in black is the total best-fit model (including the contribution the from nebular emission component), in orange the dust-attenuated stellar emission, in magenta the emission from dust heated by star-formation and in green the emission from dust heated by the AGN. To estimate the maximum contribution of synchrotron emission to the 870 μm flux density, we parametrized this emission as a power law with spectral index $\alpha_r = -1.25$ (dashed red line), derived based on the 1.4 and 5.5 GHz data. On the plot we show the estimated contribution (in percentage) from dust heated by the AGN and from synchrotron emission to the 870 μm flux estimated from the dust emission template.

region of the diagnostic diagram from Stanley et al. (2018), the SED fitting would imply that the AGN only contributes 0.3% and 6.4%, respectively, to the 870 μm flux.

Although we are limited by photometric coverage at long wavelengths in most of the SEDs, which makes the exact percentage of the AGN contribution uncertain, our analyses all indicate that the contribution from dust heated by the AGN to the 870 μm emission, and hence our maps produced from the ALMA data, is minimal.

In AGN, synchrotron emission can also contribute to the 870 μm flux, in particular in sources classified as 'radio loud' (e.g., Dicken et al. 2008; Falkendal et al. 2019). All our targets have flux measurements or 3σ upper limits at 1.4 GHz and/or 3 GHz obtained with the Very Large Array (VLA). The radio fluxes were collected by Circosta et al. (2018). Briefly, the two sources from E-CDF-S (XID36 and XID419) have 1.4 GHz fluxes from

Miller et al. (2013). XID36 has an additional flux measurement at 5.5 GHz taken with the Australia Telescope Compact Array (ATCA) from Huynh et al. (2012). X_N_81_44 has a 1.4 GHz flux upper limit from the VLA's FIRST survey (Becker et al. 1995). The sources from COSMOS have flux measurements from the 3 GHz VLA-COSMOS project (Smolčić et al. 2017). Two targets (cid_346 and cid_451) have also a measurement at 1.4 GHz from Schinnerer et al. (2007).

To estimate the contribution to the ALMA Band 7 flux, we extrapolate from the radio fluxes using a power-law to model the synchrotron emission (Dicken et al. 2008). For the sources that have two flux measurements, we use the slope between the two points to determine the spectral index α_r. For the five targets with only one flux measurement in the radio, the contribution from synchrotron emission is small ($< 11\%$) even assuming an extreme value of $\alpha_r = 0$, following Dicken et al. (2008). For cid_346, we measure a spectral index $\alpha_r = -0.98$ and the contribution from synchrotron emission is 0.04%. For XID36 we measure a spectral index $\alpha_r = -1.25$ and a contribution of 0.10%.

The exception is cid_451, which is classified as a radio loud AGN. For this object, the 3 GHz flux is higher than the 1.4 GHz flux. Using the ALMA Band 3 flux at ~ 100 GHz from C. Circosta et al. (2020, submitted) and the 3 GHz flux, we estimate $\alpha_r = -0.97$ and a contribution of 23.4%. We note that this source has a low signal-to-noise in the 870 μm map (S/N= 5.5), thus, it is not included in our spatially resolved analyses.

We conclude that most of the emission at 870 μm is due to dust heated by star-formation, with contribution from dust heated by the AGN $\leq 6\%$ and synchrotron contribution $\leq 23\%$. If we consider only the six targets with high S/N in the 870 μm maps, the contribution from AGN-heated dust is $\leq 5\%$ and the synchrotron contribution is $< 11\%$. The estimated contributions for each target are tabulated in Table 5.2.

5.4.2 FIR size comparison with other samples from the literature

In this section, we compare the FIR sizes of our sample with other samples of galaxies at similar redshift from the literature. We also investigate if there is any difference in the size of galaxies with and without an AGN. From our analysis, we find that the FIR effective radii derived from the fit with the 'preferred models' for our sample are in the range $0.80 - 2.13$ kpc, with a mean of 1.40 ± 0.23 kpc. These sizes are comparable to previous measurements presented from ALMA data for $z \sim 1 - 3$ AGN and star-forming galaxies (Barro et al. 2016; Hodge et al. 2016; Fujimoto et al. 2017; Gullberg et al. 2019;

Scholtz et al. 2020; Chen et al. 2020).

We investigate in more detail how our sizes compare to other samples in Figure 5.6, where we plot size as a function of 870 μm flux density. We show the 6/8 sources with high SNRs in our sample. For the sake of a more direct comparison to literature, we show the sizes from our exponential and Gaussian fits (see Section 5.2.3; Appendix 10.1), noting that these are consistent with the sizes derived from our 'preferred' models.

For this comparison, we identify five samples of sub-millimetre galaxies (SMGs) and AGN with i) similar redshift range to our sample ($z \sim 1.5-2.5$) and ii) FIR sizes measured from high-resolution (< 0.5") ALMA Band 7 continuum data: Hodge et al. (2016), Gullberg et al. (2019), Scholtz et al. (2020), Chen et al. (2020), and Tadaki et al. (2020). We consider only the sources detected with S/N> 8 (following Scholtz et al. 2020), for which it is possible to derive reliable sizes. In Table 5.4 we summarize the main properties of the literature samples (sample size, redshift, resolution and RMS sensitivity of the ALMA maps, and the model used to derive the FIR sizes).

The first sample consists of 16 SMGs from the ALESS survey (Hodge et al. 2013; Karim et al. 2013), whose FIR sizes are reported in Hodge et al. (2016). We consider the SMGs in the redshift range $z = 1.5 - 2.5$ (6 objects). Based on X-ray data (Wang et al. 2013), only one object (ALESS17.1) is confirmed as AGN. We note that two of the targets have X-ray luminosities $L_X(0.5 - 8keV) > 10^{42.2}$ erg/s, which could be due both to AGN or to star-formation.

The second sample is presented by Gullberg et al. (2019). They measure the FIR sizes from Sérsic/exponential fits for 153 SMGs from the ALMA SCUBA-2 UDS survey (AS2UDS Stach et al. 2019). Using MIR diagnostics, Stach et al. (2019) identified one third of the sample as AGN and one third as non AGN, with the final third having insufficient MIR photometry for this classification. Using stacking analyses, Gullberg et al. (2019) showed that their measured individual sizes underestimate the true sizes by $\sim 50\%$ due to the relatively low RMS (median of 0.3 mJy/beam compared to our mean 0.02 mJy/beam). Therefore, in Figure 5.6, we just show their derived median size which is corrected for this effect.

The third sample is presented in Scholtz et al. (2020) and consists of eight X-ray AGN at $z = 1.4 - 2.6$ from the KMOS AGN Survey at High-redshift (KASHz)[8]. We exclude

[8]We note that Scholtz et al. (2020) reported the effective radii as R_e=σ=FWHM/2.355. For our comparison, we convert their size measurements to R_e=FWHM/2, to be consistent with our definition.

Table 5.4. Properties of the literature samples used to compare the FIR sizes (see Section 5.4.2). (1) Number of objects considered in our comparison. (2) Redshift of the sources. (3) RMS sensitivity of the ALMA 870 μm maps. (4) Resolution of the ALMA 870 μm maps. (5) Model used to measure the FIR sizes. (6) Mean FIR size (half-light radius) derived from the 870 μm data.

Reference	N	z	RMS [mJy beam^{-1}]	resolution [arcsec]	model	$< R_e >$ [kpc]
	(1)	(2)	(3)	(4)	(5)	
This work	6	2.1-2.5	0.02-0.04	0.16-0.27	exp. (Gaussian)	1.31±0.23 (0.93±0.23)[a]
Hodge et al. (2016)	6	1.5-2.5	∼0.064	∼0.16	exp./Gaussian[b]	1.48±0.08
Gullberg et al. (2019)	153	1.5-5.8 (median 2.9)	0.09-0.34	∼0.18	exponential	1.20±0.4
Scholtz et al. (2020)	4	1.4-2.6	0.02-0.69	0.16-0.28	Gaussian	0.97±0.24
Chen et al. (2020)	4	1.5-2.5	0.03-0.07	0.17-0.25	Gaussian	1.67±0.22
Tadaki et al. (2020)	62	1.9-2.6	∼0.06	0.20-0.30	exponential	1.56±0.12

[a] For our work, we report the mean R_e obtained using both the exponential and the Gaussian model. [b] Hodge et al. (2016) fit the sample assuming a Sérsic profile with index n free. The six SMGs with $z = 1.5 - 2.5$ have FIR profiles between Gaussian and exponential (Sérsic index $n = 0.5 - 1$).

from the comparison two targets with low resolution ALMA data (beam size > 0.5") and two targets with S/N< 8.

Moreover, we consider the sample of six SMGs in the redshift range $z = 1.5 - 2.5$ presented by Chen et al. (2020). Three objects are classified as X-ray AGN, one as infrared AGN, and two as non-AGN. Two targets are also present in the sample from Hodge et al. (2016) and have consistent size measurements, thus we consider them only once in our comparison.

Finally, we consider the sample of 62 massive ($M_* > 10^{11}$ M$_\odot$) star-forming galaxies at redshift $z = 1.9 - 2.6$ from Tadaki et al. (2020). X-ray data for this sample are available from Luo et al. (2017) and Kocevski et al. (2018). Based on a threshold of intrinsic X-ray luminosity $L_X > 10^{42}$ erg s^{-1}, 13 objects are classified as AGN.

The mean effective radius obtained with the exponential fit for our sample (1.31 ± 0.23 kpc) is consistent with the mean sizes from Hodge et al. (2016) (1.48 ± 0.08 kpc), Gullberg et al. (2019) (1.2 ± 0.4 kpc), and Tadaki et al. (2020) (1.56 ± 0.12 kpc), that also used the exponential fit. Using the Gaussian fit, we obtained a mean radius of 0.93 ± 0.12 kpc, which is consistent with Scholtz et al. (2020) (1.14 ± 0.29 kpc) and a bit smaller than the mean size from Chen et al. (2020) (1.67 ± 0.22 kpc), both obtained assuming a Gaussian profile. We note that our sample has a smaller range of flux densities ($F_{870\mu m} = 0.3 - 2.6$ mJy) compared to the other samples ($F_{870\mu m} = 0.7 - 9.0$ mJy), which include also SMGs, i.e. galaxies selected because of their high submm flux.

We also separate the sample in AGN and non-AGN (see open and filled symbols in Figure 5.6), to investigate whether there is a difference in their FIR sizes. We consider the sizes measured assuming a Gaussian profile, to use a consistent method for all samples. We note that if we were to use the sizes measured with the exponential profile fit, we would obtain the same qualitative results. We exclude from this analysis the sample from Gullberg et al. (2019), for which we only have the 'median' size of the sample that includes both AGN and non-AGN.

The mean size for AGN is 1.16 ± 0.11 kpc, while the mean size for non-AGN is 1.69 ± 0.13 kpc. Applying the two-samples Kolmogorov-Smirnov test, we find that the distribution of sizes for the AGN and non-AGN are significantly different ($p-$value$= 0.03$). We note that the AGN sample has a low mean flux density ($F_{870\mu m} = 2.0 \pm 0.3$ mJy) compared with the non-AGN sample ($F_{870\mu m} = 2.8 \pm 0.2$ mJy). Therefore, it is possible that the difference in FIR sizes is partly related to the difference in flux density, and not

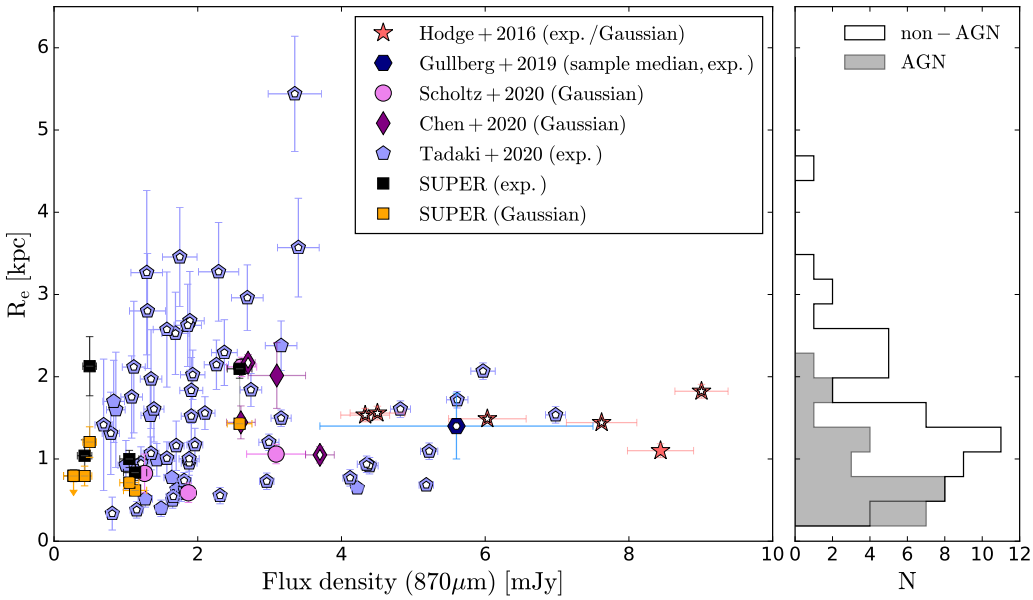

Figure 5.6. FIR effective radii versus observed 870 μm flux density for our targets and other samples from the literature at similar redshift ($z \sim 2$), derived from ALMA observations at similar resolution (< 0.5"). The effective radii are measured assuming a Gaussian profile for the Scholtz et al. (2020) and Chen et al. (2020) samples; an exponential profile for the Gullberg et al. (2019) and Tadaki et al. (2020) sample; and a Sérsic profile with index n between Gaussian and exponential for the Hodge et al. (2016) sample. For the Gullberg et al. (2019) sample, we show the median value of the sample. For SUPER, we show the radii measured from the fit of the visibilities assuming both a Gaussian and an exponential profile. Filled symbols are used for AGN and empty symbols for galaxies with no AGN signature. The Gullberg et al. (2019) sample is a mixture of AGN and non-AGN. The histograms on the right show the distributions of FIR effective radii for AGN (filled histogram) and star-forming galaxies with no AGN (empty histogram).

to the presence of an AGN. To test this, we limit the samples to object with flux densities < 4 mJy, and we find that the difference between AGN and non-AGN becomes even larger: the mean size for AGN is 1.19 ± 0.11 kpc and for non-AGN is 1.80 ± 0.16 kpc.

Some previous studies found smaller sizes in galaxies hosting AGN. For example, Lutz et al. (2018) find smaller FIR sizes in nearby ($z < 0.06$) X-ray selected AGN than in non-AGN at the same FIR luminosity. They interpret this result as a support of the AGN-host co-evolution scenario in which the same gas reservoir is fuelling both the central black hole and the central star-formation. Chang et al. (2020) also find smaller FIR sizes in obscured IR-selected AGN compared to non-AGN at $z \sim 1$. Recently, Ni et al. (2020) report a relation between the black hole accretion rate and the compactness of the host galaxy.

They also interpret this relation as a link between the black hole growth and the central gas density.

In order to confirm our results, it would be important to have a control sample matched in SFR, stellar mass, redshift and with similar FIR sensitivity and resolution.

5.4.3 Ionized gas and FIR emission

Comparison of spatial distribution of FIR, optical, Hα, and [OIII] emission

In this section we compare the spatial distribution of the FIR, optical, Hα and [O III] emission. In Figure 5.3, we showed the FIR continuum contours, with overlaid the [O III] and Hα contours, created using the 'central' 600 km s^{-1} wide maps. We measure the positions of the FIR, Hα and [O III] emission by fitting a 2D Gaussian to the images using the python routine `scipy.optimize.curve_fit` (see Sec. 5.3.4). The positions of the centroids are plotted as crosses on the images, with circles indicating the corresponding uncertainties. The position of the rest-frame optical continuum (see Section 5.3.2) is also shown in lightblue.

In Figure 5.7 we directly compare the difference in position between the FIR continuum, optical continuum, Hα and [O III] emission. The two targets with low S/N in the ALMA maps are marked with empty symbols. The uncertainties are computed by adding in quadrature the uncertainties from the 2D Gaussian fit, from the registration of coordinates of the SINFONI maps and from the pixel size.

The rest-frame optical is in general agreement with the position of the FIR continuum (see left panel of Figure 5.7). The offset between optical and FIR continuum is smaller than the uncertainties for all targets, with the exception of cid_1057 and X_N_81_44. cid_1057 has low S/N in the ALMA maps (S/N= 3.5), therefore the FIR position is not well constrained. X_N_81_44 shows an offset larger than the uncertainties, but still small ($<$ 0.05"). In the Type 1s, the optical continuum is dominated by the AGN emission, while in the Type 2s it is probably tracing the stars emission. The good alignment between the FIR continuum emission and the optical continuum suggests that the FIR is aligned with the host galaxy position. However, we do not have other information about the host galaxy morphology. For three sources, there are HST/WFC3 images available, but the images show only strong point sources, so we cannot derive any information about the host galaxy morphology.

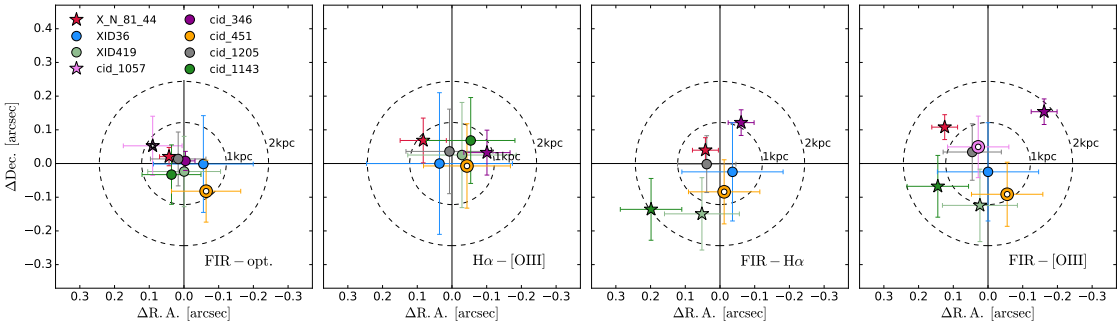

Figure 5.7. Comparison of the position of (from left to right): FIR and optical continuum, Hα and [O III] emission, FIR and Hα emission, and FIR and [O III] emission. The coordinates are derived from the centroid of a 2D Gaussian fit to the images. The Hα and [O III] images were created by integrating the spectra over the [-300,300] km s^{-1} velocity range. The uncertainties on the position combine the uncertainties on the coordinate registration, on the Gaussian fit and the pixel size. The objects with a significant offset (i.e. difference in R.A. or Dec. larger than the uncertainty) are shown as star symbols in each plot. , while the ones with no significant offset are shown as circles. The dashed circles show the offset corresponding to 1 kpc and 2 kpc at the median redshift of the sample. The two objects with ALMA low S/N$<$ 8 are shown as empty symbols (cid_1057 and cid_451).

For the majority of the sources with reliable FIR positions (4/6), the Hα and [O III] centroid positions are not consistent with the FIR position (see Figure 5.7). The offsets between the FIR and Hα position are in the range $0.3-1.9$ kpc, with a mean offset of 0.9 ± 0.2 kpc. The offsets between the FIR and [O III] are in the range $0.2-1.8$ kpc, with a mean offset of 1.0 ± 0.2 kpc. Three objects have an offset >1 kpc, both for Hα and [O III]: XID419, cid_346 and cid_1143. Scholtz et al. (2020) measured the offset between the FIR emission and the Hα emission in a sample of eight AGN at redshift $1.4-2.6$. They found projected offsets between Hα and FIR in the range $0.8-2.8$ kpc, with a mean offset of 1.4 ± 0.6 kpc. The offsets found by Scholtz et al. (2020) are a bit larger but consistent with our findings. However, we note that their observations have a lower spatial resolution (FWHM PSF $\sim 0.6-1$") compared to the AO observations presented here.

To summarise, we find that the peak of the FIR emission is typically significantly offset from the [O III] and Hα peaks. However, we note that there can still be significant overlap between the emissions even if the peaks are offset. We discuss more this point in Section 5.4.5.

The Hα and [O III] positions are in general in agreement with each other, with offsets in the range $0.3-0.9$ kpc and mean offset 0.6 ± 0.1 kpc (see second panel in Figure 5.7). Only

two objects (X_N_81_44 and cid_346) show a Hα-[O III] offset larger than the uncertainties. In X_N_81_44 the morphologies of Hα and [O III] emission are also different, extending in two almost perpendicular directions. In cid_346 instead the Hα and [O III] emissions are extended along the same axis, but while [O III] is extended only in the S-E direction, Hα is considerably extended also in the opposite direction (N-W).

For most of our targets, we find an offset between the central position of the ionized gas emission and the FIR emission. One possible explanation is that the dust and the ionized gas have different location. It is also possible that the dust is obscuring part of the Hα and [O III] emission, especially where the peak of the dust emission is located. Unfortunately, in most of our objects, we do not have a measurement of the Balmer decrement, because of the low S/N of the Hα and Hβ emission lines. However, even the Balmer decrement could underestimate the level of obscuration, because in the most obscured regions the ionized gas emission may be totally obscured by dust (see Chen et al. 2020).

In Figure 5.3, which presents the Hα and [O III] maps, we also show the position angle along the major axis of the FIR emission for the three targets where it can be reliably determined (XID419, cid_346, and cid_1143). The Hα and [O III] emission are offset from the FIR emission in a direction roughly perpendicular to the FIR major axis. This could be indicative of AGN ionization cones, extending perpendicular to the plane/main-axis of the galaxy (e.g., Crenshaw et al. 2010; Venturi et al. 2017, 2018). This would favour a scenario where a significant fraction of the ionized gas has a different location with respect to the FIR emission. However, we cannot rule out that dust is obscuring part of the ionized gas emission.

Following Chen et al. (2020) and Scholtz et al. (2020), we also compare the sizes of the FIR, Hα, and [O III] emission in Figure 5.8. We use the FIR sizes derived with the best model fit of the *uv*-visibilities. In general, the Hα and [O III] sizes are comparable or larger than the FIR sizes. The only exception is cid_1143, for which the upper limits on the Hα and [O III] sizes are smaller that the FIR sizes. We note that the FIR emission of this object is significantly elongated (axis ratio = 4.6). The mean ratios are $R_e(\mathrm{H}\alpha)/R_e(\mathrm{FIR}) = 1.54 \pm 0.19$ and $R_e([\mathrm{O\,III}])/R_e(\mathrm{FIR}) = 1.49 \pm 0.23$. Larger H$\alpha$ sizes compared to FIR sizes have also been observed by Scholtz et al. (2020), Chen et al. (2020) and Tadaki et al. (2020), who find mean ratio $R_e(\mathrm{H}\alpha)/R_e(\mathrm{FIR})$ of 3.1 ± 0.6, 2.1 ± 0.3, and 2.3 respectively.

The larger sizes of the ionized gas emission compared to the FIR sizes can be due to different reasons. One possibility is that the ionized gas is more extended because of the

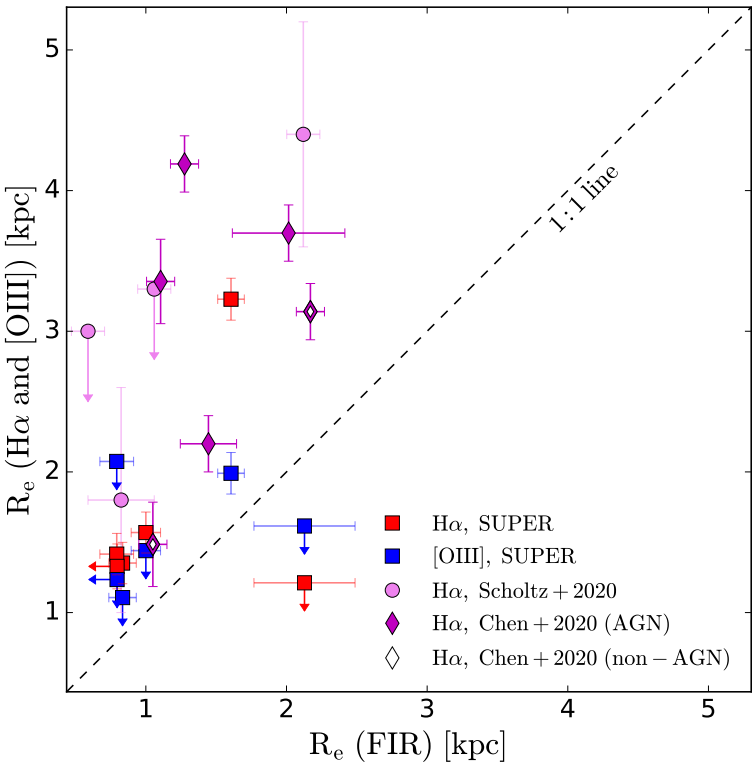

Figure 5.8. Comparison of the size of the FIR emission with the sizes of the Hα (red) and [O III] (blue) emission. The effective radii of the FIR emission are measured from the best fit on the visibilities. The Hα and [O III] sizes are measured by fitting a 2D Gaussian to the images. If the measured size is smaller than the beam, we show the point as an upper limit. The two objects with low S/N (< 8) in the ALMA data are not shown (cid_1057 and cid_451). The FIR and Hα sizes of the sample of $z \sim 2$ AGN from Scholtz et al. (2020) and from Chen et al. (2020) are shown with violet circles and magenta diamonds, respectively. The white diamonds are non-AGN from Chen et al. (2020). In general the FIR sizes are smaller than the Hα and [O III] sizes.

AGN, that ionizes the gas to larger distances (e.g. Scholtz et al. 2020). However, larger Hα sizes compared to the FIR have been observed also in star-forming galaxies not hosting AGN (Chen et al. 2020; Tadaki et al. 2020). In $z \sim 2$ star-forming galaxies, the optical continuum is found to be systematically larger than the FIR sizes by a factor of $2 - 3$, suggesting that the FIR emission is tracing a compact star-burst region (e.g., Barro et al. 2016; Tadaki et al. 2017; Elbaz et al. 2018; Fujimoto et al. 2017, 2018; Lang et al. 2019).

However, we cannot exclude that the FIR sizes are underestimated because the high-resolution ALMA observations are not sensitive to more diffuse emission.

Origin of the Hα emission

The Hα emission can be used to trace the spatial distribution of the unobscured star-formation to investigate the impact of AGN outflows on star-formation (Cano-Díaz et al. 2012; Cresci et al. 2015b; Carniani et al. 2016). However, Scholtz et al. (2020) argued that Hα emission must be used with caution as a star-formation tracer in AGN hosts, since it can also be ionized by the AGN and it can suffer from significant obscuration (see also Kewley et al. 2013b; D'Agostino et al. 2019). Thus, it is important to determine what is the dominant source of the Hα emission in our sample.

For this purpose, we use a BPT-like diagram (Baldwin et al. 1981) which uses the optical line ratios [O III]/Hβ and [N II]/Hα to separate galaxies depending on the different source of ionization (HII region, Seyfert, LINER, composite). The maximum line ratios that can be produced by star-formation increase with redshift (e.g. Shapley et al. 2005; Erb et al. 2006; Liu et al. 2008; Shapley et al. 2015; Steidel et al. 2014), therefore we decide to use the redshift-dependent emission lines diagnostics derived based on theoretical models and observations by Kewley et al. (2013b,a). This curve separates the pure star-forming systems from 'composite' (AGN/star-forming) objects. We note that this diagnostics has been empirically tested only for small samples of high-redshift galaxies (e.g. Kewley et al. 2013a; Coil et al. 2015).

In Figure 5.9 we show the line ratios [O III]/Hβ and [N II]/Hα for our targets. The blue dashed curve is the separation between star-formation and 'composite' (AGN/star-forming) at the mean redshift of our sample ($z = 2.3$) from Kewley et al. (2013a). As a reference, we also show in black the $z = 0$ lines from Kauffmann et al. (2003) (separating 'pure star-forming' and composite objects), Kewley et al. (2001) (separating composite and Seyferts), and Schawinski et al. (2007) (separating LINERs and Seyferts). In five targets, the Hβ line is not detected, based on a detection threshold of S/N$>$ 3. For these objects, we derive a 5σ upper limit for their Hβ flux (see Sec. 5.3.3). In four targets, both the Hα and [N II] lines are not detected, therefore the [N II]/Hα line ratio is unconstrained.

In general, most of our objects lie on the boundary between the composite and Seyfert regions. This is not surprising, because we have selected X-ray AGN which also have a lot of on-going star-formation. For five objects the [O III]/Hβ line ratio is a lower limit. Three of them are in the star-formation region, but the lower limits do not exclude that they could be dominated by AGN emission.

Our sources lie within the scatter of the [O III]-X-ray luminosity relation derived by Kakkad et al. (2020) using data from SUPER and from X-ray selected AGN at $z \sim 1.1-2.5$ from the KASHz survey (Harrison et al. 2016a). This suggests that the [O III] emission is mainly ionized by the AGN, as traced by the X-rays. As discussed in the previous section, the central position of Hα and [O III] are in general in agreement (see Figure 5.7). Consequently, given the similar spatial distribution of Hα and [O III], probably also the Hα emission is partly ionized by the AGN. There are only two objects (X_N_81_44 and cid_346), where there is a small offset (< 1 kpc) between the peak positions of Hα and [O III]. This could suggest that the Hα emission has an additional contribution from a different source (e.g. star-formation) in these two objects.

Given the many non-detections, we cannot identify the main source of the Hα emission from the BPT analysis. Based on the line ratios, we cannot rule out that the Hα emission is contaminated (or dominated) by AGN emission. For this analysis, we have considered spatially integrated spectra, but there may be spatial variations in the line ratios and some of the emission is probably more AGN dominated (e.g., towards the centre). Unfortunately, with the current resolution we are not able to investigate spatial variations or de-couple AGN and star-formation contributions, which is possible in the local Universe (e.g. D'Agostino et al. 2019).

The fact that the Hα and FIR emission are not co-spatial has implications if we want to use the Hα emission to trace the total star-formation in the host galaxies (e.g., following Cano-Díaz et al. 2012; Cresci et al. 2015b; Carniani et al. 2016). First, the assumption that Hα emission is dominated by star-formation is likely not to be true in most cases. Second, even if we could derive the extinction correction for the Hα emission, we will still not be able to recover the total SFR of the galaxy, since we will not be sampling the same region as that covered by the FIR emission.

The FIR emission can provide information on the spatial location of the dust-obscured star-formation. However, the FIR luminosity measures the SFR averaged over longer timescales ($\sim$ 100 Myr) than the Hα luminosity ($\sim$ 10 Myr) (Kennicutt & Evans 2012). For our galaxies, we do not have a good indicator of short term star-formation. As an alternative to Hα, star-formation on short time-scales can be traced using rest-frame UV observations, which however could suffer from AGN contamination and dust-obscuration as well.

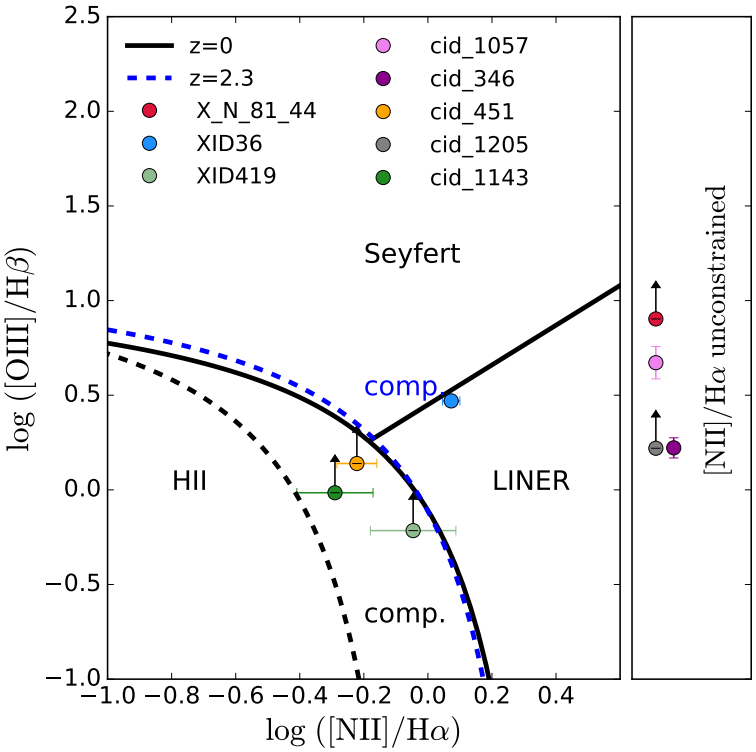

Figure 5.9. Emission lines diagnostic diagram. The blue curve shows the separation between star-forming galaxies and 'composite' (AGN/star-forming) objects at redshift $z = 2.3$ from Kewley et al. (2013b). The black curves and line show the separation between HII region, Composite, LINER and Seyfert derived at redshift $z = 0$ as indicated by the labels (Kewley et al. 2001; Kauffmann et al. 2003; Schawinski et al. 2007). For four targets, the [N II]/Hα ratio is unconstrained, due to the low S/N of the emission lines.

5.4.4 Ionized outflows and star-formation

In this section, we qualitatively compare the spatial distribution of the [O III] outflows and star-formation. As we have shown in Section 5.4.1, the 870 μm emission in our targets is mostly due to star-formation, while we cannot rely on the Hα emission as a star-formation indicator. Thus, here we focus on the spatial comparison of the outflows and FIR emission.

Following Kakkad et al. (2020), we consider as outflow the [O III] emission with absolute velocities > 300 km s^{-1} with respect to the zero velocity (see Section 5.3.4). In Figure 5.10 we show the [O III] maps in three velocity channels: blue-shifted emission < -300 km s^{-1}, central emission [-300, 300] km s^{-1}, and red-shifted emission > 300 km s^{-1}. We create the maps by collapsing the continuum subtracted spectra over the selected velocity channels for each spaxel. We check that our conclusions are not sensitive to the choice of the

threshold adopted to select the blue- or red-shifted emission (i.e. absolute velocities > 300 km s^{-1}). By selecting only the extreme velocity wings (e.g. > 600 km s^{-1}), the qualitative conclusions remain the same.

All our targets apart from cid_1205 show blue-shifted emission (above 4σ), in agreement with the analyses of Kakkad et al. (2020) on the Type 1 targets. We note that the [O III] data-cube of cid_1205 presents an artefact (horizontal stripe) in the region South of the target.[9]

The most extended blue-shifted emissions (> 4.5 kpc) are detected in cid_1143, and cid_1057. The red-shifted emission is fainter and detected above 5σ in only 5/8 objects (X_N_81_44, XID36, cid_1057, cid_451 and cid_1205). These objects show a significant extended (~ 2.5 kpc) red-shifted emission. From the [O III] line profiles, we can see that the blue-wing is generally more prominent than the red-wing. This effect can be due to dust that is obscuring the receding side of the outflow.

In cid_1143, the direction of the outflows is perpendicular to the major axis of the FIR emission. This may suggest that the outflow is moving along the path of least resistance (Gabor & Bournaud 2014). If the stellar disk is oriented as the dust emission, the blue-shifted [O III] emission can be interpreted as an outflow perpendicular to the disk. In XID36 and cid_451, the blue-shifted emission is symmetric and the shape is similar to the emission in the central velocity channel. A possible interpretation is that the outflow is aligned in the direction of our line-of-sight.

We do not see evidence that the obscured star-formation (traced by the FIR emission) is suppressed or disturbed in the location of the outflow. We discuss more this result in the next section. We do not trust Hα as a SF-tracer, however, we note that there are no signs of cavities or suppression of the Hα emission in the location of the outflow.

5.4.5 Implications of our results

The main goal of this study was to trace with high spatial resolution the star-formation in the host galaxies of AGN with powerful outflows, to assess the impact that these may have on the mass build-up of the galaxies.

[9] To remove this artefact from the data-cube, we create a map for each spectral channel and we subtract to each row its median value. Then, we recombine the channel-maps to form the data-cube. After removing the artefact, we do not see significant emission in the blue-shifted map, but we cannot exclude the presence of a faint outflow that has been suppressed when we removed the artefact. However, the [O III] spectrum of this target shows only weak emission at velocities < -300 km s^{-1}, therefore we do not expect to see a strong [O III] outflow in this target.

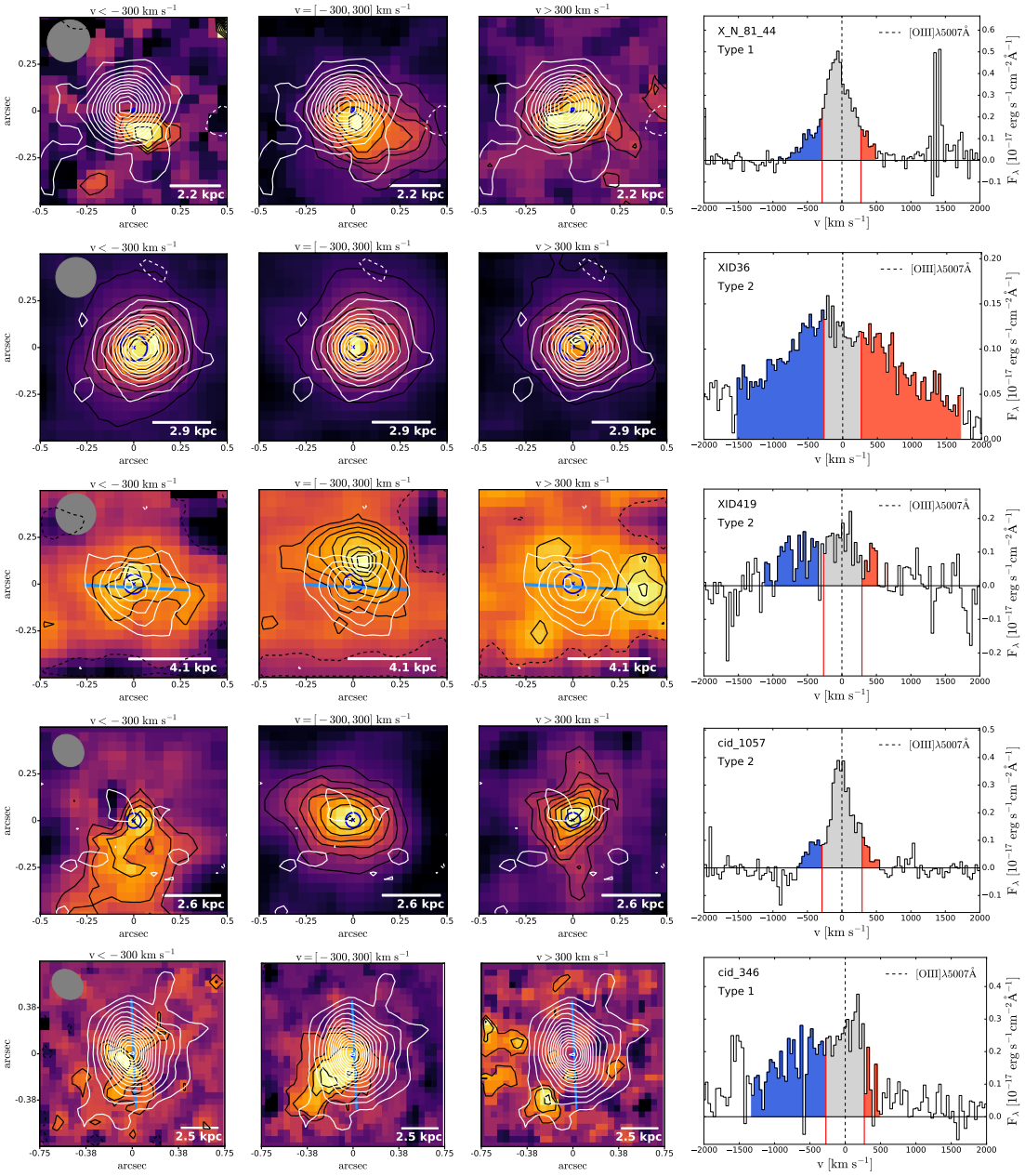

Figure 5.10. Maps of [O III] emission in three different velocity channels: blue-shifted emission (< -300 km s^{-1}, *first column*), central channel ([-300, 300] km s^{-1}, *second column*), red-shifted emission (> 300 km s^{-1}, *third column*). The interval over which the spectrum has been integrated is indicated on the right plot. In black are the [O III] emission contours starting from 2σ and increasing in intervals of 1σ (and in intervals of 2σ for XID36, cid_451 and cid_1143, to improve presentation). In white are the FIR emission contours, starting from 2σ and increasing in intervals of 2σ. Negative -2σ contours are shown with dashed curves. The grey ellipse shows the size of the ALMA beam, while the white scale-bar shows the size of the PSF of the [O III] image in kpc. The blue cross and circle show the position and uncertainty of the optical continuum. The lightblue bar indicates the position angle along the major axis of the FIR emission, when it can be reliably determined (see Section 5.2.3). *Fourth column:* spectrum around the [O III]λ5007 emission line. The coloured areas show the spectral regions over which the emission was integrated to create the three images on the left.

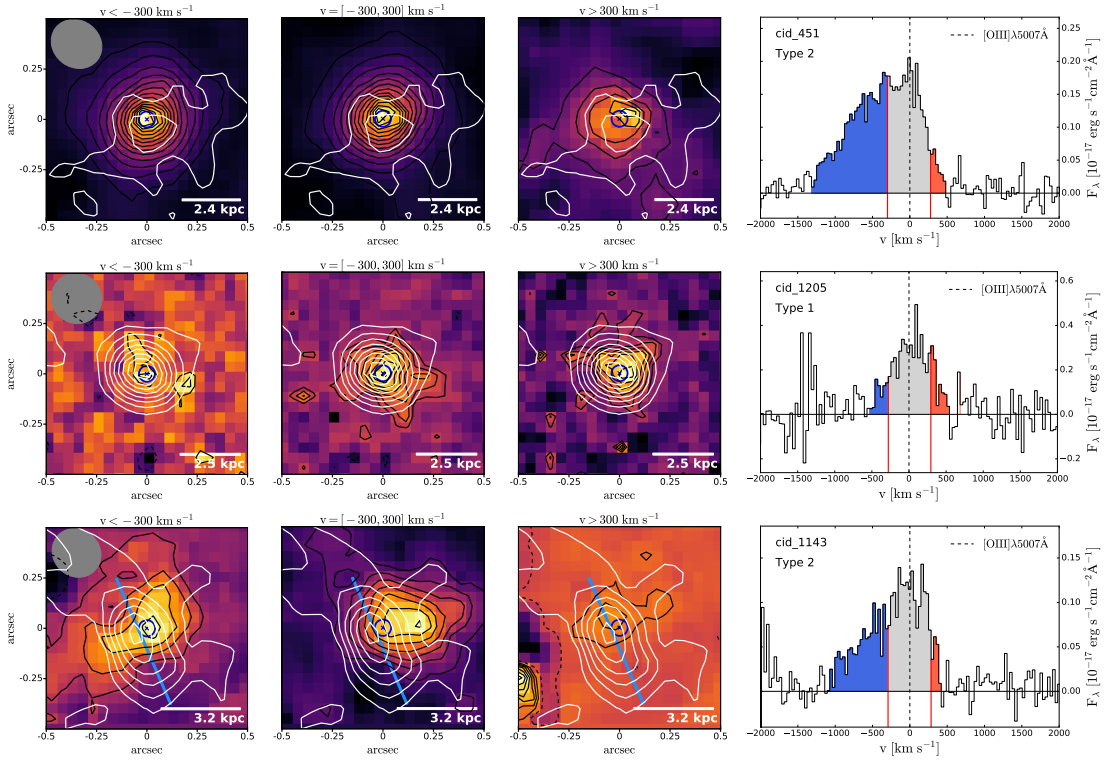

Figure 5.10. – continued.

We originally planned to combine the FIR-traced star-formation (not affected by dust obscuration and sampling time scales of $\sim$ 100 Myr), with that derived using Hα emission (which is prone to dust obscuration, but samples shorter timescales $\sim$ 10 Myr). Unfortunately, our analysis suggests that in our sample Hα cannot be used as a reliable tracer of SFR (see Section 5.4.3). From the optical emission line ratio diagnostics, we cannot rule out the possibility that the AGN is contributing to the Hα emission. However, due to many upper limits on the emission line fluxes, for most of the targets we cannot determine whether the AGN or star-formation is dominating the Hα emission.

In Section 5.4.4 we compared the spatial distribution of the [O III] outflows and FIR emission. We did not see any evidence for suppression of star formation, e.g., through cavities or 'holes' in the FIR emission. The Hα emission also do not show signs of cavities or suppression due to the outflows, as has been presented in the literature by Cresci et al. (2015b) (but see Scholtz et al. 2020).

In the context of galaxy evolution, we do not see evidence for suppression of star-formation due to AGN ionized outflows on the relatively long time-scales probed by the FIR observations. We note that in order to have a good understanding of the star-

formation in AGN hosts, it is necessary to also have a good tracer of star-formation on short time-scales (e.g. UV).

It is also possible that the outflow needs some time to produce an effect on the star-formation. Thus, there is a delay between the moment the outflow is visible and when the star-formation decreases. Episodes of AGN activity happen on shorter time-scales compared to time-scales of star-formation variations (Gabor & Bournaud 2014; Hickox et al. 2014). The outflow may need more time to remove a substantial quantity of gas from the host galaxy and to cause a suppression of star-formation. Simulations by Gabor & Bournaud (2014) show that AGN-driven outflows do not cause instantaneous quenching, but they may remove a substantial amount of gas on long time-scales ($\gtrsim 1$ Gyr) . Recently, Costa et al. (2020) found that AGN feedback acts in two modes in their simulations: a rapid mode that removes dense gas from the nucleus, and a slower mode that prevents halo gas accretion. The first mode alone will not cause a decrease in the star-formation, but the combination of the two modes will suppress star-formation in the long-term.

An additional limitation of our study is the resolution of our observations. We do not see signs of star-formation suppression at the scales probed by our observations (~ 2 kpc), but it is possible that the impact of the outflows is only visible at smaller scales. Outflows may influence star-formation only in a small region of the galaxy, on scale < 1 kpc (e.g., Croft et al. 2006; Alatalo et al. 2015; Cresci et al. 2015a; Querejeta et al. 2016; Rosario et al. 2019; Shin et al. 2019; Husemann et al. 2019).

We observe that, at least in two targets (cid_346 and cid_1143), the ionized gas is located preferentially perpendicular to the dust. This may indicate that the outflow is propagating following the path of least resistance. Simulations have shown that AGN-driven outflows propagate preferably away from the plane of the galaxy, avoiding dense gas regions in the galactic disk (Gabor & Bournaud 2014; Costa et al. 2014).

To interpret our results, we also need to consider how representative is our sample of the parent population. Due to the requirement to have FIR detections, our targets tend to have higher SFRs compared to the average of the parent SUPER sample, in which there are many SFR upper limits (see Figure 5.1). It is possible that if we were to target AGN with lower SFRs, we would be more likely to observe suppression of star-formation due to outflows. To test this hypothesis, it would require deep ALMA continuum observations to get spatially resolved maps of the dust continuum emission for the whole SUPER sample.

5.5 Summary and conclusions

We present ALMA Band 7 870 μm continuum high resolution ($\sim$0.2", corresponding to $\sim$2 kpc) observations of eight X-ray AGN at redshift $z \sim 2$ from the SUPER sample. The ALMA targets were selected from the parent SUPER sample based on photometric detections in the FIR (i.e. > 24 μm) and [O III] detections in the SINFONI IFU maps. The selected sample has a range of X-ray luminosities which is representative of the parent sample ($L_X = 10^{43.8} - 10^{45.2}$ erg s^{-1}). They have SFRs in the range $42 - 384$ $M_\odot$ yr^{-1} and most of targets lie within 0.3 dex of the main-sequence definition of Schreiber et al. (2015), with the exception of XID419 and cid_451 that lie slightly below (-0.5 and -0.7 dex below the MS).

The main conclusions of this work are:

- From the SED decomposition, we find that the contribution of AGN-heated dust to the total 870 μm emission is $\leq 6\%$ in our sample. The contribution from synchrotron emission is small in most of the targets ($< 11\%$), with the exception of cid_451, for which the estimated synchrotron contribution is 23%. We conclude that the major contribution to the 870 μm flux is due to dust heated by star-formation (see Section 5.4.1).

- We detect 6/8 of our targets with S/N$>$ 8 in the ALMA 870 μm continuum maps. We model the 870μm data in the visibilities versus uv-distance space using different models (point source, Gaussian, exponential profile, Gaussian+point source). From the 'best fit' models, we measure flux densities in the range $0.27 - 2.59$ mJy and half-light radii in the range $R_e = 0.80 - 2.13$ kpc (median 1.31 ± 0.23 kpc) for the 6/8 high S/N targets (Section 5.2.3).

- We compare the FIR sizes of our sample with other samples of SFGs and AGN at similar redshift, for which the FIR sizes are measured from ALMA 870 μm observations of similar resolution and sensitivity (see Section 5.4.2). Our sample is in agreement with the literature samples of Hodge et al. (2016), Gullberg et al. (2019), Scholtz et al. (2020), Chen et al. (2020) and Tadaki et al. (2020). We find that the mean FIR size of AGN ($R_e = 1.16 \pm 0.11$ kpc) is smaller than the mean FIR size of non-AGN ($R_e = 1.69 \pm 0.13$ kpc). A possible interpretation is that a compact dust/gas configuration favours the accretion to the central SMBH.

- We use the redshift-dependent BPT diagnostic diagram from Kewley et al. (2013b,a) to identify the main process responsible for gas ionization in our sample. Our objects lie between the HII and Seyfert regions (see Section 5.4.3). This means that we cannot rule out that part of the Hα emission is due to the AGN. Additionally, we find a good agreement between the spatial location of Hα and [O III] in most of the targets (see Section 5.4.3). This suggests that the same mechanism responsible for the [O III] emission, i.e. the AGN, is also partly responsible for the Hα emission. One object, X_N_81_44, shows an offset between the Hα and [O III] emission, which can be interpreted as a sign that part of the Hα emission is due to star-formation.

- In most of our targets (4/6) there is an offset between the central position of the ionized gas emission and the FIR emission. We also find that the ionized gas emission tends to be larger than the FIR emission by a factor of $\sim$ 1.5. This is further evidence that dust and ionized gas emission are not connected and that the ionized gas might be tracing the AGN ionization cones. In two sources (cid_1143 and cid_346) we observe that the ionized gas is perpendicular to the dust emission, which also suggests the presence of ionization cones.

- Comparing the position of the [O III] blue-shifted emission with the FIR emission, we find that the FIR emission is unaffected by the ionized outflow, showing no evidence for star-formation suppression due to the ionized outflows at the scale probed by our observations ($\sim$ 2 kpc). However, we do not have a resolved map of a good tracer of very recent star formation (e.g., UV emission). Additionally, we cannot rule out that the outflow needs longer time-scales to significantly affect star-formation.

  In one object (cid_1143), the outflow is almost perpendicular to the direction of the major axis of the FIR emission, which can be an indication that the outflow propagates following the path of least resistance.

A limitation of our study is that our sample has relatively high SFRs. To confirm that the ionized outflows do not have an impact on star-formation, we need to obtain spatially-resolved FIR maps also for the SUPER targets with lower SFRs. Moreover, we need a better tracer of star-formation on short time-scales to combine with the long-term SFR traced by the FIR.

Future IFU observations with higher spatial resolution (e.g., with ELT/HARMONI) will help to get spatially-resolved emission-line ratio diagnostics that will allow us to map

and identify the ionization sources of Hα in a spatially-resolved way. Additionally, we need more clear indications from simulations to predict the time-scales (and physical scales) on which we may expect impact from the outflows.

This page was intentionally left blank

Chapter 6

Conclusions and Future Work

In this thesis, we study different properties of the ISM in star-forming galaxies and AGN and how they vary with cosmic time.

We study two tracers of molecular gas: the CO(3-2) emission line and the dust mass. Our analysis of the CO(3-2)/CO(1-0) line ratio shows that CO(3-2) is a valid alternative to CO(1-0) as a tracer of molecular gas, at least in main-sequence star-forming galaxies and in local AGN. Moreover, we expand our knowledge of the dust properties of galaxies by applying Bayesian statistics to the SED fit of statistical samples of galaxies. By characterizing the variations of the dust emission with redshift and galaxy properties, we can improve the measurements of dust masses both in the local Universe and at high-redshift.

Additionally, we conduct multiple studies to asses the impact of AGN activity on the ISM. First, we investigate whether the excitation of the low CO rotational transitions can be affected by AGN activity, finding that AGN do not have a significant impact on the total CO(3-2)/CO(1-0) line ratio in the local Universe. Second, we study the FIR sizes in $z \sim 2$ galaxies, and we find that the FIR sizes tend to be smaller in AGN than in non-AGN. Finally, we investigate whether ionized outflows have an impact on the distribution of the dust-obscured star-formation in $z \sim 2$ AGN, and we do not find evidence of SF suppression in our sample. These results are important for 1) understanding the impact that AGN can have on the gas and dust in the ISM and indirectly on the star-formation in the host; 2) finding possible biases that can affect the measurements of dust and molecular gas masses in galaxies hosting an AGN.

In the following, we give a summary of the main conclusions of this work, and an overview of future projects.

6.1 Summary of this Thesis

6.1.1 CO excitation properties of nearby star-forming galaxies and AGN

In Chapter 2, we study the CO excitation properties in nearby ($z < 0.05$) star-forming galaxies and AGN. In particular, we focus on the $r_{31} = L'_{\rm CO(3\text{-}2)}/L'_{\rm CO(1\text{-}0)}$ line luminosity ratio. CO(3-2) is commonly used as a tracer of molecular gas, in particular at high-redshift. By modeling r_{31} using the code `UCL-PDR`, we find that the gas density is the main parameter responsible for the variations of r_{31}, while the interstellar radiation field and the cosmic-ray ionization rate play only a minor role.

Using the r_{31} measurements for a sample of ~ 100 star-forming galaxies and AGN, we find a trend for r_{31} to increase with star-formation efficiency (SFE). Together with the modeling results, this suggests a relation between the SFE and the gas density.

We do not find a difference in the mean r_{31} of star-forming galaxies and AGN host galaxies, when the galaxies are matched in SSFR ($< r31 >= 0.52 \pm 0.04$ for SFGs and $< r31 >= 0.53 \pm 0.06$ for AGN hosts). This is in agreement with the results from the `UCL-PDR` models, showing that X-rays can contribute to the enhancement of r_{31} only for strong X-ray fluxes and high gas densities, likely to occur only very close to the central SMBH and for very powerful AGN.

The scatter of the Kennicutt-Schmidt relation does not change significantly when using the molecular gas mass surface-density traced by CO(3-2) ($R = 0.83$) rather than by CO(1-0) ($R = 0.78$). This suggests that the CO(3-2) luminosity can be used to study the relation between SFR and molecular gas for normal SFGs at high-redshift, and to compare it with studies of low-redshift galaxies, as is common practice.

6.1.2 Dust properties of galaxies and their relations with global galaxy properties

Chapter 3 presents the study of dust properties of nearby galaxies from the JINGLE and HRS samples and their connections with other global galaxy characteristics, as for example the SFR, stellar mass and gas fraction.

To measure the dust properties, we model the FIR SED using modified black-body (MBB) models. By applying a hierarchical Bayesian approach, we are able to reduce the degeneracy between the dust temperature T and the emissivity index β.

Using the results of the single modified black-body (SMBB) fit, we investigate the relations between the dust properties, in particular T and β, and other global galaxy properties. We find a strong correlation between T and the star-formation divided by dust mass ($R = 0.73$), while β correlates with the stellar mass surface density ($R = 0.62$) and anticorrelates with the HI mass fraction (M_{HI}/M_*, $R = -0.65$). We derive linear scaling relations between these quantities that can be used to estimate T and β in galaxies with insufficient photometric data available to measure them directly through SED fitting.

In Chapter 4, we expand our analysis to galaxies at high redshift ($z = 1 - 3.5$) using the A^{3}COSMOS photometric catalog. Using simulated SEDs in the range $z = 1 - 3$, we test the ability of our hierarchical Bayesian SED fitting code to recover the input dust parameters, focusing in particular on the cold dust temperature (T_{cold}). We consider two models: a two modified black-body model (TMBB) and a combination of SMBB and power-law model (SMBB+PL, Casey 2012). We find that the TMBB model is able to recover the input T_{cold}, while the SMBB+PL model systematically overestimates T_{cold} (by $\sim 4-8$ K). The code performs better when the sample is divided in redshift bins and each bin is fitted separately, rather than when all bins are fitted together.

We apply the TMBB model to main-sequence galaxies from the A^{3}COSMOS sample, divided in five redshift bins between $z = 1-3.5$. We find a trend for T_{cold} to increase with redshift, as has been reported in the literature. However, our measured T_{cold} are smaller than the mean dust temperature measured at the same redshift by Magnelli et al. (2014) and Schreiber et al. (2018). This discrepancy can be due to the different methods used to measure T_{cold} or to the different sample selection.

We find positive correlation between T_{cold} and SFR, SSFR, and SFR/M$_{dust}$, consistent with the results obtained at $z = 0$. Since the mean SFR of our sample increases with redshift, it is not clear whether the relation of T_{cold} with redshift or with SFR is more fundamental.

6.1.3 Obscured star-formation in high-z AGN and the elusive evidence of outflows influencing star-formation

In Chapter 5, we study the dust-obscured star-formation in eight $z \sim 2$ AGN from the SUPER sample. We use ALMA 870μm (rest-frame $\sim 250\mu$m) maps with ~ 0.2" resolution (~ 2 kpc) to trace the dust emission in the FIR. Combining our sample with other samples from the literature with FIR observations at similar resolution and sensitivity, we find that AGN have mean FIR sizes ($R_e = 1.16 \pm 0.11$ kpc) smaller than non-AGN ($R_e = 1.69 \pm 0.13$ kpc). A possible explanation is that a compact configuration of the ISM in the center favours the accretion to the central SMBH.

The main aim of this project was to compare the distribution of obscured and unobscured star-formation with the distribution of ionized outflows to investigate the possible feedback effects due to the outflows. Using a redshift-dependent emission line diagnostics, we find that the Hα emission in our sample is likely due to a mixture of AGN and star-formation. Therefore, we can not rely on Hα as a tracer of unobscured star-formation. Using the FIR observations to map the dust-obscured star-formation, we do not see evidence of star-formation suppression due to the AGN ionized outflows. However, we can not rule out that AGN feedback is acting on smaller spatial scales (< 2 kpc) or on different time-scales than the ones probed by our observations.

6.2 Future work

6.2.1 Study the dust properties of AGN through Bayesian SED fitting

By applying hierarchical Bayesian statistics to FIR SED fitting, we demonstrate the power of this approach in reducing the degeneracy between fitting parameters. We use this method to study the dust properties in main-sequence galaxies and we focus in particular on the relation between the dust temperature and the star-formation activity. This approach could be applied to investigate the dust properties of galaxies hosting an AGN.

The FIR part of the spectrum is believed to be dominated by dust heated by star-formation in most AGN, and thus it is commonly used as a tracer of star-formation. However, some studies suggest that the AGN could contribute significantly to the FIR emission by heating the dust at kiloparsec scales (e.g., Symeonidis et al. 2016; Schneider

et al. 2015; Ichikawa et al. 2019). The AGN could contribute to the FIR emission in two ways: (1) direct AGN emission in UV/optical can escape without being reprocessed by the torus dust and then be absorbed by the dust in the host galaxy, 2) the infrared radiation from the torus can be absorbed and re-radiated at longer wavelengths, if the host is sufficiently optically thick (e.g., Schneider et al. 2015). Using our hierarchical Bayesian SED fitting code, we plan to expand the studies of dust properties also to galaxies hosting AGN. This will allow us to test whether the cold dust properties of AGN show any difference to the ones of star-forming galaxies at the same redshift.

Nearby AGN: The first part of the study will focus at low redshift using the BAT AGN sample. This sample is selected in the hard X-rays, thus it is not biased against obscured objects. Additionally, multi-wavelength properties of this sample are available through the BASS project[1]. *Herschel* observations for $\sim$ 300 BAT AGN were presented by Shimizu et al. (2017) and additional 850μm SCUBA-2 observations are available for a sub-sample (Rahimi et al. in prep.), giving a photometric coverage similar to the one available for JINGLE. We expect the warm component to be more prominent in AGN, due to the emission from the torus, but it is important to test whether the cold dust properties are influenced as well. By applying our hierarchical SED fitting code, we could measure the cold dust temperature and emissivity index β for this sample. The comparison of the dust properties of the BAT sample with a sample of non-AGN, as for example the JINGLE and HRS samples, will allow us to investigate whether AGN show any difference in their cold dust properties.

High-redshift AGN: This analysis can be expanded also to higher redshift using the A^{3}COSMOS sample. AGN in the COSMOS field have been identified through X-ray observations (Hsu et al. 2014; Laigle et al. 2016). Using observations and simulations of mock SEDs, we could determine how well the cold dust properties of galaxies hosting AGN can be recovered using data from A^{3}COSMOS. Additionally, we could investigate whether the cold dust properties of AGN follow the scaling relations derived for non-AGN, or whether there are any differences.

This will give useful indication also for the SUPER survey. Most of the AGN in the SUPER sample do not have a good coverage of the FIR SED. Using the A^{3}COSMOS sample, it may be possible to derive some priors on the distribution of dust temperatures and β for X-ray selected AGN at redshift $z \sim 2$. These priors can be used to infer the dust

[1] www.bass-survey.com

masses of the host galaxies of SUPER AGN. This information can be used to estimate how much obscuration we may expect in the Hα maps. Moreover, combined with the CO observations presented in Circosta et al. (submitted), we could be able to study the dust-to-molecular-gas mass ratio in these systems.

6.2.2 Impact of ionized outflows on star-formation

Our analysis of the spatially resolved star-formation properties of SUPER AGN and their connection to the outflow location was limited by some factors. In particular, the following two points need to be addressed:

- *Spatially resolved BPT diagram*: Using the integrated spectra, we find that the ionization of the gas is due to a mixture of AGN and star-formation in most of the source. Due to the low S/N of the spectra in the individual spaxels, we could not investigate in a spatially resolved way the ionisation source responsible for the Hα emission.

- *Balmer decrement*: For most of our objects, the Hβ emission line was not detected and therefore we could not use the Balmer decrement to estimate the extinction in the location of the Hα emission. Thus, we could not derive the intrinsic Hα luminosity of our targets.

To solve these issues, we would need to have deeper observations, to be able to: 1) detect Hβ and measure the Balmer decrement; 2) model the different Gaussian components (systemic and outflow) in a spatially-resolved way; 3) identify the ionization source of Hα in the different regions of the sources. We also need higher resolution to test whether the outflow is influencing the SF at smaller spatial scales. These observations will be feasible with the HARMONI integral field spectrograph, one of the first-light instruments to be mounted on the European Extremely Large Telescope (E-ELT, Theuns & Srianand 2006; Thatte et al. 2010). HARMONI will operates in the visible and near-infrared ($0.47 - 2.45$ μm) with a resolving power R ($= \lambda/\Delta\lambda$) in the range $\sim 4000 - 20000$. HARMONI could achieve a spatial resolution of < 0.01", a factor of ten better than our SINFONI observations.

6.2.3 Open questions

In this Thesis we have addressed some questions regarding the properties of the ISM, but there are other questions that remain open.

Studies of galaxies at very high redshift (> 6) report the presence of high dust masses (e.g., Morgan & Edmunds 2003; Rowlands et al. 2014; Watson et al. 2015; Knudsen et al. 2017; Laporte et al. 2017; Hashimoto et al. 2019), which are difficult to explain with current dust formation models. This problem is known as the 'dust budget crisis'. Different hypotheses have been proposed to explain these observations: different dust formation and destruction mechanisms, or systematic biases in the measurements of dust masses. For example, Fanciullo et al. (2020) suggested that the dust absorption coefficients currently used to model dust emission may over-estimate the dust masses by a factor of $2 - 20$, but additional laboratory measurements and more observational tests are necessary to confirm this hypothesis.

Several works, including our study of the A^{3}COSMOS data, have investigated the dust properties of galaxies up to redshift $z \sim 3 - 4$. However, at $z > 4$ the dust temperatures have been measured in only a handful of galaxies and have large uncertainties (see Figure 1.17 from Faisst et al. 2020). An accurate estimate of the dust temperature is crucial to measure accurate dust masses. The number of galaxies known at $z > 4$ is growing and it is now possible to study not only individual galaxies but galaxy samples (e.g., Venemans et al. 2020). Exploiting the capability of ALMA, in the next years it will be possible to observe a statistical sample of galaxies at $z > 4$ in multiple bands and derive more accurate dust temperatures and dust masses.

Another open question is the exact evolution of the cosmic density of molecular gas. Over the last few years, numerous studies focused on measuring the molecular-gas cosmic density, like for example ASPECS (Decarli et al. 2019), VLA COLDz (Riechers et al. 2019), and PHIBBS (Lenkić et al. 2020). These projects have placed constraints by measuring CO transitions, but large uncertainties remain due to small number statistics and the impact of cosmic variance, and to uncertainties in the measurements (see Figure 1.9 from Lenkić et al. 2020). Liu et al. (2019b) and Magnelli et al. (2020) expanded the available sample by including molecular masses estimated from the dust emission. However, the measurements remain limited to $\lesssim 6$ and still have large uncertainties.

By increasing the number of high redshift galaxies with molecular line and dust con-

tinuum observations and by improving the measurements of molecular gas masses, it will be possible to constrain how the molecular gas cosmic density evolve with time, eventually all the way back into the epoch of reionization. This thesis has highlighted how a detailed understanding of galaxies in the Universe today is essential if we want to shed light onto the process of star-formation in the very first galaxies.

Chapter 7

Appendix A

7.1 Optical images of the galaxies and CO spectra

In this section of the Appendix, we present the optical images and the CO(3-2) spectra of the galaxies from xCOLD GASS and BASS used in Chapter 2.

7.2 Tables

We present here the tables with the general properties and the CO measurements for the galaxies from the xCOLD GASS (Tables 7.1 and 7.2) and BASS (Tables 7.3 and 7.4) samples used in Chapter 2.

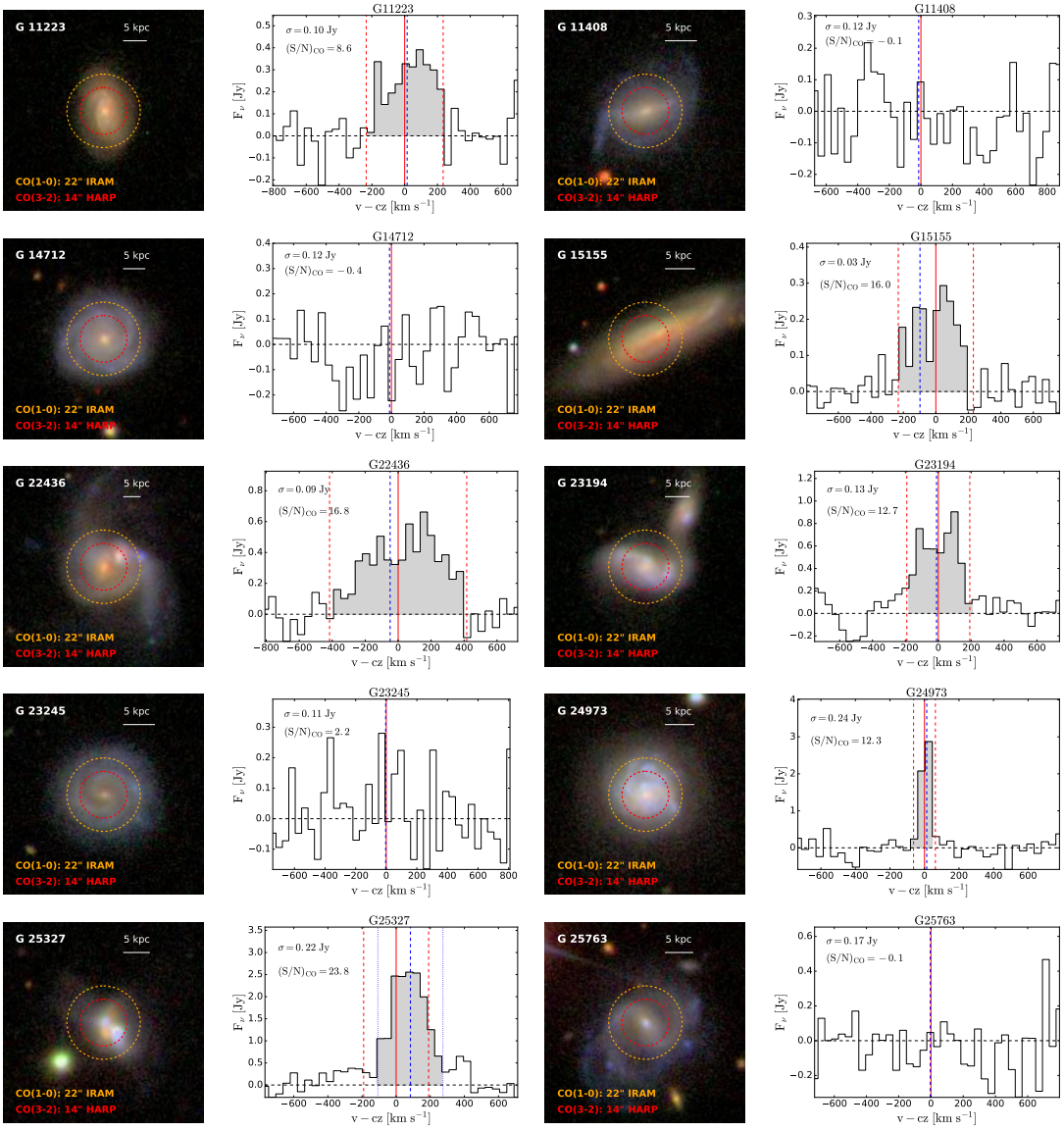

Figure 7.1. Continued from Figure 2.2 in Chapter 2. *First and third columns*: SDSS images of the xCOLD GASS sample. Every image has dimension 60" × 60" (1′ × 1′) and shows the the size of the IRAM-30m and JCMT HARP beams. *Second and fourth columns*: CO(3-2) spectra of the xCOLD GASS sample taken with HARP on the JCMT. The spectra are centred at the position of the CO(3-2) line. The solid red line is the central velocity of the line based on the spectroscopic redshift from SDSS and the dashed red lines indicate the interval where the CO(3-2) flux was integrated, based on the FWHM of the CO(1-0) line. The blue solid line indicates the central velocity of the CO(1-0) line. For the two galaxies (G7493 and G2527) where the CO(3-2) line flux was measured based on the position of the CO(1-0) line, the blue dotted line shows the interval where the CO(3-2) flux was integrated.

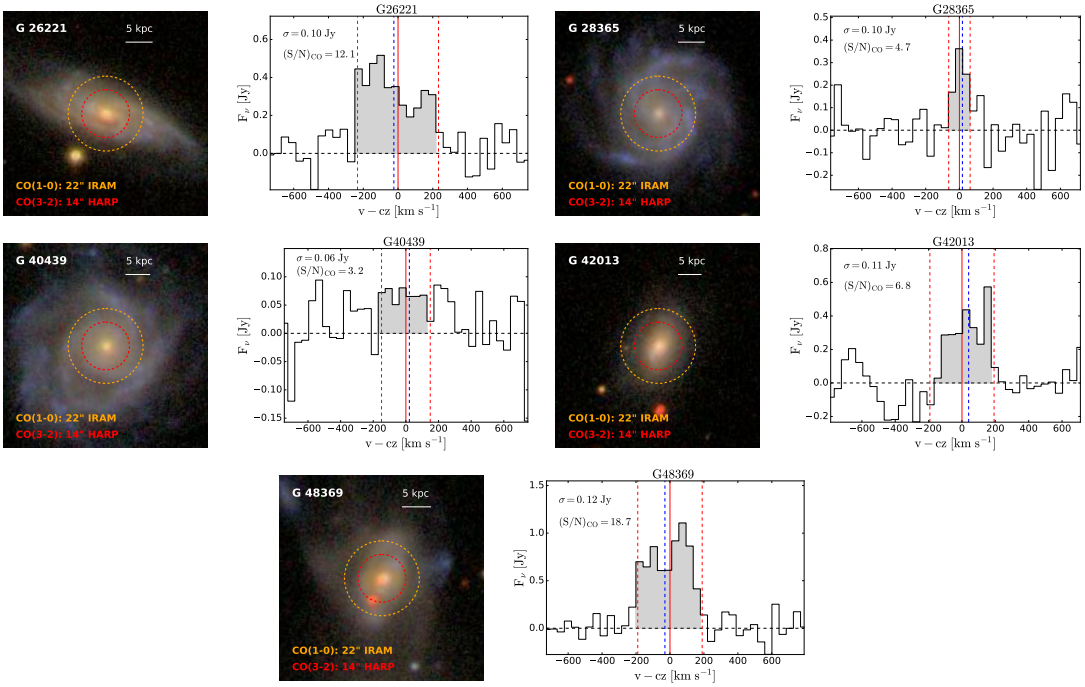

Figure 7.1. – continued.

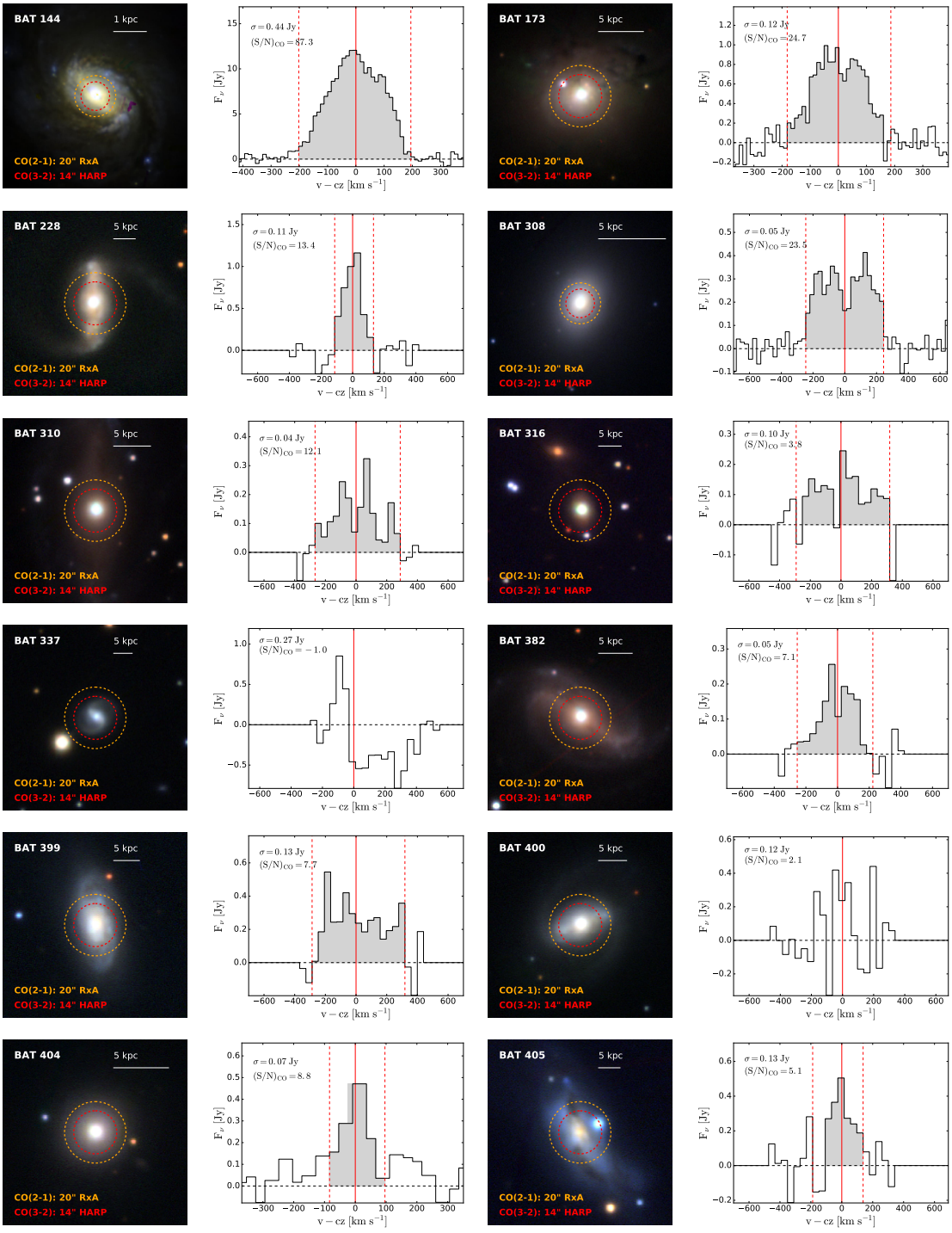

Figure 7.2. *First and third columns*: Pan-STARRS (PS1) *gri* images of the BASS sample. The images have dimensions that range from $1' \times 1'$ to $3' \times 3'$ for the larger galaxies and show the the size of the JCMT RxA and JCMT HARP beams. *Second and fourth columns*: CO(3-2) spectra of the BASS sample taken with HARP on the JCMT. The spectra are centred at the position of the CO(3-2) line. The solid red line is the central velocity of the line based on the CO(2-1) spectroscopic redshift and the dashed red lines indicate the interval where the CO(3-2) flux was integrated.

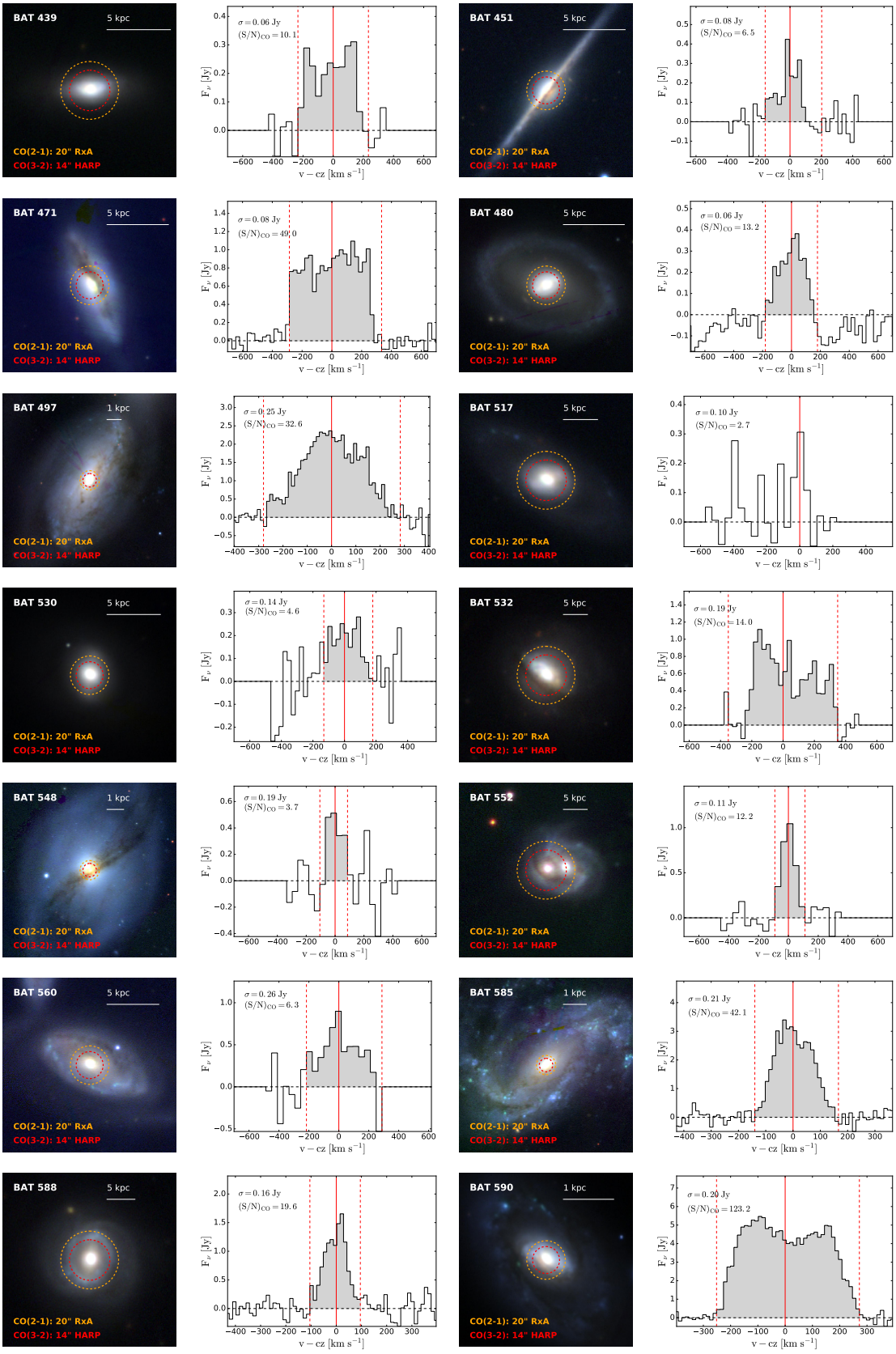

Figure 7.2. – continued.

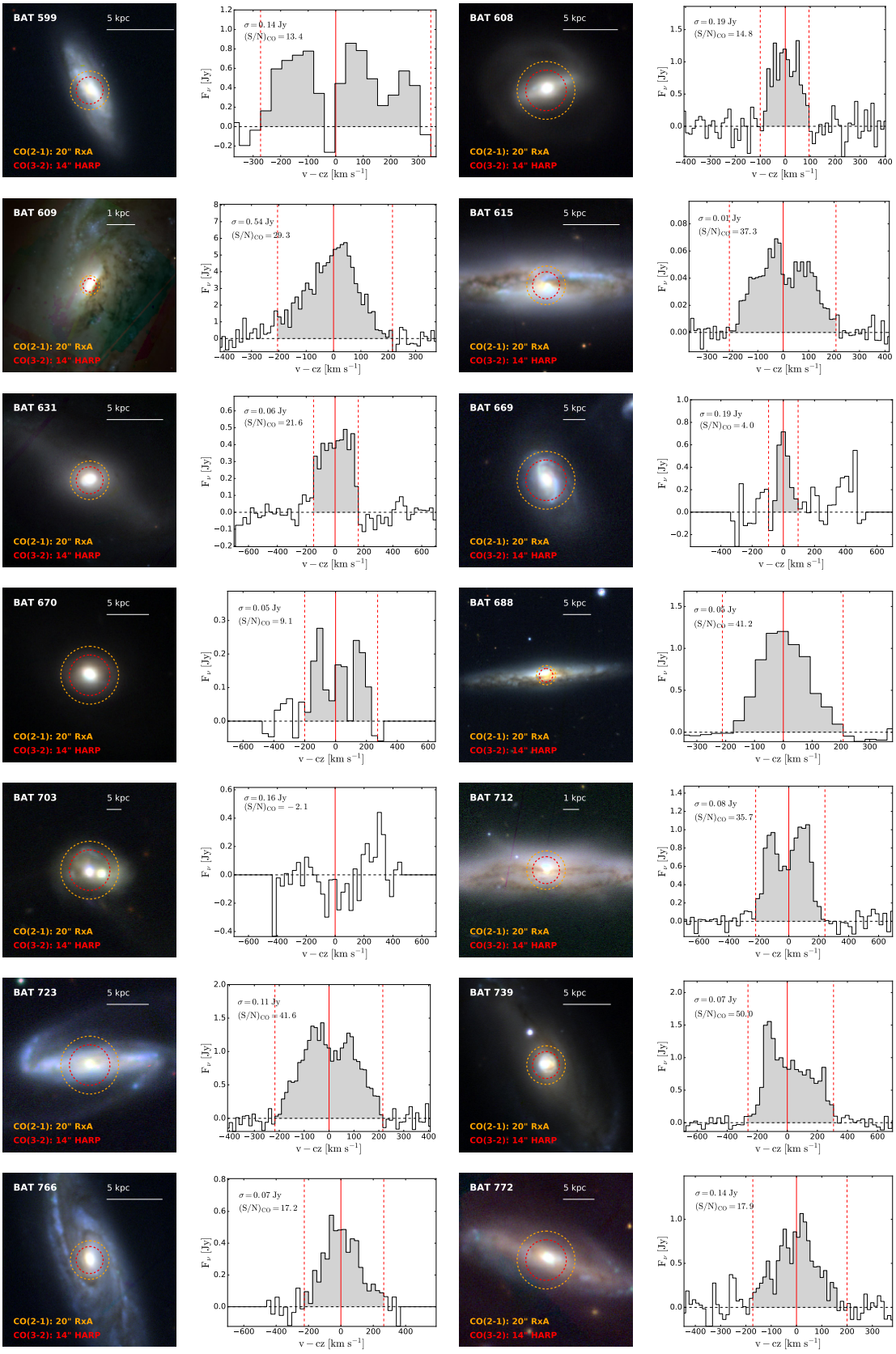

Figure 7.2. – continued.

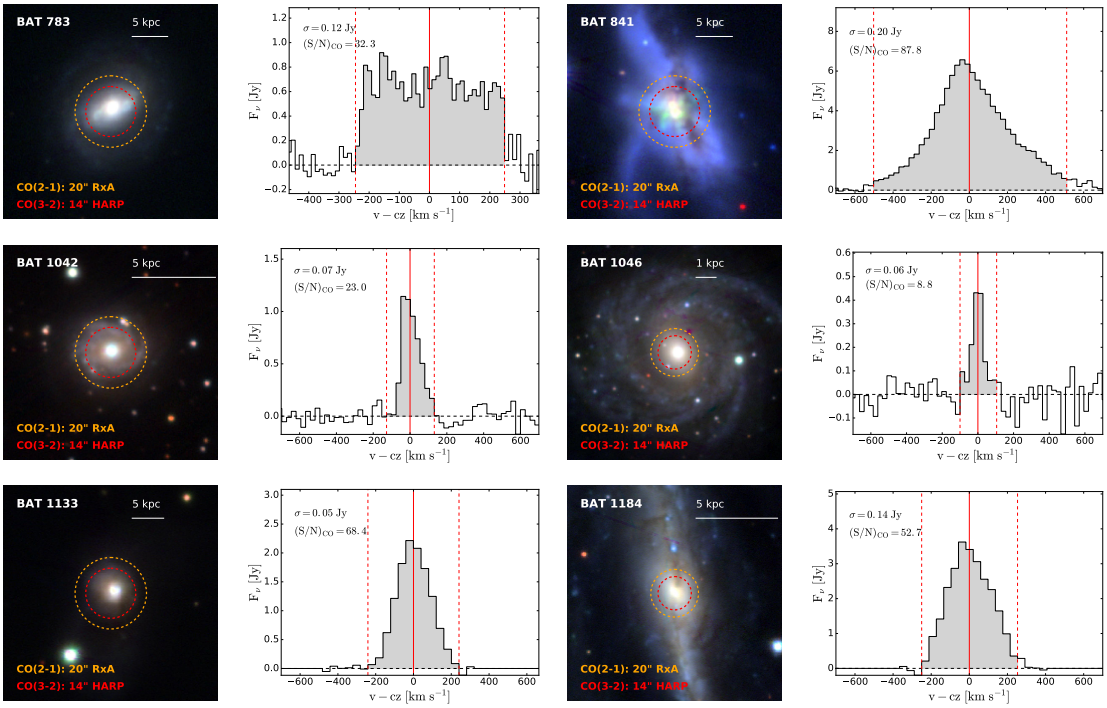

Figure 7.2. – continued.

Table 7.1. Properties of the xCOLD GASS sample.

Index	RA [deg]	Dec [deg]	z	D_{25} [arcsec]	log M_* [log $M_\odot$]	log SFR [log $M_\odot yr^{-1}$]	α_{CO} $\left[\frac{M_\odot}{K\ km\ s^{-1} pc^2}\right]$	log $M(H_2)$ [log $M_\odot$]
522	171.07767	0.64373	0.02637	51.7	10.08	0.40	4.35	9.13
1115	214.56213	0.89111	0.02595	69.3	10.11	0.76	4.35	9.61
1137	215.81121	0.97835	0.04007	38.8	10.28	0.56	4.35	9.42
1221	218.85558	0.33433	0.03455	23.4	10.20	0.84	4.35	9.73
3819	25.42996	13.67579	0.04531	27.7	10.67	1.03	4.35	9.98
3962	30.99646	14.31038	0.04274	46.3	10.90	0.80	4.35	10.06
4045	32.88983	13.91716	0.02651	43.5	10.47	0.66	4.35	9.71
7493	216.83387	2.83838	0.02644	46.1	10.56	0.41	4.35	9.64
9551	216.88492	4.82163	0.02688	60.3	10.91	0.28	4.35	9.97
11112	345.66796	13.32907	0.02765	51.6	10.81	0.46	4.35	9.85
11223	346.56850	13.98231	0.03554	33.6	10.64	0.67	4.35	9.94
11408	350.61417	13.81586	0.026	45.4	10.05	0.08	4.35	9.12
14712	139.74192	5.88840	0.03827	35.5	10.55	0.63	4.35	9.82
15155	160.22996	5.99141	0.02773	79.6	10.19	0.57	4.35	9.88
22436	139.97725	32.93328	0.04916	58.8	10.42	1.54	1.00	9.75
23194	158.38929	11.87138	0.03404	41.0	10.59	0.70	1.00	9.22
23245	160.91283	12.06066	0.02623	42.9	10.11	-0.05	4.35	8.76
24973	218.82654	35.11868	0.0285	47.5	10.61	1.09	1.00	9.33
25327	203.10100	11.10636	0.03144	41.6	10.03	1.40	1.00	9.72
25763	135.79688	10.15197	0.02962	54.0	10.11	0.22	4.35	9.39
26221	154.15996	12.57738	0.03166	75.5	10.98	0.57	4.35	10.07
28365	235.34412	28.22975	0.03209	56.1	10.36	0.60	4.35	9.65
40439	196.06267	9.22346	0.03501	70.8	10.95	0.73	4.35	9.89
42013	229.01862	6.84763	0.03681	39.7	10.77	0.70	4.35	9.96
48369	167.80421	28.71190	0.02931	20.2	10.32	0.67	1.00	9.42

Table 7.2. CO(3-2) measurements for the xCOLD GASS sample. (1) Index. (2) Standard deviation of the noise. (3) Integrated S/N of the CO(3-2) line. (4) Flag for the detection of the CO(3-2) line based on a peak S/N > 3. 1: detected, 2: non-detected. (5) Velocity-integrated flux S_{CO32} within the 14" JCMT HARP beam. (6) CO(3-2) luminosity within the 14" JCMT HARP beam. (7) CO(1-0) luminosity within the 22" IRAM beam. (8) Beam corrected luminosity ratio $r_{31} = L'_{CO(32)}/L'_{CO(10)} \cdot$ beam correction. (9) Beam correction factor for extrapolating the CO(3-2) flux from the 14" JCMT HARP to the 22" IRAM beam.

Index	σ_{CO32} rms [mK]	S/N_{CO32}	$flag_{CO32}$	S_{CO32} [Jy km s^{-1}]	$\log L'_{CO(32)}$ [log K km s^{-1}pc^2]	$\log L'_{CO(10)}$ [log K km s^{-1}pc^2]	r_{31}	beam corr. 14" to 22"
(1)	(2)	(3)	(4)	(5)	(6)	(7)	(8)	(9)
522	3.00	3.47	1	22.63 ±3.67	7.90 ±0.13	8.34 ±0.07	0.54 ± 0.18	1.48
1115	2.73	6.62	1	50.81 ±8.24	8.24 ±0.07	8.75 ±0.07	0.43 ± 0.09	1.41
1137	1.80	-1.83	2	-7.37 ±3.58	< 8.10	8.72 ±0.05	< 0.31	1.28
1221	2.22	12.03	1	76.36 ±8.69	8.67 ±0.04	9.04 ±0.04	0.50 ± 0.07	1.18
3819	4.56	6.53	1	86.85 ±9.42	8.96 ±0.07	9.30 ±0.04	0.52 ± 0.10	1.15
3962	6.52	1.33	2	29.70 ±11.12	< 9.01	9.35 ±0.04	< 0.55	1.19
4045	7.50	8.56	1	139.84 ±13.38	8.70 ±0.05	9.03 ±0.04	0.53 ± 0.08	1.15
7493	2.24	9.32	1	87.24 ±12.32	8.49 ±0.05	8.93 ±0.05	0.44 ± 0.07	1.23
9551	3.06	10.97	1	152.23 ±22.25	8.75 ±0.04	9.25 ±0.04	0.40 ± 0.05	1.27
11112	2.07	0.04	2	0.38 ±16.14	< 8.19	9.11 ±0.05	< 0.16	1.36
11223	3.24	8.65	1	118.99 ±12.47	8.88 ±0.05	9.24 ±0.04	0.51 ± 0.08	1.17
11408	3.99	-0.09	2	-0.79 ±3.63	< 7.98	8.36 ±0.06	< 0.60	1.44
14712	3.87	-0.38	2	-4.21 ±8.72	< 8.53	9.12 ±0.04	< 0.34	1.33
15155	1.14	16.03	1	76.42 ±14.23	8.47 ±0.03	9.07 ±0.05	0.34 ± 0.05	1.35
22436	2.88	16.83	1	277.51 ±16.61	9.54 ±0.03	9.64 ±0.05	0.97 ± 0.12	1.24
23194	4.32	12.70	1	209.96 ±11.39	9.09 ±0.03	9.15 ±0.05	1.15 ± 0.15	1.30
23245	3.68	2.18	2	17.48 ±2.17	< 7.79	8.05 ±0.06	< 0.84	1.53
24973	8.11	12.31	1	218.30 ±18.02	8.95 ±0.04	9.22 ±0.05	0.71 ± 0.09	1.32
25327	7.48	23.79	1	677.88 ±43.03	9.53 ±0.02	9.69 ±0.04	0.79 ± 0.08	1.14
25763	5.56	-0.15	2	-1.77 ±4.66	< 8.31	8.57 ±0.07	< 0.75	1.36
26221	3.17	12.09	1	161.63 ±17.63	8.91 ±0.04	9.30 ±0.05	0.54 ± 0.07	1.31
28365	3.22	4.65	1	33.01 ±7.23	8.24 ±0.09	8.89 ±0.05	0.33 ± 0.08	1.49
40439	1.92	3.15	1	20.48 ±7.69	8.11 ±0.14	8.96 ±0.08	0.25 ± 0.09	1.80
42013	3.81	6.81	1	100.05 ±13.38	8.84 ±0.06	9.27 ±0.04	0.43 ± 0.08	1.16
48369	3.99	18.72	1	283.35 ±26.96	9.09 ±0.02	9.41 ±0.04	0.52 ± 0.05	1.08

Table 7.3: Properties of the BASS sample.

BAT index	Name	RA [deg]	Dec [deg]	z	Rk20 [arcsec]	log M_* [log $M_\odot$]	log SFR [log $M_\odot yr^{-1}$]	α_{CO} $\left[\frac{M_\odot}{K\ km\ s^{-1} pc^2}\right]$	log $M(H_2)$ [log $M_\odot$]
144	NGC1068	40.66960	-0.01330	0.00303	95.0	10.54	...	4.35	9.79
173	NGC1275	49.95070	41.51170	0.01658	62.9	11.13	...	4.35	...
228	Mrk618	69.09300	-10.37600	0.03464	18.1	10.62	1.19	4.35	10.19
308	NGC2110	88.04740	-7.45620	0.00739	54.9	10.56	0.15	4.35	8.62
310	MCG+08-11-011	88.72340	46.43930	0.02019	54.8	10.72	-0.43	4.35	9.84
316	IRAS05589+2828	90.54365	28.47205	0.03309	0.0	10.57	0.35	4.35	9.75
337	VIIZW073	98.19654	63.67367	0.04042	34.3	10.46	1.13	4.35	9.98
382	Mrk79	115.63670	49.80970	0.02213	30.9	10.49	0.46	4.35	...
399	2MASXJ07595347+2323241	119.97280	23.39010	0.02894	21.1	10.72	...	4.35	10.32
400	IC0486	120.08740	26.61350	0.02656	19.9	10.57	0.49	4.35	9.75
404	Mrk1210	121.02440	5.11380	0.01354	15.2	9.93	-0.18	4.35	...
405	MCG+02-21-013	121.19330	10.77670	0.03486	19.6	10.76	0.33	4.35	10.28
439	Mrk18	135.49300	60.15200	0.01101	18.0	9.74	0.01	4.35	8.73
451	IC2461	139.99200	37.19100	0.00753	40.5	10.06	-0.45	4.35	9.20
471	NGC2992	146.42520	-14.32640	0.00757	50.9	10.22	0.34	4.35	9.30
480	NGC3081	149.87310	-22.82630	0.00763	54.3	9.96	-0.33	4.35	8.85
497	NGC3227	155.87740	19.86510	0.00329	92.6	10.06	0.35	4.35	9.74
517	UGC05881	161.67700	25.93130	0.02048	14.5	10.17	0.42	4.35	9.42
530	NGC3516	166.69790	72.56860	0.00871	40.8	10.65	-0.28	4.35	8.73
532	IC2637	168.45700	9.58600	0.02915	18.1	10.60	1.04	4.35	10.10
548	NGC3718	173.14520	53.06790	0.00279	75.5	10.03	-0.83	4.35	8.49
552	Mrk739E	174.12200	21.59600	0.02945	20.4	10.60	0.89	4.35	9.98
560	NGC3786	174.92700	31.90900	0.00897	49.0	10.32	-0.06	4.35	9.52

Continued on next page

Table 7.3 – continued from previous page

BAT index	Name	RA [deg]	Dec [deg]	z	Rk20 [arcsec]	log M_* [log $M_\odot$]	log SFR [log $M_\odot yr^{-1}$]	α_{CO} $\left[\frac{M_\odot}{K\ km\ s^{-1} pc^2}\right]$	log $M(H_2)$ [log $M_\odot$]
585	NGC4051	180.79010	44.53130	0.00203	102.6	9.82	0.17	4.35	9.80
588	UGC07064	181.18060	31.17730	0.02508	21.9	10.60	0.76	4.35	10.10
590	NGC4102	181.59630	52.71090	0.00185	68.6	10.18	0.54	4.35	9.57
599	NGC4180	183.26200	7.03800	0.00700	40.0	9.96	0.17	4.35	...
608	Mrk766	184.61050	29.81290	0.01292	25.6	10.11	0.35	4.35	9.26
609	M106	184.73960	47.30400	0.00168	263.9	10.22	-0.10	4.35	9.29
615	NGC4388	186.44480	12.66210	0.00834	92.9	10.08	-0.09	4.35	7.91
631	NGC4593	189.91430	-5.34430	0.00835	80.6	10.46	...	4.35	9.24
669	NGC5100NED02	200.24830	8.97830	0.03259	21.9	10.71	1.19	4.35	...
670	MCG-03-34-064	200.60190	-16.72860	0.01682	25.3	10.47	0.68	4.35	9.34
688	NGC5290	206.32990	41.71260	0.00854	89.0	10.39	-0.03	4.35	9.86
703	Mrk463	209.01200	18.37210	0.05015	14.0	10.59	...	4.35	...
712	NGC5506	213.31190	-3.20750	0.00609	74.6	9.92	-0.26	4.35	8.84
723	NGC5610	216.09540	24.61440	0.01691	39.4	10.34	0.70	4.35	9.91
739	NGC5728	220.59970	-17.25320	0.00990	80.4	10.31	0.19	4.35	9.34
766	NGC5899	228.76350	42.04990	0.00844	67.8	10.37	0.54	4.35	9.74
772	MCG-01-40-001	233.33630	-8.70050	0.02285	43.7	10.57	0.81	4.35	9.84
783	NGC5995	237.10400	-13.75780	0.02442	24.3	10.87	1.04	4.35	10.18
841	NGC6240	253.24540	2.40090	0.02386	39.9	11.02	1.75	1.00	10.07
1042	2MASXJ19373299-0613046	294.38800	-6.21800	0.01036	19.8	9.97	-0.17	4.35	9.29
1046	NGC6814	295.66940	-10.32350	0.00576	71.7	10.32	0.14	4.35	9.16
1133	Mrk520	330.17242	10.55221	0.02753	14.4	10.33	...	4.35	...
1184	NGC7479	346.23610	12.32290	0.00705	87.9	10.41	0.57	4.35	9.86

Table 7.4: CO(3-2) and CO(2-1) measurements for the BASS sample. (1) BAT index. (2) Integrated S/N of the CO(3-2) line. (3) Flag for the detection of the CO(3-2) line based on a peak S/N > 3. 1: detected, 2: non-detected. (4) Velocity-integrated flux $S_{\rm CO32}$ within the 14" JCMT HARP beam. (5) CO(3-2) luminosity within the 14" JCMT HARP beam. (6) CO(2-1) luminosity within the 20" JCMT RxA beam. Galaxies which do not have CO(2-1) observations have empty entries (...). (7) Beam corrected luminosity ratio $r_{31} = L'_{CO(32)}/L'_{CO(10)} \cdot$ beam correction. (8) Beam correction factor for extrapolating the CO(3-2) flux from the 14" to the 22" beam. (9) Beam correction factor for extrapolating the CO(2-1) flux from the 20" beam to the total flux. The star * indicates that the corrections are derived from simulated galaxy profiles, because the FIR images were not available.

BAT index (1)	S/N CO(32) (2)	flag CO(32) (3)	$S_{\rm CO32}$ [Jy km s^{-1}] (4)	$\log L'_{\rm CO(32)}$ [log K km s^{-1}pc^2] (5)	$\log L'_{\rm CO(21)}$ [log K km s^{-1}pc^2] (6)	r_{31} (7)	beam corr. 14" to 20" (8)	beam corr. tot 20" to total (9)
144	87.30	1	2787.72 ±251.40	8.08 ±0.00	8.49 ±0.00	0.61 ± 0.00	1.95*	3.62*
173	24.65	1	198.29 ±21.54	8.44 ±0.02	...	...	1.80*	2.32*
228	13.39	1	159.38 ±40.79	8.99 ±0.03	9.26 ±0.04	0.48 ± 0.13	1.13	1.54
308	23.52	1	132.00 ±11.37	7.65 ±0.02	7.65 ±0.02	1.01 ± 0.26	1.25	1.73
310	12.13	1	72.27 ±10.06	8.17 ±0.04	8.32 ±0.11	0.52 ± 0.07	1.31	4.33
316	3.83	1	62.35 ±10.48	8.54 ±0.11	8.76 ±0.00	0.54 ± 0.20	1.14	1.80
337	-0.97	2	-25.80 ±40.08	< 9.04	8.86 ±0.10	< 0.92	1.14	1.63
382	7.05	1	51.22 ±9.23	8.10 ±0.06	...	...	1.31	2.50
399	7.70	1	153.57 ±18.33	8.81 ±0.06	9.20 ±0.04	0.25 ± 0.03	1.16*	1.61*
400	2.09	2	31.28 ±21.74	< 8.43	9.09 ±0.08	< 0.53	1.17	2.21
404	8.81	1	49.19 ±12.64	7.66 ±0.05	...	...	1.09	1.92
405	5.08	1	72.40 ±19.39	8.65 ±0.09	8.81 ±0.12	0.22 ± 0.04	1.14	1.91
439	10.14	1	88.24 ±13.24	7.73 ±0.04	7.80 ±0.10	0.69 ± 0.10	1.08	1.46
451	6.49	1	47.50 ±10.23	7.58 ±0.07	8.09 ±0.06	0.33 ± 0.11	1.33	2.34
471	48.97	1	469.43 ±34.53	8.10 ±0.01	8.33 ±0.01	0.59 ± 0.15	1.27	1.69
480	13.18	1	71.51 ±11.22	7.13 ±0.03	7.64 ±0.03	0.32 ± 0.09	1.28	2.94
497	32.63	1	700.29 ±52.40	7.82 ±0.01	8.33 ±0.00	0.33 ± 0.08	1.33	4.71
517	2.69	2	27.21 ±11.45	< 8.03	8.34 ±0.11	< 0.30	1.05	1.60

Continued on next page

Table 7.4 – continued from previous page

BAT index	S/N CO(32)	flag CO(32)	S_{CO32} [Jy km s^{-1}]	$\log L'_{CO(32)}$ [log K km s^{-1}pc^2]	$\log L'_{CO(21)}$ [log K km s^{-1}pc^2]	r_{31}	beam corr. 14" to 20"	beam corr. tot 20" to total
530	4.60	1	55.56 ±12.08	7.62 ±0.09	7.72 ±0.12	0.75 ± 0.32	1.19	1.88
532	13.95	1	354.36 ±30.97	9.18 ±0.03	9.34 ±0.02	0.91 ± 0.07	1.13	1.54
548	3.73	1	63.49 ±25.16	6.70 ±0.12	7.00 ±0.07	0.59 ± 0.24	1.48	5.77
552	12.19	1	118.93 ±33.69	8.72 ±0.04	9.07 ±0.04	0.48 ± 0.04	1.16	1.75
560	6.33	1	217.02 ±36.42	8.18 ±0.07	8.57 ±0.03	0.41 ± 0.13	1.25	1.64
585	42.09	1	539.72 ±64.87	7.50 ±0.01	7.87 ±0.01	0.47 ± 0.12	1.36	15.66
588	19.59	1	157.45 ±25.70	8.70 ±0.02	9.05 ±0.02	0.37 ± 0.02	1.20	1.80
590	123.24	1	1978.99 ±126.31	8.35 ±0.00	8.56 ±0.00	0.61 ± 0.15	1.25	1.87
599	13.42	1	273.82 ±36.99	7.83 ±0.03	...	...	1.31	1.99
608	14.83	1	148.61 ±24.68	8.10 ±0.03	8.26 ±0.05	0.49 ± 0.04	1.12	1.47
609	29.31	1	1166.84 ±109.02	7.25 ±0.01	7.66 ±0.01	0.52 ± 0.13	1.67	7.88
615	37.34	1	14.89 ±1.29	6.25 ±0.01	6.58 ±0.02	0.53 ± 0.14	1.44	3.89
631	21.62	1	115.15 ±14.23	7.53 ±0.02	8.03 ±0.03	0.47 ± 0.00	1.89*	2.99*
669	4.00	1	56.64 ±19.80	8.48 ±0.11	...	...	1.48	1.21
670	9.10	1	61.93 ±10.29	7.95 ±0.05	8.42 ±0.09	0.30 ± 0.10	1.13	1.50
688	41.19	1	251.32 ±46.05	7.92 ±0.01	8.44 ±0.01	0.37 ± 0.09	1.54	4.87
703	-2.11	2	-26.24 ±14.73	< 8.90	...	...	1.41*	1.09*
712	35.71	1	295.07 ±29.45	7.66 ±0.01	7.85 ±0.03	0.64 ± 0.17	1.24	1.81
723	41.60	1	341.24 ±30.06	8.69 ±0.01	8.98 ±0.02	0.59 ± 0.03	1.21	1.84
739	50.02	1	420.76 ±36.26	8.02 ±0.01	8.32 ±0.02	0.52 ± 0.13	1.28	1.93
766	17.23	1	131.36 ±16.03	7.71 ±0.03	8.27 ±0.02	0.37 ± 0.10	1.64	5.48
772	17.93	1	167.87 ±18.64	8.65 ±0.02	8.73 ±0.06	0.82 ± 0.23	1.22	2.40
783	32.29	1	317.22 ±20.31	8.98 ±0.01	9.21 ±0.02	0.55 ± 0.14	1.16	1.70
841	87.81	1	2897.27 ±170.89	9.92 ±0.00	9.85 ±0.01	1.22 ± 0.02	1.18	1.48

Continued on next page

Table 7.4 – continued from previous page

BAT index	S/N CO(32)	flag CO(32)	S_{CO32} [Jy km s^{-1}]	$\log L'_{CO(32)}$ [log K km s^{-1}pc^2]	$\log L'_{CO(21)}$ [log K km s^{-1}pc^2]	r_{31}	beam corr. 14" to 20"	beam corr. tot 20" to total
1042	23.03	1	135.31 ±22.74	7.86 ±0.02	8.29 ±0.03	0.37 ± 0.10	1.24	1.86
1046	8.78	1	37.78 ±8.56	6.72 ±0.05	7.51 ±0.04	0.23 ± 0.07	1.73	8.32
1133	68.37	1	494.40 ±81.07	9.28 ±0.01	...	...	1.41*	1.10*
1184	52.72	1	993.78 ±131.74	8.49 ±0.01	8.65 ±0.00	0.72 ± 0.18	1.31	2.97

Chapter 8

Appendix B

Here we present appendix material related to Chapter 3.

8.1 Normal distribution vs. Student's t-distribution

In this section we investigate how the choice of the prior distributions affects the results. In particular, the distribution of the parameter population $p(\vec{\theta}|\vec{\mu}, \Sigma)$ and the noise distribution $p(F_j^{obs}|\vec{\theta}, F^e rr_j, \delta_j)$.

The Student's t-distribution is appropriate for robust statistical models (Kelly et al. 2012; Gelman et al. 2004) and it is recommended when the measurement errors are assumed to be Gaussian, but their standard deviation is not known but only estimated. If we assume that the true variance σ^2 follows a Scaled Inverse-χ^2 distribution with scale parameter σ'^2 (the estimated variance), then modelling the noise as a Student's t-distribution with standard deviation σ' is equivalent to the assumption that the noise is normal distributed with a standard deviation σ (Gelman et al. 2004). For the choice of the degrees of freedom we follow Kelly et al. (2012) and used $f = 3$, since it is the smallest value for which mean and variance of the distribution are finite. The results do not depends strongly on change on f which are less than an order of magnitude and $f < 10$ is a typical choice for robust models (e.g. Gelman et al. 2004). For a Student's t-distribution with $f = 3$, (61.5%, 86.5%, 94.6%) of the distribution lie within (1σ, 2σ, 3σ) from the mean, respectively. In comparison, for a Gaussian distribution the percentages are (68.3%, 95.4%, 99.7%).

First, we focus on the population distribution of the parameters given the hyper-parameters (mean and standard deviation). We consider two distributions: normal and Student's t-distribution, which compared to the normal distribution allows for more outliers in the tail of the distribution. For the Student's t-distribution we use $f = 8$ degrees of freedom, which is the value we use for the analysis in this work. As we can see from Fig. 8.1, the results do not change much. The dust masses do not vary depending on the choice of the sample distribution. Temperature and β show small differences, within the uncertainties, and no systematic offset. We conclude that the choice of the distribution does not affect the results critically.

The second assumption on the priors is about the noise distribution. We consider also in this case a normal and a Student's t-distribution with three degrees of freedom (see description in Sec.3.2.4). The Student's t-distribution is less sensitive to flux points which may be outliers, due to large uncertainties or to the noise being underestimate. Figure 8.2 shows the comparison plots. Again, the dust masses are robust with respect to the choice of the noise distribution. Temperature and β, on the other hand, show some variations, with the results obtained using the Student's t-distribution covering a smaller range of T and β values with respect to the results from the normal distribution ($T = 18 - 27$ K, $\beta = 1.1 - 2.1$ for the Student's t-distribution, $T = 17 - 30$ K, $\beta = 0.6 - 2.2$ for the normal distribution). The values of T or β which differ more from the mean values are determined mostly by the flux points at long (850 μm) or short wavelengths (100 μm). These are also the flux points which on average have the largest measurement uncertainties. With the assumption of a Student's t-distribution, we imply that the deviation of the SED shape from a SMBB with mean parameter values is not due to a change in T or β, but is more likely due to uncertainties in the flux measurements, which lead to 'outlier' flux points. Therefore the measured T and β will cover a smaller range of values.

The choice of the noise distribution affects consequently also the derived relation between T and β, shown in Fig. 8.3. Assuming a Student's t-distribution for the noise, the results show a weak anti-correlation ($R = -0.12$) between T and β. This is similar to the result obtained from the fit without the 850 μm point. The fit with Student noise assumes that the variations at 850 μm are due to larger uncertainties on the estimate of the 850 μm uncertainties, rather than to a real variations in the sub-mm slope of the SED. Therefore the fit tends to 'ignore' the extreme 850 μm flux points. In some cases the 850 μm point does not follow the same SED slope as the other points, but it shows

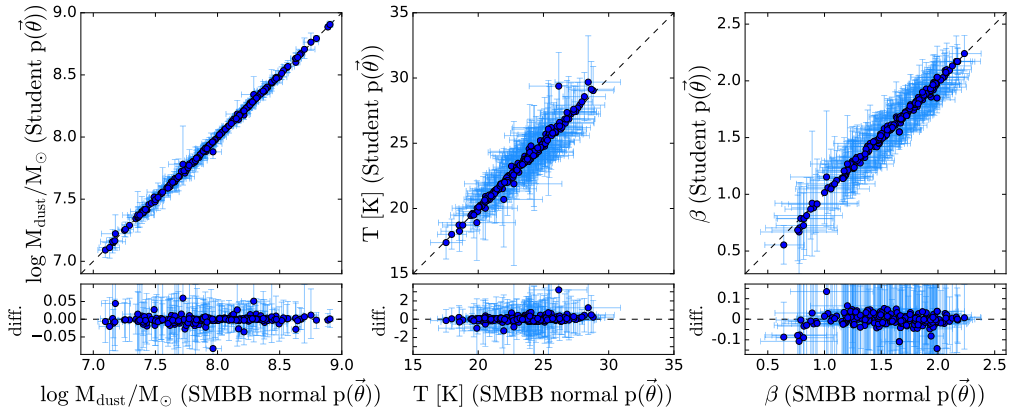

Figure 8.1. Comparison of the dust masses, temperatures and emissivity index obtained through the fit of a single modified black-body (SMBB) using the hierarchical approach, assuming a normal or a Student's t-distribution with 8 degrees of freedom for the distribution of the parameters given the hyper-parameters $p(\vec{\theta}|\vec{\mu}, \Sigma)$.

an excess or a deficit. We have two ways to model this type of SED. One possibility is to assume that the true uncertainties on the 850 μm point are larger than the estimated ones, and therefore model the SED assuming a Student's t-distribution. If instead we believe that the different behaviour of the SED at wavelengths longer than 500 μm is real, we can model the noise using a normal distribution. In this work, we decide to model the noise using a normal distribution.

8.2 Upper limits formalism

In the case of a non-detection in one of the bands, the likelihood needs to be modified to include an upper limit for the non-detection. Following the formalism described in **?**, the upper limit of an observation provides a limit on the evaluation of a definite integral. For a measured flux, F_j, which is clearly detected, the probability of observing our data, given the true value of the observables F_j^{true} and the measurement uncertainties F_j^{err}, is:

$$p(F_j|F_j^{true}, F_j^{err}). \tag{8.1}$$

In the case of a single non-detection, we consider the upper limit $F_{lim,j}$, and the probability is:

$$p(F_{lim,j}|F_j^{true}, F_j^{err}) = \int_{-\infty}^{F_{lim,j}} p(F_j|F_j^{true}, F_j^{err}) dF_j. \tag{8.2}$$

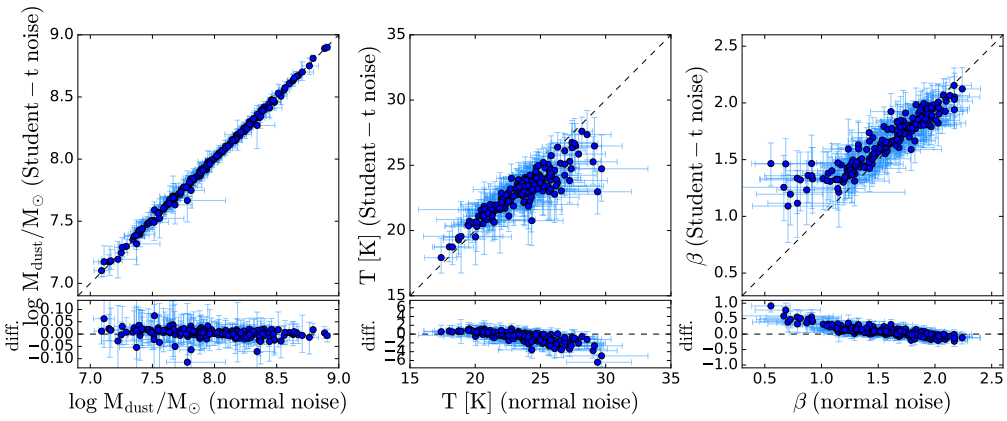

Figure 8.2. Comparison of the dust masses, temperatures and emissivity index obtained through the fit of a single modified black-body (SMBB) using the hierarchical approach, assuming a normal distribution or a Student's t-distribution with three degrees of freedom for the noise.

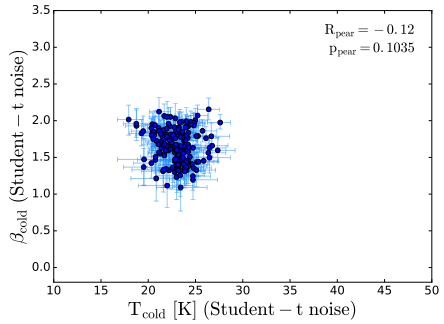

Figure 8.3. Relation between the dust temperature and dust emissivity index (T-β relation) from the SMBB hierarchical fit of the JINGLE sample assuming a Student's t-distribution with three degrees of freedom for the noise.

Non-hierarchical: in the non-hierarchical approach, the likelihood in case of a non detection on the j-th flux measurement is given by:

$$p(\vec{F}^{obs}|\vec{\theta}) = \int_{-\infty}^{F_{lim,j}} \text{MultiNormal}(\vec{F}^{obs}|\vec{F}^{mod}(\vec{\theta}), C) dF_j^{obs}. \tag{8.3}$$

Since the likelihood evaluation in case of upper limits includes the computation of integrals, the use of upper limit is computationally expensive. Thus, we allow our code to perform the SED fit with one flux point as upper limit at most, to avoid that the code has to calculate too many integrals. If more than one band has an upper limit, we consider only the upper limit in one band and we neglect the other flux point. We prefer to keep

the 850 μm point, if it is an upper limit, since it is the longest wavelength point and it is the one that places more constraints on the SED slope.

Hierarchical: similarly, for the hierarchical method the likelihood for the i-th galaxy in case of a non-detection in the j-th band is:

$$p(\vec{F_i}^{obs}|\vec{\theta_i}) = \int_{-\infty}^{F_{lim,i,j}} \text{MultiNormal}(\vec{F_i}^{obs}|\vec{F_i}^{mod}(\vec{\theta_i}), C_i) dF_{i,j}^{obs}. \tag{8.4}$$

If the upper limit is in a band whose uncertainties are not correlated with other bands (i.e. the SCUBA-2 850 μm band or the IRAS 60 μm band), the expression for the upper limit can be divided in two parts, and the part that does not depend on $F_{i,j}$ can be taken out of the integral:

$$\begin{aligned} p(\vec{F_i}^{obs}|\vec{\theta_i}) &= \text{MultiNormal}(\vec{F_i'}^{obs}|\vec{F_i'}^{mod}(\vec{\theta_i}), C_i') \cdot \int_{-\infty}^{F_{lim,i,j}} p(F_{i,j}^{obs}|F_{i,j}^{mod}(\vec{\theta_i}), F_{i,j}^{err}) dF_{i,j}^{obs} \\ &= \text{MultiNormal}(\vec{F_i'}^{obs}|\vec{F_i'}^{mod}(\vec{\theta_i}), C_i') \cdot \int_{-\infty}^{F_{lim,i,j}} \text{Normal}\left(F_{i,j}^{obs}|F_{i,j}^{mod}(\vec{\theta_i}), \sqrt{C_{i,jj}}\right) dF_{i,j}^{obs}, \end{aligned} \tag{8.5}$$

where $\vec{F_i'}$ is the $(m-1)$-dimensional vector equal to the vector $\vec{F_i}$ but without the j-th component. Similarly, C_i' is equal to the covariance matrix C_i, but without the j-th component. $C_{i,jj}$ is the jj component of the covariance matrix C_i for the i-th galaxy.

The integral of the univariate normal distribution can then be computed analytically:

$$\int_{-\infty}^{y_{lim}} \text{Normal}(y|\mu,\sigma) dy = \frac{1}{\sqrt{2\pi}\sigma} \cdot \int_{-\infty}^{y_{lim}} \exp\left(-\frac{1}{2}\left(\frac{y-\mu}{\sigma}\right)^2\right) dy = \frac{1}{2}\left[\text{erf}\left(\frac{y_{lim}-\mu}{\sqrt{2}\sigma}\right) + 1\right], \tag{8.6}$$

where 'erf' is the error function. If the upper limit is in one of the *Herschel* bands, the integral can also be computed analytically, but it requires more computations and it slows down code. Therefore we decide to ignore the points with non-detections in the *Herschel* bands.

8.3 Additional simulations

In this section we present additional simulations with the inputs T and β anti-correlated and with T and β correlated.

$T - \beta$ anti-correlated:

We did an additional test to see whether the hierarchical code can recover a T-β anti-correlation. We simulated 100 SEDs with temperatures uniformly distributed in the range 20 - 30 K and the corresponding β given by the relation:

$$\beta = -0.121 \cdot T + 4.595. \tag{8.7}$$

The slope and intercept of this relation are derived from the results of the non-hierarchical fit to the real data. We also added some scatter to the $T - \beta$ anti-correlation. As before, we kept the dust mass constant ($\log M = 8$ M$_\odot$).

Fig. 8.4 shows the results from the hierarchical and non-hierarchical method. The non-hierarchical method points move in the $T - \beta$ anti-correlation direction. Thus even if the $T - \beta$ anti-correlation is maintained, the differences between input values and measured values can be up to 8.6 K in temperature and 0.7 in β. The hierarchical code is also able to recover the $T - \beta$ anti-correlation. The difference between input and measured are a bit smaller than in the non-hierarchical case (< 5.8 K in temperature and 0.5 in β)

Comparing directly the input and output parameters, we see that the largest discrepancies between input and output temperatures happen for high temperature values. This is due to the fact that the FIR SED moves to lower wavelengths with increasing temperature. Thus for the high temperature models ($T > 30$ K), the peak of the SED is at wavelengths < 100 μm, which are not sampled by our data points. This problem affects also the measurements of β: if the temperature is not well constrained, also β will not be determined with high precision, due to the degeneracy between the two parameters. Additionally, due to the assumed T-β anti-correlation, high T values correspond to low β values, i.e. shallower slopes of the SED. This will also contribute to the difficulties of accurately measure T and β.

T-β correlated:

We did the same test for positive correlation between T and β, parametrized by the relation:

$$\beta = 0.121 \cdot T - 1.325. \tag{8.8}$$

As we can see from the left panel of Fig. 8.5, the non-hierarchical method is not able to recover the positive correlation. The results of the fitting move away from the input values

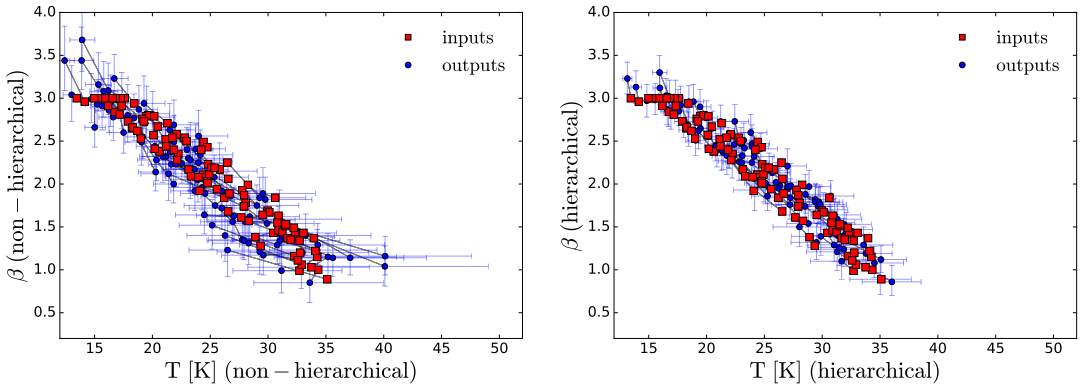

Figure 8.4. Results of temperature and β derived from the fit of 100 simulated SMBB SEDs with $T-\beta$ anti-correlated and the same dust mass ($\log M_{dust} = 8$ $M_{\odot}$.). The temperature are linearly distributed and some scatter is added around a linear $T-\beta$ relation. We added to every band Gaussian noise with an amplitude proportional to the level of noise present in our data in that band. The output values are derived with the non-hierarchical (left panel) and hierarchical (right panel) fitting approach. In red are shown the input values and in blue are the measured values (outputs), the grey lines connect the corresponding inputs and outputs.

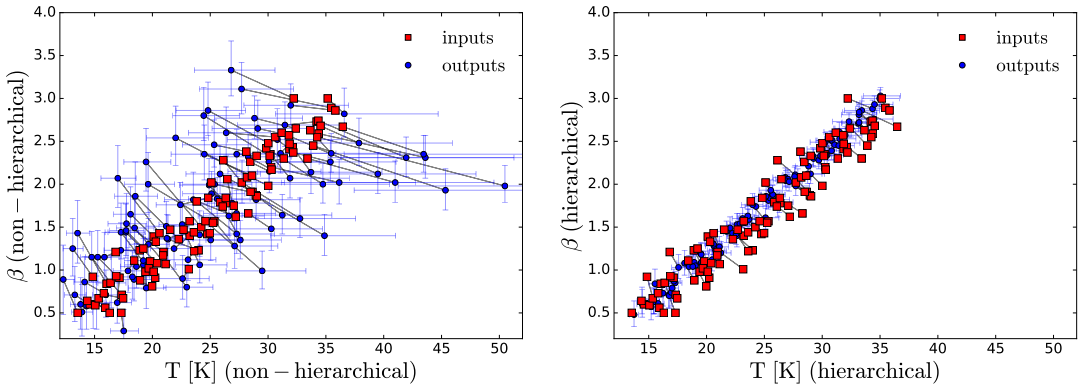

Figure 8.5. Results of temperature and β derived from the fit of 100 simulated SMBB SEDs with $T-\beta$ correlated and the same dust mass ($\log M_{dust} = 8$ $M_{\odot}$.). The temperature are linearly distributed and some scatter is added around a linear $T-\beta$ relation. We added to every band Gaussian noise with an amplitude proportional to the level of noise present in our data in that band. The output values are derived with the non-hierarchical (left panel) and hierarchical (right panel) fitting approach. In red are shown the input values and in blue are the measured values (outputs), the grey lines connect the corresponding inputs and outputs.

along diagonal lines in the $T-\beta$ plane, following the anti-correlation line. The right panel of Fig. 8.5 shows the results from the hierarchical SED fitting. The code can recover the input values and the trend quite well. We note that the difference between input and output is often larger than the error bars. The points tend to move along diagonal lines in the $T-\beta$ plane, following the anti-correlation line. Therefore some points move outside the input correlation. However, the difference between input and output are small enough, that the $T-\beta$ positive correlation is visible also in the outputs value.

From these tests we can conclude that the hierarchical approach performs better than the non-hierarchical approach in all three cases of single input, $T-\beta$ correlation, and anti-correlation. In the case of a positive correlation, we note that even in the hierarchical approach the difference between input and output values can sometimes be larger than our errorbars. The differences in temperature are < 3 K , and the difference in β are < 0.3. For comparison, in the non-hierarchical case, the differences in temperature are < 16 K, and the difference in β are < 0.8.

8.4 Images of the SED fit of the JINGLE galaxies

We show here the fit of the SEDs of a sub-sample of JINGLE galaxies obtained with the hierarchical Bayesian approach. For each galaxy, we show the fit using the single modified black-body (SMBB), broken-emissivity law modified black-body (BMBB), and two modified black-body (TMBB) model. Additional figures showing the entire sample of 192 JINGLE galaxies are available online:
(https://academic.oup.com/mnras/article/489/3/4389/5552673#supplementary-data).

8.5 Tables

Here we present the tables related to Chapter 3. In Tables 8.1, 8.2, and 8.3 we show the result parameters from the hierarchical SED fitting using the SMBB, BMBB and TMBB models, respectively.

The results of the analysis of the correlation of dust emissivity index β and dust temperature with combinations of other galaxy properties are shown in Tables 8.4 and 8.5, repectively.

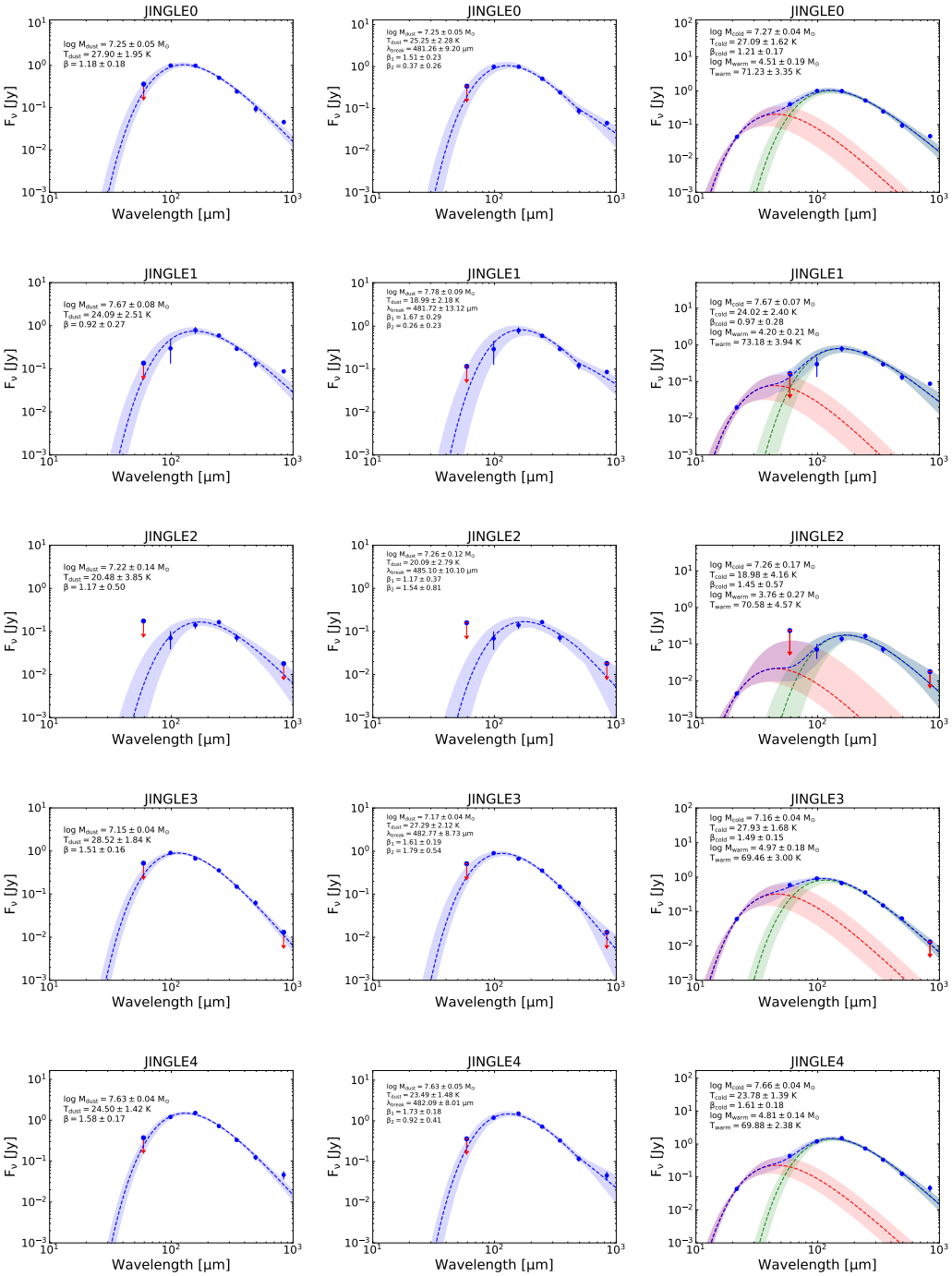

Figure 8.6. FIR SEDs of the galaxies of the JINGLE sample, fitted with the hierarchical approach using the three models: SMBB (left panel), BMBB (middle panel) and TMBB(right panel). The shaded regions show the lower and upper 1-sigma uncertainties on the SED models , defined by taking the maximum and minimum flux values of the models with likelihood values in the highest 68th percentile.

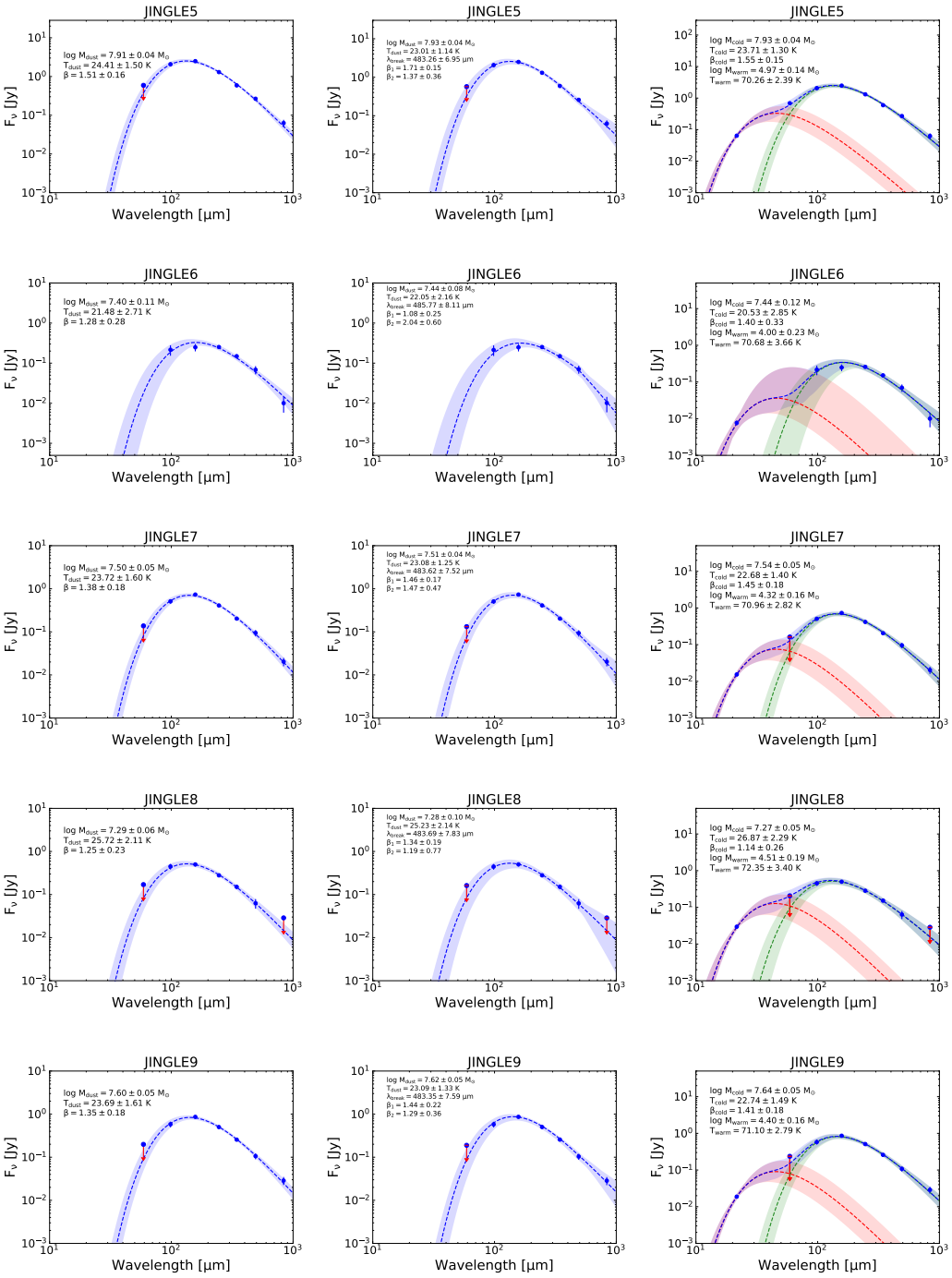

Figure 8.6. – continued.

Table 8.1. Result parameters from the hierarchical SED fitting using the single modified black-body (SMBB) model. The parameters of the model are the dust mass ($\log M_c$), temperature (T_c), and emissivity index (β_c). The last column is the natural logarithm of the likelihood, i.e. the probability of the observed fluxes given the model parameters ($p\left(\vec{F}|\vec{\theta}\right)$). This table is available in its entirety in a machine-readable form in the online journal (link to online journal). A portion is shown here for guidance regarding its form and content.

JINGLE ID	SDSS name	$\log M_c$ [$M_\odot$]	T_c [K]	β_c	$\ln L$
0	J131616.82+252418.7	7.25±0.05	27.92±1.98	1.17±0.18	11.82
1	J131453.43+270029.2	7.66±0.07	24.33±2.48	0.91±0.26	7.28
2	J131526.03+330926.0	7.22±0.14	20.69±3.78	1.15±0.51	11.54
3	J125606.09+274041.1	7.15±0.04	28.57±1.84	1.51±0.16	14.33
4	J132134.91+261816.8	7.63±0.04	24.50±1.56	1.57±0.18	12.13
5	J091728.99-003714.1	7.91±0.04	24.40±1.47	1.52±0.16	10.40
6	J132320.14+320349.0	7.40±0.11	21.51±2.77	1.29±0.29	16.99
7	J132051.75+312159.8	7.50±0.05	23.84±1.57	1.37±0.18	16.89
8	J091642.17+001220.0	7.29±0.06	25.76±2.15	1.24±0.23	12.67
9	J131547.11+315047.1	7.60±0.05	23.76±1.70	1.34±0.19	15.55

Table 8.2. Result parameters from the hierarchical SED fitting using the broken emissivity law modified black-body (BMBB) model. The parameters are the dust mass ($\log M_c$), temperature (T_c), emissivity index before the break (β_1) and after the break (β_2), and the wavelength of the break (λ_{break}). The last column is the natural logarithm of the likelihood, i.e. the probability of the observed fluxes given the model parameters ($p\left(\vec{F}|\vec{\theta}\right)$). This table is available in its entirety in a machine-readable form in the online journal (link to online journal). A portion is shown here for guidance regarding its form and content.

JINGLE ID	SDSS name	$\log M_c$ [$M_\odot$]	T_c [K]	β_1	β_2	λ_{break} [μm]	$\ln L$
0	J131616.82+252418.7	7.25±0.05	25.25±2.28	1.51±0.23	0.37±0.26	481.26±9.20	14.59
1	J131453.43+270029.2	7.78±0.09	18.99±2.18	1.67±0.29	0.26±0.23	481.72±13.12	10.86
2	J131526.03+330926.0	7.26±0.12	20.09±2.79	1.17±0.37	1.54±0.81	485.10±10.10	11.55
3	J125606.09+274041.1	7.17±0.04	27.29±2.12	1.61±0.19	1.79±0.54	482.77±8.73	14.52
4	J132134.91+261816.8	7.63±0.05	23.49±1.48	1.73±0.18	0.92±0.41	482.09±8.01	13.42
5	J091728.99-003714.1	7.93±0.04	23.01±1.14	1.71±0.15	1.37±0.36	483.26±6.95	10.59
6	J132320.14+320349.0	7.44±0.08	22.05±2.16	1.08±0.25	2.04±0.60	485.77±8.11	17.54
7	J132051.75+312159.8	7.51±0.04	23.08±1.25	1.46±0.17	1.47±0.47	483.62±7.52	16.85
8	J091642.17+001220.0	7.28±0.10	25.23±2.14	1.34±0.19	1.19±0.77	483.69±7.83	12.65
9	J131547.11+315047.1	7.62±0.05	23.09±1.33	1.44±0.22	1.29±0.36	483.35±7.59	15.65

Table 8.3. Result parameters from the hierarchical SED fitting using the two modified black-bodies (TMBB) model. The parameters are the dust mass ($\log M_c$), temperature (T_c), and emissivity index (β_c) of the cold dust component, and the dust mass ($\log M_w$) and temperature (T_w) of the warm dust component. The emissivity index of the warm component has been fixed to $\beta_w = 1.5$. The last column is the natural logarithm of the likelihood, i.e. the probability of the observed fluxes given the model parameters ($p\left(\vec{F}|\vec{\theta}\right)$). This table is available in its entirety in a machine-readable form in the online journal (link to online jounrnal). A portion is shown here for guidance regarding its form and content.

JINGLE ID	SDSS name	$\log M_c$ [$M_\odot$]	T_c [K]	β_c	$\log M_w$ [$M_\odot$]	T_w [K]	$\ln L$
0	J131616.82+252418.7	7.27±0.04	27.09±1.62	1.21±0.17	4.51±0.19	71.23±3.35	18.37
1	J131453.43+270029.2	7.67±0.07	24.02±2.40	0.97±0.28	4.20±0.21	73.18±3.94	11.78
2	J131526.03+330926.0	7.26±0.17	18.98±4.16	1.45±0.57	3.76±0.27	70.58±4.57	18.19
3	J125606.09+274041.1	7.16±0.04	27.93±1.68	1.49±0.15	4.97±0.18	69.46±3.00	20.09
4	J132134.91+261816.8	7.66±0.04	23.78±1.39	1.61±0.18	4.81±0.14	69.88±2.38	18.57
5	J091728.99-003714.1	7.93±0.04	23.71±1.30	1.55±0.15	4.97±0.14	70.26±2.39	15.79
6	J132320.14+320349.0	7.44±0.12	20.53±2.85	1.40±0.33	4.00±0.23	70.68±3.66	22.82
7	J132051.75+312159.8	7.54±0.05	22.68±1.40	1.45±0.18	4.32±0.16	70.96±2.82	22.50
8	J091642.17+001220.0	7.27±0.05	26.87±2.29	1.14±0.26	4.51±0.19	72.35±3.40	17.26
9	J131547.11+315047.1	7.64±0.05	22.74±1.49	1.41±0.18	4.40±0.16	71.10±2.79	21.20

Table 8.4: Results of the analysis of the correlation between dust emissivity index β and combinations of other galaxy properties. The table shows the coefficients a_j of the best polynomial expression $\beta_{model}(x_1, ..., x_k) = \sum_{j=1}^{k} a_j \log(x_j) + b$, to estimate β using combinations of two or three galaxy properties. (1) BIC: Bayesian Information Criterion (Schwarz 1978), calculated as BIC $= -2 \cdot \ln(L) + q \cdot \ln(m)$ where L is the likelihood (i.e. the probability of the data given the parameter $p(\vec{F}|\vec{\theta})$), q is the number of free parameters of the model, and m is the number of data points (wavebands). (2) Pearson correlation coefficient.

	emissivity index β								
Nr. of param.	$\log M_*$ [$M_\odot$]	log SFR [$M_\odot$ yr^{-1}]	log Area [kpc^2]	12+log(O/H)	$\log M_{dust}$ [$M_\odot$]	$\log M_{HI}$ [$M_\odot$]	intercept	BIC (1)	R (2)
2 parameters	0.22 ± 0.03	-0.01 ± 0.03					-0.44 ± 0.25	226.29	0.53
	0.42 ± 0.02		-0.37 ± 0.03				-1.97 ± 0.18	53.19	0.64
	0.08 ± 0.02			0.73 ± 0.10			-5.34 ± 0.66	164.7	0.61
	0.49 ± 0.04				-0.31 ± 0.04		-0.79 ± 0.15	172.34	0.55
	0.39 ± 0.02					-0.3 ± 0.02	0.64 ± 0.15	68.67	0.63
		0.32 ± 0.02	-0.22 ± 0.03				2.02 ± 0.04	228.43	0.47
		0.04 ± 0.02		0.88 ± 0.08			-5.89 ± 0.7	172.41	0.61
		0.15 ± 0.04			0.04 ± 0.03		1.43 ± 0.26	299.18	0.45
		0.44 ± 0.03				-0.35 ± 0.03	5.01 ± 0.27	138.35	0.54
			-0.21 ± 0.02	1.39 ± 0.07			-10.03 ± 0.63	91.25	0.62
			-0.43 ± 0.03		0.45 ± 0.03		-1.15 ± 0.17	151.77	0.55
			0.05 ± 0.03			-0.01 ± 0.03	1.65 ± 0.22	435.98	0.21
				1.07 ± 0.09	-0.03 ± 0.02		-7.35 ± 0.65	173.7	0.61
				1.19 ± 0.07		-0.13 ± 0.02	-7.42 ± 0.55	131.88	0.62
					0.48 ± 0.03	-0.43 ± 0.03	2.05 ± 0.16	117.7	0.58
3 parameters	0.37 ± 0.03	0.08 ± 0.03	-0.38 ± 0.03				-1.46 ± 0.26	51.04	0.65
	0.09 ± 0.03	-0.01 ± 0.03		0.73 ± 0.09			-5.46 ± 0.74	169.97	0.61
	0.55 ± 0.04	0.26 ± 0.04			-0.59 ± 0.06		0.78 ± 0.27	132.11	0.56
	0.28 ± 0.02	0.23 ± 0.03				-0.41 ± 0.03	2.76 ± 0.32	21.40	0.66

Continued on next page

Table 8.4 – continued from previous page

emissivity index β									
Nr. of param.	$\log M_*$ [$M_\odot$]	log SFR [$M_\odot$ yr^{-1}]	log Area [kpc^2]	12+log(O/H)	$\log M_{dust}$ [$M_\odot$]	$\log M_{HI}$ [$M_\odot$]	intercept	BIC (1)	R (2)
3 parameters	0.28 ± 0.03		-0.38 ± 0.03	0.8 ± 0.09			-7.48 ± 0.64	-14.37	0.70
	0.41 ± 0.04		-0.37 ± 0.03		0.01 ± 0.05		-1.97 ± 0.19	58.63	0.64
	0.46 ± 0.02		-0.25 ± 0.03			-0.18 ± 0.03	-0.85 ± 0.26	18.08	0.67
	0.39 ± 0.04			0.85 ± 0.09	-0.37 ± 0.04		-6.67 ± 0.68	96.94	0.64
	0.28 ± 0.03			0.54 ± 0.1		-0.28 ± 0.02	-3.14 ± 0.67	41.97	0.67
	0.32 ± 0.04				0.11 ± 0.06	-0.34 ± 0.03	0.92 ± 0.22	70.94	0.63
		0.19 ± 0.02	-0.32 ± 0.03	1.15 ± 0.08			-7.77 ± 0.69	33.69	0.66
		0.04 ± 0.04	-0.42 ± 0.03		0.41 ± 0.05		-0.89 ± 0.35	156.46	0.55
		0.46 ± 0.02	-0.06 ± 0.03			-0.32 ± 0.03	4.77 ± 0.28	140.08	0.54
		0.23 ± 0.04		1.17 ± 0.09	-0.25 ± 0.04		-6.49 ± 0.65	142.45	0.62
		0.29 ± 0.03		0.8 ± 0.08		-0.33 ± 0.03	-2.14 ± 0.72	38.58	0.66
		0.23 ± 0.04			0.3 ± 0.04	-0.46 ± 0.03	3.7 ± 0.31	85.63	0.60
			-0.40 ± 0.03	1.00 ± 0.09	0.25 ± 0.03		-8.25 ± 0.7	38.36	0.65
			-0.21 ± 0.03	1.38 ± 0.08		0.00 ± 0.03	-10.02 ± 0.67	96.77	0.62
			-0.31 ± 0.03		0.63 ± 0.03	-0.35 ± 0.03	0.56 ± 0.22	42.80	0.63
				0.63 ± 0.10	0.29 ± 0.04	-0.34 ± 0.03	-2.89 ± 0.78	84.11	0.63

Table 8.5: Same as table 8.4, but for the correlation between dust temperature T and galaxy properties. (1) BIC: Bayesian Information Criterion (Schwarz 1978), calculated as BIC $= -2 \cdot \ln(L) + q \cdot \ln(m)$ where L is the likelihood (i.e. the probability of the data given the parameter $p(\vec{F}|\vec{\theta})$), q is the number of free parameters of the model, and m is the number of data points (wavebands). (2) Pearson correlation coefficient.

Dust temperature T									
Nr. of param.	log M_* [$M_\odot$]	log SFR [$M_\odot$ yr^{-1}]	log Area [kpc^2]	12+log(O/H)	log M_{dust} [$M_\odot$]	log M_{HI} [$M_\odot$]	intercept	BIC (1)	R (2)
2 parameters	-2.14 ± 0.20	2.50 ± 0.22					44.24 ± 1.93	914.52	0.54
	0.10 ± 0.18		-0.59 ± 0.24				22.62 ± 1.53	1046.44	0.24
	0.24 ± 0.17			-2.86 ± 0.77			45.26 ± 5.44	1038.07	0.18
	-1.07 ± 0.34				0.89 ± 0.35		26.50 ± 1.20	1045.98	0.14
	-0.59 ± 0.17					0.53 ± 0.19	23.62 ± 1.27	1045.69	0.17
		1.93 ± 0.18	-2.17 ± 0.22				26.21 ± 0.33	931.29	0.53
		1.50 ± 0.15		-5.74 ± 0.61			72.73 ± 5.45	948.15	0.41
		4.19 ± 0.29			-3.73 ± 0.30		51.88 ± 2.20	849.60	0.68
		1.78 ± 0.22				-1.52 ± 0.23	37.27 ± 2.12	985.74	0.36
			-0.21 ± 0.18	-1.69 ± 0.59			37.74 ± 5.05	1038.7	0.22
			-1.19 ± 0.30		0.65 ± 0.22		19.53 ± 1.40	1038.33	0.25
			-1.38 ± 0.24			1.00 ± 0.22	15.42 ± 1.78	1026.52	0.29
				-3.47 ± 0.72	0.45 ± 0.18		49.50 ± 5.74	1032.98	0.17
				-2.65 ± 0.60		0.33 ± 0.15	42.65 ± 4.65	1035.02	0.18
					-0.54 ± 0.22	0.54 ± 0.25	21.84 ± 1.24	1051.14	0.14
3 parameters	-1.56 ± 0.23	2.83 ± 0.22	-1.40 ± 0.25				40.58 ± 2.08	887.83	0.61
	-1.65 ± 0.23	2.52 ± 0.21		-2.89 ± 0.74			64.51 ± 5.56	905.66	0.55
	0.19 ± 0.37	4.24 ± 0.29			-3.96 ± 0.48		51.72 ± 2.11	854.86	0.68
	-1.92 ± 0.21	3.04 ± 0.25				-0.97 ± 0.24	51.26 ± 2.56	903.19	0.58
	0.64 ± 0.22		-0.65 ± 0.24	-2.98 ± 0.72			43.22 ± 5.51	1036.39	0.25

Continued on next page

Table 8.5 – continued from previous page

Dust temperature T									
Nr. of param.	$\log M_*$ [$M_\odot$]	log SFR [$M_\odot$ yr^{-1}]	log Area [kpc^2]	12+log(O/H)	$\log M_{dust}$ [$M_\odot$]	$\log M_{HI}$ [$M_\odot$]	intercept	BIC (1)	R (2)
3 parameters	-1.24 ± 0.34		-1.3 ± 0.29		1.9 ± 0.41		22.31 ± 1.50	1030.77	0.26
	-0.20 ± 0.19		-1.25 ± 0.27			1.07 ± 0.24	16.49 ± 1.95	1031.0	0.29
	-0.64 ± 0.36			-3.11 ± 0.79	1.02 ± 0.33		48.37 ± 5.39	1035.13	0.18
	-0.04 ± 0.24			-2.57 ± 0.75		0.35 ± 0.21	42.16 ± 5.75	1040.49	0.19
	-0.94 ± 0.36				0.53 ± 0.46	0.32 ± 0.28	25.04 ± 1.74	1050.03	0.16
		2.43 ± 0.19	-1.85 ± 0.22	-4.66 ± 0.63			66.19 ± 5.50	885.12	0.61
		4.09 ± 0.29	-0.50 ± 0.29		-3.32 ± 0.38		49.48 ± 2.51	851.99	0.69
		2.15 ± 0.22	-1.94 ± 0.26			-0.47 ± 0.27	30.33 ± 2.38	933.86	0.54
		4.06 ± 0.29		-1.85 ± 0.75	-3.31 ± 0.31		64.70 ± 5.44	848.76	0.68
		2.85 ± 0.23		-6.20 ± 0.62		-1.71 ± 0.22	92.99 ± 6.09	897.60	0.57
		4.19 ± 0.31			-3.70 ± 0.32	-0.06 ± 0.27	52.12 ± 2.55	855.07	0.68
			-1.42 ± 0.29	-4.09 ± 0.71	1.49 ± 0.26		48.84 ± 4.95	1013.67	0.30
			-1.10 ± 0.27	-1.74 ± 0.60		1.01 ± 0.22	30.02 ± 5.51	1023.57	0.29
			-1.46 ± 0.29		0.13 ± 0.26	0.93 ± 0.26	15.14 ± 1.93	1031.79	0.29
				-3.47 ± 0.81	0.46 ± 0.34	-0.01 ± 0.29	49.36 ± 6.84	1038.49	0.17

This page was intentionally left blank

Chapter 9

Appendix C

9.1 Table

In this section of the appendix, we present the table with the results of the hierarchical SED fitting of the A^{3}COSMOS sample using the TMBB model.

Table 9.1: Result parameters from the hierarchical SED fitting of the A^{3}COSMOS sample using the two modified black-bodies (TMBB) model. The parameters are the dust mass ($\log M_c$), temperature (T_c), and emissivity index (β_c) of the cold dust component, and the dust mass ($\log M_w$) and temperature (T_w) of the warm dust component. The emissivity index of the warm component has been fixed to $\beta_w = 1.5$. The horizontal lines separate the five redshift bins (from $z = 1$ to $z = 3.5$ with $\Delta z = 0.5$).

A^{3}COSMOS ID	z	$\log M_c$ [M$_\odot$]	T_c [K]	β_c	$\log M_w$ [M$_\odot$]	T_w [K]
372951	1.0989	9.30±0.07	20.27±0.92	2.73±0.20	7.68±0.18	51.66±3.37
384461	1.469	9.45±0.07	20.58±1.09	2.84±0.21	8.08±0.21	54.35±3.87
390270	1.1682	9.21±0.10	20.28±0.99	2.75±0.22	7.68±0.18	51.37±2.98
405986	1.3544	9.36±0.08	20.40±0.96	2.63±0.20	7.80±0.19	51.90±3.30
423073	1.232	9.37±0.08	20.59±1.05	2.75±0.19	7.97±0.20	53.63±3.41
441394	1.153	9.17±0.13	20.48±1.07	2.60±0.27	7.73±0.18	51.29±3.25
478411	1.1915	9.32±0.07	20.43±0.92	2.75±0.18	7.92±0.16	54.04±3.16
485345	1.1885	9.29±0.10	20.47±1.04	2.74±0.24	7.79±0.18	52.18±3.14
517302	1.248	9.19±0.08	20.45±1.00	2.84±0.21	7.85±0.16	54.08±3.11
541203	1.212	9.32±0.08	20.27±0.93	2.65±0.19	7.73±0.15	51.72±2.78
588570	1.156	9.47±0.11	20.32±1.06	2.58±0.22	7.88±0.16	53.42±3.31
598441	1.3654	9.26±0.11	20.40±0.97	2.83±0.24	7.81±0.16	53.03±3.32

Continued on next page

Table 9.1 – continued from previous page

A^{3}COSMOS ID	z	$\log M_c$ [$M_\odot$]	T_c [K]	β_c	$\log M_w$ [$M_\odot$]	T_w [K]
634894	1.098	9.25±0.08	20.31±0.94	2.66±0.20	7.66±0.18	51.18±3.48
667343	1.46	9.24±0.08	20.43±1.03	2.94±0.23	7.90±0.16	55.01±3.65
670126	1.149	9.28±0.09	20.35±0.97	2.57±0.23	7.71±0.18	51.32±3.32
694031	1.1484	9.78±0.08	20.27±1.13	2.44±0.21	7.94±0.26	52.85±5.15
741524	1.1055	9.32±0.10	20.24±1.00	2.64±0.19	7.70±0.17	51.46±3.29
760036	1.057	9.51±0.10	20.42±1.05	2.72±0.21	7.98±0.18	54.02±3.74
766157	1.456	9.31±0.05	20.51±0.98	2.88±0.19	7.96±0.18	54.27±3.45
815019	1.371	9.20±0.09	20.42±0.98	2.76±0.21	7.81±0.16	52.58±2.92
816106	1.42	9.22±0.08	20.47±1.02	2.91±0.20	7.90±0.17	54.46±3.37
829949	1.0913	9.26±0.07	20.38±0.89	2.76±0.18	7.85±0.14	53.20±2.75
831023	1.21	9.09±0.11	20.54±1.12	2.83±0.22	7.89±0.15	53.94±3.11
835513	1.3995	9.25±0.09	20.48±0.97	2.83±0.20	7.91±0.15	54.88±3.28
888048	1.185	9.21±0.09	20.46±1.00	2.80±0.20	7.87±0.15	53.16±2.77
888769	1.453	9.27±0.06	20.39±0.95	2.83±0.18	7.84±0.15	52.85±2.79
894931	1.322	9.34±0.09	20.28±0.99	2.67±0.20	7.77±0.17	52.20±3.15
934366	1.4011	9.34±0.09	20.45±1.00	2.61±0.20	7.91±0.17	53.12±3.05
964509	1.019	9.27±0.10	20.18±1.00	2.66±0.23	7.60±0.27	50.56±4.80
969105	1.362	9.28±0.07	20.57±1.05	2.93±0.22	8.01±0.19	55.08±3.79
375061	1.9892	9.67±0.10	22.15±2.80	2.19±0.36	8.36±0.29	51.76±2.51
410945	1.959	9.85±0.10	22.28±2.32	2.31±0.41	7.93±0.32	51.70±2.89
528505	1.9945	9.57±0.13	19.94±2.77	2.02±0.47	8.01±0.24	51.99±2.48
531775	1.77	9.50±0.13	20.33±2.85	2.16±0.40	8.10±0.25	51.83±2.61
596108	1.8022	9.45±0.12	20.05±2.53	2.29±0.41	7.81±0.17	51.39±2.57
672158	1.9502	9.62±0.11	19.75±2.66	2.11±0.42	7.92±0.17	52.42±2.57
672861	1.5931	9.64±0.10	21.27±2.31	2.46±0.38	7.97±0.28	51.77±2.38
674634	1.5238	9.41±0.11	21.03±2.74	2.38±0.56	7.76±0.20	51.59±2.82
682463	1.581	9.52±0.08	22.08±2.36	2.33±0.36	8.25±0.16	51.55±2.27
690669	1.8343	9.34±0.17	20.72±3.25	2.16±0.47	8.27±0.20	51.66±2.31
702734	1.798	9.63±0.09	23.07±2.57	2.56±0.38	8.33±0.24	51.84±2.77
709850	1.8009	9.69±0.10	20.99±2.35	2.37±0.40	8.03±0.17	52.09±2.43
714907	1.5817	9.52±0.10	22.49±3.07	2.40±0.42	8.50±0.24	51.89±2.78
830116	1.8251	9.49±0.14	19.52±2.97	1.95±0.46	8.10±0.17	52.35±2.41
839509	1.8226	9.61±0.13	21.40±2.67	2.10±0.33	8.14±0.23	51.43±2.39
887050	1.9922	9.58±0.10	22.33±2.54	2.30±0.33	8.22±0.27	51.58±2.41
919414	1.887	9.46±0.14	21.24±3.35	2.07±0.40	8.54±0.20	51.64±2.39
980250	1.7598	9.74±0.08	21.63±2.47	2.50±0.43	7.94±0.29	51.77±2.48
1263541	1.894	9.70±0.11	22.32±2.65	2.15±0.34	8.17±0.30	51.41±2.49
1264091	1.651	9.59±0.11	21.50±2.79	2.07±0.41	8.35±0.32	51.95±2.47
462117	2.1571	9.69±0.09	25.50±2.06	2.11±0.20	8.29±0.19	57.05±2.92
475050	2.0468	9.49±0.07	24.60±1.77	2.06±0.22	8.02±0.15	59.18±2.92
479133	2.0316	9.16±0.15	25.18±2.11	2.24±0.29	7.71±0.36	57.06±5.06

Continued on next page

Table 9.1 – continued from previous page

A^{3}COSMOS ID	z	$\log M_c$ [$M_\odot$]	T_c [K]	β_c	$\log M_w$ [$M_\odot$]	T_w [K]
518250	2.4348	9.72±0.06	24.85±2.05	2.12±0.24	8.34±0.18	59.55±3.27
569615	2.3545	9.84±0.06	24.58±1.71	2.04±0.23	8.03±0.23	58.11±4.37
583333	2.1	9.68±0.06	24.81±1.74	2.10±0.22	8.12±0.16	58.39±2.81
587450	2.459	9.69±0.08	24.95±1.92	2.03±0.20	8.19±0.18	58.72±3.18
600465	2.1021	9.53±0.10	25.38±2.01	2.25±0.25	8.01±0.22	56.09±3.47
600601	2.1065	9.87±0.06	25.01±2.00	2.03±0.21	8.41±0.14	59.66±2.71
623091	2.2071	9.68±0.08	24.77±1.83	2.02±0.20	8.11±0.18	56.82±3.10
623536	2.4368	9.79±0.09	24.02±2.11	1.88±0.29	8.23±0.15	59.26±3.06
667642	2.2765	9.32±0.19	23.92±2.24	2.05±0.31	7.63±0.28	58.19±4.48
685079	2.3888	9.51±0.10	24.95±1.91	2.18±0.24	7.98±0.29	57.14±3.15
700080	2.0001	9.15±0.12	25.42±2.26	2.23±0.28	7.73±0.28	57.18±3.91
700373	2.1738	9.47±0.16	24.88±1.94	2.14±0.26	7.91±0.22	57.82±4.33
702910	2.3777	9.83±0.04	24.99±1.67	2.09±0.20	8.04±0.17	56.96±2.77
709365	2.0283	9.65±0.05	25.40±1.86	2.06±0.19	8.01±0.19	56.12±3.26
709682	2.2078	9.02±0.15	25.23±2.36	2.18±0.29	7.70±0.25	56.53±4.53
754372	2.4355	9.81±0.16	23.95±2.72	1.77±0.37	8.40±0.14	60.15±3.39
767831	2.3057	9.60±0.11	24.40±1.83	2.05±0.23	8.01±0.18	58.30±3.05
806401	2.2503	9.71±0.19	24.62±2.18	1.95±0.26	8.16±0.28	58.37±3.86
831167	2.0818	9.73±0.07	24.87±1.82	2.06±0.21	8.19±0.15	58.21±3.18
920788	2.1737	9.58±0.10	24.17±2.13	2.05±0.27	8.04±0.25	58.94±3.30
932331	2.1143	9.78±0.11	24.70±2.02	2.02±0.27	8.29±0.26	58.73±3.37
969701	2.0757	9.18±0.17	25.43±2.60	2.26±0.28	7.82±0.28	56.20±3.74
1187361	2.125	9.54±0.13	23.98±2.13	1.97±0.26	7.93±0.22	58.09±4.78
1188847	2.348	9.64±0.08	25.20±2.18	2.18±0.26	8.24±0.21	58.45±3.14
1190148	2.396	9.28±0.14	24.81±2.14	2.17±0.31	7.92±0.24	56.68±4.87
1196061	2.469	9.70±0.12	24.28±1.99	1.97±0.22	8.12±0.20	58.24±3.08
423273	2.5845	9.67±0.11	24.74±3.41	1.98±0.32	7.61±0.27	75.61±5.75
427827	2.709	9.30±0.11	30.62±3.01	2.24±0.27	7.70±0.25	74.25±5.43
494175	2.584	9.63±0.13	28.87±2.65	2.10±0.27	7.73±0.25	74.66±5.53
561437	2.5645	9.44±0.09	29.11±2.47	2.14±0.26	7.49±0.33	74.29±5.61
573836	2.8818	9.10±0.13	31.35±3.65	2.21±0.29	7.95±0.23	74.60±5.24
610723	2.6033	9.50±0.12	28.11±2.71	2.03±0.28	7.35±0.33	74.23±5.64
624284	2.5358	9.32±0.17	27.55±3.76	2.12±0.30	8.05±0.17	76.06±4.67
640145	2.9412	9.43±0.10	27.53±2.99	2.10±0.28	7.92±0.17	76.95±5.12
681603	2.6653	9.63±0.13	23.74±3.47	2.01±0.36	7.50±0.20	76.33±5.51
682558	2.6161	9.80±0.07	27.72±3.17	1.99±0.28	7.79±0.39	75.68±6.09
683281	2.513	9.31±0.11	29.41±3.25	2.19±0.26	7.62±0.39	74.42±5.51
686297	2.5272	9.21±0.13	29.82±2.53	2.14±0.27	7.17±0.29	72.91±6.11
693902	2.8922	9.44±0.09	25.88±2.71	2.06±0.29	7.40±0.22	75.64±5.55
728449	2.5411	9.20±0.13	29.63±2.64	2.12±0.31	7.04±0.37	72.56±7.15
746328	2.9304	9.34±0.07	27.37±2.60	2.09±0.26	7.39±0.23	73.07±5.37

Continued on next page

Table 9.1 – continued from previous page

A^{3}COSMOS ID	z	$\log M_c$ [$M_\odot$]	T_c [K]	β_c	$\log M_w$ [$M_\odot$]	T_w [K]
816984	2.7185	9.63±0.10	25.20±3.22	1.98±0.33	7.33±0.38	74.67±6.03
841273	2.9023	9.58±0.06	27.87±1.97	2.12±0.25	7.42±0.20	74.93±5.23
882859	2.5565	9.61±0.13	28.53±2.35	2.08±0.28	7.65±0.23	75.16±5.39
932436	2.5283	9.56±0.09	27.06±2.96	2.00±0.29	7.58±0.30	74.91±5.67
1190833	2.831	9.11±0.17	30.47±3.49	2.18±0.28	7.74±0.20	73.83±4.84
1191132	2.986	9.34±0.07	30.36±2.47	2.15±0.25	7.66±0.23	73.39±5.07
590368	3.0021	9.18±0.06	31.26±3.15	2.24±0.30	7.24±0.22	83.72±5.73
593906	3.17	9.53±0.16	30.08±4.73	1.95±0.44	7.69±0.37	84.18±5.72
598630	3.2366	8.82±0.13	33.08±4.08	2.43±0.43	7.15±0.25	82.90±5.82
646184	3.308	9.24±0.09	31.56±3.91	2.30±0.36	7.39±0.42	83.87±5.80
681816	3.0613	9.11±0.10	30.63±3.62	2.23±0.35	7.00±0.46	83.60±5.97
711773	3.3334	8.98±0.15	29.88±3.80	2.14±0.43	6.90±0.52	83.25±6.01
813703	3.024	9.01±0.10	31.96±4.51	2.26±0.34	7.72±0.28	84.13±5.43
842140	3.0313	10.09±0.17	24.86±5.88	1.87±0.58	7.45±0.52	83.98±6.54
897299	3.2737	9.35±0.10	33.10±3.70	2.32±0.36	7.53±0.25	84.16±5.80
1233443	3.401	9.13±0.15	31.54±4.10	2.25±0.39	7.75±0.59	84.26±5.71

Chapter 10

Appendix D

Here we present appendix material related to Chapter 5.

10.1 Comparison of 870 μm sizes and flux densities derived using different methods

In Figure 10.1, we compare the FIR sizes and and flux densities of the 870 μm ALMA emission, measured using four different methods: 1) fit on the image assuming a 2D Gaussian profile, 2) fit with `uvmodelfit` assuming a 2D Gaussian profile, 3) fit of the uv-visibilities assuming an exponential profile (equivalent to a Sérsic profile with $n = 1$), and 4) fit of the uv-visibilities with the 'preferred' model according to the BIC (point, Gaussian, exponential or Gaussian+point model, see Section 5.2.2). For the 2D Gaussian fit on the image plane, we show two points representing the sizes of the major and minor axis (in violet) and the mean value (in magenta). For `uvmodelfit`, we show the mean value between the major and minor axis. For cid_1057 and cid_451, the S/N is very low (3.6 and 5.5, respectively), therefore we do not consider their size measurements to be reliable. These two sources are highlighted with a grey band in Figure 10.1.

In general, the sizes measured with different methods are in agreement within the uncertainties. We note that the sizes measured with the exponential profile are larger than the sizes measured with the Gaussian profile (factor of 1.38 on average) by construction,

since the exponential profile does not go rapidly to zero at larger radii and thus considers a larger amount of flux at large radii.

The flux densities are mostly insensitive to the method used. The only notable difference are for cid_1057 and cid_346. cid_1057 has a very low S/N, thus the flux measurements are not very reliable. For cid_346, the Gaussian fit with `uvmodelfit` measures a lower flux than the other methods. The 870 μm emission of this galaxy is better described by a Gaussian+point source or by an exponential profile, therefore the Gaussian model can not fit well the central flux peak and underestimates the total flux.

Here we comment more specifically on each target:

- X_N_81_44: for this target the preferred model, according to the BIC, is the exponential profile. The sizes measured with the different methods are in general agreement and close to the size of the ALMA beam.
- XID36: the difference in BIC between the exponential and Gaussian model is less than two, therefore it is not clear than one model is performing better than the other.
- XID419: is better fit by a Gaussian profile. The sizes measured with the different methods are in agreement.
- cid_1057: the S/N is too low and both the size and flux density measurements are unreliable.
- cid_346: the preferred model is a Gaussian plus a point source. According to the BIC, the Gaussian profile is not a good fit for this source, while the exponential profile produces a reasonable fit. The size measured with the exponential profile is larger than the size measured by the Gaussian+point profile. This is because the Gaussian+point profile assumes that a larger fraction of the flux is concentrated in the center compared to the exponential profile.
- cid_451: the S/N is low (S/N= 5.5). However, the sizes and flux densities measured with the different methods are consistent with each other, albeit with large uncertainties.
- cid_1205: the preferred model according to the BIC is a point source. This source is also consistent with a point source in the `uvmodelfit` results.

In Tables 10.1 and 10.2, we provide all the measurements obtained with the different methods. We note that when we compare our measurements to literature values in Section 5.4.2, we used the sizes obtained with the same method used in the literature.

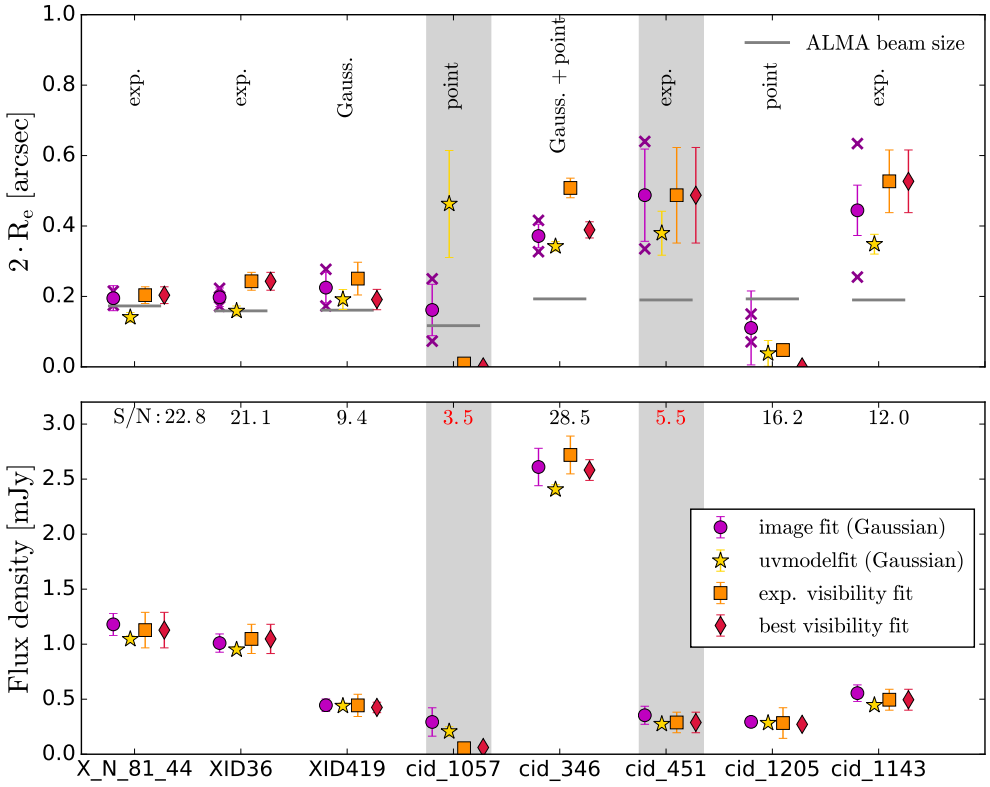

Figure 10.1. Comparison of the FIR sizes and flux densities derived using different methods: fit of a 2D Gaussian on the image plane (circles), fit of a 2D Gaussian using `uvmultifit` (stars), fit of the visibilities assuming an exponential profile (squares), and fit of the visibilities with the 'preferred model' according to the BIC (diamonds). The preferred model for each object is written on the top part of the figure. *Upper panel*: Size measurements expressed as two times the effective radius (R_e). The grey horizontal lines represent the size of the ALMA beam for each object. For the 2D Gaussian fit on the image plane, the two magenta crosses represent the sizes of the major and minor axis. *Bottom panel:* integrated flux densities measured with different methods. The peak signal-to-noise (S/N) of the ALMA images is written on the top part of the panel. The results for the two objects with S/N too low to obtain reliable measurements (cid_1057 and cid_451) are highlighted with background grey shading.

Table 10.1. ALMA 870 μm flux densities (F), effective radii (R_e), and ratio between major and minor axes obtained with two methods: 1) fit on the image (created with natural weighting) and 2) using `uvmodelfit`. For both methods we assume a 2D Gaussian profile. (*) If the peak S/N < 8 in the ALMA maps, we do not consider the size measurements to be reliable.

Method:		image fit			`uvmodelfit`		
ID	S/N	F [mJy]	R_e [mas]	axial ratio	F [mJy]	R_e [mas]	axial ratio
X_N_81_44	22.8	1.18±0.10	98±18	1.23±0.32	1.05±0.03	70±5	1.00±0.11
XID36	21.1	1.01±0.08	99±13	1.30±0.25	0.95±0.03	79±5	1.22±0.12
XID419	9.4	0.45±0.06	112±22	1.60±0.46	0.44±0.03	96±14	2.88±0.80
cid_1057*	3.5	0.29±0.13	81±36	3.42±3.05	0.21±0.04	231±61	1.16±0.41
cid_346	28.5	2.61±0.17	186±17	1.27±0.16	2.41±0.04	171±5	1.31±0.06
cid_451*	5.5	0.35±0.08	244±66	1.91±0.76	0.27±0.02	190±36	3.15±0.83
cid_1205	16.2	0.29±0.02	55±52	2.11±3.17	0.28±0.01	19±13	1.00±1.00
cid_1143	12.0	0.56±0.07	222±36	2.49±0.60	0.45±0.02	174±18	4.60±0.70

Table 10.2. ALMA 870 μm flux densities (F) and effective radii (R_e), obtained through the fit on the visibilities using python, assuming different symmetric (i.e. axis ratio = 1) models. The model with the smallest BIC (Bayesian Information Criterion) value is the preferred model. The stars (*) mark the targets with the peak S/N < 8 in the ALMA maps, for which we do not consider the size measurements to be reliable. [a]For the Gaussian+point model, we report: the total flux F(tot)=F(point)+F(Gaussian), the flux of the point source F(point), the half-light radius of the total profile R_e(tot), the half-light radius of the Gaussian component R_e(Gauss). [b]For XID36, the difference in BIC between the exponential and Gaussian model is < 2, therefore it is not clear than one model is performing better than the other.

Model:	point		Gaussian			exponential			Gauss.+point [a]					
ID	F [mJy]	BIC	F [mJy]	R_e [mas]	BIC	F [mJy]	R_e [mas]	BIC	F(tot) [mJy]	F(point) [mJy]	R_e(tot) [mas]	R_e(Gauss) [mas]	BIC	preferred model
X_N_81_44	0.73±0.03	155.81	1.06±0.05	75±7	80.73	1.13±0.16	102±12	74.57	1.13±0.19	0.29±0.10	84±20	111±20	77.75	exp.
XID36	0.58±0.03	176.01	0.97±0.05	86±7	51.46	1.05±0.13	122±13	50.02	0.98±0.13	0.08±0.06	90±11	96±11	55.44	exp./Gauss.[b]
XID419	0.23±0.02	84.32	0.43±0.05	96±14	42.34	0.44±0.10	125±23	45.77	0.42±0.08	0.02±0.02	97±17	101±17	47.23	Gauss.
cid_1057*	0.06±0.02	51.69	0.07±0.02	9±8	55.66	0.05±0.03	5±2	55.85	0.07±0.05	0.03±0.02	1±8	9±8	59.72	point
cid_346	1.01±0.03	673.49	2.41±0.08	173±7	79.40	2.72±0.17	254±14	42.91	2.58±0.14	0.35±0.05	194±11	219±11	38.77	Gauss.+point
cid_451*	0.11±0.02	68.82	0.28±0.05	194±42	45.88	0.29±0.09	244±68	45.46	0.29±0.08	0.04±0.02	212±53	236±53	47.28	exp.l
cid_1205	0.27±0.02	43.71	0.28±0.02	9±7	46.80	0.28±0.14	24±9	45.30	0.28±0.18	0.13±0.09	3±9	10±9	50.45	point
cid_1143	0.18±0.01	145.47	0.39±0.04	149±23	71.61	0.50±0.10	263±44	60.68	0.50±0.08	0.08±0.02	234±55	269±55	67.56	exp.

10.2 Models used to fit the FIR profile

To assess the morphology of the FIR emission, we fit the visibilities versus uv-distances using the following models: point source, Gaussian, Gaussian+point source, and exponential profile. We apply the Fourier-transform to the models in order to be able to perform the fit in the visibilities vs. uv-distance plane. The models in the visibilities vs. uv-distance plane are defined as:

- *Point source*: a point source is represented as a constant model as a function of uv-distance:

$$f(x, F) = F, \tag{10.1}$$

  where F is the flux density in mJy and x is the uv-distance in units of kλ, where λ is the wavelength of the observation.

- *Gaussian profile*: the Fourier transform of a Gaussian model is also a Gaussian defined as:

$$f(x, F, \sigma_{uv}) = F \cdot \exp\left(-\frac{1}{2}\left(\frac{x}{\sigma_{uv}}\right)^2\right), \tag{10.2}$$

  where F is the flux density in mJy and σ_{uv} is the scale parameter. σ_{uv} is related to the effective radius R_e (in radians) as:

$$R_e[\text{rad}] = \frac{FWHM}{2} = \frac{2.355}{2} \cdot \sigma = \frac{2.355}{2} \cdot \frac{1}{2\pi\sigma_{uv} \cdot 10^3}, \tag{10.3}$$

  where the factor 10^3 is necessary to convert from kλ to λ. The effective radius in arcsec is obtained as $R_e[\text{arcsec}] = R_e[\text{rad}]\frac{180 \cdot 3600}{\pi}$.

- *Gaussian+point source*: this model combines the previous two models:

$$f(x, F_{Gauss.}, \sigma_{uv}, F_{point}) = f_{Gauss}(x, F_{Gauss}, \sigma_{uv}) + F_{point}, \tag{10.4}$$

  where $F_{Gauss.}$ and F_{point} are the flux densities of the Gaussian and point source components, respectively. The total flux density is given by $F(tot) = F_{Gauss.} + F_{point}$.

- *Exponential profile*: the exponential profile is modelled as :

$$f(x, F, \sigma_{uv}) = F \cdot \frac{\sigma_{uv}}{\sigma_{uv}^2 + x^2}, \tag{10.5}$$

Table 10.3. Range of priors used for the fit of the visibilities vs. *uv*-distances. I is the flux density

Model	parameter	priors
point	F	$0-1000$ mJy
Gaussian	F	$0-1000$ mJy
	σ_{uv}	$0-10000$ kλ
Gaussian+point	F(Gauss)	$0-5$ mJy
	σ_{uv}	$0-10000$ kλ
	F(point)	$0-5$ mJy
exponential	F	$0-1000$ mJy
	σ_{uv}	$0-20000$ kλ

where σ_{uv} is related to the effective radius R_e (in radians) as:

$$R_e[\mathrm{rad}] = 1.6783 \cdot \sigma = 1.6783 \cdot \frac{1}{2\pi\sigma_{uv} \cdot 10^3}. \tag{10.6}$$

The priors used for the Bayesian fitting are reported in Table 10.3.

10.3 Astrometry of the SINFONI data

In this Section, we explain the details of the registration of the astrometry of the SINFONI data-cubes. As explained in Section 5.3.2, the absolute position of the SINFONI cubes, as provided in the header, is not sufficiently accurate for our purposes. The small field of view of the SINFONI images (3×3 arcsec^2) does not allow us to correct the astrometry using nearby stars, since usually the target is the only visible source in the field of view. Therefore, we have to derive the absolute coordinates from other images.

Reference coordinates: We use H-band and K-band images with a large field of view (3×3 arcmin^2) to determine the reference coordinates of our targets that we later use to register the astrometry of the SINFONI data-cubes.

We use K-band and H-band images from the VLT/VISTA instrument taken as part of the UltraVISTA survey for COSMOS (**?**) and as part of the VHS (VISTA Hemisphere Survey) for XMM-XXL (**?**). For CDF-S, we use K- and H-band images from VLT/ISAAC (**?**).

To determine the coordinates from the H/K-band images, we apply the following procedure. First, we align the H/K-band images to the *Gaia* DR2 catalog, using the Graphical Astronomy and Image Analysis Tool (GAIA) that is part of the `Starlink` software (Currie

et al. 2014). There are at least five objects in common between the *Gaia* DR2 catalog and each image that allow us to accurately align the images to the *Gaia* astrometry [1]. Then, we determine the centroid position of our target in the 'astrometry corrected' image by fitting a 2D Gaussian to the source.

We apply this procedure to both the H-band and K-band images. The offsets between the coordinates derived from the H-band and K-band are smaller than one pixel (< 0.07"), therefore we can assume that the H-band and K-band emission peak at the same position. We decide to use the coordinates derived from the K-band corrected images to register the astrometry of both the H-band and K-band SINFONI images.

We compare the K-band coordinates with the *Gaia* coordinates for the two objects detected in *Gaia*. For cid_346, the K-band coordinates agree very well with the *Gaia* coordinates (offset 7.3 mas). For X_N_81_44, the K-band coordinates are shifted by 0.05" to the West with respect to the coordinates from *Gaia*. Given the low resolution of the K-band image for this target (FWHM PSF 1.04"), we decide to use the coordinates from *Gaia* for this source. We note that these two targets are Type 1 AGN, and are dominated by the point source emission of the AGN across the optical and near-infrared bands. Finally, we note that XID419 is only marginally detected in the K-band image (peak S/N$<$ 6) and thus it is difficult to determine its position. Therefore for this target we rely on the coordinates derived from the *HST*/WFC3 images reported in Scholtz et al. (2020).

Registration of the SINFONI images: We use these coordinates to register the position of the peak of the emission in the SINFONI data cubes. The emission of the H/K-band filters is dominated by the continuum, but there is also some contribution from the emission lines.

For the Type 1 AGN, we check that the position of the continuum and the position derived by collapsing the total SINFONI data-cubes are in agreement, both in the H- and K-band (offset $< 0.02''$).

For the Type 2, the continuum is significantly detected in the SINFONI maps only in one object (XID36). For this target, we test that the position of the continuum and the position derived by collapsing the total data-cube are in agreement (offset $< 0.007''$), both in the H- and K-band. For the other targets, we use the SINFONI spectra to estimate the relative contribution of continuum and emission lines to the total emission in the H/K

[1] There is an exception: cid_1205 that has only 3 sources in common between the GAIA catalog and the H/K-band image. For this object the H/K-band position is in perfect agreement with the FIR position measured from the ALMA map, therefore we consider the H/K-band coordinates to be reliable.

band VISTA and ISAAC filters. The continuum contribution is $> 70\%$ for all targets. There is the possibility that the SINFONI IFU is less sensitive to the continuum emission than the VISTA and ISAAC filters. Consequently, there would be a larger contribution from the line emission to the position derived from the total collapsed SINFONI data-cube. We test that for XID36 this is not a problem. For the other targets, we can not rule out this possibility with the current data. Given that for the other targets the line emission is very faint, probably it would not contribute much to the total emission in the SINFONI cubes.

Uncertainties on the coordinate registration: The typical uncertainty on the *Gaia* coordinates is ≤ 4 mas. The precision of the alignment of the K-band images with the *Gaia* images is about half pixel (75 mas for COSMOS and 130 mas for CDF-S). The uncertainties from the 2D Gaussian fit of the VISTA or ISAAC K-band images are in the range $1 - 49$ mas (median 4 mas). We also consider the uncertainties due to the size of the VISTA or ISAAC K-band PSF (0.78-1.04"), calculated as PSF/(2·S/N) following **?**, which are in the range $3 - 40$ mas. The uncertainties on the position of the emission of the SINFONI cubes is $\sim$ half pixel (25 mas).

To estimate the total uncertainties of the derived K-band coordinates, we add in quadrature all the above uncertainties. These uncertainties are dominated by the pixel size of the K-band images. In summary, the uncertainties on the derived SINFONI astrometry for our sample are in the range $0.03 - 0.14$".

10.4 Spectral energy distributions (SEDs)

In Figure 10.2, we show the spectral energy distributions of our targets (rest-frame wavelength range 0.1 μm$-$10 cm), together with the best fit model from Circosta et al. (2018). We use these models to predict the percentage contribution due to dust heated by the AGN at 870 μm. We also show the synchrotron emission contribution at 870 μm, predicted based on the available radio photometry. The different sources that can contribute to the 870 μm flux are discussed in Section 5.4.1.

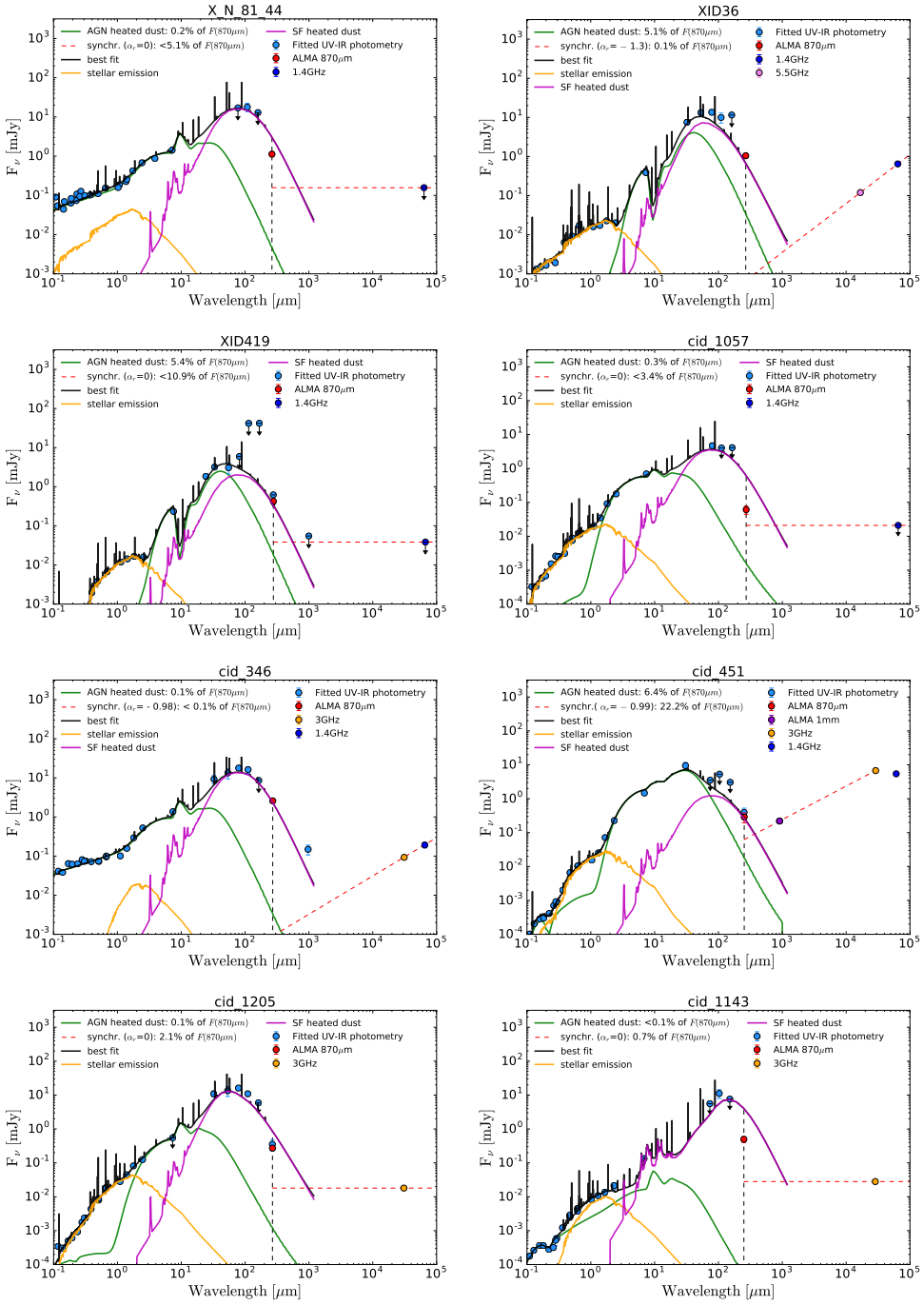

Figure 10.2. Rest-frame spectral energy distribution (SED) of our sample. The light blue data points represent the UV-IR photometry that was used for the SED fitting (Circosta et al. 2018). The red point shows our ALMA Band 7 flux measurements. The violet point in cid_451 shows the ALMA Band 3 flux from Cicosta et al. (2020, submitted). The blue, orange, and pink points show the radio fluxes at 1.4, 3, and 5 GHz, respectively. The arrows indicate 3σ upper limits. The solid curves show the results of the SED fitting with CIGALE: in black is the total best-fit model (including the contribution the from nebular emission component), in orange the dust-attenuated stellar emission, in magenta the emission from dust heated by star-formation and in green the emission from dust heated by the AGN. To estimate the maximum contribution of synchrotron emission to the 870 μm flux density we parametrized this emission as a power law with spectral index α_r (dashed red line), normalized at 3 GHz (10cm) or 1.4 GHz (21cm), depending on the available radio data. For the galaxies with radio fluxes in two bands, we derived α_r based on the two fluxes. On the plot we show the estimated contribution (in percentage) from dust heated by the AGN and from synchrotron emission to the 870 μm flux estimated from the dust emission template.

This page was intentionally left blank

Bibliography

Aalto S., et al., 1995, A&A, 300, 369

Abazajian K. N., et al., 2009, The Astrophysical Journal Supplement, 182, 543

Abdo A. A., et al., 2010, The Astrophysical Journal, 710, 133

Accurso G., et al., 2017a, Monthly Notices of the Royal Astronomical Society, 464, 3315

Accurso G., et al., 2017b, Monthly Notices of the Royal Astronomical Society, 470, 4750

Aird J., et al., 2017, Monthly Notices of the Royal Astronomical Society, 465, 3390

Alatalo K., et al., 2015, The Astrophysical Journal, 798, 31

Alonso-Herrero A., et al., 2018, The Astrophysical Journal, 859, 144

Alonso-Herrero A., et al., 2019, A&A, 628, A65

Aravena M., et al., 2016, The Astrophysical Journal, 833, 68

Aravena M., et al., 2019, The Astrophysical Journal, 882, 136

Armus L., et al., 2009, Publications of the Astronomical Society of the Pacific, 121, 559

Assef R. J., et al., 2013, The Astrophysical Journal, 772, 26

Azadi M., et al., 2015, The Astrophysical Journal, 806, 187

Baes M., et al., 2003, Monthly Notice of the Royal Astronomical Society, 343, 1081

Bakx T. J. L. C., et al., 2020, Monthly Notices of the Royal Astronomical Society, 493, 4294

Baldry I. K., et al., 2012, Monthly Notices of the Royal Astronomical Society, 421, 621

Baldwin J. A., et al., 1981, Astronomical Society of the Pacific, 93, 5

Balog Z., et al., 2014, Experimental Astronomy, 37, 129

Banerji M., et al., 2009, The Astrophysical Journal, 703, 2249

Barlow M. J., 1978, Monthly Notices of the Royal Astronomical Society, 183, 417

Barnard J., et al., 2000, Statistica Sinica, 10

Barro G., et al., 2016, The Astrophysical Journal Letters, 827, L32

Baumgartner W. H., et al., 2013, The Astrophysical Journal Supplement, 207, 19

Bayet E., et al., 2011, Monthly Notices of the Royal Astronomical Society, 414, 1583

Becker R. H., et al., 1995, Astrophysical Journal v.450, 450, 559

Beckmann R. S., et al., 2017, Monthly Notices of the Royal Astronomical Society, 472, 949

Behroozi P. S., et al., 2013, The Astrophysical Journal, 770, 57

Bell T. A., et al., 2005, Monthly Notices of the Royal Astronomical Society, 357, 961

Bell T. A., et al., 2006, Monthly Notices of the Royal Astronomical Society, 371, 1865

Bendo G. J., et al., 2006, The Astrophysical Journal, 652, 283

Bendo G. J., et al., 2013, Monthly Notices of the Royal Astronomical Society, 433, 3062

Bergin E. A., Tafalla M., 2007, Annual Review of Astronomy and Astrophysics, 45, 339

Bergin E. A., et al., 2013, Nature, 493, 644

Berta S., et al., 2016, A&A, 587, A73

Bertemes C., et al., 2018, Monthly Notices of the Royal Astronomical Society, 478, 1442

Bertoldi F., et al., 2003, A&A, 406, L55

Best P. N., et al., 2005, Monthly Notices of the Royal Astronomical Society, 362, 25

Béthermin M., et al., 2015, A&A, 573, A113

Béthermin M., et al., 2020, arXiv, p. arXiv:2002.00962

Bevan A., Barlow M. J., 2016, Monthly Notices of the Royal Astronomical Society, 456, 1269

Bevan A., et al., 2017, Monthly Notices of the Royal Astronomical Society, 465, 4044

Bianchi S., 2008, A&A, 490, 461

Bianchi S., 2013, A&A, 552, A89

Bianchi S., Schneider R., 2007, Monthly Notices of the Royal Astronomical Society, 378, 973

Bianchi S., et al., 2018, A&A, 620, A112

Bieri R., et al., 2017, Monthly Notices of the Royal Astronomical Society, 464, 1854

Bigiel F., et al., 2008, The Astronomical Journal, 136, 2846

Bîrzan L., et al., 2004, The Astrophysical Journal, 607, 800

Bisbas T. G., et al., 2015, The Astrophysical Journal, 803, 37

Bisbas T. G., et al., 2017, The Astrophysical Journal, 839, 90

Bischetti M., et al., 2019a, A&A, 628, A118

Bischetti M., et al., 2019b, A&A, 630, A59

Bluck A. F. L., et al., 2014, Monthly Notices of the Royal Astronomical Society, 441, 599

Bohlin R. C., et al., 1978, Astrophysical Journal, 224, 132

Boissay R., et al., 2016, A&A, 588, A70

Bolatto A. D., et al., 2008, The Astrophysical Journal, 686, 948

Bolatto A. D., et al., 2013, Annual Review of Astronomy and Astrophysics, 51, 207

Bolzonella M., et al., 2010, A&A, 524, A76

Bonfield D. G., et al., 2011, Monthly Notices of the Royal Astronomical Society, 416, 13

Boquien M., et al., 2019, A&A, 622, A103

Boselli A., Gavazzi G., 2006, The Publications of the Astronomical Society of the Pacific, 118, 517

Boselli A., et al., 2010a, Publications of the Astronomical Society of Pacific, 122, 261

Boselli A., et al., 2010b, A&A, 518, L61

Boselli A., et al., 2012, A&A, 540, A54

Boselli A., et al., 2013, A&A, 550, A114

Bot C., et al., 2010, A&A, 523, A20

Bothwell M. S., et al., 2013, Monthly Notices of the Royal Astronomical Society, 429, 3047

Boulanger F., et al., 1996, A&A, 312, 256

Bourne N., et al., 2019, Monthly Notices of the Royal Astronomical Society, 482, 3135

Boyer M. L., et al., 2019, arXiv, p. arXiv:1904.02172

Brinchmann J., et al., 2004, Monthly Notices of the Royal Astronomical Society, 351, 1151

Brown J. B. W., et al., 1974, In Reliability and Biometry: Statistical Analysis of Lifelength Edited by: Proschan, F. and Serfling, R. J., p. 64

Brusa M., et al., 2015, Monthly Notices of the Royal Astronomical Society, 446, 2394

Brusa M., et al., 2018, A&A, 612, A29

Buckle J. V., et al., 2009, Monthly Notices of the Royal Astronomical Society, 399, 1026

Burgarella D., et al., 2005, Monthly Notices of the Royal Astronomical Society, 360, 1413

Burtscher L., et al., 2013, A&A, 558, A149

Calistro Rivera G., et al., 2018, The Astrophysical Journal, 863, 56

Cano-Díaz M., et al., 2012, A&A, 537, L8

Capetti A., et al., 1996, Astrophysical Journal v.469, 469, 554

Carilli C. L., Walter F., 2013, Annual Review of Astronomy and Astrophysics, 51, 105

Carniani S., et al., 2015, A&A, 580, A102

Carniani S., et al., 2016, A&A, 591, A28

Carniani S., et al., 2017, A&A, 605, A105

Carniani S., et al., 2019, Monthly Notices of the Royal Astronomical Society, 489, 3939

Carpenter B., et al., 2017, Journal of Statistical Software, Articles, 76, 1

Carvajal R., et al., 2020, A&A, 633, A160

Casasola V., et al., 2017, A&A, 605, A18

Casasola V., et al., 2020, A&A, 633, A100

Casey C. M., 2012, Monthly Notices of the Royal Astronomical Society, 425, 3094

Casey C. M., et al., 2014, Physics Reports, 541, 45

Catinella B., et al., 2013, Monthly Notices of the Royal Astronomical Society, 436, 34

Cazzoli S., et al., 2016, A&A, 590, A125

Ceccarelli C., et al., 2018, Monthly Notices of the Royal Astronomical Society, 476, 1371

Chabrier G., 2003, The Publications of the Astronomical Society of the Pacific, 115, 763

Chang Y.-Y., et al., 2020, The Astrophysical Journal, 888, 44

Chary R., Elbaz D., 2001, The Astrophysical Journal, 556, 562

Chawner H., et al., 2019, Monthly Notices of the Royal Astronomical Society, 483, 70

Chen C.-C., et al., 2015, The Astrophysical Journal, 799, 194

Chen C.-C., et al., 2017, The Astrophysical Journal, 846, 108

Chen C.-C., et al., 2020, A&A, 635, A119

Cherchneff I., Dwek E., 2010, The Astrophysical Journal, 713, 1

Cicone C., et al., 2012, A&A, 543, A99

Cicone C., et al., 2014, A&A, 562, A21

Cicone C., et al., 2015, A&A, 574, A14

Cicone C., et al., 2018, Nature Astronomy, 2, 176

Ciesla L., et al., 2012, A&A, 543, A161

Circosta C., et al., 2018, A&A, 620, A82

Circosta C., et al., 2019, A&A, 623, A172

Civano F., et al., 2016, The Astrophysical Journal, 819, 62

Clark C. J. R., et al., 2015, Monthly Notices of the Royal Astronomical Society, 452, 397

Clark C. J. R., et al., 2016, Monthly Notices of the Royal Astronomical Society, 459, 1646

Clark C. J. R., et al., 2019, Monthly Notices of the Royal Astronomical Society, 489, 5256

Clarke A. O., et al., 2017, A&A, 601, A25

Clemens M. S., et al., 2013, Monthly Notices of the Royal Astronomical Society, 433, 695

Clements D. L., et al., 1996, Monthly Notices of the Royal Astronomical Society, 279, 459

Coil A. L., et al., 2015, The Astrophysical Journal, 801, 35

Combes F., et al., 2019, A&A, 623, A79

Compiègne M., et al., 2011, A&A, 525, A103

Concas A., Popesso P., 2019, Monthly Notices of the Royal Astronomical Society: Letters, 486, L91

Concas A., et al., 2019, A&A, 622, A188

Conley A., et al., 2011, The Astrophysical Journal Letters, 732, L35

Corcho-Caballero P., et al., 2020, arXiv

Cortese L., et al., 2012, A&A, 540, A52

Cortese L., et al., 2014, Monthly Notices of the Royal Astronomical Society, 440, 942

Cortzen I., et al., 2020, A&A, 634, L14

Costa T., et al., 2014, Monthly Notices of the Royal Astronomical Society, 444, 2355

Costa T., et al., 2018, Monthly Notices of the Royal Astronomical Society, 479, 2079

Costa T., et al., 2020, Monthly Notices of the Royal Astronomical Society, 497, 5229

Coupeaud A., et al., 2011, A&A, 535, A124

Cowie L. L., Songaila A., 1977, Nature, 266, 501

Crain R. A., et al., 2015, Monthly Notices of the Royal Astronomical Society, 450, 1937

Crenshaw D. M., et al., 2010, The Astrophysical Journal, 708, 419

Cresci G., Maiolino R., 2018, Nature Astronomy, 2, 179

Cresci G., et al., 2015a, A&A, 582, A63

Cresci G., et al., 2015b, The Astrophysical Journal, 799, 82

Croft S., et al., 2006, The Astrophysical Journal, 647, 1040

Currie M. J., et al., 2014, in Astronomical Data Analysis Software and Systems XXIII. Proceedings of a meeting held 29 September - 3 October 2013 at Waikoloa Beach Marriott. pp 391–

D'Agostino J. J., et al., 2019, Monthly Notices of the Royal Astronomical Society: Letters, 485, L38

D'Amato Q., et al., 2020, A&A, 636, A37

Daddi E., et al., 2007, The Astrophysical Journal, 670, 156

Daddi E., et al., 2009, The Astrophysical Journal, 694, 1517

Daddi E., et al., 2010, The Astrophysical Journal, 713, 686

Dale D. A., Helou G., 2002, The Astrophysical Journal, 576, 159

Dale D. A., et al., 2014, The Astrophysical Journal, 784, 83

Davé R., et al., 2019, Monthly Notices of the Royal Astronomical Society, 486, 2827

Davies J. I., et al., 2017, Publications of the Astronomical Society of the Pacific, 129, 044102

De Looze I., et al., 2014a, A&A, 568, A62

De Looze I., et al., 2014b, A&A, 571, A69

De Looze I., et al., 2017, Monthly Notices of the Royal Astronomical Society, 465, 3309

De Looze I., et al., 2020, Monthly Notices of the Royal Astronomical Society, 496, 3668

De Vis P., et al., 2017, Monthly Notices of the Royal Astronomical Society, 464, 4680

Decarli R., et al., 2014, The Astrophysical Journal, 782, 78

Decarli R., et al., 2016, The Astrophysical Journal, 833, 70

Decarli R., et al., 2019, The Astrophysical Journal, 882, 138

Decin L., Eriksson K., 2007, A&A, 472, 1041

Dell'Agli F., et al., 2015, Monthly Notices of the Royal Astronomical Society, 454, 4235

Demyk K., et al., 2001, A&A, 368, L38

Demyk K., et al., 2017a, A&A, 600, A123

Demyk K., et al., 2017b, A&A, 606, A50

Désert F. X., et al., 1990, Astronomy and Astrophysics (ISSN 0004-6361), 237, 215

Désert F. X., et al., 2008, A&A, 481, 411

Devereux N. A., Young J. S., 1990, Astrophysical Journal, 359, 42

Dicken D., et al., 2008, The Astrophysical Journal, 678, 712

Dickman R. L., et al., 1986, Astrophysical Journal, 309, 326

Downes D., Solomon P. M., 1998, The Astrophysical Journal, 507, 615

Draine B. T., 1978, Astrophysical Journal Supplement Series, 36, 595

Draine B. T., 2003, Annual Review of Astronomy &Astrophysics, 41, 241

Draine B. T., Hensley B., 2012, The Astrophysical Journal, 757, 103

Draine B. T., Lee H. M., 1984, Astrophysical Journal, 285, 89

Draine B. T., Li A., 2001, The Astrophysical Journal, 551, 807

Draine B. T., Li A., 2007, The Astrophysical Journal, 657, 810

Duane S., et al., 1987, Physics Letters B, 195, 216

Duley W. W., 1987, Monthly Notices of the Royal Astronomical Society (ISSN 0035-8711), 229, 203

Dullemond C. P., van Bemmel I. M., 2005, A&A, 436, 47

Dumke M., et al., 2004, A&A, 414, 475

Dunne L., et al., 2000, Monthly Notices of the Royal Astronomical Society, 315, 115

Dupac X., et al., 2003, A&A, 404, L11

Dwek E., et al., 1997, The Astrophysical Journal, 475, 565

Eales S., et al., 2010, Publications of the Astronomical Society of the Pacific, 122, 499

Eales S., et al., 2017, Monthly Notices of the Royal Astronomical Society, 465, 3125

Edmunds M. G., 2001, Monthly Notices of the Royal Astronomical Society, 328, 223

Elbaz D., et al., 2007, A&A, 468, 33

Elbaz D., et al., 2011, A&A, 533, A119

Elbaz D., et al., 2018, A&A, 616, A110

Elitzur M., Shlosman I., 2006, The Astrophysical Journal, 648, L101

Ellison S. L., et al., 2016, Monthly Notices of the Royal Astronomical Society: Letters, 458, L34

Elvis M., et al., 1994, The Astrophysical Journal Supplement Series, 95, 1

Erb D. K., et al., 2006, The Astrophysical Journal, 647, 128

Fabian A. C., 1994, Annual Review of Astronomy and Astrophysics, 32, 277

Fabian A. C., 2012, Annual Review of Astronomy and Astrophysics, 50, 455

Faisst A. L., et al., 2020, The Astrophysical Journal Supplement Series, 247, 61

Falkendal T., et al., 2019, A&A, 621, A27

Fanciullo L., et al., 2020, arXiv, p. arXiv:2009.10304

Fang J. J., et al., 2013, The Astrophysical Journal, 776, 63

Feigelson E. D., Nelson P. I., 1985, Astrophysical Journal, 293, 192

Ferrara A., et al., 2016, Monthly Notices of the Royal Astronomical Society: Letters, 463, L112

Ferrarotti A. S., Gail H. P., 2006, A&A, 447, 553

Feruglio C., et al., 2010, A&A, 518, L155

Feruglio C., et al., 2017, A&A, 608, A30

Fiore F., et al., 2017, A&A, 601, A143

Fluetsch A., et al., 2019, Monthly Notices of the Royal Astronomical Society, 483, 4586

Fluetsch A., et al., 2020, arXiv

Foreman-Mackey D., 2016, The Journal of Open Source Software, 24

Foreman-Mackey D., et al., 2013, Publications of the Astronomical Society of Pacific, 125, 306

Förster Schreiber N. M., et al., 2014, The Astrophysical Journal, 787, 38

Fritz J., et al., 2006, Monthly Notices of the Royal Astronomical Society, 366, 767

Fujimoto S., et al., 2017, The Astrophysical Journal, 850, 83

Fujimoto S., et al., 2018, The Astrophysical Journal, 861, 7

Gabor J. M., Bournaud F., 2014, Monthly Notices of the Royal Astronomical Society, 441, 1615

Gaches B. A. L., et al., 2019, The Astrophysical Journal, 883, 190

Gaia Collaboration et al., 2016, A&A, 595, A1

Gaia Collaboration et al., 2018, A&A, 616, A1

Galametz M., et al., 2009, A&A, 508, 645

Galametz M., et al., 2011, A&A, 532, A56

Galametz M., et al., 2012, Monthly Notices of the Royal Astronomical Society, 425, 763

Gall C., Hjorth J., 2018, The Astrophysical Journal, 868, 62

Gall C., et al., 2011, The Astronomy and Astrophysics Review, 19, 43

Gall C., et al., 2014, Nature, 511, 326

Gallagher R., et al., 2019, Monthly Notices of the Royal Astronomical Society, 485, 3409

Galliano F., 2018, Monthly Notices of the Royal Astronomical Society

Galliano F., et al., 2003, A&A, 407, 159

Galliano F., et al., 2011, A&A, 536, A88

Galliano F., et al., 2018, Annual Review of Astronomy and Astrophysics, 56, 673

Gallimore J. F., et al., 2016, The Astrophysical Journal Letters, 829, L7

Gao Y., Solomon P. M., 2004a, The Astrophysical Journal Supplement Series, 152, 63

Gao Y., Solomon P. M., 2004b, The Astrophysical Journal, 606, 271

García-Burillo S., et al., 2012, A&A, 539, A8

García-Burillo S., et al., 2016, The Astrophysical Journal Letters, 823, L12

Gelman A., Hill J., 2007, Cambridge University Press

Gelman A., Rubin D. B., 1992, Statistical Science, 7, 457

Gelman A., et al., 2004, Chapman and Hall/CRC

Genzel R., et al., 2015, The Astrophysical Journal, 800, 20

George I. M., Fabian A. C., 1991, Monthly Notices of the Royal Astronomical Society (ISSN 0035-8711), 249, 352

George M. R., et al., 2008, Monthly Notices of the Royal Astronomical Society: Letters, 388, L59

Ginsburg A., Mirocha J., 2011, PySpecKit: Python Spectroscopic Toolkit (ascl:1109.001)

Glover S. C. O., Clark P. C., 2016, Monthly Notices of the Royal Astronomical Society, 456, 3596

González-Alfonso E., et al., 2017, The Astrophysical Journal, 836, 11

Goodman J., Weare J., 2010, Communications in Applied Mathematics and Computational Science, 5, 65

Gordon K. D., et al., 2014, The Astrophysical Journal, 797, 85

Gould R. J., Salpeter E. E., 1963, Astrophysical Journal, 138, 393

Gracia-Carpio J., et al., 2008, A&A, 479, 703

Greenberg J. M., 1986, Universitaets-Sternwarte Jena, 128, 17

Grimmett L. P., et al., 2020, Monthly Notices of the Royal Astronomical Society, 495, 1392

Groves B. A., et al., 2015, The Astrophysical Journal, 799, 96

Gullberg B., et al., 2019, Monthly Notices of the Royal Astronomical Society, 490, 4956

Gunn J. E., Gott J. R. I., 1972, Astrophysical Journal, 176, 1

Haardt F., Maraschi L., 1991, Astrophysical Journal, 380, L51

Hada K., et al., 2013, The Astrophysical Journal, 779, 6

Hambrick D. C., et al., 2011, The Astrophysical Journal, 738, 16

Hao C.-N., et al., 2011, The Astrophysical Journal, 741, 124

Hardcastle M. J., et al., 2013, Monthly Notices of the Royal Astronomical Society, 429, 2407

Harris A. I., et al., 2010, The Astrophysical Journal, 723, 1139

Harrison C. M., 2014, PhD Thesis, Durham University

Harrison C. M., 2017, Nature Astronomy, 1, 0165

Harrison C. M., et al., 2012, Monthly Notices of the Royal Astronomical Society, 426, 1073

Harrison C. M., et al., 2016a, Monthly Notices of the Royal Astronomical Society, 456, 1195

Harrison C. M., et al., 2016b, Monthly Notices of the Royal Astronomical Society: Letters, 457, L122

Harrison C. M., et al., 2018, Nature Astronomy, 2, 198

Hashimoto T., et al., 2019, Publications of the Astronomical Society of Japan, 71, 71

Heckman T. M., Best P. N., 2014, Annual Review of Astronomy and Astrophysics, 52, 589

Heinis S., et al., 2013, Monthly Notices of the Royal Astronomical Society, 429, 1113

Hermelo I., et al., 2016, A&A, 590, A56

Herrera-Camus R., et al., 2015, The Astrophysical Journal, 800, 1

Herrera-Camus R., et al., 2019, The Astrophysical Journal, 871, 37

Herrera-Camus R., et al., 2020, A&A, 635, A47

Hickox R. C., Alexander D. M., 2018, Annual Review of Astronomy and Astrophysics, 56, 625

Hickox R. C., et al., 2009, The Astrophysical Journal, 696, 891

Hickox R. C., et al., 2014, The Astrophysical Journal, 782, 9

Hildebrand R. H., 1983, Quarterly Journal of the Royal Astronomical Society, 24, 267

Hirashita H., 2012, Monthly Notices of the Royal Astronomical Society, 422, 1263

Hoaglin D. C., et al., 1983, Wiley Series in Probability and Mathematical Statistics

Hodge J. A., da Cunha E., 2020, arXiv, p. arXiv:2004.00934

Hodge J. A., et al., 2013, The Astrophysical Journal, 768, 91

Hodge J. A., et al., 2015, The Astrophysical Journal Letters, 798, L18

Hodge J. A., et al., 2016, The Astrophysical Journal, 833, 103

Hollenbach D. J., Tielens A. G. G. M., 1999, Reviews of Modern Physics, 71, 173

Hönig S. F., 2019, The Astrophysical Journal, 884, 171

Hönig S. F., Kishimoto M., 2010, A&A, 523, A27

Hönig S. F., Kishimoto M., 2017, The Astrophysical Journal Letters, 838, L20

Hönig S. F., et al., 2012, The Astrophysical Journal, 755, 149

Hönig S. F., et al., 2013, The Astrophysical Journal, 771, 87

Hopkins P. F., et al., 2016, Monthly Notices of the Royal Astronomical Society, 458, 816

Hsu L.-T., et al., 2014, The Astrophysical Journal, 796, 60

Hughes T. M., et al., 2013, A&A, 550, A115

Hughes T. M., et al., 2017, A&A, 602, A49

Hunt L. K., et al., 2015, A&A, 576, A33

Hunt L. K., et al., 2019, A&A, 621, A51

Hunter J. D., 2007, Computing in Science and Engineering, 9, 90

Husemann B., et al., 2017, Monthly Notices of the Royal Astronomical Society, 470, 1570

Husemann B., et al., 2019, A&A, 627, A53

Huynh M. T., et al., 2012, Monthly Notices of the Royal Astronomical Society, 426, 2342

Ichikawa K., et al., 2019, The Astrophysical Journal, 870, 31

Ikarashi S., et al., 2015, The Astrophysical Journal, 810, 133

Imanishi M., et al., 2016, The Astrophysical Journal Letters, 822, L10

Indriolo N., McCall B. J., 2012, The Astrophysical Journal, 745, 91

Indriolo N., et al., 2015, The Astrophysical Journal, 800, 40

Isobe T., et al., 1990, Astrophysical Journal, 364, 104

Israel F. P., 1997, A&A, 328, 471

Israel F. P., et al., 2010, A&A, 519, A67

Ivison R. J., et al., 2011, Monthly Notices of the Royal Astronomical Society, 412, 1913

Jahnke K., Macciò A. V., 2011, The Astrophysical Journal, 734, 92

Jansen F., et al., 2001, A&A, 365, L1

Janssen A. W., et al., 2016, The Astrophysical Journal, 822, 43

Jarrett T. H., et al., 2011, The Astrophysical Journal, 735, 112

Jarvis M. E., et al., 2020, Monthly Notices of the Royal Astronomical Society

Jiang X.-J., et al., 2020, Monthly Notices of the Royal Astronomical Society, 494, 1276

Jiao Q., et al., 2017, The Astrophysical Journal Letters, 840, L18

Jiao Q., et al., 2019, The Astrophysical Journal, 880, 133

Jones A. P., Nuth J. A., 2011, A&A, 530, A44

Jones A. P., et al., 1987, Monthly Notices of the Royal Astronomical Society (ISSN 0035-8711), 229, 213

Jones A. P., et al., 2013, A&A, 558, A62

Jones A. P., et al., 2017, A&A, 602, A46

Jones G. C., et al., 2020, arXiv, p. arXiv:2009.00674

Juvela M., et al., 2013, A&A, 556, A63

Kaasinen M., et al., 2019, The Astrophysical Journal, 880, 15

Kaasinen M., et al., 2020, arXiv, p. arXiv:2007.03697

Kakkad D., et al., 2017, Monthly Notices of the Royal Astronomical Society, 468, 4205

Kakkad D., et al., 2020, arXiv, p. arXiv:2008.01728

Karim A., et al., 2013, Monthly Notices of the Royal Astronomical Society, 432, 2

Karouzos M., et al., 2014, The Astrophysical Journal, 784, 137

Kauffmann G., et al., 2003, Monthly Notices of the Royal Astronomical Society, 346, 1055

Kelly B. C., et al., 2012, The Astrophysical Journal, 752, 55

Kennicutt R. C. J., 1998, The Astrophysical Journal, 498, 541

Kennicutt R. C., Evans N. J., 2012, Annual Review of Astronomy and Astrophysics, 50, 531

Kennicutt R. C., et al., 2011, Publications of the Astronomical Society of the Pacific, 123, 1347

Kewley L. J., et al., 2001, The Astrophysical Journal, 556, 121

Kewley L. J., et al., 2013a, The Astrophysical Journal Letters, 774, L10

Kewley L. J., et al., 2013b, The Astrophysical Journal, 774, 100

King A., Nixon C., 2015, Monthly Notices of the Royal Astronomical Society: Letters, 453, L46

King A., Pounds K., 2015, Annual Review of Astronomy and Astrophysics, 53, 115

Kirchschlager F., et al., 2020, The Astrophysical Journal, 893, 70

Kirkpatrick A., et al., 2014, The Astrophysical Journal, 789, 130

Kirkpatrick A., et al., 2019, American Astronomical Society, 233, 310.07

Knudsen K. K., et al., 2016, Monthly Notices of the Royal Astronomical Society: Letters, 462, L6

Knudsen K. K., et al., 2017, Monthly Notices of the Royal Astronomical Society, 466, 138

Kocevski D. D., et al., 2018, The Astrophysical Journal Supplement Series, 236, 48

Köhler M., et al., 2015, A&A, 579, A15

Kohno K., et al., 2002, Publications of the Astronomical Society of Japan, 54, 541

Komugi S., et al., 2007, Publications of the Astronomical Society of Japan, 59, 55

Kormendy J., Ho L. C., 2013, Annual Review of Astronomy and Astrophysics, 51, 511

Kormendy J., Richstone D., 1995, Annual Review of Astronomy and Astrophysics, 33, 581

Koss M., et al., 2017, The Astrophysical Journal, 850, 74

Koss M. J., et al., 2020, arXiv, p. arXiv:2010.15849

Kreckel K., et al., 2013, The Astrophysical Journal, 771, 62

Lagos C. D. P., et al., 2011, Monthly Notices of the Royal Astronomical Society, 418, 1649

Laigle C., et al., 2016, The Astrophysical Journal Supplement Series, 224, 24

Lamperti I., et al., 2019, Monthly Notices of the Royal Astronomical Society, 489, 4389

Lamperti I., et al., 2020, The Astrophysical Journal, 889, 103

Lang D., 2014, The Astronomical Journal, 147, 108

Lang P., et al., 2019, The Astrophysical Journal, 879, 54

Laporte N., et al., 2017, The Astrophysical Journal Letters, 837, L21

Larson R. B., et al., 1980, Astrophysical Journal, 237, 692

Lau R. M., et al., 2015, Science, 348, 413

Leech J., et al., 2010, Monthly Notices of the Royal Astronomical Society, 406, 1364

Leftley J. H., et al., 2018, The Astrophysical Journal, 862, 17

Lenkić L., et al., 2020, The Astronomical Journal, 159, 190

Leroy A. K., et al., 2008, The Astronomical Journal, 136, 2782

Leroy A. K., et al., 2009, The Astronomical Journal, 137, 4670

Leroy A. K., et al., 2011, The Astrophysical Journal, 737, 12

Leslie S. K., et al., 2016, Monthly Notices of the Royal Astronomical Society: Letters, 455, L82

Lewandowski D., et al., 2009, Journal of Multivariate Analysis, 100:1989–2001, 556

Li A., Draine B. T., 2001, The Astrophysical Journal, 554, 778

Li A., Draine B. T., 2002, The Astrophysical Journal, 576, 762

Liang L., et al., 2019, Monthly Notices of the Royal Astronomical Society, 489, 1397

Lilly S. J., et al., 1996, Astrophysical Journal Letters v.460, 460, L1

Lilly S. J., et al., 2013, The Astrophysical Journal, 772, 119

Lisenfeld U., et al., 2002, A&A, 382, 860

Liu X., et al., 2008, The Astrophysical Journal, 678, 758

Liu D., et al., 2019a, The Astrophysical Journal Supplement Series, 244, 40

Liu D., et al., 2019b, The Astrophysical Journal, 887, 235

Loiacono F., et al., 2019, Monthly Notices of the Royal Astronomical Society, 489, 681

López-Gonzaga N., et al., 2014, A&A, 565, A71

López-Gonzaga N., et al., 2016, A&A, 591, A47

Lu N., et al., 2017, The Astrophysical Journal Supplement Series, 230, 1

Luo B., et al., 2017, The Astrophysical Journal Supplement Series, 228, 2

Lutz D., et al., 2010, The Astrophysical Journal, 712, 1287

Lutz D., et al., 2011, A&A, 532, A90

Lutz D., et al., 2018, A&A, 609, A9

Ma X., et al., 2019, Monthly Notices of the Royal Astronomical Society, 487, 1844

Madau P., Dickinson M., 2014, Annual Review of Astronomy and Astrophysics, 52, 415

Madau P., Shull J. M., 1996, Astrophysical Journal v.457, 457, 551

Madau P., et al., 1996, Monthly Notices of the Royal Astronomical Society, 283, 1388

Madau P., et al., 1998, The Astrophysical Journal, 498, 106

Madden S. C., et al., 1997, The Astrophysical Journal, 483, 200

Madden S. C., et al., 2013, Publications of the Astronomical Society of the Pacific, 125, 600

Maddox S. J., et al., 2018, The Astrophysical Journal Supplement Series, 236, 30

Magdis G. E., et al., 2010, The Astrophysical Journal, 714, 1740

Magdis G. E., et al., 2011, The Astrophysical Journal Letters, 740, L15

Magdis G. E., et al., 2012, The Astrophysical Journal, 760, 6

Magnelli B., et al., 2014, A&A, 561, A86

Magnelli B., et al., 2020, The Astrophysical Journal, 892, 66

Magorrian J., et al., 1998, The Astronomical Journal, 115, 2285

Mainieri V., et al., 2002, A&A, 393, 425

Mainieri V., et al., 2011, A&A, 535, A80

Maiolino R., et al., 2012, Monthly Notices of the Royal Astronomical Society: Letters, 425, L66

Maiolino R., et al., 2017, Nature, 544, 202

Mancini C., et al., 2011, The Astrophysical Journal, 743, 86

Mao R.-Q., et al., 2010, The Astrophysical Journal, 724, 1336

Marasco A., et al., 2020, arXiv, p. arXiv:2009.11294

Marchesi S., et al., 2016, The Astrophysical Journal, 817, 34

Marconi A., et al., 2004, Monthly Notices of the Royal Astronomical Society, 351, 169

Martig M., et al., 2009, The Astrophysical Journal, 707, 250

Mashian N., et al., 2015, The Astrophysical Journal, 802, 81

Masoura V. A., et al., 2018, A&A, 618, A31

Mathis J. S., et al., 1977, Astrophysical Journal, 217, 425

Matsuura M., et al., 2019, Monthly Notices of the Royal Astronomical Society, 482, 1715

Matt G., et al., 1991, Astronomy and Astrophysics (ISSN 0004-6361), 247, 25

Matthews T. A., et al., 1964, Astrophysical Journal, 140, 35

Mauersberger R., et al., 1999, A&A, 341, 256

McClure M. K., et al., 2016, The Astrophysical Journal, 831, 167

McKee C. F., Ostriker E. C., 2007, Annual Review of Astronomy and Astrophysics, 45, 565

McNamara B. R., Nulsen P. E. J., 2007, Annual Review of Astronomy and Astrophysics, 45, 117

McNamara B. R., Nulsen P. E. J., 2012, New Journal of Physics, 14, 055023

Meijerink R., Spaans M., 2005, A&A, 436, 397

Meijerink R., et al., 2006, The Astrophysical Journal, 650, L103

Meisner A. M., et al., 2016, American Astronomical Society, 227, 140.03

Meléndez M., et al., 2014, The Astrophysical Journal, 794, 152

Meny C., et al., 2007, A&A, 468, 171

Metropolis N., et al., 1953, The Journal of Chemical Physics, 21, 1087

Micelotta E. R., et al., 2016, A&A, 590, A65

Michałowski M. J., 2015, A&A, 577, A80

Miller N. A., et al., 2013, The Astrophysical Journal Supplement, 205, 13

Miville-Deschênes M.-A., Lagache G., 2005, The Astrophysical Journal Supplement Series, 157, 302

Morgan H. L., Edmunds M. G., 2003, Monthly Notice of the Royal Astronomical Society, 343, 427

Morganti R., et al., 2015, A&A, 580, A1

Morganti R., et al., 2016, A&A, 593, A30

Morokuma-Matsui K., Muraoka K., 2017, The Astrophysical Journal, 837, 137

Moster B. P., et al., 2013, Monthly Notices of the Royal Astronomical Society, 428, 3121

Mullaney J. R., et al., 2011, Monthly Notices of the Royal Astronomical Society, 414, 1082

Mullaney J. R., et al., 2015, Monthly Notices of the Royal Astronomical Society: Letters, 453, L83

Muraoka K., et al., 2007, Publications of the Astronomical Society of Japan, 59, 43

Murphy K. D., Yaqoob T., 2009, Monthly Notices of the Royal Astronomical Society, 397, 1549

Murphy E. J., et al., 2011, The Astrophysical Journal, 737, 67

Mushotzky R., 2004, Supermassive Black Holes in the Distant Universe. Edited by Amy J. Barger, 308, 53

Nandra K., Pounds K. A., 1994, Monthly Notices of the Royal Astronomical Society, 268, 405

Nanni A., et al., 2013, Monthly Notices of the Royal Astronomical Society, 434, 2390

Nanni A., et al., 2014, Monthly Notices of the Royal Astronomical Society, 438, 2328

Nardini E., et al., 2015, Science, 347, 860

Neal R. M., 1994, Journal of Computational Physics (ISSN 0021-9991), 111, 194

Neal R., 2011, MCMC using Hamiltonian dynamics. In Brooks, S., AGelman, A., Jones, G.L. and Meng, X.L., editors, *Handbook of Markov Chain Monte Carlo*, Chapman and Hall/CRC., pp 116–162

Nenkova M., et al., 2002, The Astrophysical Journal, 570, L9

Nersesian A., et al., 2020, A&A, 637, A25

Netzer H., 2013, The Physics and Evolution of Active Galactic Nuclei

Ni Q., et al., 2020, arXiv, p. arXiv:2007.04987

Noeske K. G., et al., 2007, The Astrophysical Journal, 660, L43

Noll S., et al., 2009, A&A, 507, 1793

Novak G. S., et al., 2011, The Astrophysical Journal, 737, 26

Nulsen P. E. J., 1982, Monthly Notices of the Royal Astronomical Society, 198, 1007

Obreschkow D., et al., 2009, The Astrophysical Journal, 702, 1321

Oh K., 2014, PhD Thesis, The Graduate School Yonsey University

Oliver S. J., et al., 2012, Monthly Notices of the Royal Astronomical Society, 424, 1614

Olsen K., et al., 2017, The Astrophysical Journal, 846, 105

Omont A., 2007, Reports on Progress in Physics, 70, 1099

Oosterloo T., et al., 2017, A&A, 608, A38

Osterbrock D. E., Ferland G. J., 2006, Astrophysics of gaseous nebulae and active galactic nuclei

Packham C., et al., 2005, The Astrophysical Journal, 618, L17

Padovani P., 2017, Nature Astronomy, 1, 0194

Padovani M., et al., 2009, A&A, 501, 619

Page M. J., et al., 2012, Nature, 485, 213

Pannella M., et al., 2009, The Astrophysical Journal Letters, 698, L116

Pannella M., et al., 2015, The Astrophysical Journal, 807, 141

Papadopoulos P. P., Greve T. R., 2004, The Astrophysical Journal, 615, L29

Papadopoulos P. P., et al., 2012, Monthly Notices of the Royal Astronomical Society, 426, 2601

Peng C. Y., 2007, The Astrophysical Journal, 671, 1098

Peng Y.-j., et al., 2010, The Astrophysical Journal, 721, 193

Peng Y.-j., et al., 2012, The Astrophysical Journal, 757, 4

Perna M., et al., 2017, A&A, 606, A96

Perna M., et al., 2018, A&A, 619, A90

Perna M., et al., 2020, arXiv, p. arXiv:2009.03353

Peterson J. R., Fabian A. C., 2006, Physics Reports, 427, 1

Pettini M., Pagel B. E. J., 2004, Monthly Notices of the Royal Astronomical Society, 348, L59

Piconcelli E., et al., 2005, A&A, 432, 15

Pier E. A., Krolik J. H., 1992, Astrophysical Journal, 401, 99

Pierre M., et al., 2016, A&A, 592, A1

Pilbratt G. L., et al., 2010, A&A, 518, L1

Pineda J. L., et al., 2013, A&A, 554, A103

Polletta M., et al., 2000, A&A, 362, 75

Pope A., et al., 2006, Monthly Notices of the Royal Astronomical Society, 370, 1185

Popescu C. C., et al., 2011, A&A, 527, A109

Popesso P., et al., 2020, Monthly Notices of the Royal Astronomical Society, 496, 2531

Popping G., et al., 2014a, Monthly Notices of the Royal Astronomical Society, 442, 2398

Popping G., et al., 2014b, Monthly Notices of the Royal Astronomical Society, 444, 1301

Priddey R. S., et al., 2003, Monthly Notices of the Royal Astronomical Society, 344, L74

Priestley F. D., et al., 2017, Monthly Notices of the Royal Astronomical Society, 472, 4444

Privon G. C., et al., 2018, The Astrophysical Journal, 867, 102

Querejeta M., et al., 2016, A&A, 593, A118

Radomski J. T., et al., 2008, The Astrophysical Journal, 681, 141

Rafferty D. A., et al., 2006, The Astrophysical Journal, 652, 216

Ramasawmy J., et al., 2019, Monthly Notices of the Royal Astronomical Society, 486, 4320

Ramos Almeida C., Ricci C., 2017, Nature Astronomy, 1, 679

Relaño M., et al., 2018, A&A, 613, A43

Rémy-Ruyer A., et al., 2013, A&A, 557, A95

Rémy-Ruyer A., et al., 2014, A&A, 563, A31

Rémy-Ruyer A., et al., 2015, A&A, 582, A121

Rho J., et al., 2018, Monthly Notices of the Royal Astronomical Society, 479, 5101

Ricci C., et al., 2011, A&A, 532, A102

Ricci C., et al., 2017, The Astrophysical Journal Supplement Series, 233, 17

Riechers D. A., et al., 2011, The Astrophysical Journal Letters, 739, L31

Riechers D. A., et al., 2013, Nature, 496, 329

Riechers D. A., et al., 2019, The Astrophysical Journal, 872, 7

Risaliti G., Elvis M., 2004, Supermassive Black Holes in the Distant Universe. Edited by Amy J. Barger, 308, 187

Roberts-Borsani G. W., Saintonge A., 2019, Monthly Notices of the Royal Astronomical Society, 482, 4111

Robitaille T., Bressert E., 2012, Astrophysics Source Code Library, p. ascl:1208.017

Rodighiero G., et al., 2011, The Astrophysical Journal Letters, 739, L40

Rodighiero G., et al., 2015, The Astrophysical Journal Letters, 800, L10

Roos O., et al., 2015, The Astrophysical Journal, 800, 19

Rosario D. J., et al., 2013, A&A, 560, A72

Rosario D. J., et al., 2018, Monthly Notices of the Royal Astronomical Society, 473, 5658

Rosario D. J., et al., 2019, The Astrophysical Journal Letters, 875, L8

Rosenberg M. J. F., et al., 2015, The Astrophysical Journal, 801, 72

Rowlands K., et al., 2014, Monthly Notices of the Royal Astronomical Society, 441, 1040

Saintonge A., et al., 2011a, Monthly Notices of the Royal Astronomical Society, 415, 32

Saintonge A., et al., 2011b, Monthly Notices of the Royal Astronomical Society, 415, 61

Saintonge A., et al., 2012, The Astrophysical Journal, 758, 73

Saintonge A., et al., 2013, The Astrophysical Journal, 778, 2

Saintonge A., et al., 2016, Monthly Notices of the Royal Astronomical Society, 462, 1749

Saintonge A., et al., 2017, The Astrophysical Journal Supplement Series, 233, 22

Saintonge A., et al., 2018, Monthly Notices of the Royal Astronomical Society, 481, 3497

Sakamoto K., et al., 1999, The Astrophysical Journal, 525, 691

Salpeter E. E., 1955, Astrophysical Journal, 121, 161

Sanders D. B., et al., 2003, The Astronomical Journal, 126, 1607

Santini P., et al., 2014, A&A, 562, A30

Santini P., et al., 2015, The Astrophysical Journal, 801, 97

Sargent M. T., et al., 2012, The Astrophysical Journal Letters, 747, L31

Schaerer D., et al., 2020, arXiv, p. arXiv:2002.00979

Schawinski K., et al., 2007, Monthly Notices of the Royal Astronomical Society, 382, 1415

Schawinski K., et al., 2015, Monthly Notices of the Royal Astronomical Society, 451, 2517

Schaye J., et al., 2015, Monthly Notices of the Royal Astronomical Society, 446, 521

Schinnerer E., et al., 2007, The Astrophysical Journal Supplement Series, 172, 46

Schlickeiser R., et al., 2016, The Astrophysical Journal, 824, 89

Schmidt M., 1959, Astrophysical Journal, 129, 243

Schneider R., et al., 2014, Monthly Notices of the Royal Astronomical Society, 442, 1440

Schneider R., et al., 2015, A&A, 579, A60

Schödel R., et al., 2003, The Astrophysical Journal, 596, 1015

Scholtz J., et al., 2018, Monthly Notices of the Royal Astronomical Society, 475, 1288

Scholtz J., et al., 2020, Monthly Notices of the Royal Astronomical Society, 492, 3194

Schreiber C., et al., 2015, A&A, 575, A74

Schreiber C., et al., 2018, A&A, 609, A30

Schwarz G., 1978, Ann. Statist., 6(2), 461

Scourfield M., et al., 2020, arXiv, pp 5308–5329

Scoville N., et al., 2007, The Astrophysical Journal Supplement Series, 172, 1

Scoville N., et al., 2014a, American Astronomical Society, 223, 130.04

Scoville N., et al., 2014b, The Astrophysical Journal, 783, 84

Scoville N., et al., 2016, The Astrophysical Journal, 820, 83

Scoville N., et al., 2017, The Astrophysical Journal, 837, 150

Shakura N. I., Sunyaev R. A., 1973, A&A, 24, 337

Shangguan J., et al., 2020, The Astrophysical Journal Supplement Series, 247, 15

Shankar F., et al., 2009, The Astrophysical Journal, 690, 20

Shapiro S. L., et al., 1983, Physics Today, 36, 89

Shapley A. E., et al., 2005, The Astrophysical Journal, 635, 1006

Shapley A. E., et al., 2015, The Astrophysical Journal, 801, 88

Sharon C. E., et al., 2016, The Astrophysical Journal, 827, 18

Shaw G., et al., 2008, The Astrophysical Journal, 675, 405

Sheth K., et al., 2005, The Astrophysical Journal, 632, 217

Shetty R., et al., 2009a, The Astrophysical Journal, 696, 676

Shetty R., et al., 2009b, The Astrophysical Journal, 696, 2234

Shibatsuka T., et al., 2003, Publications of the Astronomical Society of Japan, 55, 87

Shimizu T. T., et al., 2017, Monthly Notices of the Royal Astronomical Society, 466, 3161

Shin J., et al., 2019, The Astrophysical Journal, 881, 147

Siebenmorgen R., Kruegel E., 1992, Astronomy and Astrophysics (ISSN 0004-6361), 259, 614

Siebenmorgen R., Krügel E., 2007, A&A, 461, 445

Siebenmorgen R., et al., 2014, A&A, 561, A82

Silva L., et al., 1998, The Astrophysical Journal, 509, 103

Simpson J. M., et al., 2015, The Astrophysical Journal, 799, 81

Skibba R. A., et al., 2011, The Astrophysical Journal, 738, 89

Smail I., Walter F., 2014, The Messenger, 157, 41

Smethurst R. J., et al., 2017, Monthly Notices of the Royal Astronomical Society, 469, 3670

Smith M. W. L., et al., 2012a, The Astrophysical Journal, 748, 123

Smith M. W. L., et al., 2012b, The Astrophysical Journal, 756, 40

Smith M. W. L., et al., 2019, Monthly Notices of the Royal Astronomical Society

Smolčić V., et al., 2009, The Astrophysical Journal, 696, 24

Smolčić V., et al., 2017, A&A, 602, A1

Solomon P. M., et al., 1987, Star formation in galaxies, 2466

Solomon P. M., et al., 1992, Astrophysical Journal, 387, L55

Solomon P. M., et al., 1997, The Astrophysical Journal, 478, 144

Solovyov D. I., Verkhodanov O. V., 2011, Astrophysical Bulletin, 66, 416

Somerville R. S., et al., 2008, Monthly Notices of the Royal Astronomical Society, 391, 481

Sommovigo L., et al., 2020, Monthly Notices of the Royal Astronomical Society, 497, 956

Spingola C., et al., 2020, Monthly Notices of the Royal Astronomical Society, 495, 2387

Stacey G. J., et al., 2010, The Astrophysical Journal, 724, 957

Stach S. M., et al., 2019, Monthly Notices of the Royal Astronomical Society, 487, 4648

Stalevski M., et al., 2017, Monthly Notices of the Royal Astronomical Society, 472, 3854

Stan Development Team 2017, Stan Modeling Language: User's Guide and Reference Manual. Version 2.17.0. (http://mc-stan.org)

Stan Development Team 2018, PyStan: the Python interface to Stan, Version 2.17.1.0

Stanley F., et al., 2015, Demographics and Environment of AGN from Multi-Wavelength Surveys, p. 103

Stanley F., et al., 2018, Monthly Notices of the Royal Astronomical Society, 478, 3721

Stäuber P., et al., 2005, A&A, 440, 949

Steidel C. C., et al., 2014, The Astrophysical Journal, 795, 165

Strateva I., et al., 2001, The Astronomical Journal, 122, 1861

Strong A. W., Mattox J. R., 1996, A&A, 308, L21

Sturm E., et al., 2011, The Astrophysical Journal Letters, 733, L16

Symeonidis M., 2017, Monthly Notices of the Royal Astronomical Society, 465, 1401

Symeonidis M., et al., 2013, Monthly Notices of the Royal Astronomical Society, 431, 2317

Symeonidis M., et al., 2016, Monthly Notices of the Royal Astronomical Society, 459, 257

Szokoly G. P., et al., 2004, The Astrophysical Journal Supplement Series, 155, 271

Tacconi L. J., et al., 2013, The Astrophysical Journal, 768, 74

Tacconi L. J., et al., 2018, The Astrophysical Journal, 853, 179

Tacconi L. J., et al., 2020, arXiv, p. arXiv:2003.06245

Tadaki K.-i., et al., 2017, The Astrophysical Journal, 834, 135

Tadaki K.-i., et al., 2020, arXiv, p. arXiv:2009.01976

Tak H., et al., 2018, Monthly Notices of the Royal Astronomical Society, 481, 277

Talia M., et al., 2018, Monthly Notices of the Royal Astronomical Society, 476, 3956

Tamm A., et al., 2012, A&A, 546, A4

Tan Q.-H., et al., 2018, The Astrophysical Journal, 860, 165

Taylor M. B., 2005, Astronomical Data Analysis Software and Systems XIV ASP Conference Series, 347, 29

Temim T., et al., 2015, The Astrophysical Journal, 799, 158

Temim T., et al., 2017, The Astrophysical Journal, 836, 129

Thatte N., et al., 2010, in McLean I. S., et al., eds, Society of Photo-Optical Instrumentation Engineers (SPIE) Conference Series Vol. 7735, Ground-based and Airborne Instrumentation for Astronomy III. p. 77352I

The Astropy Collaboration et al., 2013, A&A, 558, A33

Theuns T., Srianand R., 2006, in Whitelock P., et al., eds, Vol. 232, The Scientific Requirements for Extremely Large Telescopes. pp 464–471

Thirlwall J. J., et al., 2020, Monthly Notices of the Royal Astronomical Society, 495, 835

Thronson H. A. J., 1988, Galactic and Extragalactic Star Formation, 232, 621

Tombesi F., et al., 2010, A&A, 521, A57

Tombesi F., et al., 2013, Monthly Notices of the Royal Astronomical Society, 430, 1102

Tremonti C. A., et al., 2004, The Astrophysical Journal, 613, 898

Tristram K. R. W., et al., 2014, A&A, 563, A82

Utomo D., et al., 2019, The Astrophysical Journal, 874, 141

Valentino F., et al., 2018, The Astrophysical Journal, 869, 27

Vallini L., et al., 2015, The Astrophysical Journal, 813, 36

Van Der Walt S., et al., 2011, Computing in Science and Engineering, 13, 22

Vantyghem A. N., et al., 2014, Monthly Notices of the Royal Astronomical Society, 442, 3192

Velusamy T., Langer W. D., 2014, A&A, 572, A45

Venemans B., et al., 2020, arXiv e-prints

Veneziani M., et al., 2013, The Astrophysical Journal, 772, 56

Ventura P., et al., 2012, Monthly Notices of the Royal Astronomical Society, 424, 2345

Venturi G., et al., 2017, Frontiers in Astronomy and Space Sciences, 4, 46

Venturi G., et al., 2018, A&A, 619, A74

Verstocken S., et al., 2020, A&A, 637, A24

Viaene S., et al., 2017, A&A, 599, A64

Viaene S., et al., 2020, A&A, 638, A150

Vogelsberger M., et al., 2013, Monthly Notices of the Royal Astronomical Society, 436, 3031

Waelkens C., et al., 1996, A&A, 315, L245

Walter F., et al., 2014, The Astrophysical Journal, 782, 79

Walter F., et al., 2016, The Astrophysical Journal, 833, 67

Wang S. X., et al., 2013, The Astrophysical Journal, 778, 179

Ward M., et al., 1987, Astrophysical Journal, 315, 74

Waters L. B. F. M., et al., 1996, A&A, 315, L361

Watson D., et al., 2015, Nature, 519, 327

Weisskopf M. C., et al., 2000, Proc. SPIE Vol. 4012, 4012, 2

Wesson R., et al., 2015, Monthly Notices of the Royal Astronomical Society, 446, 2089

Whitaker K. E., et al., 2012, The Astrophysical Journal Letters, 754, L29

Whitaker K. E., et al., 2014, The Astrophysical Journal, 790, 143

White R. L., et al., 2000, The Astrophysical Journal Supplement Series, 126, 133

Williams T. G., et al., 2019, Monthly Notices of the Royal Astronomical Society, 487, 2753

Wilson C. D., et al., 2009, The Astrophysical Journal, 693, 1736

Wilson C. D., et al., 2012, Monthly Notices of the Royal Astronomical Society, 424, 3050

Woo J.-H., et al., 2016, The Astrophysical Journal, 817, 108

Wright C. M., et al., 1999, The Astrophysical Journal, 515, L29

Wright E. L., et al., 2010, The Astronomical Journal, 140, 1868

Wu J., et al., 2010, The Astrophysical Journal Supplement, 188, 313

Wylezalek D., et al., 2016, Monthly Notices of the Royal Astronomical Society, 457, 745

Yang M., Phillips T., 2007, The Astrophysical Journal, 662, 284

Yao L., et al., 2003, The Astrophysical Journal, 588, 771

Yesuf H. M., Ho L. C., 2019, The Astrophysical Journal, 884, 177

Ysard N., et al., 2018, A&A, 617, A124

Yuan F., Narayan R., 2014, Annual Review of Astronomy and Astrophysics, 52, 529

Zanella A., et al., 2018, Monthly Notices of the Royal Astronomical Society, 481, 1976

Zhang Z.-Y., et al., 2014, The Astrophysical Journal Letters, 784, L31

Zheng X. Z., et al., 2007, The Astrophysical Journal, 670, 301

Zhukovska S., 2014, A&A, 562, A76

Zinn P. C., et al., 2013, The Astrophysical Journal, 774, 66

Zubko V., et al., 2004, The Astrophysical Journal Supplement Series, 152, 211

da Cunha E., et al., 2008, Monthly Notices of the Royal Astronomical Society, 388, 1595

da Cunha E., et al., 2013, The Astrophysical Journal, 766, 13

da Cunha E., et al., 2015, The Astrophysical Journal, 806, 110

de Vries B. L., et al., 2010, A&A, 516, A86

van der Tak F. F. S., et al., 2018, Publications of the Astronomical Society of Australia, 35, e002